DISSERTATION

TROPICAL WARM POOL RAINFALL VARIABILITY AND IMPACT ON UPPER OCEAN

VARIABILITY THROUGHOUT THE MADDEN-JULIAN OSCILLATION

Submitted by

Elizabeth J. Thompson

Department of Atmospheric Science

In partial fulfillment of the requirements

For the Degree of Doctor of Philosophy

Colorado State University

Fort Collins, Colorado

Spring 2016

Doctoral Committee:

      Advisor: Steven A. Rutledge
      Co-Advisor: James N. Moum

      Eric D. Maloney
      Richard H. Johnson
      V. Chandrasekar
      Christopher W. Fairall

ABSTRACT

TROPICAL WARM POOL RAINFALL VARIABILITY AND IMPACT ON UPPER OCEAN

VARIABILITY THROUGHOUT THE MADDEN-JULIAN OSCILLATION

Heating and rain freshening often stabilize the upper tropical ocean, bringing the ocean

mixed layer depth to the sea surface. Thin mixed layer depths concentrate subsequent fluxes of

heat, momentum, and freshwater in a thin layer. Rapid heating and cooling of the tropical sea

surface is important for controlling or triggering atmospheric convection. Ocean mixed layer

depth and SST variability due to rainfall events have not been as comprehensively explored as

the ocean's response to heating or momentum fluxes, but are very important to understand in the

tropical warm pool where precipitation exceeds evaporation and many climate phenomena such

as ENSO and the MJO (Madden Julian Oscillation) originate.

The first part of the dissertation investigates tropical, oceanic convective and stratiform

rainfall variability and determines how to most accurately estimate rainfall accumulation with

radar from each rain type. The second, main part of the dissertation uses central Indian Ocean

salinity and temperature microstructure measurements and surrounding radar-derived rainfall

maps throughout two DYNAMO MJO events to determine the impact of precipitating systems

on upper-ocean mixed layer depth and resulting SST variability. The ocean mixed layer was as

shallow as 0-5 m during 528/1071 observation hours throughout 2 MJOs (54% of the data

record). Out of 43 observation days, thirty-eight near-surface mixed layer depth events were

attributed to freshwater stabilization, called rain-formed mixed layers (RFLs). Thirty other mixed

layer stratification events were classified as diurnal warm layers (DWLs) due to stable

temperature stratification by daytime heating. RFLs and DWLs were observed to interact in two ways: 1) RFLs fill preexisting DWLs and add to total near-surface mixed layer stratification, which occurred ten times; 2) RFLs last long enough to heat, creating a new DWL on top of the RFL, which happened nine times. These combination stratification events were responsible for the highest SST warming rates and some of the highest SSTs leading up to the most active precipitation and wind stage of the each MJO. DWLs without RFL interaction helped produce the highest SSTs in suppressed MJO conditions. As storm intensity, frequency, duration, and the ability of storms to maintain stratiform rain areas increased, RFLS became more common in the disturbed and active MJO phases. Along with the barrier layer, DWL and RFL stratification events helped suppress wind-mixing, cooling, and mixed layer deepening throughout the MJO. We hypothesize that both salinity and temperature stratification events, and their interactions, are important for controlling SST variability and therefore MJO initiation in the Indian Ocean.

Most RFLs were caused by submesoscale and mesoscale convective systems with stratiform rain components and local rain accumulations above 10 mm but with winds mostly below 8 m s^{-1}. We hypothesize that the stratiform rain components of storms helped stratify the ocean by providing weak but widespread, steady, long-lived freshwater fluxes. Although generally limited to rain rates ≤ 10 mm hr^{-1}, it is demonstrated that stratiform rain can exert a strong buoyancy flux into the ocean, i.e. as high as maximum daytime solar heating. Storm morphology and the preexisting vertical structure of ocean stability were critical in determining ocean mixed layer depth variability in the presence of rain. Therefore, we suggest that high spatial and temporal resolution coupled ocean-atmosphere models that can parameterize or resolve storm morphology as well as ocean mixed layer and barrier layer evolution are needed to reproduce the diurnal and intraseasonal SST variability documented throughout the MJO.

ACKNOWLEDGEMENTS

TABLE OF CONTENTS

2.8 Case study #4: as in Fig. 2.5 but for shallow convection at 21:15 UTC 14 Dec 2011 with 2DVD data spanning 21:14-21:22 UTC, time increases as the colored markers go from blue to red

2.9 Case study #5: as in Fig. 2.5 but for light rain at 07:45 23 Nov 2011 with 2DVD data spanning 07:30-08:10 UTC, time increases as the colored markers go from blue to red

2.10 Case study #6: as in Fig. 2.5 but for stratiform rain at 22 Nov 2011 with 2DVD data spanning 20:21-20:55 UTC, time increases as the colored markers go from blue to red

2.11 Case study #7: as in Fig. 2.5 but for weak stratiform rain at 10:45 UTC 26 Oct 2011 with 2DVD data spanning 10:35-10:55 UTC, time increases as the colored markers go from blue to red

2.12 Case study #8: as in Fig. 2.5 but for a transition from a leading convection line to strong stratiform rain at at (1) 04:30, (2) 05:00, (3) 05:30, (4) 06:00 UTC on 24 Oct 2011 with 2DVD data spanning 04:20-06:25 UTC. Numbers 1-4 correspond to call out points in the 2DVD data based on the time of the radar scans, where time increases as the colored markers go from blue to red

2.13 Case study #9: as in Fig. 2.5 but for a transition from convection embedded in stratiform rain to strong stratiform rain at (1) 03:00, (2) 03:15, (3) 03:30, (4) 04:15 UTC on 23 Nov 2011 with 2DVD data spanning 03:02-04:20 UTC. Numbers 1-4 correspond to call out points in the 2DVD data based on the time of the radar scans, where time increases as the colored markers go from blue to red.

2.14 Manus Is. $LWC(D_0)$ and $N_w(D_0)$ scatter plots color-coded by 2DVD rain rate (R) and reflectivity (Z_h) with the original subtropical, continental Bringi et al. (2009 - BR09) and updated tropical, oceanic C/S $\log_{10}N_w^{SEP}$ separation lines. Similar distributions found at Gan Is.

2.15 Manus Is. a) $R(D_0)$, b) $R(LWC)$, c) $z(LWC)$, and d) $R(\lambda)$ partitioned by the $\log_{10}N_w^{SEP}$ line (stratiform = blue, convection = red). $z(LWC)$ and $R(\lambda)$ regression lines are over-plotted in c) and d) respectively for the entire DSD dataset (green) and each convective and stratiform population (black lines:convective (stratiform) relationship on top (bottom) overlaying red (blue) points). Similar distributions observed at Gan Is.

2.16 $R(z)$ for case studies #1-9 where time increases as the colored markers go from blue to red. $R(z)_C$ (upper), $R(z)_{ALL}$ (middle), and $R(z)_S$ (lower) best-fit equations shown.

2.17 a) Gan and Manus Is. 2DVD Z_h and R with linear regression best-fit lines for each location. b) Normalized histograms of the orthogonal distance from each [z,R] point at each location to the Manus Is. best-fit line. Distances are in logarithmic $R(z)$ units in both directions.
2.18 Gan and Manus Is. $R(z)$ smoothed 2D histograms contoured by frequency of occurrence with linear regression best-fit line from Manus Is. Gan Is: 180 bins in each direction and 6 bin Gaussian filter width. Manus Is. # bins in each direction: all = 280, conv = 200, strat = 235; 10 bin Gaussian filter width.

(positive N^2) due to salinity or temperature. Mixed layer, stable layer, and thermocline depth calculated in the current study based on total N^2 are denoted. Suppressed, disturbed, active, and westerly wind burst (WWB) MJO conditions are denoted. Pink, green, and purple lines atop each plot signify times when the 10 m zonal wind exceeded 6 m s^{-1}, the net heat flux $< $ -20 W m^{-2} was heating the ocean, and when local ship rain rate exceeded 0.5 mm hr^{-1}.

3.5 Normalized histograms of upper central Indian Ocean mixed layer depth, stable layer depth, and thermocline depth according to N^2 methodology in the current study. The stable layer exists at the base of the mixed layer, marked by stable temperature and/or salinity gradients beneath the well-mixed surface layer.

3.6 16 Nov 2011, suppressed MJO central Indian Ocean daily time series of SST, near-surface zonal current, SSS, and rain rate at the *R/V Revelle* in the central Indian Ocean. Time vs. depth plots of N_S^2: salt stratification, N_T^2: temperature stratification, and their sum, N^2: total stratification. Color shading is depicted below markers that indicate sunrise, sunset, cloudiness compared to modeled clear-sky downwelling solar radiation, color scaled rightward pointing triangles for zonal surface wind speed, grey squares to indicate local precipitation with dark grey diamonds for convective rain, bold vertical black lines to denote atmospheric cold pool passage, and upward pointing blue triangles representing duration of enhanced latent heat flux out of the ocean due to cold pool passage, which was used to determine cold pool recovery time.

3.7 As in Fig. 3.5 for 09 Oct 2011, suppressed MJO central Indian Ocean daily time series.

3.8 As in Fig. 3.5 for 07 Oct 2011, suppressed MJO central Indian Ocean daily time series.

3.9 As in Fig. 3.5 for 15 Nov 2011, suppressed MJO central Indian Ocean daily time series.

3.10 As in Fig. 3.5 for 27 Oct 2011, westerly wind burst MJO central Indian Ocean daily time series.

3.11 As in Fig. 3.5 for 15 Oct 2011, disturbed MJO central Indian Ocean daily time series.

3.12 As in Fig. 3.5 for 22 Oct 2011, active MJO central Indian Ocean daily time series.

3.13 As in Fig. 3.5 for 05 Oct 2011, suppressed MJO central Indian Ocean daily time series.

3.14 As in Fig. 3.5 for 16 Oct 2011, disturbed MJO central Indian Ocean daily time series.

3.15 As in Fig. 3.5 for 21 Oct 2011, active MJO central Indian Ocean daily time series.

3.16 As in Fig. 3.5 for 23 Oct 2011, active MJO central Indian Ocean daily time series.

3.17 As in Fig. 3.5 for 13 Oct 2011, disturbed MJO central Indian Ocean daily time series.

3.18 As in Fig. 3.5 for 19 Oct 2011, disturbed MJO central Indian Ocean daily time series.

3.19 As in Fig. 3.5 for 24 Nov 2011, suppressed MJO central Indian Ocean daily time series.

3.20 As in Fig. 3.5 for 28 Nov 2011, suppressed MJO central Indian Ocean daily time series.

3.21 Box and whisker plots of 10 m zonal wind speed, surface zonal current, stable layer duration, inferred dimension given the local current speed, N_S^2, N_T^2, N_{S+T}^2, latent heat flux, sensible heat flux, solar heat flux, and percent cloudiness conditions experienced during 30 diurnal warming-formed mixed layers (DWL) and 38 rain-formed mixed layers (RFL).

3.22 5th, 25th, 50th (median), 75th, and 95th percentiles of central Indian Ocean precipitating system total event local rainfall accumulation and instantaneous 10 m zonal wind speeds during (a) all stratifying and non-stratifying storms; (b) all storms based on radar-indicated storm type: isolated non-linear (IC) and linear (LC) convection, sub-mesoscale non-linear (ICS) and linear (LCS) convective systems with stratiform rain, and mesoscale convective systems (MCSs); (c) stratifying storms by storm type; and (d) non-stratifying storms by storm type.

3.23 Surface buoyancy mass flux into the ocean from rain freshening – evaporation and rain cooling for either dSST = 1°C or dSST = 2°C as a function of rain rate as well as maximum daytime solar heating as a reference (1000 W m^{-2}).

3.24 Box and whisker plots of (a) warming rates > 0°C hr^{-1} and (b) cooling rates < 0° C hr^{-1} during central Indian Ocean time periods when DWLs formed on top of heated RFLs, when DWLs caught RFLs, when only a DWL or RFL occurred without interaction, when the mixed layer depth was between certain vertical levels or merged with the thermocline (TC), and times without diurnal warm layer or rain freshening layer regardless of ocean mixed layer depth. Sample size of distributions shown on each box (n = …).

3.25 Box and whisker plots of warming rates > 0° C hr^{-1} during central Indian Ocean MJO (a) suppressed, (b) disturbed, (c) active, and (d) westerly wind burst time periods when DWLs formed on top of heated RFLs, when DWLs caught RFLs, when only a DWL or RFL occurred without interaction, and times without diurnal warm layer or rain freshening layer regardless of ocean mixed layer depth. Sample size of distributions shown on each box (n = …).

3.26 Box and whisker plots of SST during central Indian Ocean time periods when DWLs formed on top of heated RFLs, when DWLs caught RFLs, when only a DWL or RFL occurred without interaction, when the mixed layer depth was between certain vertical levels or merged with the thermocline (TC), and times without diurnal warm layer or rain freshening layer regardless of ocean mixed layer depth. Sample size of distributions shown on each box (n= …).

3.27 Box and whisker plots of SST °C during central Indian Ocean MJO (a) suppressed, (b) disturbed, (c) active, and (d) westerly wind burst time periods when DWLs formed on top of heated RFLs, when DWLs caught RFLs, when only a DWL or RFL occurred without interaction, and times without diurnal warm layer or rain freshening layer regardless of ocean mixed layer depth. Sample size of distributions shown on each box (n= …).

CHAPTER 1: INTRODUCTION

To first order, the tropical, equatorial ocean and atmosphere are coupled by the net surface heat flux (mainly latent heating and solar insolation) and wind-driven momentum fluxes (Brainerd and Gregg 1995, Lau and Waliser 2005, Soloviev and Lukas 2006, Demott et al. 2014, 2015). A conceptual diagram is shown in **Fig. 1.1** from Brainerd and Gregg (1995).
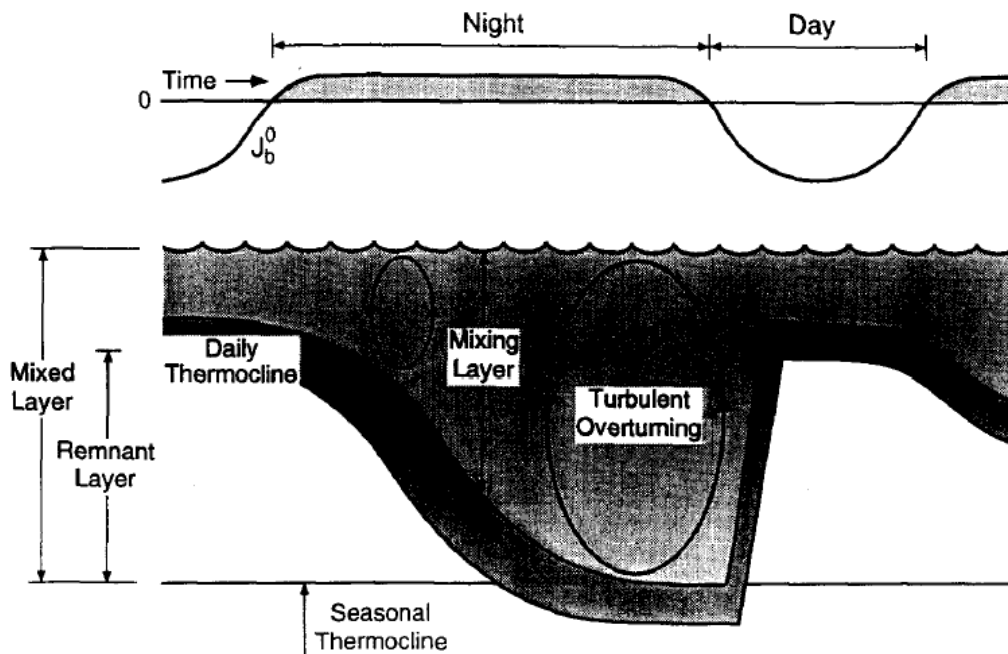
Fig. 5.   Diagram showing depth zones in a typical diurnal mixed layer cycle.

Figure 1.1: Idealized conceptual ocean mixed layer model driven by wind mixing and the net heat flux from Brainerd and Gregg (1995). Vertical axis is depth in lower panel.

The ocean mixed layer depth is determined by, and evolves according to, the competition between stabilizing buoyancy forces (i.e. freshwater or heating at the surface) and the generation of turbulent kinetic energy by wind stress, current shear, and waves. Turbulence is higher from the surface through the mixing layer, where it evenly distributes surface momentum, heat, and freshwater fluxes. The mixed layer depth is determined by the maximum extent of recent mixing

1

in the column, which concentrates stable density (salinity and temperature) gradients in the transition or entrainment layer, akin to the atmospheric boundary layer (Stull 1988). The daily mixed layer depth is sometimes called the daily or diurnal thermocline, when determined by temperature gradients. The maximum depth of mixing over several days or longer determines the equilibrium seasonal thermocline, distinguishing regions of the ocean that have been in contact with the surface in recent history. Turbulence can increase at it the base of the mixed layer due to shear, since momentum fluxes from the atmosphere are concentrated in the mixed layer. Internal waves due to tides and other stable flow regimes, flow over underwater topography, and current shear-driven mixing are the major sources of mixing in the deep ocean below the mixed layer.

Under sunny skies and calm winds, SST warms and the mixed layer usually shoals a couple hours after sunrise due to daytime heating. The pycnocline (level of very high density gradients) mixes downward due to wind mixing throughout the day, and collapses downward due to momentum accumulation and cooling near the sea surface when the net heat flux switches sign near sunset. The remnant stable layer or pycnocline, which previously defined the deepest extent of the mixed layer, can linger at an intermediate depth until shoaling begins the next day. These processes can be modeled (Miller 1976, Niller and Kraus 1977, Price 1979, Price et al. 1986, Lombardo and Gregg 1989, Brainerd and Gregg 1995, 1997, Webster et al. 1996, Yoshikawa 2015). Diurnal warm layers (DWLs) are known to shoal the mixed layer to the surface for extended periods of time due to heating induced stable ocean temperature gradients (Lukas and Lindstrom 1991, Webster et al. 1996, Fairall et al. 1996a, Ward 2006, Kawai and Wada 2007, Matthews et al. 2014). These stable layers are common over large (+1000 km) areas of the ocean when winds and upper ocean turbulence are relatively light (winds < 6 m s^{-1}) while solar insolation is high (Bellenger and Duvel 2009). DWLs boost SST and SST heating rates

enough to increase surface sensible and latent heat fluxes by 10 W m^{-2} or more compared to "bulk SST" measured at 1 m depth or lower, even under light winds (Fairall et al. 1996b, Clayson and Bogdanoff 2013). These 1-4°C diurnal warming anomalies can invigorate atmospheric storm activity and cloud organization (Bellenger et al. 2010, Seo et al. 2014, Ruppert and Johnson 2015). Diurnal warm layers often exhibit some slight mixed layer salinity increase due to evaporation, but this is very small compared to the temperature stabilization due to near-surface heating (Soloviev and Lukas 2006, Drushka et al. 2014b, Asher et al. 2015).

The tropical warm pool mixed layer heat budget can be mostly explained by these 1D heating and mixing processes, except during strong westerly wind burst events associated with the Madden-Julian oscillation (MJO, Zhang 2005). WWBs enhance near surface zonal currents, upper ocean turbulence, entrainment mixing and cooling from below, downwelling on the equator and upwelling off the equator, as well as zonal and meridional advection (Wrytki 1973, Lukas and Lindstrom 1991, Smyth et al. 1996a,b, Cronin and McPhaden 1997, 1998, 2002, Wijesekera et al. 1999). The mixed layer salinity budget is understandably modulated by rainfall, but more affected by advection in these regions, especially during and after WWBs. Advection, subduction, and local rain forcing can also create vertical salinity gradients at intermediate depths between 10-40 m in the tropical warm pool region, which affect daily mixing and shoaling cycles. These mid-level stable layers due to salinity are known as barrier layers because they confine surface heating to waters above and prevent entrainment cooling from below (Godfrey and Lindstrom 1989, Lukas and Lindstrom 1991, Sprintall and Tomczak 1992, Drushka et al. 2014a, Chi et al. 2014).

These relatively well-studied, and well-understood air-sea interaction processes are strongly modulated by high-frequency and sometimes large magnitude mixed layer depth and

SST variability due to precipitation systems. Clayson and Chen (2002) summarized two major "outstanding issues" precluding better understanding or improvement in simulating high frequency air-sea interactions relevant to air-sea coupled climate phenomena such as ENSO, the MJO, and monsoons. These areas of further research included the effects of precipitation on the ocean, the feedback processes of these rain-ocean mixed layer interactions back to the atmosphere, as well as the role of such short time scale events on larger, longer time scale variability. Of utmost importance to these air-sea coupled processes is the mixed layer depth because it regulates the ocean's heat capacity, responsiveness to atmospheric forcing, SST, and therefore the ocean's ability to provide heat and moisture back to the atmosphere. It is well-established that SST and SST gradients affect atmospheric circulations and convection (Lindzen and Nigam 1987, Back and Bretherton 2009a,b, Clement et al. 2008, Li and Carbone 2012, Carbone and Li 2015).

The DYNAMO (Dynamics of the Madden-Julian oscillation, MJO) campaign in 2011-2012 was motivated by many unresolved questions about the nature of atmospheric convection and air-sea interactions during the initiation of the MJO in the central Indian Ocean (Yoneyama et al. 2013). This came after a similarly-focused major field campaign effort in the equatorial western Pacific Ocean in 1992-1993, a region whose atmospheric and oceanic variability is also dominated by the MJO (TOGA-COARE, Webster and Lukas 1992). This history has ensured that there is much more information about the western Pacific warm pool than the central Indian Ocean portion of the combined tropical warm pool. This introduction chapter summarizes observational and modeling research to date concerning rain effects on the upper equatorial ocean mixed layer in the context of tropical warm pool rain variability, which motivates the work undertaken in this dissertation.

Many physical oceanographers have noted ocean surface freshening, slight cooling, and mixed layer stratification (shoaling) due to rain events (Katsaros and Buettner 1969, Ostapoff et al. 1973, Miller et al. 1976, Price 1979, Soloviev and Vershinsky 1982, Lukas and Lindstrom 1991, You 1995, Smyth et al. 1996b, Wijesekera and Gregg 1996, Anderson et al. 1996, Brainerd and Gregg 1997, Cronin and McPhaden 1998, 1999, Wijesekera et al. 1999, Soloviev and Lukas 2006, Reverdin et al. 2012, Asher et al. 2014). Despite wind mixing effects during many rain events, the freshwater flux can create stable salinity stratification of the upper ocean since the seawater below is much denser. There is consensus amongst these works that not all rain events lead to salinity stratification and shoaling of the mixed layer. Some rain events are accompanied by sufficient wind that they merely deepen the mixed layer, some near-surface rain-formed mixed layers may last a several hours despite wind forcing, while other salinity stratification layers left behind by rain linger only until the nighttime mixing and deepening cycle begins. Some rain events can also restratify a remnant mixed layer lingering at some intermediate depth in the ocean. Thus, the history and vertical structure of upper ocean mixing prior to the rain event seems important in understanding the ocean's subsequent response to new rain events. Rain-formed mixed layers are often observed to form immediately following the end of the rain event, potentially due to the kinetic energy of raindrops hitting the surface and other mixing related to wind gustiness. It might take time for the buoyancy forcing due to rain to overcome these local turbulence sources.

If the rain-formed mixed layer can remain intact until clouds dissipate and solar heating can commence again, these stable, shallow layers can heat to form new diurnal warm layers in the upper most meters of the ocean (Soloviev and Lukas 2006). Some rain freshening stable layers can also form on top of or inside preexisting diurnal warm layers, adding to surface

5

stability instead of breaking it. However, evidence of heated fresh water lenses and rain freshening stable layers forming inside diurnal warm layers have been anecdotal and not comprehensively studied. It is unknown how often these events occur, how long they last, or how these combination, salinity and temperature stratified layers beneath mixed layers affect or project onto the intraseasonal cycle of SST in the tropical warm pool. Rain-formed mixed layers can suppress turbulence below the stable salinity gradient at any time in the diurnal cycle, including nighttime, whereas diurnal warm layers only suppress turbulence below the mixed layer during the daytime (Brainerd and Gregg 1997). In addition to heating effects, some authors have noted that thin rain-formed mixed layers can also maintain a cool sea surface when cool rain water is trapped at the surface and winds continue to blow from mesoscale atmospheric variability (i.e. through the sensible heat flux). This could encourage eventual oceanic convective overturning and inhibit future atmospheric convection (Ostapoff et al. 1973, Miller 1976, Brainerd and Gregg 1995, Lukas and Lindstrom 1991).

Lukas and Lindstrom (1991) suggested rain-formed near surface mixed layer depths were very common and about equally attributable to salinity or temperature stratification in the west Pacific warm pool. These pools have been observed to be about as wide as precipitating areas (10-100 km) and last several hours locally. Freshwater lenses sitting atop the vertical salinity stratification are known to behave similarly to a buoyant density current by propagating laterally, diffusing vertically and horizontally, and thinning vertically over time (Soloviev and Lukas 2006). However, no comprehensive classifications or tracking of diurnal warm layers and rain-formed mixed layers in the tropical warm pool have been achieved, and their heating characteristics have not been studied further than these anecdotal reports.

Even if the vertical structure of shallow rain-formed mixed layers could be resolved by oceanographic measurements, many of these aforementioned studies have noted that the local rain rate data provided by ships or moored buoys is not sufficient for understanding the evolution of trapped freshwater puddles observed near the surface. Advection of rain from upstream of the ship to oceanography sensors by the current and storm-induced wind are important factors involved in creating local salinity stratification. This has underscored the need for contextual rain information, such as from radar or satellite, to understand the formation of freshwater lenses and their stratification of the mixed layer.

Early observational and laboratory research by Green and Houk (1979), Hsiao et al. (1988), Rodriguez and Mesler (1988), and Prosperetti and Oguz (1993) also found that the penetration depth of rain drops varied by drop size, where drops less than 0.4 mm -1 mm radius (the critical Weber number) usually stayed on the surface while larger drops were able to coalesce deeper into the sea. **Fig. 1.2** is from laboratory experiments by Katsaros and Buettner (1982), showing that the dilution of sea water with depth varied by artificial rain drop size. Note that seawater is never completely salt free following rain.

Fractional Change of Salt Content
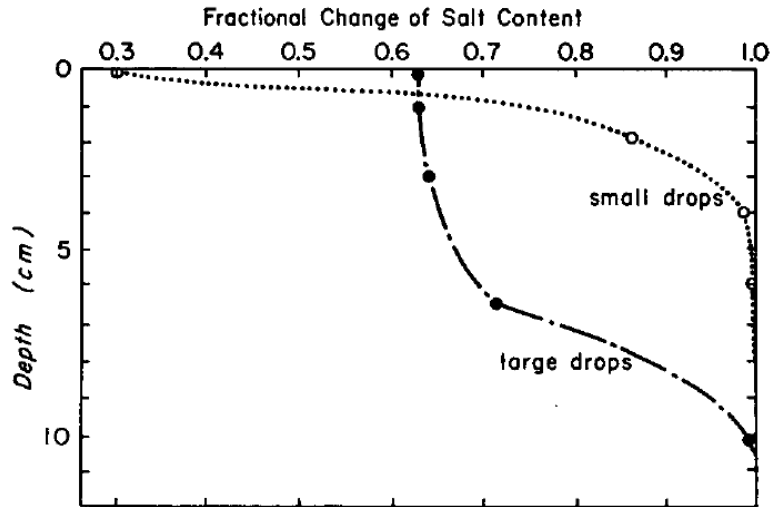
FIG. 1. Laboratory tests of salt content change at different depths in a salt water tank into which artificial rain has fallen. The abscissa is the fractional change of salinity (see text), where a value of 1 corresponds to undiluted salt water and a value of 0 to pure rain water. Heavy line: drop size 3 mm, rain rate 1.7 cm hr^{-1}, time 90 min after start of rain; dotted line: drop size $\leq$1.2 mm, rain rate 0.42 cm hr^{-1}, time 2 hr after start of rain.

Fig. 1.2: laboratory results from Katsaros and Buettner (1969) laboratory studies.

In reality, rain consists of many drops of various sizes, so more observational studies should be conducted to investigate rain dilution as a function of depth further. This has important implications for whether rain freshening can even be detected by certain subsurface measurements. Disdrometer measurements of raining drop size distributions from Chapter 2 show that most DSD exceed the critical Weber number (**Fig. 1.3**). Convection produces drops of this size at rain rates as low as 0.1 – 1 mm hr^{-1} while stratiform rain can do so between 0.05 – 0.1 mm hr^{-1}.
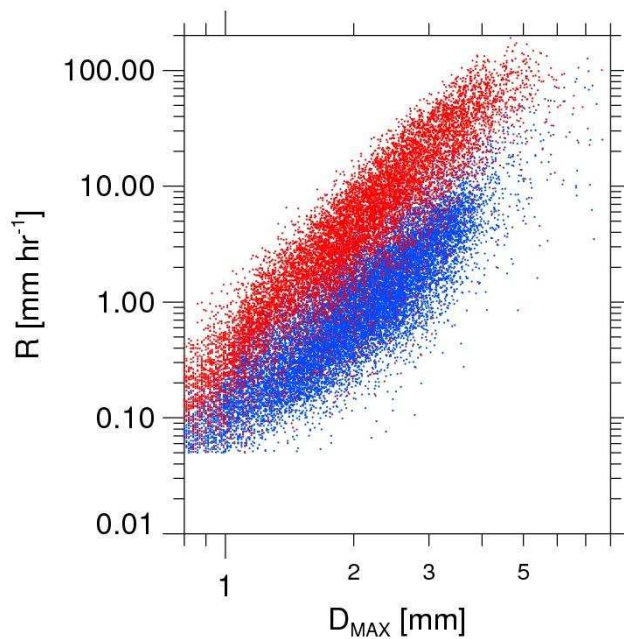
Fig. 1.3: Manus Island DSD D_{MAX} as a function of rain rate for convective (red) and stratiform (blue) DSD.

Recent studies have focused more on sea surface salinity (SSS) changes due to rain because of the advent of deriving this quantity from space and hopefully assimilating SSS observations into operational ocean models (Henocq et al. 2010, Prytherech et al. 2013, Boutin et al. 2013, Drushka et al. 2014b). Near surface freshening and salinity stratification due to rainfall can cause discrepancies between radiometrically-sensed skin SSS versus the 1 m or 5 m depth routine ocean salinity measurements made by moorings or ARGO profiling floats, respectively. Rain-induced salinity gradients in the ocean must be understood in order to calibrate and understand this suite of measurements. Asher et al. (2014) went further to determine that rain rates (R) greater than 6 mm hr^{-1} were highly correlated with the magnitude of the 0.1 – 0.3 m vertical salinity gradient following rainfall events. The width or depth of stable vertical salinity

9

gradient layer at the base of the rain-formed mixed layer have also been hypothesized to be a function of the Richardson number, or critical sheared flow stability criterion (Price 1979).

At rain rates below 6 mm hr^{-1}, Asher et al. (2014) hypothesized that salinity stratification was uncorrelated to rain rate because rain cooling (only about 2°C cooler than the sea surface at most) induced destabilization of the near surface density gradient, which nearly outweighed the freshening effect at these low rain rates. Brainerd and Gregg (1997) considered the sensible heat flux due to rain a small average component of the net surface heat flux (3.2 W m^{-2} on average), but a term that can become large at times (maximum value 300 W m^{-2}, also see Fairall et al. 1996b). At weak rain rates, the salinity stratification seemed more correlated with wind speed. Asher et al. (2014) found that lower winds and very low rain rates still yielded some vertical salinity gradients. At higher wind speeds, R < 6 mm hr^{-1} was not capable of producing consistent surface stratification of the ocean mixed layer because the weak stabilization was more susceptible to mixing. Miller (1976) attempted to model rain-formed mixed layers and also noted that the initialization of light precipitation with strong winds resulted in no detectable SSS or SST change, while the greatest SST and SSS change occurred for heavy precipitation under light winds.

If mentioned at all in these previous studies, authors have always attributed rain-induced mixed layer formation and freshening events to "heavy" and/or "convective" rain or "squalls". However, these previous studies do not qualify use of these descriptive words with any standard deviation of rain rate, rain rate time series, or radar reflectivity structure observations (Steiner et al. 1995, Thurai et al. 2010, Bringi et al. 2012, Thompson et al. 2015). The work by Asher et al. (2014) quantified that rain rates less than 6 mm hr^{-1} may not be capable of contributing to consistent upper ocean stability, but did not account for total accumulated rain over the course of

rain events or rain morphology. Stratiform rain has never been mentioned in the literature concerning rain effects on the upper ocean, although stratiform rain can contribute over half of the total rainfall in many mesoscale convective systems (e.g. Houze 2015), and accounts for roughly 20% of total rainfall climatologically over the warm pool (Thompson et al. 2015). Many of the tropical, equatorial freshwater puddle and salinity stratification studies cited previously have focused on a few strong rain events, such as during westerly wind bursts associated with the MJO. Storms at this stage in the intraseasonal cycle are most likely to be mesoscale convective systems with long-lived stratiform rain regions and very strong winds augmented by convective downdrafts and enhanced mean winds in the most active MJO phases (Houze et al. 2000, Barnes and Houze 2013, Demott et al 2014, Xu and Rutledge 2015a). These intense, large storms are responsible for the majority of tropical rainfall accumulation, but are the rarest in terms of climatological rain event frequency (Rickenbach and Rutledge 1998). Therefore, leading up to this study it is still unclear how the full organizational spectrum of precipitating systems known to occur over the tropical oceans affects the upper ocean. What types of storms are most capable of producing salinity stratification and shoaling of the ocean mixed layer, and why? Moreover, it is unknown how often rain-formed mixed layers occur relative to the intraseasonal and semidiurnal (predawn and late afternoon) cycles of precipitation in the tropical warm pool (Sui et al. 1997, Cronin and McPhaden 1999, Yang and Slingo 2000). In the ultimate goal of understanding the coupled climate system, it is also unclear how or whether shallow rain-formed mixed layers last long enough or occur often enough to affect the intraseasonal SST cycle by trapping heat in a shallow mixed layer and/or reducing nighttime turbulent mixing and cooling from below.

Despite these lingering unanswered questions, all aforementioned studies underscore the importance of assessing the vertical profile of salinity as well as temperature when assessing the stability structure and mixed layer depth of the ocean. The isothermal depth may not be equivalent to the isohaline depth for several reasons outlined previously (e.g. Sprintall and Tomczak 1992, Cronin and McPhaden 2002). Unlike the original conceptual models of the ocean mixed layer (i.e. **Fig. 1.1**), current ocean mixed layer parameterization schemes should include salinity effects (Miller 1976, Anderson et al. 1996). However, realistic initialization of rainfall into these models is still problematic. Most state-of-the-art climate models are not coupled to the ocean on time scales or with vertical resolutions that can resolve precipitation variability or the diurnal cycle of the ocean mixed layer (Lombardo and Gregg 1989, Webster et al. 1996, Lin et al. 2006, DeMott et al. 2014, Demott et al. 2015, Wang et al. 2015). These studies have shown that as the temporal and spatial resolution of air-sea coupled MJO simulations have become more physically realistic recently, their improved performance over atmosphere-only MJO simulations has been well-recognized.

Advancements in simulating or resolving the feedback cycles between rain and the upper ocean mixed layer have been precluded by insufficient observations of physical processes at the interface with which to better understand these phenomena, properly initialize models, and validate numerical simulations. The net heat flux and momentum fluxes at the air-sea interface are better understood, less impulsive in magnitude or spatiotemporal variability, and routinely measured. In contrast, rainfall observations surrounding high vertical resolution, near-surface observations of ocean temperature and salinity are rare to obtain and difficult to interpret due to the known importance of freshwater advection from upstream of the ship. Ocean measurements in the uppermost meter were "inaccessible" before free-falling microstructure profilers could

control instrument motion (Soloviev and Vershinsky 1982). TAO and RAMMA moored buoys only take ocean measurements in the top 1 and 5 meters at 10 minute resolution. ARGO profiling floats begin measurements at 5 m and only make vertical profiles about once every 9 days. New ocean instrumentation such as autonomous gliders and drifters still struggle to measure salinity with depth because its derivation from conductivity measurements also requires very accurate determination of ocean temperature gradients. Thus, most modern, routine observational datasets cannot adequately resolve near surface mixed layers due to rain and/or temperature stratification. Research-quality microstructure measurements are critical to diagnose mixed layer evolution, and are usually only available during field campaigns. Leading up to this study, we do not have a complete picture of mixed layer, barrier layer, and thermocline evolution in the central Indian Ocean or west Pacific Ocean, especially as a function of the MJO cycle.

There are also many long-standing difficulties associated with accurate estimation of oceanic rainfall. Ship or buoy rain gauges are often not representative of a surrounding area because of flow blocking and degraded performance in high winds. Rainfall naturally varies on timescales of minutes and in log-normal magnitudes. These scales are much smaller than what can be resolved by available satellite measurements or operational numerical weather prediction models. For instance, many studies have attempted to correlate hourly-averaged, and sometimes areally-averaged, rainfall magnitudes with ocean mixed layer variability, only to find weak correlations between the two coevolving phenomena (Anderson et al. 1996, Cronin and McPhaden 1999). These hourly-averaged rainfall products smear out the natural high magnitude, log-normally distributed variability of rainfall and do not account for rainfall morphology. For instance, quasi-circular convective precipitation cells can be organized into linear features and/or become more long-lived with large attendant stratiform precipitation regions and varying

magnitudes of surface downdraft wind gusts as atmospheric instability and wind shear increase. The progression from infrequent, small, shallow, isolated, short duration convective cells in the suppressed phase to larger, longer-lived, deeper precipitating systems with some stratiform rain areas and then finally to mesoscale convective systems with heavy convective cells or convective lines embedded in stratiform rain happens systematically from suppressed to active phases of the MJO (Lemone et al. 1998, Rickenbach and Rutledge 1998, Saxen and Rutledge 1998, Johnson et al. 1999, Houze et al. 2000, Riley et al. 2011, Zuluaga and Houze 2013, Barnes and Houze 2013, Xu and Rutledge 2014, 2015a,b, and other studies).

Convective rain can produce orders of magnitude more rainfall accumulation, but covers a much smaller area and lasts a much shorter time than stratiform rain (Tokay and Short 1996, Short et al. 1997, Tokay et al. 1999, Thompson et al. 2015). Therefore, the window of opportunity for stratiform rain to affect the upper ocean is larger, but to our knowledge has never been discussed in the literature. Moreover, there were still conflicting accounts about the variability of and distinctions between shallow, congestus, and deep convection versus stratiform rain over tropical oceans leading up to this dissertation (e.g. Austin and Geotis 1979, Williams et al. 1995, Atlas et al. 1999, 2000, Tokay and Short 1996, Yuter and Houze 1997, Yuter and Houze 1998, Bringi and Chandrasekar 2001, Bringi et al. 2003, 2009, Thurai et al. 2010). Many earlier studies of rainfall variability were hindered by instrument detection limitations of rain drop size. This is important because early oceanographic work cited a drop-size dependence on the penetration of rain drops into the ocean, which affects whether oceanographic sensors can even detect rain freshening (Soloviev and Lukas 2006). A comprehensive study of tropical, warm pool rain drop size and rain rate distributions had not been completed prior to this dissertation, despite much advancement regarding subtropical and midlatitude precipitation

regimes. Incomplete understanding of tropical, oceanic rain drop size distributions and rainfall rate variability also left questions about the accuracy of radar reflectivity-based rainfall estimation methods, which affects convective versus stratiform rain accumulation and frequency estimates.

DYNAMO presented new opportunities to investigate rainfall variability in the tropical warm pool and its resulting impact on upper ocean mixed layer stability. Rain drop size distributions and very accurate rain rate calculations over two atolls in the equatorial Indian and West Pacific Oceans during and following the field experiment provided an unprecedentedly large and high-resolution dataset to characterize the potential differences between convective and stratiform rain drop sizes and accumulation. This is covered in Chapter 2 of the dissertation, which is a published manuscript in the AMS *Journal of the Atmospheric Sciences*. Understanding the spatial and temporal variability of rainfall and ensuring the accuracy of radar-derived rainfall estimates was necessary before using radar-based rainfall data to assess the impact of rain on ocean mixed layer depth and therefore SST variability in Chapter 3 of this dissertation. Ten minute resolution radar observations of precipitating clouds surrounding and collocated with high vertical and temporal resolution upper ocean measurements were collected throughout two MJO events during DYNAMO. This multivariate dataset allowed for tracking of precipitation intensity and morphology relative to upper ocean mixed layer behavior below. While many oceanographers have found rain-formed near-surface mixed layers that can trap heat in the upper ocean and affect SST, the origins and decay processes of rain-formed mixed layers have never been comprehensively studied or studied in the context of the natural variability of rain. The meteorological conditions conducive to rain-formed near-surface mixed layer formation and maintenance have not been nearly as well studied as for diurnal warm layers. Prior

to this dissertation, it was also still unknown how rain interactions with the mixed layer either prevented or augmented the ocean's diurnal and intraseasonal heating cycle. These topics are covered in Chapter 3. Chapter 4 synthesizes the results of these two chapters and concludes the dissertation.

Given this literature review, we hypothesize that ocean mixed layer depth response to rain depends on the morphology and intensity of precipitating systems. Since precipitation morphology varies on diurnal and intraseasonal timescales in the tropical warm pool region, we hypothesize that the impacts of rain on the upper ocean mixed layer depth will not be constant throughout these time periods while both fluids continuously coevolve.

CHAPTER 2: DROP SIZE DISTRIBUTIONS AND RADAR OBSERVATIONS OF

CONVECTIVE AND STRATIFORM RAIN OVER THE EQUATORIAL INDIAN AND

WEST PACIFIC OCEANS[*]

2.1 Background and Motivation

The majority of the world's rainfall occurs in the tropics, particularly over the Warm Pool

spanning the Equatorial Indian and West Pacific Oceans. Attributing rainfall to certain cloud

types, i.e. shallow, congestus, or deep convection, stratiform rain, or a mixture thereof, is of

critical importance for diagnosing the resulting vertical distribution of latent heating (Johnson

et al. 1999; Schumacher et al. 2004), which can drive convergence and vertical motion

(Matsuno 1966; Yanai et al. 1973; Zhang and Hagos 2009). Toward this end, identifying

dominant modes of tropical, oceanic rain variability is important because this is still a major

source of uncertainty in ground-based, ship-borne, and space-borne radar rainfall estimation

(Munchak et al. 2012). For example, many studies have thoroughly detailed why and how cloud

microphysical processes and vertical motions differ during convective (C) and stratiform (S)

rain, which lead to characteristically different drop size distributions (DSDs) in each rain type

(Williams et al. 1995; Tokay and Short 1996; Houze 1997; Tokay et al. 1999; Atlas

et al. 1999, 2000; Bringi et al. 2003; Houze 2004; Bringi et al. 2009; Thurai

et al. 2010; Schumacher et al. 2015; Zhu et al. 2015). There is also a region where (or time

period when) active convective updrafts might be decaying into stratiform precipitation

(Biggerstaff and Houze 1993; Braun and Houze 1994; Williams et al. 1995; Uijlenhoet

et al. 2003; Sharma et al. 2009). These resulting DSD lie between convective and stratiform. Additionally, marked differences exist between continental and maritime DSDs, both of which produce convective and stratiform rain of varying intensities, efficiencies, and integral[†] rain parameters based on differences in updraft intensity and sub-cloud processes (Twomey 1977; Ulbrich and Atlas 1978; Zipser and LeMone 1980; Zipser 2003; Ulbrich and Atlas 2007; Minor et al. 2011; Wilson et al. 2013; Kumjian and Prat 2014).

The primary goal of this study is to investigate drop size distributions (DSDs) of equatorial, oceanic rainfall, which are less studied due to their remote location despite their contribution to the global hydrologic cycle. To do so, we take advantage of two long-term 2D video disdrometer (2DVD) datasets over the Equatorial Indian and West Pacific Oceans, at Gan (3.5 month record) and Manus (18 month record) Island, respectively (**Fig. 2.1**).
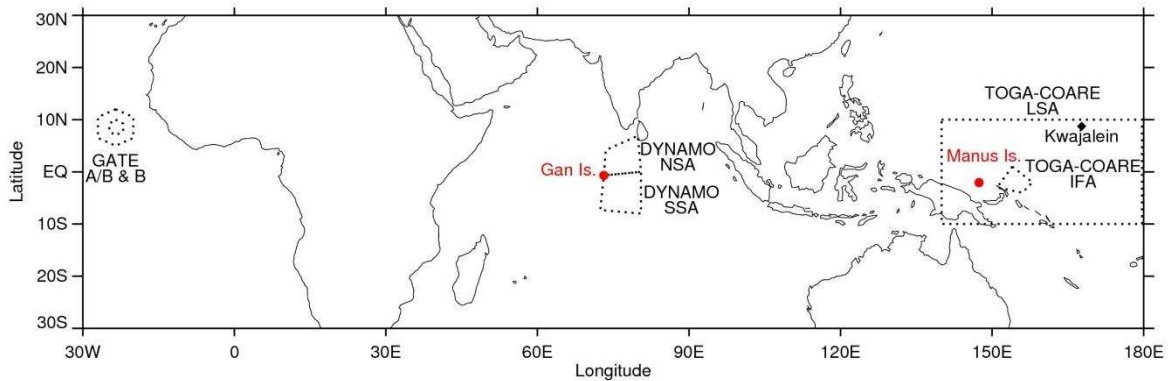
Figure 2.1: DYNAMO Northern and Southern Sounding Arrays (NSA, SSA), TOGA COARE Intensive Flux and Large Sounding Arrays (IFA, LSA), and GATE domains. The MISMO domain was a triangle in the same place as the DYNAMO NSA but without the northwest island. Gan Is. is within the DYNAMO and MISMO domains while Manus Is. and Kwajalein (diamond) were included in the TOGA COARE array.

Bringi et al. (2003) (henceforth BR03) identified maritime and continental convective DSD "clusters" as well as a linear variation of stratiform rain in the $N_W(D_0)$ (normalized gamma

---

[†] integral rain parameters are those found by integrating the DSD (Ulbrich and Atlas 1978)

number concentration and median volume diameter) plane, which can be measured by disdrometers or derived from dual-polarization radar data. Their work involved DSD quantities from selected rain events in Florida, coastal Australia, Austria, Puerto Rico, Brazil, Kwajalein, Colorado, Papua New Guinea, the South China Sea, and a *mean* of many W. Pacific Warm Pool events. A separation line between convective and stratiform rain was determined by Bringi et al. (2009; henceforth BR09) using the Darwin, Australia datasets. DSD were considered convective/stratiform if N_W was greater/less than a naturally emerging separator line: $\log_{10}N_W^{SEP} = -1.6D_0 + 6.3$. This partitioning method was found to be consistent with data from selected rain events in BR03 and with more data from Darwin by Thurai et al. (2010; henceforth TH10) and Penide et al. (2013). TH10 also found agreement between the DSD-based $N_W(D_0)$ C/S partitioning method and the widely-used Steiner et al. (1995) radar reflectivity-based partitioning algorithm using data from Darwin. This radar method identifies convective cores based on a reflectivity threshold and whether localized regions of reflectivity stand out relative to the smoothed, background reflectivity field, which can be modified for particular regions and radar data resolutions (Yuter and Houze 1997, 1998).

The classification and rain attribution of shallow, weak cumulus convection is critical because this cloud type is ubiquitous across the Warm Pool (Johnson et al. 1999; Rauber et al. 2007; Jakob and Schumacher 2008; Barnes and Houze 2013) where the atmosphere is conditionally unstable below the θ_e (equivalent potential temperature) minimum (Lilly 1960). However, this relatively shallow and weak oceanic convection is not dominant in coastal or continental boundary layers, likely explaining its under-representation in BR03, BR09, and TH10, whose work comprised of data mostly from midlatitude and subtropical land locations near oceans. Shallow, maritime, tropical convective clouds moisten the lower troposphere (Nitta

and Esbensen 1974; Lin and Johnson 1996; Johnson and Lin 1997; Johnson et al. 1999) and may play an important role in Madden-Julian Oscillation evolution (Kemball-Cook and Weare 2001; Kiladis et al. 2005; Benedict and Randall 2007; Seo et al. 2014; Ruppert and Johnson 2015; Barnes et al. 2015). However, they are difficult to detect and track because of limited vertical, horizontal, and temporal resolution and the minimum detectable signals of many remote sensing platforms (Schumacher and Houze 2003; Jakob and Schumacher 2008; Funk and Schumacher 2013; Ruppert and Johnson 2015). The "stretched building block" hypothesis by Mapes et al. (2006) explains how stratiform clouds and all three major convective cloud types (shallow, congestus, and deep) are usually present over relatively large areas of the tropics, but some become more dominant than others during certain phases of the MJO. This is also consistent with recent MJO observational studies in the equatorial Indian and West Pacific Oceans (Riley et al. 2011; Barnes and Houze 2013; Zuluaga and Houze 2013; Powell and Houze 2013; Rowe and Houze 2014; Xu and Rutledge 2014; Xu and Rutledge 2015a,b; Barnes et al. 2015).

Current DSD partitioning methods have not comprehensively considered tropical, oceanic convection. In fact, close inspection of Okinawa warm, shallow, convection DSD from TH10, Darwin maritime convection data from BR03, Darwin pre-monsoon season data from BR09, and Darwin wet-season data from Bringi and Chandrasekar (2001; henceforth BC01) reveals that weak, shallow, maritime convection does not uniformly lie on the convective side of the subtropical, continental BR09 separator line. In contrast to continental convection, these maritime convective storms are characteristic of warm rain processes, i.e. condensation and collision-coalescence at temperatures $> 0°C$ (Pruppacher and Klett 1997; Cotton et al. 2011). These processes result in high N_W but relatively low D_0. The inclusion of continental convection

(~hailstorms) in BR09 caused their separator line to be sloped downward toward low N_W and large D_0 (BR03). These more intense continental storms containing vigorous mixed-phase processes and much evaporation are common over tropical land, but rare over tropical oceans (Kumjian and Prat 2014; Rowe and Houze 2014). Therefore, the remote oceanic, tropical DSD of interest in the current study might warrant a different C/S separation method than the subtropical, continental BR09 line. The current study's primary goal is to analyze the C/S DSD variability and radar characteristics of a long-term tropical, equatorial, maritime dataset not available in previous studies.

The secondary goal of this study is to utilize the DSD measurements to form single-polarization radar-based rainfall estimation equations for these oceanic, tropical rain regimes. Many power law equations have been developed to relate radar reflectivity (Z_h in dBZ or z in mm^6 m^{-3}) to rainfall rate (R, mm hr^{-1}) for characteristic modes of DSD variability in particular regions based on the cloud microphysical processes encountered there (Battan 1973; Ulbrich and Atlas 1978; Atlas et al. 1984; Ulbrich and Atlas 1998; Steiner et al. 2004; Ryzhkov et al. 2005). The current study intends to build upon many previous rainfall-estimation-focused studies that used shorter time record DSD data from various instruments in the equatorial Atlantic Ocean (Cunning and Sax 1977; Austin and Geotis 1979; Hudlow 1979), West Pacific Ocean (Tokay and Short 1996; Yuter and Houze 1997; Atlas et al. 1999; Tokay et al. 1999; Atlas et al. 2000; Atlas and Ulbrich 2000; Ulbrich and Atlas 2002), as well as other coastal, subtropical locations (Keenan et al. 2001; Bringi et al. 2003, 2009, 2011, 2012; Thurai et al. 2010). The equatorial Indian Ocean has been relatively less studied.

Following this introduction, Sec. 2 describes the measurement systems and data processing involved in this study. Sec. 3 compares distributions of DSD R, z, number

concentration, drop diameters, and liquid water content from the two equatorial (Indian and West Pacific) sites, which are shown to be similar. Radar data is used in Sec. 4 to investigate the storm characteristics associated with each mode of DSD variability observed at Gan Is. Sec. 5 elaborates on a physically-based separation found between convective and stratiform rain using DSD number concentration. We also quantify the sensitivity of C/S rain statistics to this separation method. New $R(z)$ equations for all, convective, and stratiform rain are presented for the equatorial Indian and West Pacific Ocean sites. The potential sensitivity of rainfall statistics to different $R(z)$ equations is discussed in Sec. 6. Conclusions are found in Sec. 7.

2.2 Data and Methods

2.2.1 Domain and radar data

Fig. 2.1 shows Gan and Manus Is. as well as other locations of tropical, oceanic DSD research such as Kwajalein and the domains of GATE: the 1974 GARP (Global Atmospheric Research Program) Atmospheric Tropical Experiment (Hudlow 1979), TOGA-COARE: the 1992-1993 Tropical Ocean Global Atmosphere Coupled Atmosphere-Ocean Response Experiment (Webster and Lukas 1992), and MISMO: the Mirai Indian Ocean cruise for the study of MJO-Convective Onset (Yoneyama et al. 2008). The Manus Is. Two Dimensional Video Disdrometer (2DVD) has been operational since December 2011 (data record examined herein: 2 December 2011 - 21 April 2013; no continuous radar data available at Manus). An identical 2DVD was operating on Gan Island 8 km away (141˚ radial) from the NCAR S-band dual-polarization S-Pol radar (Addu Atoll) during DYNAMO (**Fig. 2.1**) - the 2011-2012 Dynamics of the MJO field campaign (Yoneyama et al. 2013; Johnson and Ciesielski 2013). The Gan 2DVD and S-Pol radar operated simultaneously from 1 October 2011 - 16 January 2012; the Gan 2DVD

22

record continues to 2 February 2012. Island conditions are considered to be similar to the surrounding ocean (Johnson and Ciesielski 2013).

Zuluaga and Houze (2013) describe the S-Pol radar deployment during DYNAMO and subsequent post-processing. S-Pol vertical cross section, or Range Height Indicator (RHI), scans were collected directly over the Gan Is. disdrometer every 15 minutes. Low-level Plan Position Indicator (PPI) scans also captured the horizontal distribution of precipitation at the same time as the vertical cross sections. Radar scans were manually investigated. We use the horizontal reflectivity (Z_h, dBZ), differential reflectivity (Z_{dr}, positive for oblate, negative for prolate, and near-zero for spherical or tumbling hydrometeors), and the correlation coefficient [ρ_{hv}, a scalar quantity, decreases from unity due to the presence of non-Rayleigh scatterers and as hydrometeors in the same radar gate become less similar, either in phase, shape, and/or orientation, see Straka et al. (2000), BC01, and Kumjian (2013)]. Radar brightband identification due to melting snow is much more reliable with dual-polarization radar variables than radar reflectivity alone (e.g. Brandes and Ikeda 2004; Thompson et al. 2014). The radar brightband is an indicator of stratiform rain morphology.

Unfortunately, we cannot analyze radar statistics of convective, stratiform, or total rainfall occurrence/accumulation over the disdrometer from PPI, RHI, or gridded horizontal reflectivity scans due to a variety of reasons. The radar was blocked to the west, rendering echoes at low levels in this direction untrustworthy. The radar was also prohibitively close to the disdrometer, which placed the 2DVD within the "cone of silence" of gridded PPI radar reflectivity fields in the lower 3 km. Additionally, RHIs were not conducted south or west of the disdrometer location and were contaminated by ground clutter surrounding the disdrometer below 1 km. Therefore, horizontal reflectivity gradients and echo evolution cannot be assessed

with either the PPI or RHI radar data within a 10 km radius surrounding the 2DVD as specified

by the Steiner et al. (1995) and Yuter and Houze (1998) radar-based C/S partitioning methods.

Select RHIs were manually investigated over the disdrometer, but quantitative rainfall estimation

above the 2DVD for all RHIs could not be conducted for statistical comparison with the 2DVD.

Lastly, there is no established way to automatically classify C/S echoes with RHI or PPI polar

coordinate radar data.

2.2.2 2DVD data

Schönhuber et al. (2008) described the third generation 2DVD in detail. The Dept. of

Energy's Atmospheric Radiation Measurement (ARM) Program 2DVDs at Gan and Manus Is.

provide one-minute drop count and drop number density[‡] measurements across fifty 0.2-mm

wide diameter bins ranging from 0.0-0.2 to 9.8-10.0 mm

(http://www.archive.arm.gov/discovery/). Only one-min DSD data with at least 100 total drops

and $R > 0.05$ mm hr^{-1} during at least a 3 minute consecutive raining period were analyzed. These

thresholds prevent DSD comprised of only a few small drops from skewing the analysis

(personal communication with Paul L. Smith, South Dakota School of Mines and Technology,

and V. N. Bringi, Colorado State Univ., 2012) and are consistent with our intent to focus on

raining DSD. The 18-month Manus Is. time series provided 27,179 one-minute raining DSD data

points, while Gan Is. had 4,446 points over 3.5 months. No smoothing or averaging was

performed. Besides the spatial sampling issues of a 100 cm^2 area on the ground and some missed

data during high winds, the chief 2DVD instrument error is the underestimation of small drops,

so we ignored data from the first size bin centered on 0.1 mm as suggested by Tokay

et al. (2013). 2DVD directly senses integral rain parameters such as liquid water content (*LWC*, g

---

[‡] number of drops per diameter bin per unit volume of air: mm^{-1}m^{-3}

m^{-3}) and rain rate (R, mm hr^{-1}), the latter equivalent to the flux of water across the catchment area (100 cm^2) given each drop's measured fall speed. In contrast, Joss Waldvogel impact disdrometers (JWDs) require drop count correction and calibration algorithms (Tokay et al. 2001, 2005, 2013), used to have worse small-drop detection capability, and must rely on an empirical fall speed relation based on drop diameter to calculate R and LWC (Gunn and Kinzer 1949; Atlas et al. 1973), which introduces additional error as described by Salles and Creutin (2003).

A drop size distribution shape or model must be chosen when solving for the remaining integral rain parameters. Rainfall and radar quantities are heavily influenced not just by particle size, but also the distribution of mass or water content across the particle size distribution, i.e. the median volume drop diameter (D_0 mm). DSD naturally exhibit a gamma-shaped distribution (Ulbrich 1983), which can be normalized so DSD of varying LWC can be easily compared (Willis 1984). For this reason, Lee et al. (2004) stated that normalized gamma DSD methods may produce more evident distinction between C/S rain types. Thurai et al. (2014) detailed the "μ-search" method used in the current study to determine the normalized gamma DSD generalized number concentration[§] or intercept parameter N_W (mm^{-1} m^{-3}) and shape parameter (μ), from which D_0 is estimated. These parameters are related by:

$$N_w = \frac{3.67^4 10^3 \text{LWC}}{\pi \rho_w D_0^4},$$

$$\tag{1}$$

[§] The normalized gamma number concentration or intercept parameter (Nw) is the same as that for an exponential-shaped distribution ($N0$) with equal LWC and $D0$ to the gamma-shaped DSD. Note, Nw is different from the non-normalized gamma intercept parameter (also denoted by $N0$) used by Ulbrich (1983), Tokay and Short (1996), and Ulbrich and Atlas (1998). This $N0$ still depends on the shape parameter μ, leading to less physical units of m$_{-3-\mu}$ mm$_{-1}$.

where ρ_w is the density of water, 1 g cm^{-3} (BC01). This μ-search technique is more accurate than the often-used method of moments because it takes more DSD information into account and iteratively seeks the gamma parameters that *most likely* describe the distribution of interest through minimization of cost functions (Smith and Kliche 2005; Kliche et al. 2008). For simplicity, $\log_{10}N_W$ is analyzed in the current study as in BR03.

2.2.3 Simulated radar variables

Surface disdrometer DSD data can be integrated to determine how a radar would sample that volume of rain and to calibrate radar-based rainfall estimates (Waterman 1971; Mishchenko et al. 1996). It is necessary to compute radar reflectivity (Z_h in dBZ, or more often the linear version z in mm^6 m^{-3} because of its larger dynamic range) based on theoretical, electromagnetic scattering calculations from the raw DSD number density data rather than using the simplified $z \sim D^6$ calculation for spheres, which ignores the effects of drop oblateness and fall behavior. Radar reflectivity was simulated assuming rain drops were liquid, had a zero mean canting angle with a standard deviation about the mean up to 7.5° (Huang et al. 2008), and followed the Thurai et al. (2007) drop shape model. Drops were considered to be at 20°C and viewed at a nearly horizontal (1°) incident angle at S band (11 cm, e.g. S-Pol). Since Z_h should be independent of wavelength for Rayleigh scatterers, S-band $R(z)$ equations can be applied to C- and X-band data. We use orthogonal linear regression to derive all power law equations, including $R(z)$, because it minimizes error in both the R and z directions perpendicular to the best-fit line, so $R(z)$ and $z(R)$ are equivalent.

2.3 Drop Size Distribution Observations

To investigate DSD variability at Gan and Manus Is., D_{MAX}, D_0, $\log_{10}N_W$, and LWC histograms normalized by the length of each dataset are shown in **Fig. 2.2**. **Table 2.1** shows that the Gan and Manus Is. datasets exhibit similar variances, means, standard deviations, minima, maxima, as well as 5th and 95th percentiles of D_{MAX}, D_0, LWC, and $\log_{10}N_W$ (**Table 2.1**). Most D_{MAX} values at both locations are between 1.0-3.6 mm. The LWC values are near ~0.03-0.1 g m^{-3}, but some values exceed 5 g m^{-3}, indicative of strong cumulonimbus clouds (Cotton et al. 2011). D_0 values are small (0.8-1 mm), but large D_0 values > 1.6 mm are observed. Potentially related to the issue of small drop detection by older instruments, many previous tropical oceanic DSD studies except Bringi et al. (2012) list slightly higher mean D_0 (**Table 2.2**). LWC, D_{MAX}, and D_0 are slightly higher at Manus compared to Gan Is. with slightly lower $\log_{10}N_W$, which is also evident in **Fig. 2.2**. Despite these minimal differences and being separated by the Maritime Continent, DSD distributions at Manus and Gan Is. still appear very similar, suggesting that the cloud microphysical processes in these two regions are analogous or nearly equivalent. Many studies have shown similar cloud population intensity, morphology, and radar echo evolution over each tropical ocean basin associated with the ITCZ and MJO (Short et al. 1997; LeMone et al. 1998; DeMott and Rutledge 1998a,b; Rickenbach and Rutledge 1988; Zuluaga and Houze 2013; Barnes and Houze 2013; Xu and Rutledge 2014; Xu and Rutledge 15a,b; Guy and Jorgensen 2014; Rowe and Houze 2014).

Table 2.1: Variance, mean, standard deviation, min, max, 5th, and 95th percentiles of integral rain parameters at Manus (27,142 points) and Gan (4,446 points) Island: DSD max diameter D_{MAX} [mm]; median diameter D_0 [mm]; liquid water content LWC [g m^{-3}]; number concentration $\log_{10}N_W$ [unitless].

PLACE	PARAMETER	VAR	MEAN	STD	MIN	5%	95%	MAX
Manus	D_{MAX}	0.73	2.16	0.85	0.80	1.00	3.66	8.54
Gan	D_{MAX}	0.69	2.06	0.83	0.80	1.01	3.55	7.61
Manus	D_0	0.11	1.11	0.33	0.34	0.61	1.65	3.83
Gan	D_0	0.10	1.08	0.32	0.35	0.62	1.62	3.35
Manus	LWC	0.58	0.35	0.76	0.00	0.01	1.72	12.64
Gan	LWC	0.43	0.32	0.65	0.01	0.02	1.56	8.75
Manus	$\log_{10}N_W$	0.28	3.70	0.53	1.57	2.89	4.55	5.22
Gan	$\log_{10}N_W$	0.29	3.72	0.54	1.97	2.95	4.59	5.57
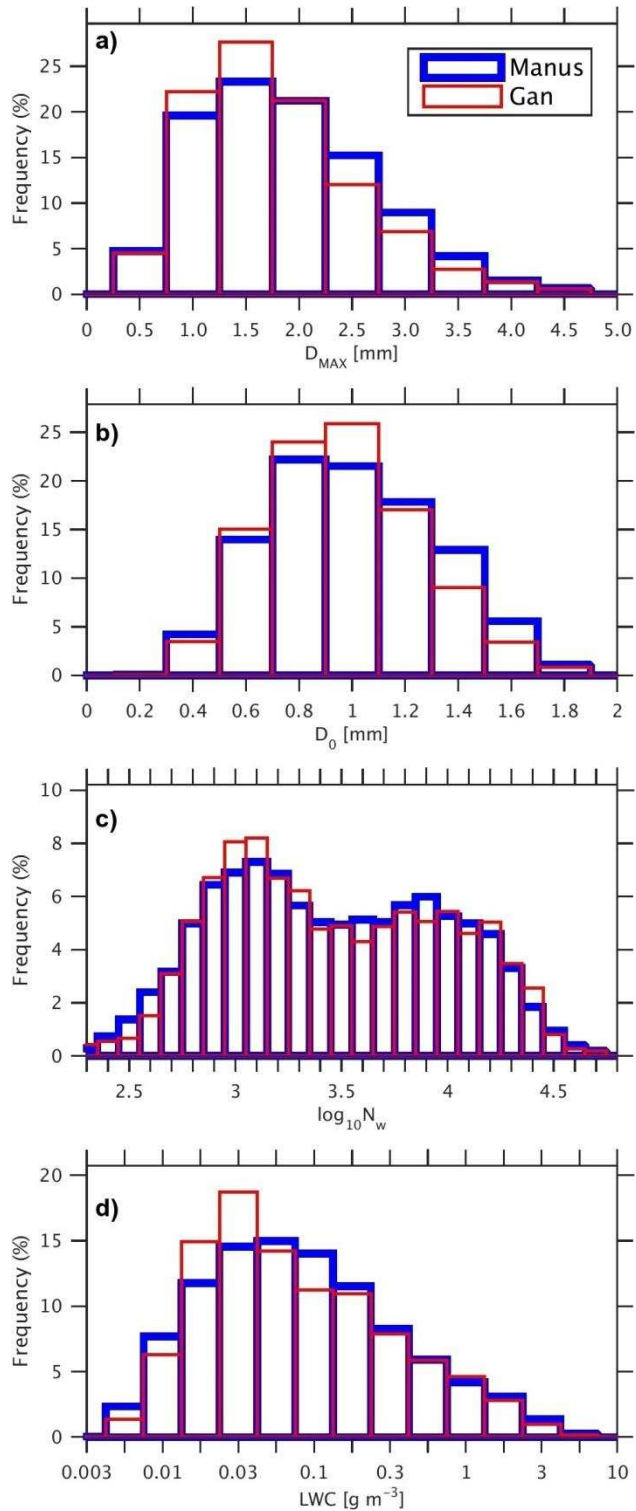
Figure 2.2: Histograms normalized by record length for Manus and Gan 2DVD DSD a) max diameter D_{MAX} [mm], b) median diameter D_0 [mm], c) number concentration $\log_{10}N_W$ [unitless], and d) liquid water content LWC [g m^{-3}, binned on a log 10 scale]

Table 2.2: Mean values of median diameter D_0 [mm] and number concentration $\log_{10}N_W$ [unitless] from previous studies of all, convective (C), and stratiform (S) rain in tropical, maritime locations.

Source	Rain	mean D_0	mean $\log_{10}N_W$
Penide et al. (2013) Australia monsoon	ALL	1.5	3.7
Islam et al. (2012) UK	ALL	1.23	3.7
Bringi and Chandrasekar (2001) Australia monsoon	ALL	1.20	3.7
Bringi et al. (2012) Kwajalein	ALL	0.9	
Tokay and Short (1996) TOGA COARE	C	1.24	
Ulbrich and Atlas (1998) TOGA COARE	C	0.8-1.0	
Tokay et al. (1999) TOGA COARE	deep C	1.31	
Tokay et al. (1999) TOGA COARE	shallow C	1.22	
Testud et al. (2001) TOGA COARE	C	1.3-1.5	
Bringi et al. (2003) Florida	C	1.6	4.6
Ulbrich and Atlas (2007) maritime	C	1.3-1.7	4.3
Bringi et al. (2009) Australia monsoon	C	1.44	4.2
Thurai et al. (2010) Australia monsoon	C	1.00	4.6
Thurai et al. (2010) Okinawa	C	1.05	4.6
Bringi et al. (2012)	C		3.9
Tokay and Short (1996) TOGA COARE	S	1.61	
Tokay et al. (1999) TOGA COARE	S	1.54	
Testud et al. (2001) TOGA COARE	S	1.3	
Bringi et al. (2009) Australia monsoon	S	1.22	3.5
Thurai et al. (2010) Australia monsoon	S	1.35	3.3
Bringi et al. (2012) Kwajalein	S		3.47

The mean $\log_{10}N_W$ for both sites is about 3.7 (**Table 2.1** and **Fig. 2.2**), which is close to the Marshall and Palmer (1948) exponential DSD concentration, $\log_{10}(8000 \text{ mm}^{-1} \text{ m}^{-3}) = 3.9$, as well as mean values listed in **Table 2.2** found by BC01, Illingworth and Blackman (2002), TH10, Islam et al. (2012), and Penide et al. (2013). The mean $\log_{10}N_W$ lies between bimodal distribution peaks at about 3.25 and 4.1, which are nearly one standard deviation (σ) from the

mean and almost 2 σ from each other. These bimodal $\log_{10}N_W$ peaks correspond to an order of magnitude difference in number concentration (N_W). Bimodal $\log_{10}N_W$ probability distribution function (PDF) peaks at other maritime locations were also found by Ulbrich and Atlas (2007), BR09, TH10, and Bringi et al. (2012) corresponding to maritime stratiform and convective populations (**Table 2.2**). Tokay and Short (1996) and Testud et al. (2001) also documented two C/S modes with higher number concentration, *LWC*, and DSD slope (λ for exponential DSD) for a given rain rate in convection compared to stratiform. This reflects the fact that stratiform rain has been affected by aggregation above and in the melting layer, which shifts mass to larger size bins, reduces number concentration, and also flattens the DSD slope (Lo and Passarelli 1982). In accordance with these previous studies, we suggest that a physically-based distinction between convective and stratiform rain produced the $\log_{10}N_W$ bimodality observed in **Fig. 2.2** for Gan and Manus Is.

BR03 and BR09 plotted $\log_{10}N_W$ against D_0 to distinguish different modes of raining DSD variability. They found a sloped separator line at $\log_{10}N_W{}^{SEP} = -1.6D_0 + 6.3$, where convective storms existed to the right of (above) the separator line. They considered mostly strong coastal tropical, coastal sub-tropical, and continental midlatitude convection. Stratiform rain was nearly always situated to the left of (below) their separation line, with decaying convection, or convection transitioning into stratiform rain, extending into the high $\log_{10}N_W$, low D_0 quadrant. TH10 investigated maritime convection and stratiform rain and found them separated by the same BR09 line but with variations in $\log_{10}N_W$ playing a significant role. They also presented weak, maritime convective DSD sample means of several thousand data points from Okinawa, Japan that were *just below* the BR09 line at high $\log_{10}N_W$ but relatively low D_0, suggestive of maritime, warm rain processes.

Fig. 2.3 shows a $\log_{10}N_W$ and D_0 smoothed 2D histograms for Gan and Manus Is. The relatively sharp cut-off of data in the lowest $N_W(D_0)$ quadrant is due to necessary rain rate and total drop number data quality thresholds. The Manus samples are more numerous, more evenly-spread, but distributed in similar spatial orientations compared to the Gan samples, as suggested by the histograms of individual parameters in **Fig. 2.2**. A large proportion of data exists near $\log_{10}N_W = 3.2$ and $D_0 = 1.0$ mm (Gan) and 0.9 mm (Manus) corresponding to stratiform rain in BR03, BR09, and TH10. A secondary peak occurs near $\log_{10}N_W = 4.1$ and $D_0 = 0.7 - 1.1$ mm, similar to the shallow, weak, convective Okinawa data from TH10. These two frequent modes of variability appear to be separated by a nearly horizontally-oriented area of lower frequency of occurrence somewhere between $\log_{10}N_W = 3.7$ and 3.9. **Fig. 2.3** shows that a very small fraction of the Manus and Gan Is. data points would be classified as convective by the BR09 separator line, which does not seem to fall between any natural breaks in this tropical, maritime $N_W(D_0)$ distribution. Although Barnes and Houze (2014) and Rowe and Houze (2014) show radar observations of graupel and small hail aloft in storms during DYNAMO in the central Indian Ocean, which result in high D_0 and low $\log_{10}N_W$, these vigorous convective processes are not frequent over the Warm Pool and certainly not to the same magnitude as the midlatitude and subtropical continental convection considered when forming the BR09 separation line. Instead, a new convective/stratiform separator line at $\log_{10}N_W^{SEP} = 3.85$ is drawn for this unique tropical, *oceanic* dataset, bifurcating the two modes of variability in **Fig. 2.3.** The placement of this line will be verified by extensive case study analysis in Sec. 4 and mathematically tested in Sec. 5.

It is worth pointing out that the $\log_{10}N_W^{SEP}$ line drawn in **Fig. 2.3** is mathematically equivalent to $LWC^{SEP} = 0.1226\,D_0^4$ through Eq. 1. The corresponding $LWC(D_0)$ distributions for Gan and Manus Is. also exhibit two modes of variability on either side of this separator line (**Fig.**

2.4), each oriented in the same direction of increasing LWC for increasing D_0 when both

variables are plotted on a logarithmic scale (illustrating the $LWC \sim D_0^4$ dependence in Eq. 1). As

seen for $N_W(D_0)$, the $LWC(D_0)$ distributions at each location also appear very spatially-correlated

except that the Gan Is. dataset has less total data points so that the contoured 2D histogram

clusters are not as well-organized as for Manus Is. 2D histograms of $LWC(D_{MAX})$ also exhibit two

modes of variability, similar to $LWC(D_0)$.
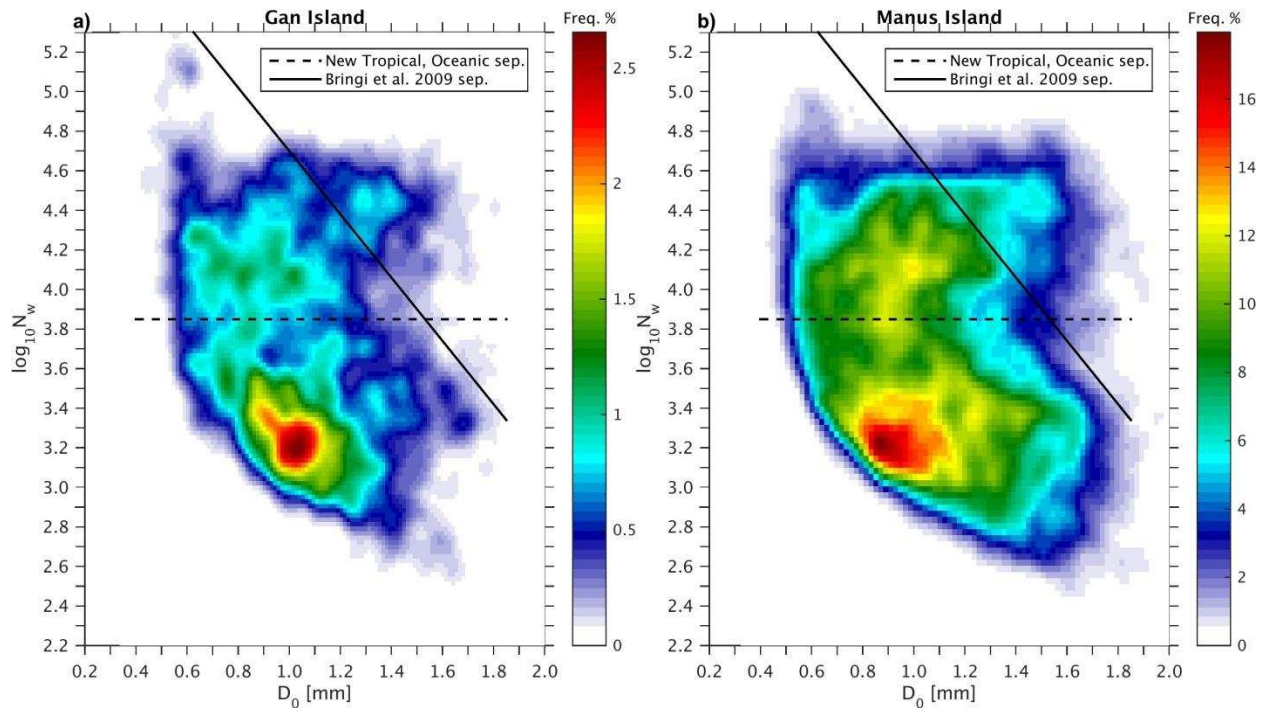
Figure 2.3: Gan and Manus Is. $N_W(D_0)$ smoothed 2D histograms contoured by frequency of occurrence with the original subtropical, continental Bringi et al. (2009) $\log_{10}N_W^{SEP} = -1.6D_0 + 6.3$ and updated tropical, oceanic convective/stratiform $\log_{10}N_W^{SEP} = 3.85$ separation lines. Gan (Manus) Is: 130 (100) bins in each direction; 13 (8) bin Gaussian filter width.

Using **Figs. 2.3** and **2.4** as references, the next section is devoted to explaining: (1) why

these two frequency peaks, in both the $N_W(D_0)$ and $LWC(D_0)$ spaces, actually correspond to

stratiform and convective tropical, oceanic rain; and (2) justifying the placement of the new

$\log_{10}N_W^{SEP}$ separation line.
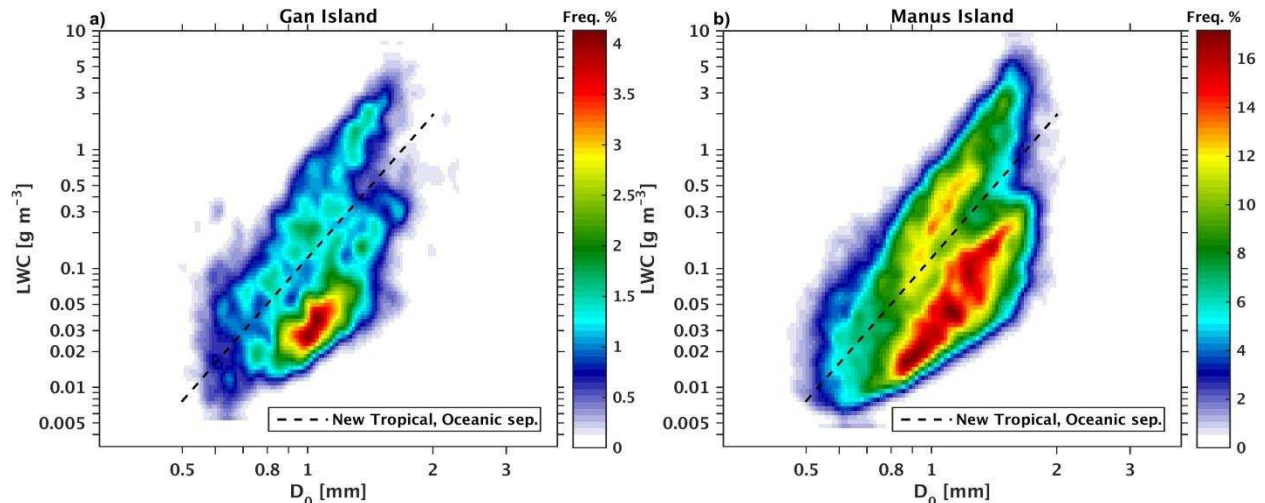
Figure 2.4: Gan and Manus Is. $LWC(D_0)$ smoothed 2D histograms contoured by frequency of occurrence with the updated tropical, oceanic C/S rain LWC^{SEP} separation line, which is equivalent to $\log_{10}N_W^{SEP} = 3.85$. Gan (Manus) Is: 105 (100) bins in each direction; 4 (2) bin Gaussian filter width.

2.4 Radar observations

The entire DYNAMO S-Pol RHI dataset was examined to find times when the radar indicated rain over the disdrometer and the disdrometer also recorded data. This resulted in 372 analyzed case studies of S-Pol vertical cross section radar scans with coincident Gan Is. 2DVD data. Analyzing sequences of paired observations helped elucidate the evolution of DSD spectra with respect to the horizontal and vertical evolution of radar echoes above and around the disdrometer. These case studies motivated why a separation line at $\log_{10}N_W^{SEP} = 3.85$ can be drawn to delineate convective and stratiform rain encountered at Manus and Gan Is. Nine of the 372 case studies analyzed are presented in this section. They are representative cases spanning the entire $N_W(D_0)$ and $LWC(D_0)$ parameter spaces, and thus the full intensity and organizational spectrum between stratiform and tropical, maritime convective rain. Note that the 0°C level was consistently between 4.5 - 5.1 km AGL (550-600 mb) during these DYNAMO case studies. Residual ground clutter (identifiable by low ρ_{hv} and negative/variable Z_{dr}) contaminates radar

34

data near the disdrometer (varying from case to case depending on atmospheric refraction of the radar beam downwards).

2.4.1 CASE #1: strong, widespread convection

Fig. 2.5 shows an example of widespread, deep convection. The S-Pol radar horizontal (PPI) and vertical (RHI) cross sections over the Gan disdrometer, 8 km away at 141° azimuth, show a large area of $Z_h > 50$ dBZ over the disdrometer and extending up to 5.5 km AGL. The differential reflectivity over the disdrometer is over 2 dB, indicating the presence of large, horizontally-oriented raindrops (BC01). High Z_{dr} of this same magnitude and low ρ_{hv} to 0.93 near 5 km AGL indicates some melting, but in a disrupted fashion due to strong convection. A horizontally-elongated, stable, stratiform rain radar brightband is not evident. As this deep convection passed over the disdrometer, $\log_{10}N_W$ and D_0 were both relatively high, between 4.3-4.6 and 1.4-1.7 mm, respectively. The *LWC* was correspondingly high, with values approaching 5 g m^{-3}, and rain rates were between 30-100 mm hr^{-1}. The BR09 method would have classified this example as convection.

2.4.2 CASE #2: strong, isolated convection

Fig. 2.6 shows another case of strong convection with near-surface reflectivity exceeding 45 dBZ, but associated with an isolated cell. Z_{dr} is above 1 dB below 2 km and ρ_{hv} is above 0.99 throughout the entirety of the echo, meaning there is no established melting layer. The number concentration ($\log_{10}N_W$) is slightly lower than the widespread deep convective case in **Fig. 2.5**, between 4.0-4.2. Since N_W is proportional to *LWC* by Eq. (1), it is not surprising that *LWC* for this case is also slightly lower, near 2-4 g m^{-3}, while rain rates were between 30-50 mm hr^{-1}. However, the median drop diameters of these DSD are slightly higher than case #1, exceeding 1.5 mm. Both the widespread and isolated strong convective cases are near the upper,
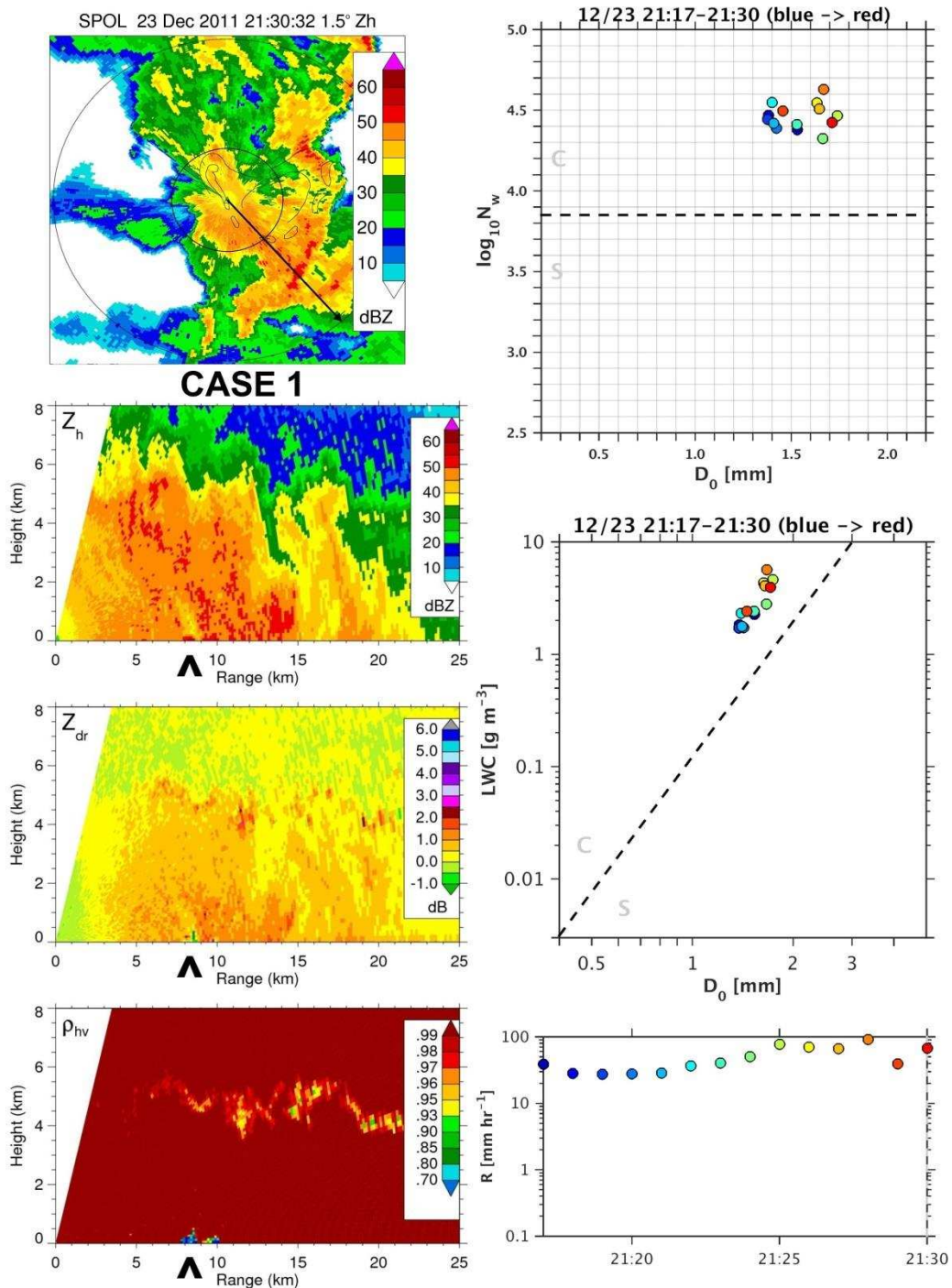
Figure 2.5: Case study #1 of widespread deep convection at 21:30 UTC 23 Dec 2011 with S-Pol radar PPI and RHI of reflectivity (Z_h), differential reflectivity (Z_{dr}), and the correlation coefficient (ρ_{hv}). Range rings at 8 and 25 km; Gan Is. 2DVD along the black arrow at 8 km range denoted by carrot on RHI in this direction. $N_W(D_0)$, $LWC(D_0)$, and R time series are plotted throughout 21:17-21:30 UTC where time increases as the colored markers go from blue to red. $\log_{10}N_W^{SEP}$ separation line and its equivalent LWC^{SEP} line are plotted to differentiate convection above and stratiform rain below.
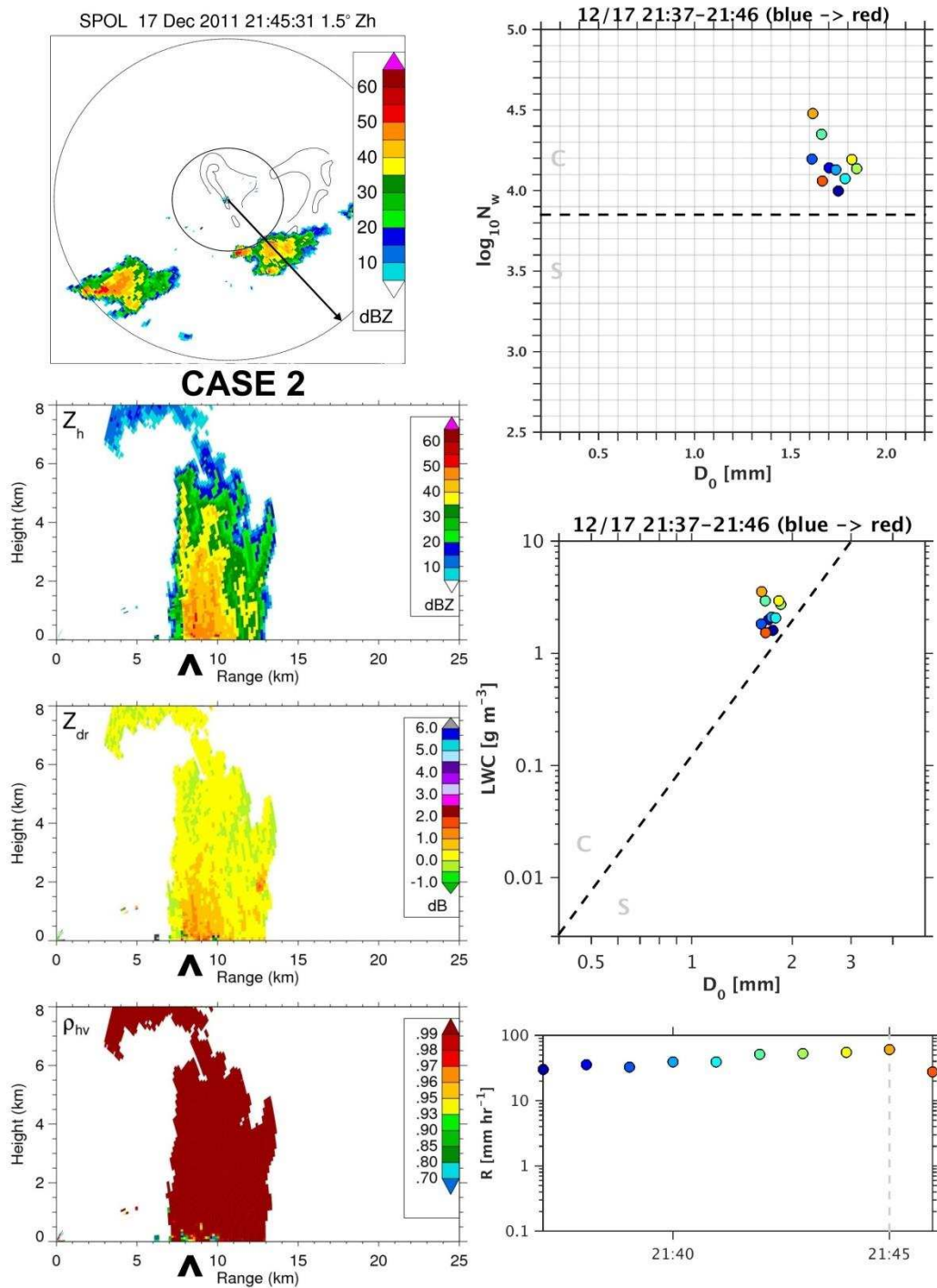
Figure 2.6: Case study #2: as in Fig. 2.5 but for isolated strong convection at 21:45 UTC 17 Dec 2011 with 2DVD data spanning 21:37 - 21:46 UTC, time increases as the colored markers go from blue to red.

right-hand edge of the $N_W(D_0)$ and $LWC(D_0)$ 2D histograms (**Fig. 2.3, 2.4**). The BR09 method would have classified this example as convection.

2.4.3 CASE #3: weak, widespread convection

Weaker convection was frequently observed according to DSD and radar observations. This type of weakly forced, weakly organized convection tended to decay rapidly. **Fig. 2.7** is an example of localized enhancements of reflectivity extending from the surface upwards that, according to radar vertical cross sections, do not even reach the 0°C level (4.5-5.1 km AGL or 600-550 mb throughout the field campaign) Therefore, these warm rain DSD could not have been influenced by vapor deposition, aggregation, or melting. This case is thus convective in nature, driven by surface buoyancy. Z_{dr} is near zero and ρ_{hv} is near unity throughout most of this shallow echo except for the leading edge at the beginning of the time series (storm propagated southeast over the 2DVD). For more than 45 minutes after this initial radar scan, the $\log_{10}N_W$ remained relatively high near 4.6-4.8, while D_0 was near 1 mm, consistent with the lower radar reflectivities seen in this example compared to stronger convection. LWC was still near 0.5-1 g m^{-3} on the "top" side of the LWC^{SEP} line with rain rates between 5-15 mm hr^{-1}. DSD in both parameter spaces were indicative of belonging to the upper mode of each bimodal distribution shown in the previous section. These DSD lie directly *on* the BR09 separation line (not shown).
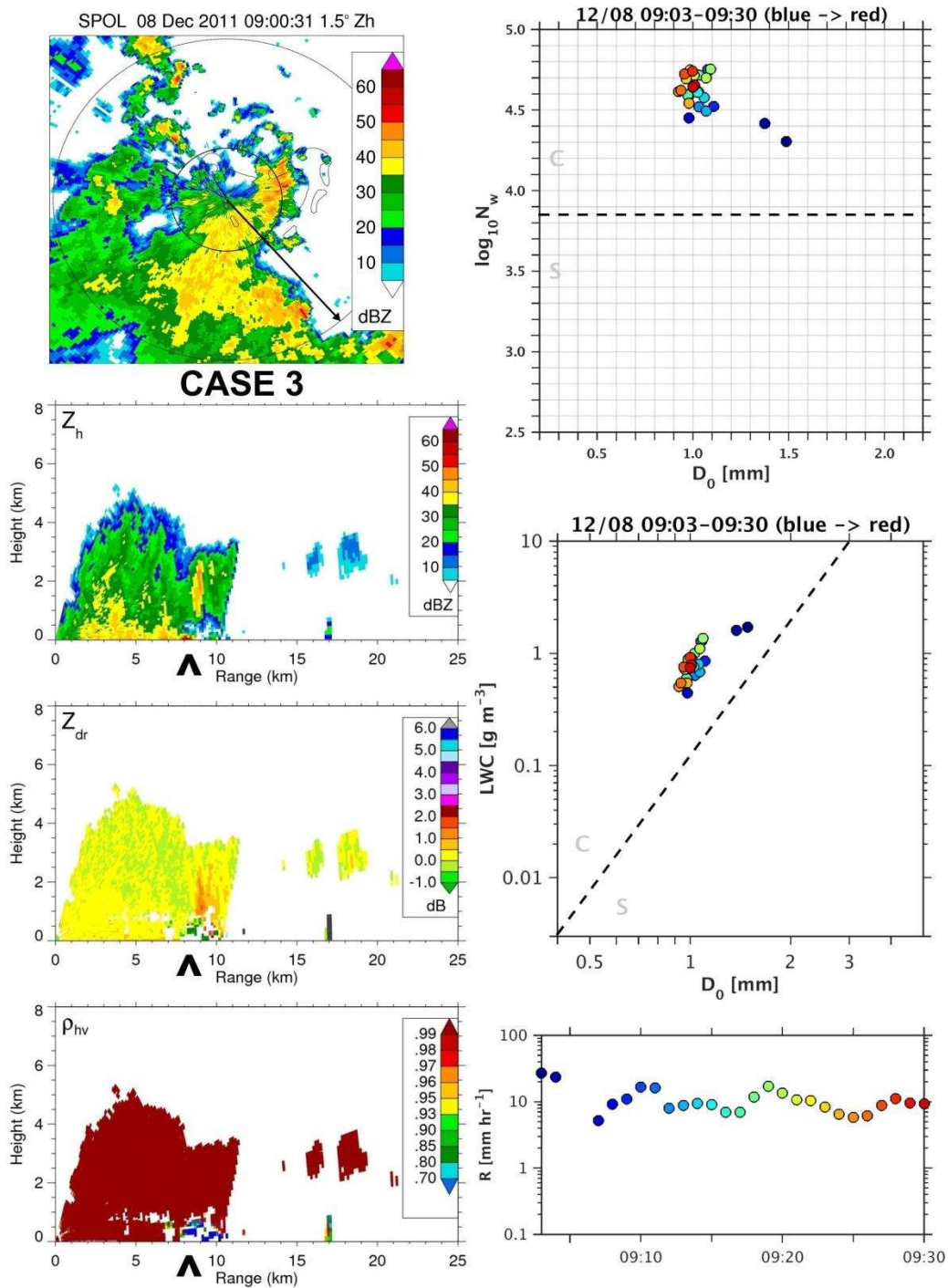
Figure 2.7: Case study #3: as in Fig. 2.5 but for widespread, shallow convection at 09:00 UTC 08 Dec 2011 with 2DVD data spanning 09:03-09:30 UTC, time increases as the colored markers go from blue to red

2.4.4 CASE #4: weaker, isolated convection

An example of even weaker, shallower convection in **Fig. 2.8** shows the same high $\log_{10}N_W$ near 4.5 as the weak, widespread convection in case #3, but with D_0 as low as 0.6 mm. The *LWC* is correspondingly lower between 0.1-0.5 g m^{-3} with R between 1-5 mm hr^{-1}. These radar echoes are also smaller in horizontal area. Radar reflectivity is mostly between 20-30 dBZ with some localized areas above 35 dBZ. The vertical elongation of these echoes upwards, but only to 4 km AGL, and the lack of any radar signatures of melting, aggregation, or ice aloft signifies that these echoes are convective in origin, driven by buoyancy within the moist marine boundary layer. The continental, subtropical BR09 separation would have classified these DSD as stratiform.

2.4.5 CASE #5: weaker, shallower convection

At the highest $\log_{10}N_W$ but lowest D_0 end of the spectrum, light rain with echo tops below 2 km AGL was observed in several cases akin to **Fig. 2.9**. The shallow cloud depth, confined below the trade wind inversion in this case, likely played a role in limiting drop growth. The maximum diameters from these DSDs ranged from 0.83-1.98 mm, with an average maximum diameter of only 1.32 mm. Median drop diameters were 0.5-0.75 mm. These light rain DSD account for the extension of the $N_W(D_0)$ 2D histogram in **Fig. 2.3** up and to the far left of the diagram, which also lie on the stratiform side of the BR09 separation line. The radar characteristics and inferred low-level heating profile of this precipitation warrant its classification as convection, albeit weak. Z_h remained below 30 dBZ, horizontal Z_h gradients were weak, Z_{dr} remained near zero, and ρ_{hv} was near unity except for obvious ground clutter where $\rho_{hv} < 0.75$ and $Z_{dr} < 0.5$ dB. As expected, rain rate was fairly low, ranging between 0.3 - 10 mm hr^{-1}.
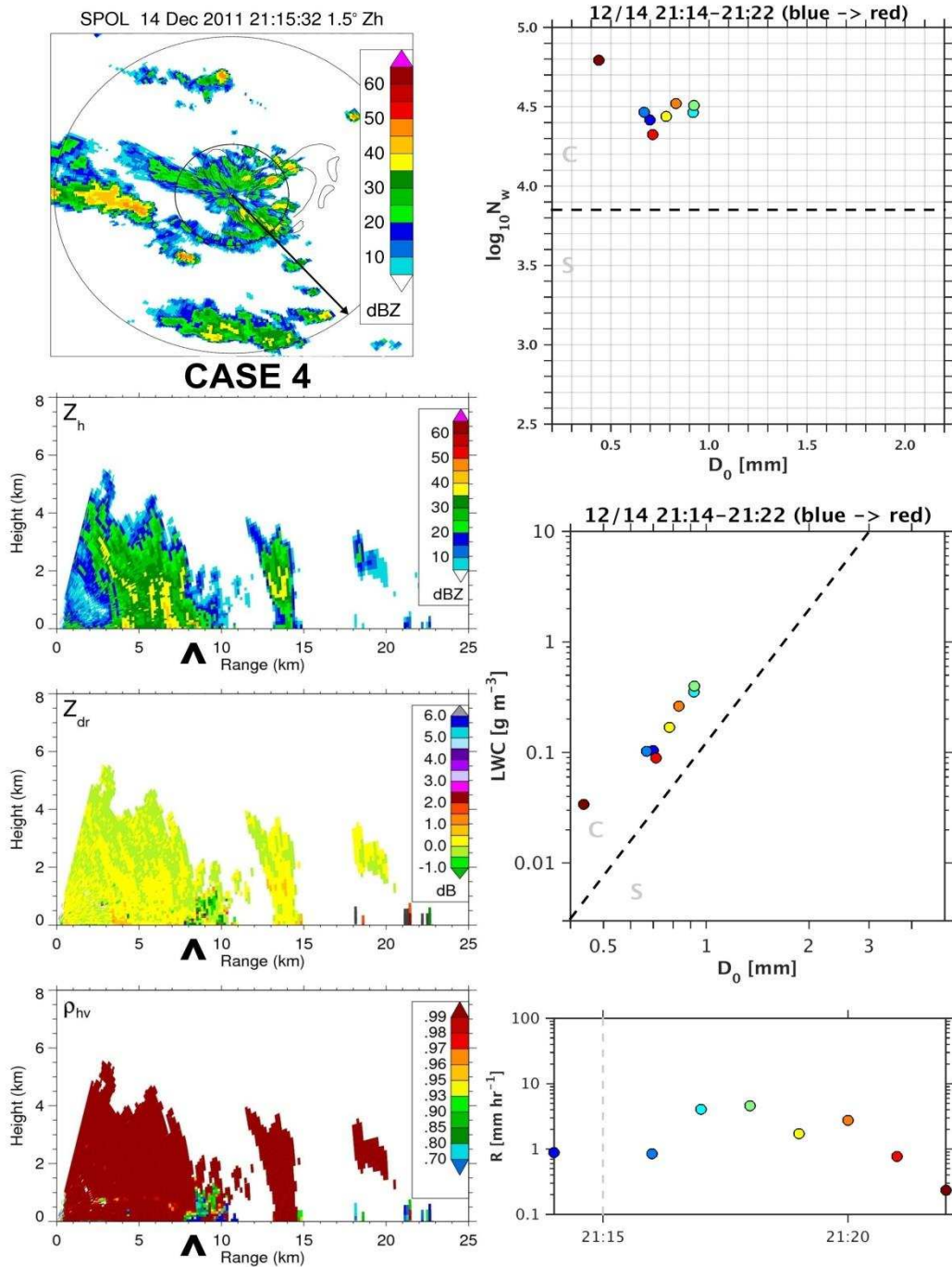
Figure 2.8: Case study #4: as in Fig. 2.5 but for shallow convection at 21:15 UTC 14 Dec 2011 with 2DVD data spanning 21:14-21:22 UTC, time increases as the colored markers go from blue to red

Figure 2.9: Case study #5: as in Fig. 2.5 but for light rain at 07:45 23 Nov 2011 with 2DVD data spanning 07:30-08:10 UTC, time increases as the colored markers go from blue to red

2.4.6 CASE #6: moderate stratiform

Moderate stratiform rain exhibits much different radar and DSD characteristics than convection (Houze 1997). For instance, stratiform rain in **Fig. 2.10** has rain rates in the same ranges as the preceding weak convection (<10 mm hr^{-1}), similarly low *LWC* between 0.1 - 0.5 g m^{-3}, but $D_0 > 1$ mm and $\log_{10}N_W$ between 3.6 - 3.85. The same R and *LWC* were apparently achieved with much lower $\log_{10}N_W$, slightly greater surface Z_h, and greater D_0. This suggests that these DSD exhibit different covariances between the integral rain parameters compared to convection (Atlas et al. 1973). The *LWC*(D_0) and N_W(D_0) points are on the stratiform side of the separation lines. Throughout inspection of all 372 radar-2DVD case studies, stratiform rain with a clear radar brightband was observed to approach, *but stay below* the $\log_{10}N_W^{SEP} = 3.85$ line. These DSD were aligned with the stratiform rain distributions in BR03, BR09, and TH10, suggesting that the stratiform N_W(D_0) ranges are not as region-dependent as convection.

2.4.7 CASE #7: weak stratiform

Widespread, weaker stratiform rain (**Fig. 2.11**) exhibited brightband signatures but with even lower surface $\log_{10}N_W$ near 3.3 and $D_0 < 1$ mm, consistent with lower surface Z_h. The *LWC*(D_0) samples during this time were on the lower side of the *LWC*^{SEP} line with R only ranging from 0.1-0.3 mm hr^{-1}. These samples were nearly coincident with the main frequency of occurrence maxima observed in **Figs. 2.3 and 2.4**. This mode of precipitation is obviously more frequently observed than the upper mode of *LWC*(D_0) and N_W(D_0) variability associated with convection, most likely because stratiform rain lasts longer and covers a wider area. This is consistent with previous tropical rainfall studies that report stratiform rain being more commonly observed per unit area and per unit time than convection even though convection is responsible for more accumulated rainfall, e.g. (Cheng and Houze 1979; Tokay and Short 1996; Zuluaga and

Houze 2013; Xu and Rutledge 2014). The BR09 method would have classified these echoes as stratiform.
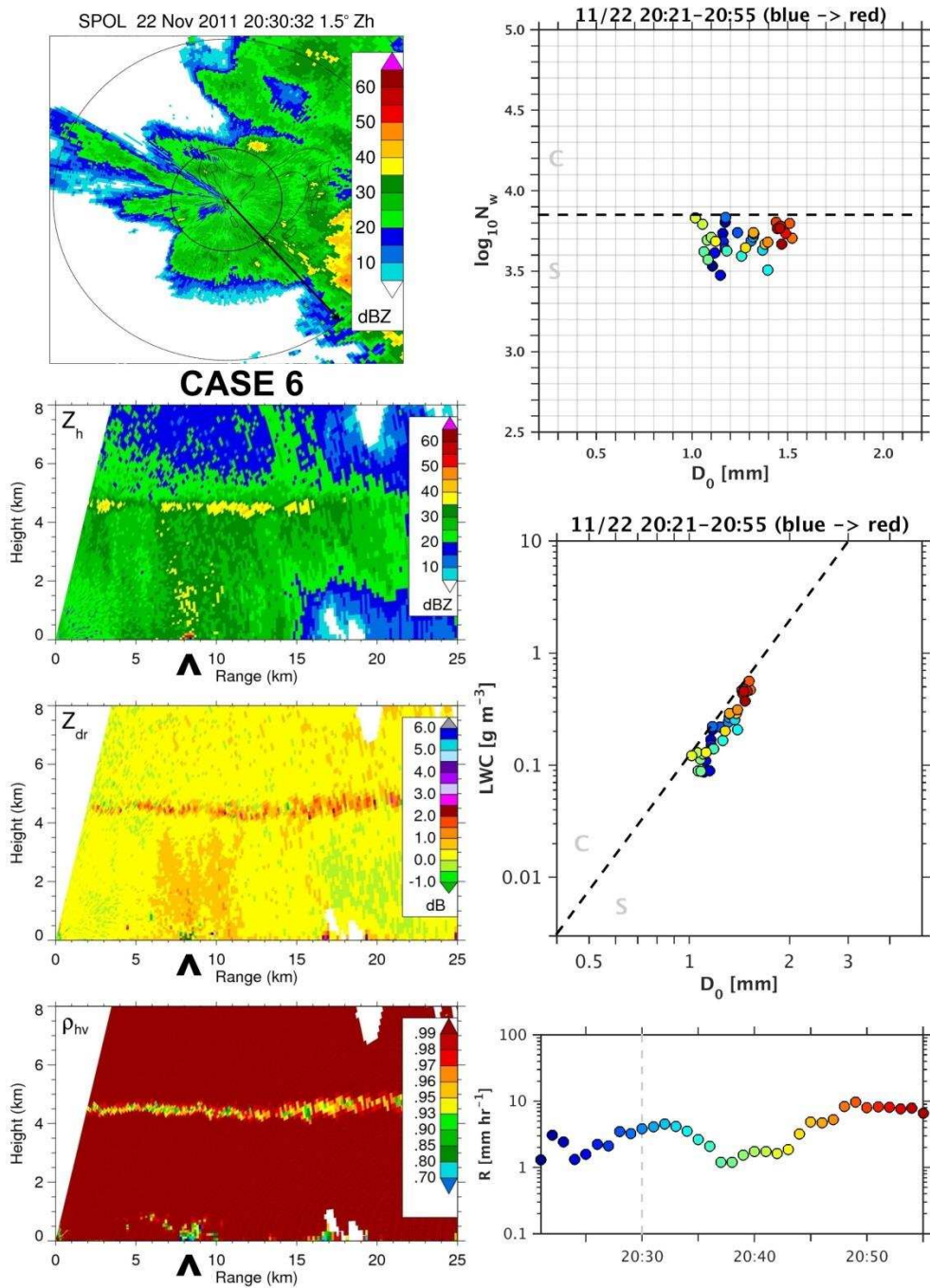
Figure 2.10: Case study #6: as in Fig. 2.5 but for stratiform rain at 22 Nov 2011 with 2DVD data spanning 20:21-20:55 UTC, time increases as the colored markers go from blue to red
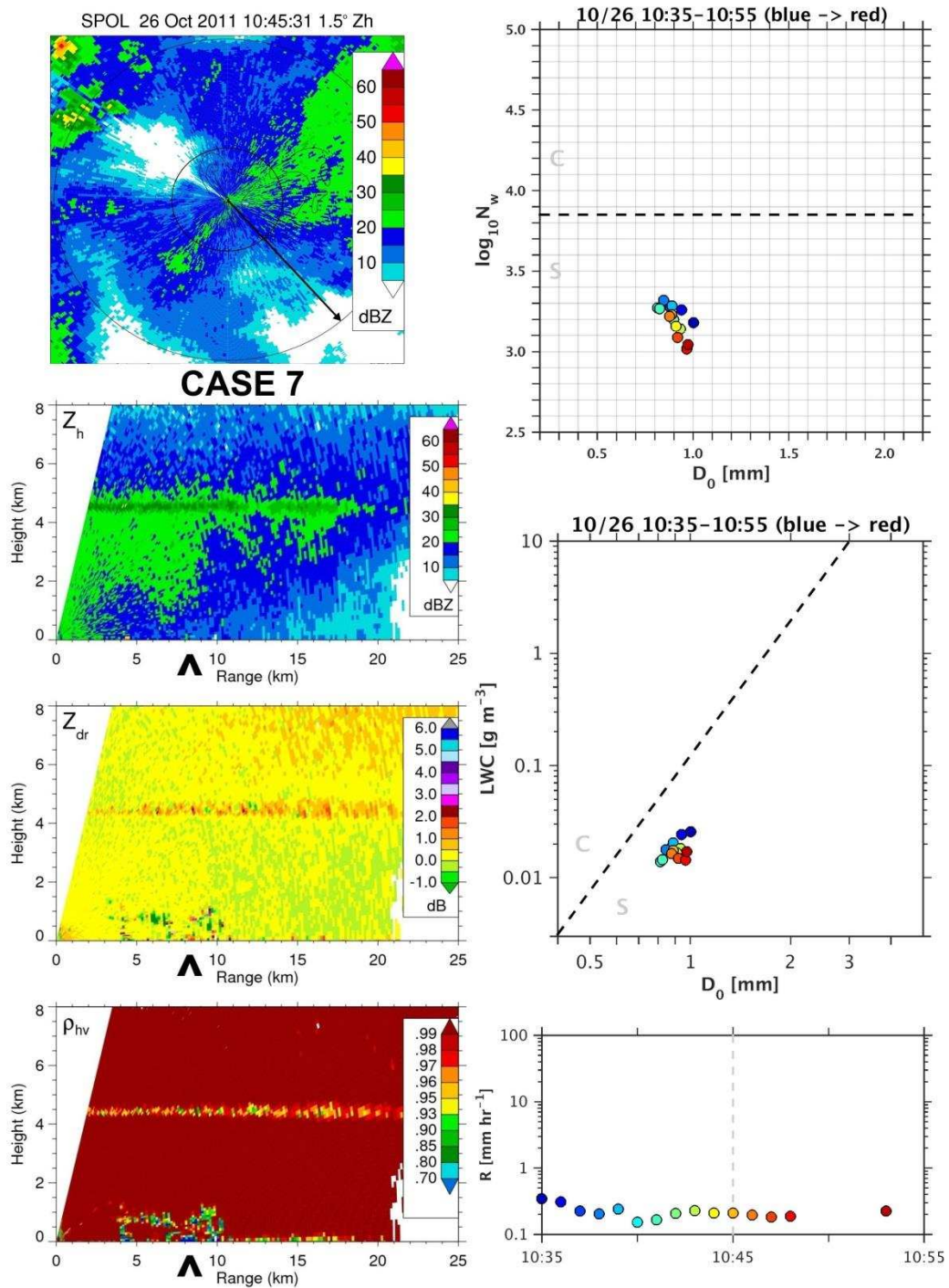
Figure 2.11: Case study #7: as in Fig. 2.5 but for weak stratiform rain at 10:45 UTC 26 Oct 2011 with 2DVD data spanning 10:35-10:55 UTC, time increases as the colored markers go from blue to red

2.4.8 CASE #8: gradual transition from embedded convection to stratiform

The last two case studies demonstrate convection transitioning to stratiform rain. **Fig. 2.12** begins with convection embedded in a widespread, long-lived stratiform rain region. Low-level reflectivity exceeds 45 dBZ. The convective updrafts and precipitation growth processes appear to have disrupted the brightband locally above the disdrometer. The $\log_{10}N_W$ during this first scan of the series was well above the new separation line at 4.3 while D_0 was nearly 1.5 mm, R was near 30 mm hr^{-1}, and LWC was just over 1 g m^{-3}. The second set of radar scans show that the convection decayed over a 30 minute period and the region of high reflectivity descended to the ground. The brightband also started to become more established and uniform during this time. However, there were still areas of enhanced reflectivity aloft, which were vertically elongated above the high-reflectivity fall streak. The DSD remained on the upper portion of the $N_W(D_0)$ and $LWC(D_0)$ distributions, but were approaching each separation line. Likewise, rain rates were 10 mm hr^{-1}.

By the time of the third radar scan 30 minutes later, an hour after strong convection passed over the disdrometer, the radar echoes were more horizontally uniform, many portions of the radar brightband showed ρ_{hv} below 0.93, DSD had crossed the $LWC(D_0)$ and $N_W(D_0)$ separation lines, and rain rates decreased to 3 mm hr^{-1}. The fourth radar scan shows an invigoration of the radar brightband to above 45 dBZ over a +15-km-wide area near 4.5 km AGL. A deep portion of the radar brightband exhibited ρ_{hv} <0.83 and Z_{dr} >2 dB. These polarimetric data are consistent with the expectation of large rain drops at the surface (Tokay et al. 1999; Brandes et al. 2004), which was verified by observations of D_0 near 1.9 mm at this time. Near-surface Z_{dr} was 0.5-1 dB and surface rain rates were just under 10 mm hr^{-1}. The layer of near-zero Z_{dr} just above the
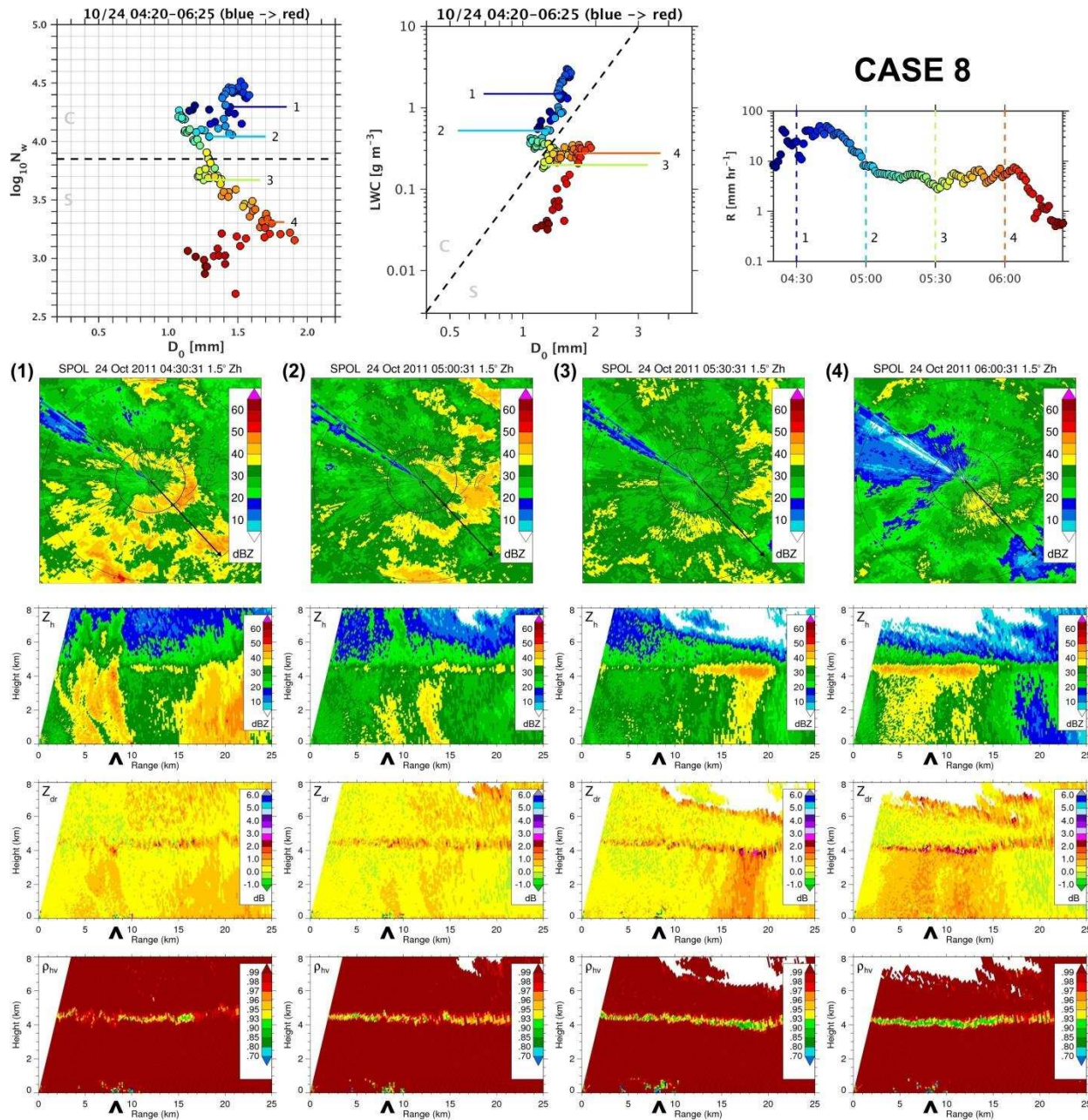
Figure 2.12: Case study #8: as in Fig. 2.5 but for a transition from a leading convection line to strong stratiform rain at at (1) 04:30, (2) 05:00, (3) 05:30, (4) 06:00 UTC on 24 Oct 2011 with 2DVD data spanning 04:20-06:25 UTC. Numbers 1-4 correspond to call out points in the 2DVD data based on the time of the radar scans, where time increases as the colored markers go from blue to red

brightband and increasing Z_{dr} with altitude toward echo top above the disdrometer suggest

pristine ice crystal growth near cloud top and subsequent aggregation above the melting layer

(Ryzhkov et al. 2005; Kennedy and Rutledge 2011; Thompson et al. 2014). Braun and

Houze (1994) highlight the role of vapor deposition aloft in producing strong stratiform

brightbands. In addition, the aggregation process can concentrate LWC into fewer, but larger

drops, which is supported by the trends observed in these DSD parameters from radar scans (2)-

(4): lower LWC near 0.3 g m^{-3}, greater D_0, and lower $\log_{10}N_W$ near 3.2 compared to (2) and (3).

This "zig-zag" migration through integral rain parameter spaces during a C/S transition was also

noted by Tokay and Short (1996) and Atlas et al. (1999). The further decrease in surface D_0,

LWC, R, Z_h, and even $\log_{10}N_W$ toward the end of this DSD sample period was associated with

much lighter stratiform rain and a weaker brightband (not shown with radar, similar to case #7).

2.4.9 CASE #9: abrupt transition from leading convection to stratiform

A different, but commonly observed transition from a leading convective line to a trailing

stratiform region is illustrated in **Fig. 2.13**. The DSD and radar echoes begin in a similar fashion

as the previous case with only faint, disrupted signatures of melting in ρ_{hv} aloft and high $\log_{10}N_W$,

LWC, and D_0 above each separation line. Rain rates reached 20 mm hr^{-1} with surface Z_h just

above 40 dBZ over the disdrometer. Radar echoes 15 minutes later in the second panel of the

series look very similar to the decaying convection observed in the previous case study, with a

fall streak of high reflectivity extending toward the ground and some lingering heterogeneity in

the reflectivity pattern above discontinuous polarimetric signatures of melting near 5 km AGL.

The DSD did not vary much between these two radar scans. Then, over the course of only five

minutes, DSD shifted to the lower side of the $\log_{10}N_W{}^{SEP}$ and LWC^{SEP} lines and rain rates
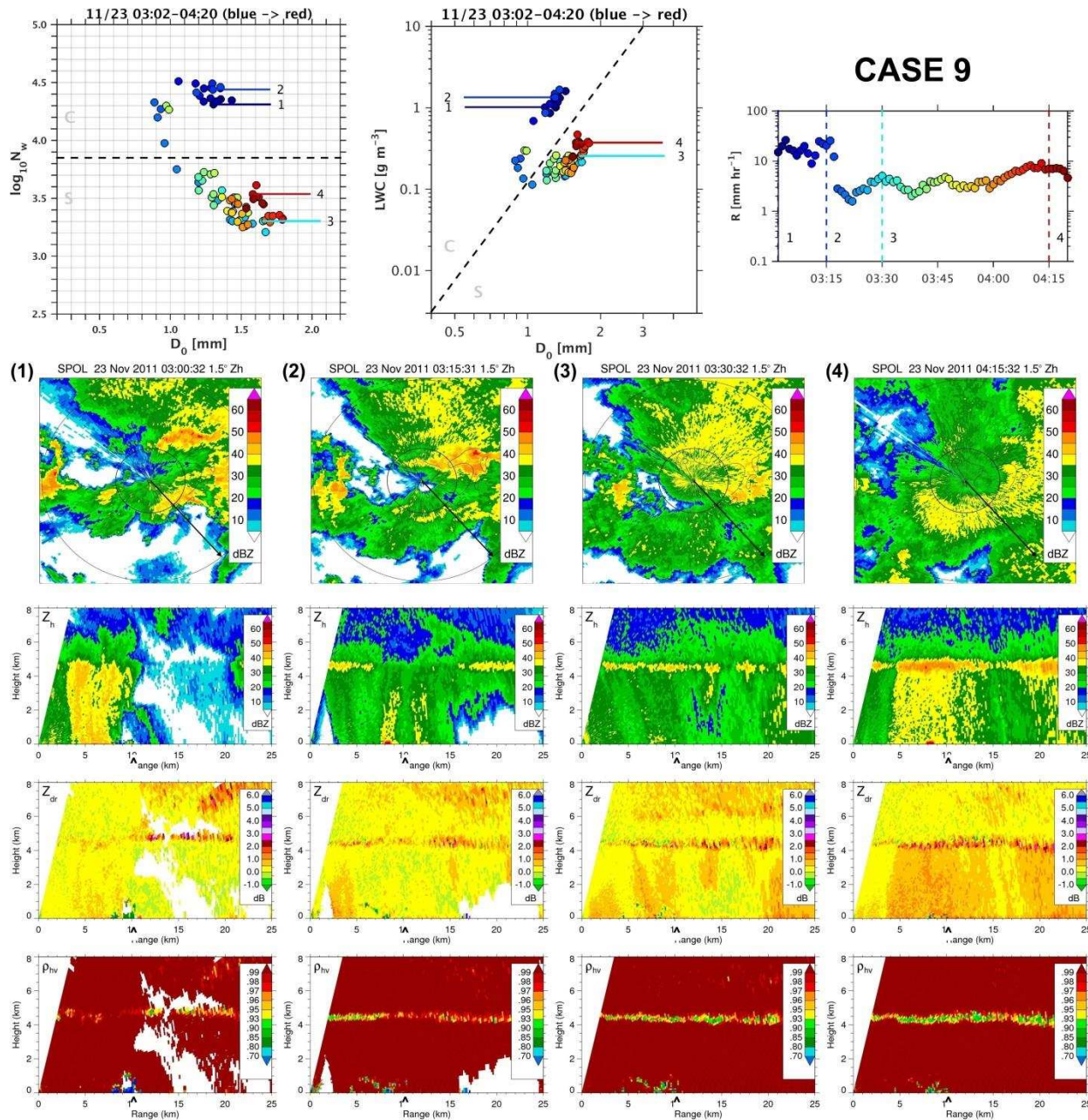
Figure 2.13: Case study #9: as in Fig. 2.5 but for a transition from convection embedded in stratiform rain to strong stratiform rain at (1) 03:00, (2) 03:15, (3) 03:30, (4) 04:15 UTC on 23 Nov 2011 with 2DVD data spanning 03:02-04:20 UTC. Numbers 1-4 correspond to call out points in the 2DVD data based on the time of the radar scans, where time increases as the colored markers go from blue to red.

decreased to around 5 mm hr^{-1}. The third set of RHIs just after the transition show more

horizontally-homogeneous reflectivity patterns above the melting layer with increased Z_{dr}, Z_h,

and reduced ρ_{hv} in the melting layer, suggesting more dominant stratiform rain processes

throughout the column. The number concentration and *LWC* rapidly decreased as D_0 increased,

consistent with the effects of snowflake aggregation aloft. The near-zero Z_{dr} layer above the

brightband also supports this hypothesis.

This abrupt C/S transition was also reported as a number concentration "jump" by

Waldvogel (1974), Tokay and Short (1996), and Braun and Houze (1994). According to the 372

case radar-2DVD case studies examined, while stratiform cases always exhibited lower

$\log_{10}N_W$ than convection, the evolution between C/S rain was not usually as quick as this

example. It is also interesting that D_0 and *LWC* vary in the same direction, or slope, as rain

intensity varies within both stratiform and convective scenes, but the transition between the two

rain types follows a different D_0 and *LWC* covariance not predicted by Eq. 1 (evidenced in both

Fig. 2.12 and 2.13).

The DSD remained relatively constant in time until 45 minutes later in the fourth radar

data example, when a strong radar brightband > 50 dBZ developed above the disdrometer and

led to Z_{dr} >1 dB between 0-4 km AGL. ρ_{hv} was below 0.93 and Z_{dr} exceeded 3 dB over a

relatively deep brightband depth compared to previous radar scans. Tokay et al. (1999) and

Brandes et al. (2004) explained how surface D_0 often increases as brightband reflectivity and

depth increase. Despite the intense stratiform brightband aloft, surface rain rates were still

limited to about 9 mm hr^{-1}.

2.4.10   Discussion

Convection was observed to rapidly evolve and decay, sometimes over very small spatial scales such that only a small portion of the convective radar echo actually went over the disdrometer. The resulting DSD observed at the surface were therefore sometimes difficult to attribute to particular convective radar echoes because of S-Pol's 15-minute update time. DSD in the intermediate time periods between convective updrafts or before and after their passage over the disdrometer were usually quite scattered. Likely due to drop size sorting in the turbulent cloud edge, the first and last few minutes of a convective DSD event sometimes exhibited very low number concentrations but very high D_0. For these reasons, Gunn and Marshall (1955) recount that rain usually begins with a *few large drops*, with moderate Z_h but only small rain rates. Despite these understandable fluctuations associated with convection, the cases with clear convective precipitation over the disdrometer were uniformly *above* the $\log_{10}N_W^{SEP} = 3.85$ line in the $N_W(D_0)$ parameter space. Stratiform rain DSD were more stable and slowly evolving. These stratiform radar echoes *did not* produce DSD above $\log_{10}N_W^{SEP} = 3.85$. Thus, we are most confident in our classification of stratiform DSD, while everything "else" warranted a convective classification. Given the consistency of radar observations in **Figs. 2.5-2.13** of convection above, stratiform below, and transitions crossing the $\log_{10}N_W^{SEP} = 3.85$ line, maritime, tropical DSD data can apparently be separated by this method.

Yuter and Houze (2002) make an important point that, even if DSD separation methods can delineate C/S populations (such as we demonstrate for this rain regime), a huge hurdle still remains if radar algorithms cannot. Radar observations in this section suggest that reflectivity texture-based algorithms and dual-polarization radar-based melting layer detection algorithms should be able to distinguish *most* types of tropical, oceanic rain consistently with this DSD-

51

based approach. TH10 demonstrate this clearly for stratiform rain and strong convection using the BR09 DSD and Steiner et al. (1995) radar-based methods. However, light convective rain in **Fig. 2.7** would be difficult to classify as convection using traditional radar-based techniques because of weak horizontal reflectivity gradients, overall low Z_h, and low echo top heights.

Another challenge for radar C/S algorithms is to detect convection embedded within stratiform rain (e.g. **Fig. 2.12**), especially if the convective echoes are shallow and exist below the radar brightband. Observations in this section showed that fall streaks within stratiform rain, associated with relatively high surface rain rate up to 10 mm hr^{-1} and Z_h up to 40 dBZ, were often the result of recently-decayed convective activity (Yuter and Houze 1997, 1998). In **Fig. 2.12** and **2.13**, the DSD settled down to the stratiform $N_W(D_0)$ and $LWC(D_0)$ mode after the fall streak ended and once the reflectivity was more horizontally-homogeneous *above* the brightband as suggested by the Williams et al. (1995) vertically-pointing radar classification method.

2.5 DSD-based convective/stratiform rain classification

In addition to analyzing 2DVD-radar case studies, we also explore a mathematical way to test which line, between $\log_{10}N_W^{SEP} = 3.7$ to 3.9, would minimize the most error in convective, stratiform, and total rainfall estimates. Since the S-Pol radar's scanning strategy prevented a paired 2DVD-radar comparison or statistical rainfall estimation analysis (see Sec. 2), the same DSD-simulated reflectivity dataset used to form the $R(z)$ equations is used in a self-consistency test to see when the 2DVD total, convective, and stratiform accumulated rainfall converged with $R(z)_C$ and $R(z)_S$ estimates. C/S $R(z)$ equations were iteratively formed with C/S R and z data as the partitioning line varied. The errors between the Gan 2DVD R and C/S $R(z)$ did not minimize for any particular separation line. However, this goal was achieved between $\log_{10}N_W^{SEP} = 3.8$-

3.85 for Manus Is. R, as seen in **Table 2.3**. The $\log_{10}N_W{}^{SEP} = 3.85$ dividing line was chosen

between these two options in light of the consistent radar-2DVD case study observations of

stratiform rain below this line in the previous section.

       Table 2.3 also shows the variability in C/S rain fraction and frequency of occurrence

estimates as the separation line varied. Moving the line from $\log_{10}N_W = 3.9$ to 3.7 accounted for a

6% decrease (increase) in convective (stratiform) rain fraction and a 10% decrease (increase) in

convective (stratiform) rain frequency of occurrence at both locations. The case studies

motivated $\log_{10}N_W{}^{SEP}$ somewhere between 3.8 to 3.9 so we consider a ± 0.05 $\log_{10}N_W$ window of

uncertainty in rainfall estimates due to this separation technique. This window corresponds to 3

(2)% of total rainfall accumulation and 5 (4)% of rain occurrences.

Table 2.3: Sensitivity of rain statistics to $\log_{10}N_W$ partitioning methods by comparing to Manus
and Gan Is. convective and stratiform 2DVD rain fractions and the percent difference between
all, convective, and stratiform rain accumulations according to the 2DVD vs. $R(z)_C$ and
$R(z)_S$ calculations. These tests were run for convective/stratiform rain partitioning methods
ranging from $\log_{10}N_W{}^{SEP} = 3.7$ to 3.9, where convection was classified above the line and
stratiform at or below the separation line.

| PLACE | $\log_{10}N_W$ SEP | 2DVD | | | | % diff. 2DVD- C/S $R(z)$ | | |
		CONV Rain fraction [%]	STRAT Rain fraction [%]	CONV Rain frequency [%]	STRAT Rain frequency [%]	R_{TOTAL} [mm]	R_C [mm]	R_S [mm]
Manus	3.70	85	15	48	52	3.56	4.12	0.38
Gan		84	16	48	52	6.30	6.94	2.93
Manus	3.75	84	16	46	54	3.52	4.16	0.22
Gan		82	18	45	55	6.44	7.13	3.27
Manus	3.80	82	17	43	57	3.37	4.05	0.21
Gan		81	19	43	57	6.60	7.38	3.32
Manus	3.85	81	19	41	59	3.40	4.17	-0.01
Gan		80	20	41	59	6.55	7.41	3.22
Manus	3.90	79	21	38	62	3.46	4.43	-0.28
Gan		78	21	39	61	6.68	7.59	3.40

The resulting Manus Island $R(z)_C$ and $R(z)_S$ equations according to the $\log_{10}N_W{}^{SEP} =$ 3.85 separation appear in **Table 2.4** along with equations from previous tropical, oceanic studies.

Table 2.4: $R(z)$ equations from GATE (Hudlow 1979), TOGA COARE (Tokay and Short 1996), and MISMO (Yoneyama et al. 2008) field experiments as well as new tropical, oceanic rain relationships derived from Manus and Gan Is. 2DVD data-see Fig. 2.1 domain.

Experiment		GATE	TOGA COARE		MISMO	Gan & Manus Is.		
Equation		ALL	C	S	ALL	ALL	C	S
$R = az^b$	a	0.013	0.032	0.011	0.027	0.021	0.037	0.026
	b	0.80	0.70	0.77	0.69	0.72	0.68	0.64
$z = aR^b$	a	230	139	367	178	216	126	291
	b	1.25	1.43	1.30	1.44	1.39	1.46	1.55

The exponents and prefactors of the equations in **Table 2.4** are consistent with the microphysical differences between C/S rain in equatorial, maritime regions documented in the previous section (Steiner et al. 2004). Statistics of D_0, D_{MAX}, $\log_{10}N_W$, and LWC for each C/S Manus Is. population are shown in **Table 2.5**. By design, $\log_{10}N_W$ is higher for convection than stratiform rain.

Table 2.5: Mean, minimum, 5th percentile, 95th percentile, and maximum integral rain parameters for convective (C) and stratiform (S) DSD at Manus Is.: max diameter D_{MAX} [mm]; median diameter D_0 [mm]; liquid water content LWC [g m^{-3}]; number concentration $\log_{10}N_W$ [unitless].

TYPE	PARAMETER	MEAN	MIN	5%	95%	MAX
C	D_{MAX}	2.17	0.80	0.95	3.91	7.65
S	D_{MAX}	2.15	0.80	1.04	3.51	8.54
C	D_0	1.04	0.34	0.56	1.59	2.29
S	D_0	1.16	0.48	0.68	1.69	3.83
C	LWC	0.71	0.01	0.03	2.88	12.64
S	LWC	0.10	0.00	0.01	0.33	4.53
C	$\log_{10}N_W$	4.25	3.85	3.89	4.68	5.22
S	$\log_{10}N_W$	3.33	1.57	2.81	3.79	3.85

The D_0 and D_{MAX} 5-95% ranges for each C/S population overlap substantially. However, there is a slight indication of higher D_0 in stratiform rain but higher D_{MAX} for convection, potentially due to the lack of vigorous riming processes in tropical, maritime convection. *LWC* is understandably much greater in convection (95% value of 2.88 g m^{-3}) than stratiform (mostly below 0.33 g m^{-3}).

The C/S rain statistics using $\log_{10} N_W^{SEP} = 3.85$ are in **Table 2.6**. Stratiform (convective) rain at both locations makes up approximately 19 (81)% of the total rain accumulation but 59 (41)% of all rain occurrences. This high-resolution dataset indicates about a 10% higher convective rain fraction than previous maritime studies utilizing JWD disdrometers (Tokay and Short 1996) and radars (Steiner et al. 1995; Short et al. 1997; Atlas et al. 2000; Thurai et al. 2010; Xu and Rutledge 2014), which are near 70/30 for C/S rain fraction and 30/70 for C/S frequency of occurrence. We hypothesize that previous radar-based methods were not able to adequately identify shallow, weak convection in this tropical, maritime rain regime because of the relatively lower resolution (~2 km) and the weak reflectivity gradients represented in interpolated, gridded radar datasets, low echo top heights compared to C/S partitioning analysis level (usually performed at ~2-3 km), and overall lower Z_h associated with these oceanic echoes compared to land-based convection (Schumacher and Houze 2003). Sec. 2 explains why radar scanning geometry relative to the disdrometer prevented testing of this hypothesis in the current study.

Table 2.6 quantifies that, at both locations, about 30% of accumulated rainfall is due to rain with $R < 10$ mm hr^{-1}, which accounts for 87% of all rain occurrences. If a simple rule, such as classifying convection as any point with $R > 10$ mm hr^{-1} were applied, the resulting, erroneous C/S rain fraction would be 87/13 and the erroneous C/S rain frequency fraction would be 71/29. Rain accumulation from this weak ($R < 10$ mm hr^{-1}) subset has equal volume contributions (14% of total rain volume each) from convective and stratiform DSD. If $R(z)_C$ and $R(z)_S$ are used on simulated reflectivity and a single $R(z)_{ALL}$ equation is used to treat these convective DSD with $R < 10$ mm hr^{-1} (14% of total rainfall at Manus Is.), the estimated percentage of rainfall due to weak convection decreases to 11%. If a stratiform $R(z)_S$ is used in this context, in the case of a misclassification of weak, shallow convection as stratiform, the percentage of rain due to this population decreases further to 8%. If the lightly raining, convective DSD are treated with the appropriate $R(z)_C$ equation developed herein, their contribution to total rainfall is preserved. Similar results are found at Gan.

These statistics also show that almost two thirds of the total raining occurrences come from stratiform rain < 10 mm hr^{-1} (58% of all rain), while one third of occurrences originate from convection < 10 mm hr^{-1} (30% of all rain volume). The remaining 12% of occurrences are from convection with $R > 10$ mm hr^{-1}. Johnson et al. (1999) also found that shallow, trade wind cumulus clouds were much more abundant than cumulus congestus and deep convection during TOGA-COARE, even though more rain fell from the latter, more intense elements. According to the Manus and Gan Is. datasets, only 18-21% of the *convective rain volume* is from samples with $R < 10$ mm hr^{-1}, while 72-75% of *stratiform rain volume* is due to these weak rain rates. Consistent with Johnson et al. (1999), 70% of all *convective occurrences* and 98% of all

Table 2.6: Convective and stratiform rainfall accumulation and frequency of occurrence fractions according to Manus and Gan Is. 2DVD rain rate (R, mm hr^{-1}) and log $10NSEP\ W = 3.85$ partitioning method, unless other $R(z)_C$, $R(z)_S$, or $R(z)_{ALL}$ method is specified for sensitivity tests on certain populations of rain. Statistics are expressed as a percentage of the total rain population unless specified as a % of either the stratiform or convective population.

Place	Rain Type	% Rain Accumulation	% Rain Occurrence
Manus	Stratiform	19	59
Gan	–	20	59
Manus	Convection	81	41
Gan	–	80	41
Manus	$R < 10$ mm hr^{-1}	29	87
Gan	–	31	87
Manus	$R < 10$ mm hr^{-1} that is convective	14	29
Gan	–	16	30
Manus	$R < 10$ mm hr^{-1} that is convective	14	–
Gan	*using $R(z)_C$ on this weak convection*	15	–
Manus	$R < 10$ mm hr^{-1} that is convective	11	–
Gan	*using $R(z)_{ALL}$ on this weak convection*	12	–
Manus	$R < 10$ mm hr^{-1} that is convective	8	–
Gan	*using $R(z)_S$ on this weak convection*	9	–
Manus	$R < 10$ mm hr^{-1} that is stratiform	15	58
Gan	–	15	58
Manus	% of convection with $R < 10$ mm hr^{-1}	18	70
Gan	–	21	73
Manus	% of stratiform with $R < 10$ mm hr^{-1}	72	98
Gan	–	75	98
Manus	% of convection with $Z_h < 40$ dBZ	33	82
Gan	–	41	86
Manus	% of stratiform with $Z_h < 40$ dBZ	80	98
Gan	–	73	97

stratiform rain occurrences exhibited $R < 10$ mm hr^{-1}. Results are similar when C/S DSD are thresholded by 40 dBZ.

Fig. 2.14 illustrates the statistics from **Table 2.6**. The $N_W(D_0)$ and $LWC(D_0)$ distributions have been colored by radar reflectivity and rain rate to show that a majority of both the convective and stratiform samples have rain rates less than 10 mm hr^{-1} and $Z_h < 40$ dBZ. For example, stratiform rain (below the new dashed separation lines) is mainly limited to below 40 dBZ and below 10 mm hr^{-1} near the surface, consistent with Tokay et al. (2001), Tokay and Short (1996), and others. It is interesting that the BR09 classification (solid separation line) is nearly synonymous with a 40 dBZ or 10 mm hr^{-1} threshold for these tropical, maritime datasets.

While convection undoubtedly appears to exceed these thresholds and stratiform rain does not, the BR09 classification is too conservative for the weak, oceanic convection frequently observed at Manus and Gan Is. as in **Figs. 2.7, 2.8, and 2.9**. Convection (above the new dashed separation lines) apparently manifests itself across the entire range of R and Z_h values (well below 10 mm hr^{-1} and 40 dBZ), which was also shown by Bell and Suhasini (1994) and Zuidema et al. (2012). Thus, a major accomplishment of this study has been to modify the $N_W(D_0)$ BR09 C/S separation methodology to properly distinguish both strong and shallow, weak maritime convection from stratiform rain in tropical, oceanic regions.
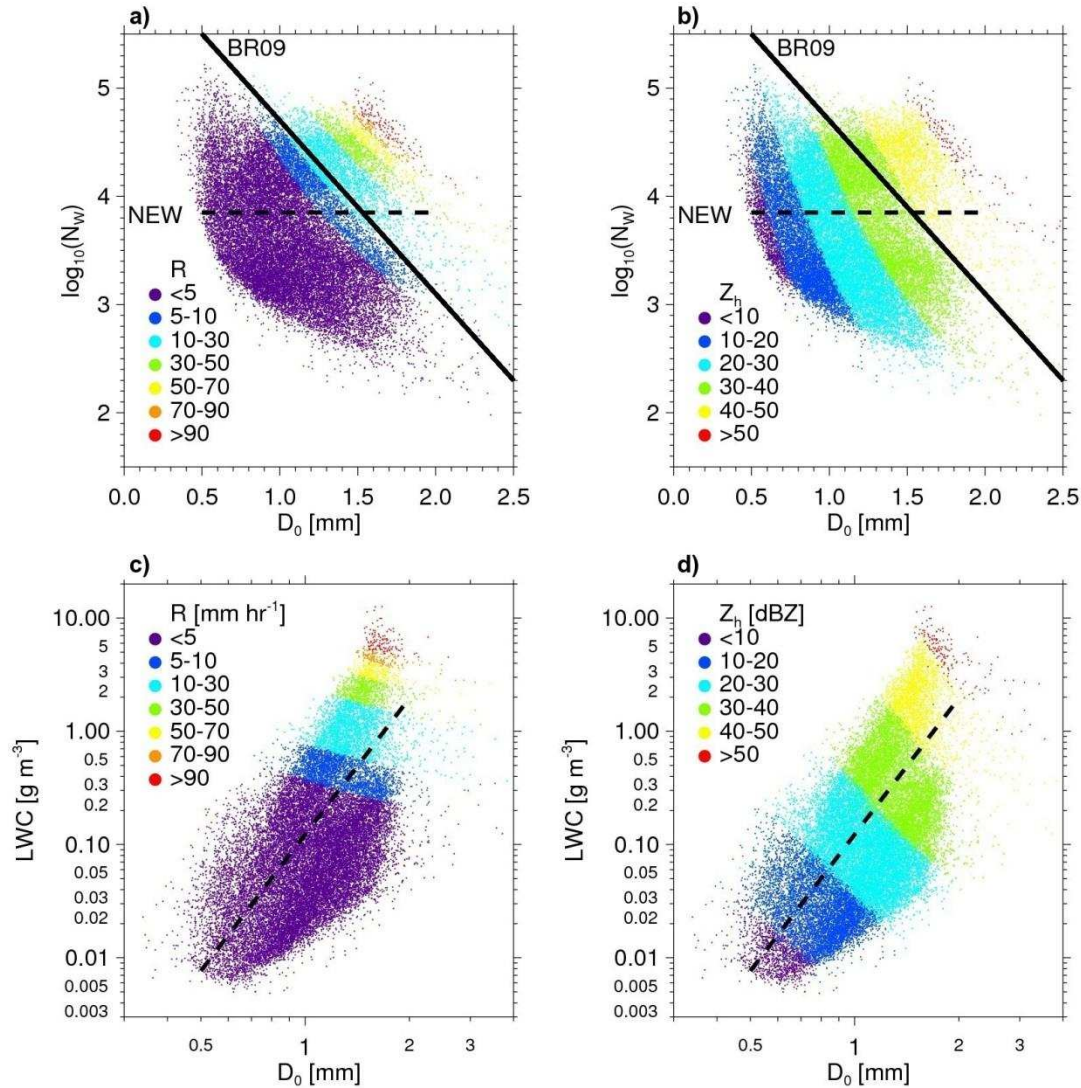
Figure 2.14: Manus Is. *LWC(D$_0$)* and N_W(D$_0$) scatter plots color-coded by 2DVD rain rate (*R*) and reflectivity (*Z$_h$*) with the original subtropical, continental Bringi et al. (2009 - BR09) and updated tropical, oceanic C/S $\log_{10}N_W^{SEP}$ separation lines. Similar distributions found at Gan Is.

2.6. Implications for radar applications

2.6.1 *C/S* **R(z)** *variability*

Fig. 2.14 also illustrates that convection has higher *R* and *Z$_h$* for a given *D$_0$* than

stratiform rain. The same *D$_0$* can lead to a variety of reflectivities and rain rates depending on the

number concentration. A physical interpretation is that higher *N$_W$* (during convection) for a given

D$_0$ (which overlap between C/S rain) leads to greater *LWC*. The need to constrain *R(z)* variability

motivates radar classification of C/S echoes as well as formation and application of separate $R(z)$ equations for each rain type. Exploration of other integral rain parameter spaces further affirms that C/S modes of DSD variability exist within the Manus and Gan Is. datasets. **Fig. 2.15** shows that $R(D_0)$, $R(LWC)$, $z(LWC)$, and $R(\lambda)$ distributions consistently exhibit two populations that can be separated by $\log_{10}N_W{}^{SEP}$ into S (blue) and C (red) modes. The separation between C/S rains in the $R(D_0)$ space is more distinct than presented by Atlas et al. (2000). Convective rain achieves the same R as stratiform but with lower D_0, higher $\log_{10}N_W$, and higher LWC. The overlapping z ranges between C/S rain reflect the fact that each of these DSD modes carry characteristically different LWC amounts for a given reflectivity (**Table 2.5**). The exponential DSD slope (λ) is flattened, or decreased, in stratiform precipitation associated with the aggregation of smaller crystals into larger snowflakes above the melting level (Lo and Passarelli 1982). Higher slope values are achieved during convection when new particles are formed via condensation, collision, and coalescence, which was also shown by Tokay and Short (1996). Orthogonal linear regression was used to relate $z(LWC)$ and $R(\lambda)$ in C/S/ALL rain, which are presented in **Table 2.7**. The green all-data lines in **Fig. 2.15** compromise a significant amount of DSD covariance described by each C/S best-fit line.

Table 2.7: Manus Is. best-fit equations for rain rate (R, mm hr^{-1}) as a function of exponential DSD slope parameter (λ, mm^{-1}) and radar reflectivity (z, mm^6 m^{-3}) as a function of liquid water content (LWC g m^{-3}) for convective rain (C), stratiform rain (S), and all rain.

$$R_{ALL} = 12440.103\lambda^{-7.019}$$
$$R_C = 4617.2045\lambda^{-5.263}$$
$$R_S = 298.63345\lambda^{-4.766}$$

$$z_{ALL} = 11668.466LWC^{1.550}$$
$$z_C = 6789.4854LWC^{1.687}$$
$$z_S = 42549.389LWC^{1.829}$$
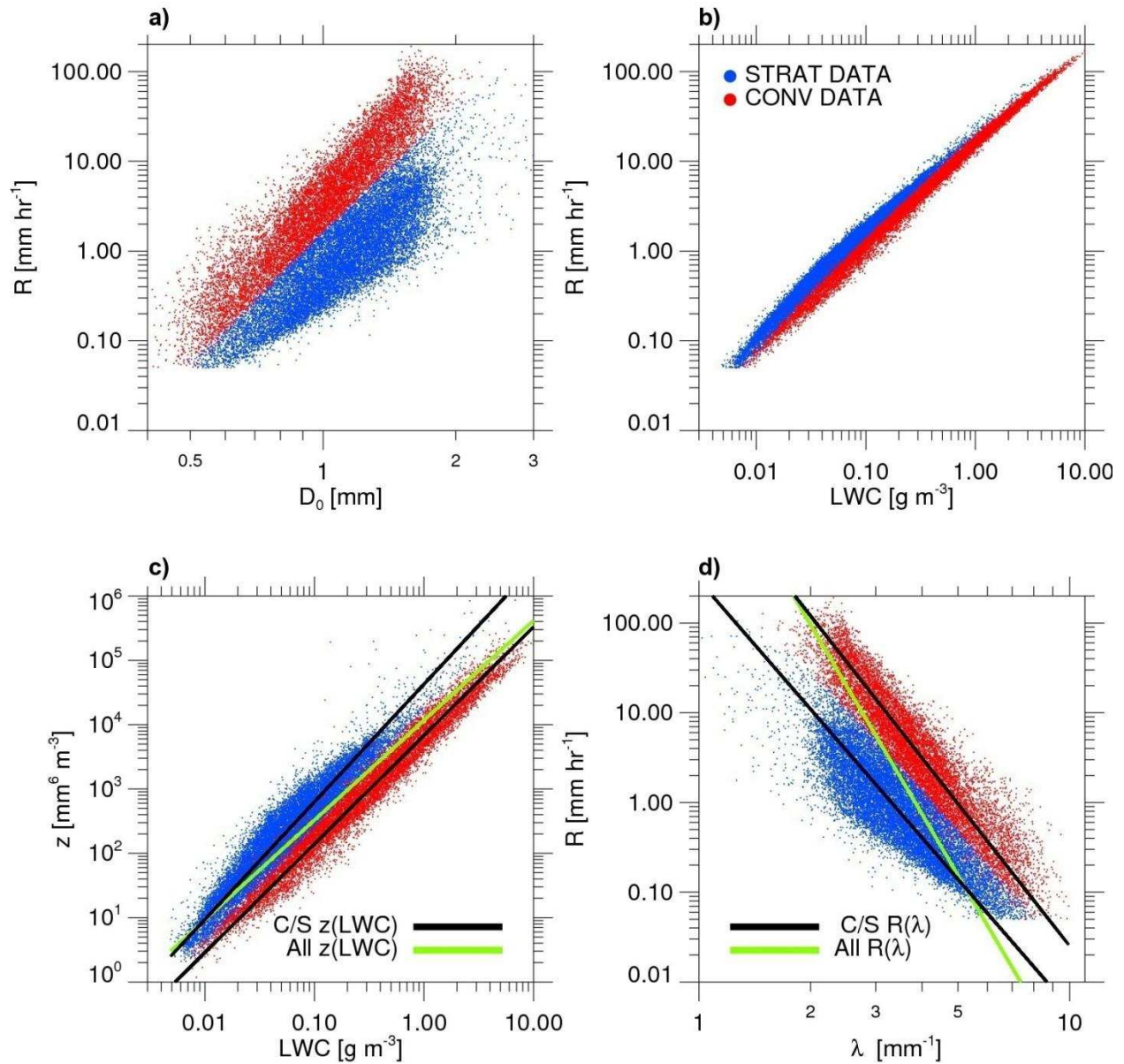
Figure 2.15: Manus Is. a) *R(D₀)*, b) *R(LWC)*, c) *z(LWC),* and d) *R(λ)* partitioned by the $\log_{10}N_W^{SEP}$ line (stratiform = blue, convection = red). *z(LWC)* and *R(λ)* regression lines are over-plotted in c) and d) respectively for the entire DSD dataset (green) and each convective and stratiform population (black lines: convective (stratiform) relationship on top (bottom) overlaying red (blue) points). Similar distributions observed at Gan Is.

To investigate whether the aforementioned C/S DSD variability can account for any $R(z)$ variability during actual raining events, $R(z)$ distributions for all nine 2DVD-radar case studies are shown in **Fig. 2.16.** $R(z)_C$, $R(z)_{ALL}$, and $R(z)_S$ from **Table 2.4** are shown for reference, with $R(z)_C$ consistently yielding higher rain rates for a given Z_h than $R(z)_S$. The $R(z)$ data from widespread as well as isolated, strong convection (case #1-2) were in the high Z_h, high R spectrum aligned with $R(z)_C$ and therefore also $R(z)_{ALL}$ since they converge there. Case #3 exhibited shallow, weaker convection below 5 km and had lower Z_h with correspondingly lower R, most in line with $R(z)_C$ and well above $R(z)_{ALL}$. The isolated, weak convection below 4 km in case #4 had much lower R ($<$10 mm hr^{-1}) but was aligned with $R(z)_C$ rather than $R(z)_S$. Even though warm rain processes in case #5 barely reached 3 km, the rain rates were slightly higher than case #4 and also on the convective $R(z)_C$ line. In contrast, moderate stratiform rain rates at nearly the same intensity as the weakest, shallowest convective rain example hovered on the stratiform $R(z)_S$ line, just below 10 mm hr^{-1}. Even lower rain rates in case #7 during weak stratiform rain were along $R(z)_S$ (in the region where $R(z)_{ALL}$ converges to $R(z)_S$). Case #8 and #9 showed transitions between embedded and leading convection, respectively, to heavy stratiform rain. Both cases showed migrations from $R(z)_C$, across $R(z)_{ALL}$, and to $R(z)_S$ with case #8's DSD *after* the fourth radar vertical cross section being more consistent with the weak stratiform rain from case #7.
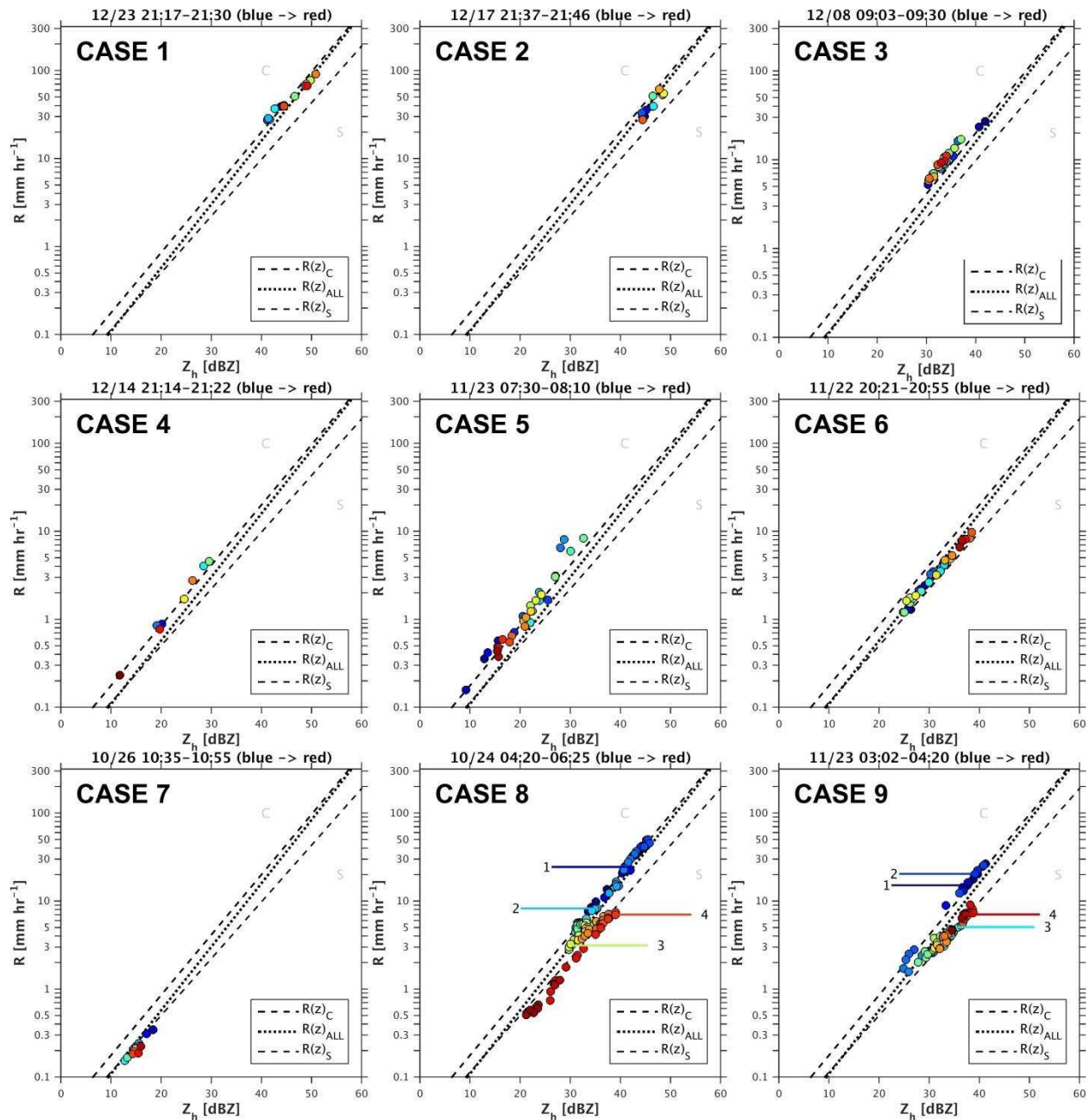
Figure 2.16: *R(z)* for case studies #1-9 where time increases as the colored markers go from blue to red. *R(z)*_C (upper), *R(z)*_ALL (middle), and *R(z)*_S (lower) best-fit equations shown.

Besides demonstrating consistency between the radar case study conclusions and the

DSD partitioning method, another important result of these *R(z)* case studies is that the

*R(z)*_ALL equation fit to the entire DSD dataset is hardly ever a "best-fit" to individual cases of

rain. The only exception is during the strongest convection or weakest stratiform rain because $R(z)_{ALL}$ converges to either $R(z)_C$ or $R(z)_S$ at either endpoint. If an appropriate C/S partitioning method can be used, we believe this motivates formation and use of separate C/S $R(z)$ equations because $R(z)_{ALL}$ lies between these two major modes of DSD variability, i.e. convective and stratiform rain.

Returning to the similarity observed between Manus and Gan Island DSD variability, **Fig. 2.17** shows simulated radar reflectivity as a function of 2DVD rain rate for both locations. The $R(z)_{ALL}$ lines for each location are plotted together, illustrating that the similar distributions yield nearly identical $R(z)_{ALL}$ equations: $R(z)_{ALL} = 0.019z^{0.729}$ for Gan Is., $R(z)_{ALL} = 0.020z^{0.721}$
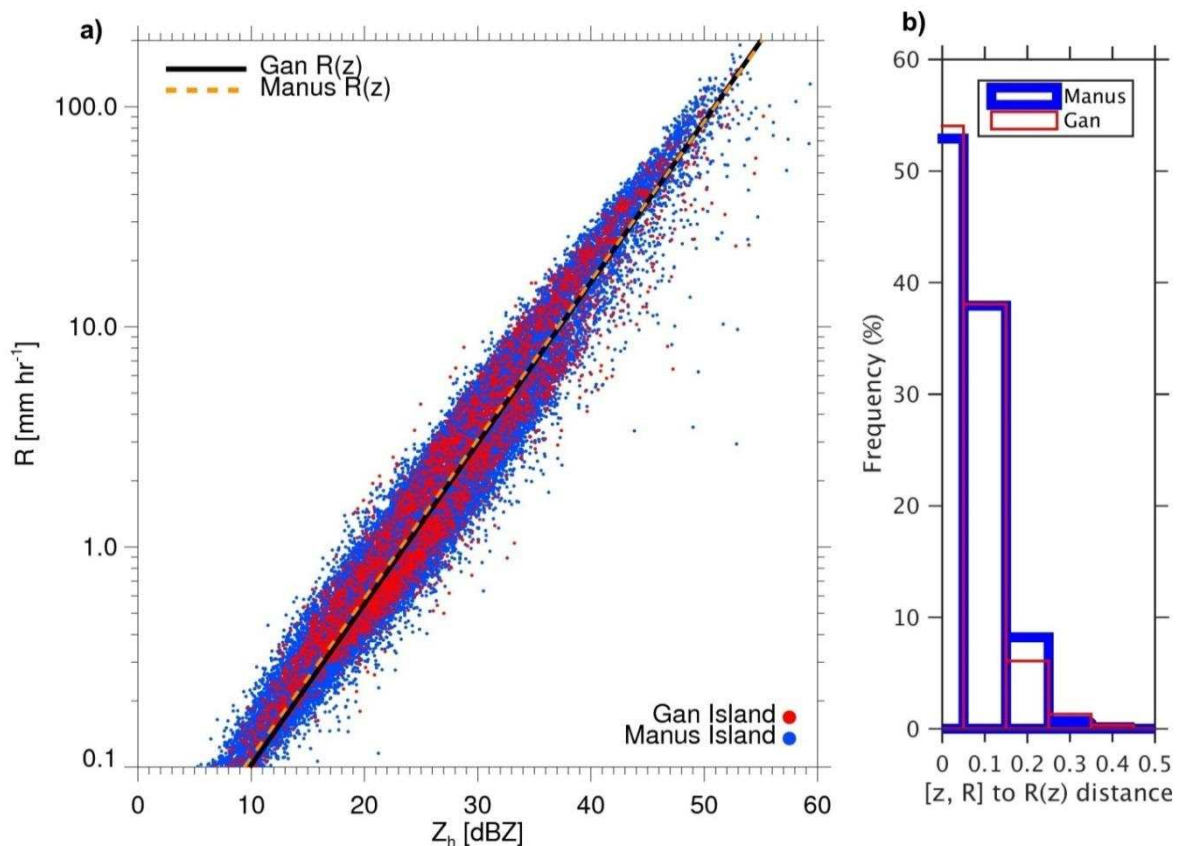
Figure 2.17: a) Gan and Manus Is. 2DVD Z_h and R with linear regression best-fit lines for each location. b) Normalized histograms of the orthogonal distance from each [z,R] point at each location to the Manus Is. best-fit line. Distances are in logarithmic $R(z)$ units in both directions.

for Manus, which are equivalent to $z(R)_{ALL} = 228\ R^{1.37}$ at Gan and $z(R)_{ALL} = 216\ R^{1.39}$ at Manus. We move forward with the Manus Is. equations (in **Table 2.4**) since they are based on seven times as many points but appear to represent the same $R(z)$ variability observed at Gan Is. For instance, the second panel in **Fig. 2.17** shows a histogram of the orthogonal distances between each $[z,\ R]$ point and the Manus Is. best-fit line. When normalized by the length of each dataset, the histograms are nearly equivalent. Both locations have the same percentage of $R(z)$ points scattered in each distance increment about the Manus Is. best-fit line.

To examine these $R(z)$ distributions further, 2D histograms of $R(z)$ contoured by frequency of occurrence for both locations appear in **Fig. 2.18 (a)** and **(b).** A majority of the points lie below the $R(z)_{ALL}$ line for $Z_h <$30-40 dBZ, with indication of another high density region of points above the line as $Z_h > 25$ dBZ. **Fig. 2.18 (c)** and **(d)** use Manus Is. data and the $\log_{10}N_W^{SEP}$ method to confirm that the lower mode is classified as stratiform rain and the higher mode is classified as convective. Both these distribution are continuous, not disjointed, suggesting that the C/S partitioning algorithm was appropriate for this dataset. The $R(z)_{ALL}$ line lies between the convective and stratiform modes in a region of lower frequency of occurrence exhibiting moderate Z_h and R ranges.
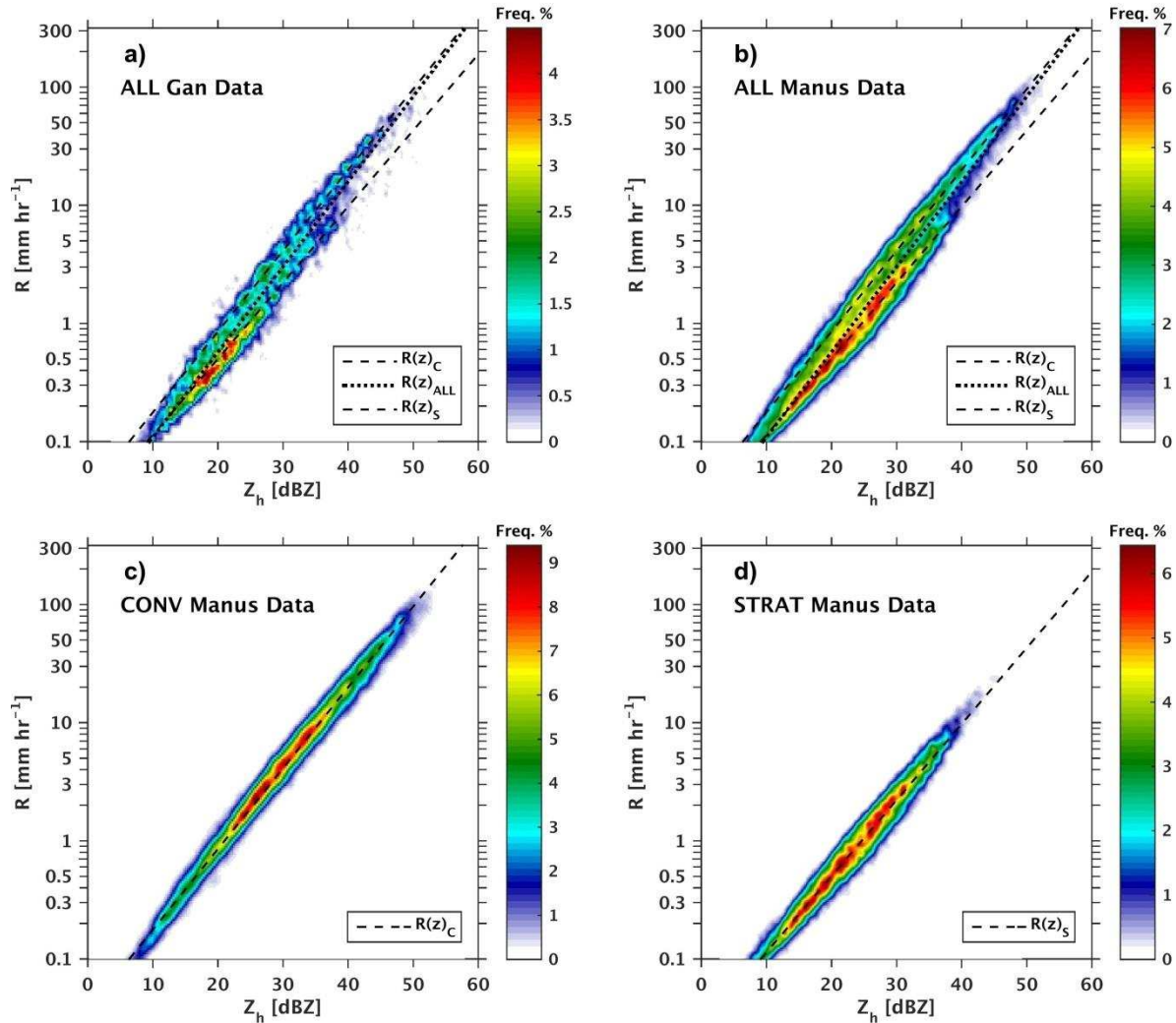
Figure 2.18: Gan and Manus Is. *R(z)* smoothed 2D histograms contoured by frequency of occurrence with linear regression best-fit line from Manus Is. Gan Is: 180 bins in each direction and 6 bin Gaussian filter width. Manus Is. # bins in each direction: all = 280, conv = 200, strat = 235; 10 bin Gaussian filter width.

Fig. 2.19 more clearly demonstrates that C/S DSD variability in $\log_{10}N_W$ explains most of the *R(z)* variability in these tropical, oceanic data. The *R(z)* distribution is colored by median drop diameter and number concentration using the fuller Manus Is. dataset (similar results found for Gan Is.; not shown), akin to the rain parameter diagram of Ulbrich and Atlas (1978, 1998); Steiner et al. (2004). Low $\log_{10}N_W$ ranges $<=3.85$ only exist in the lower (stratiform) mode of the *R(z)* distribution in **Fig. 2.18**. Likewise, high $\log_{10}N_W$ ranges >3.85 are

66
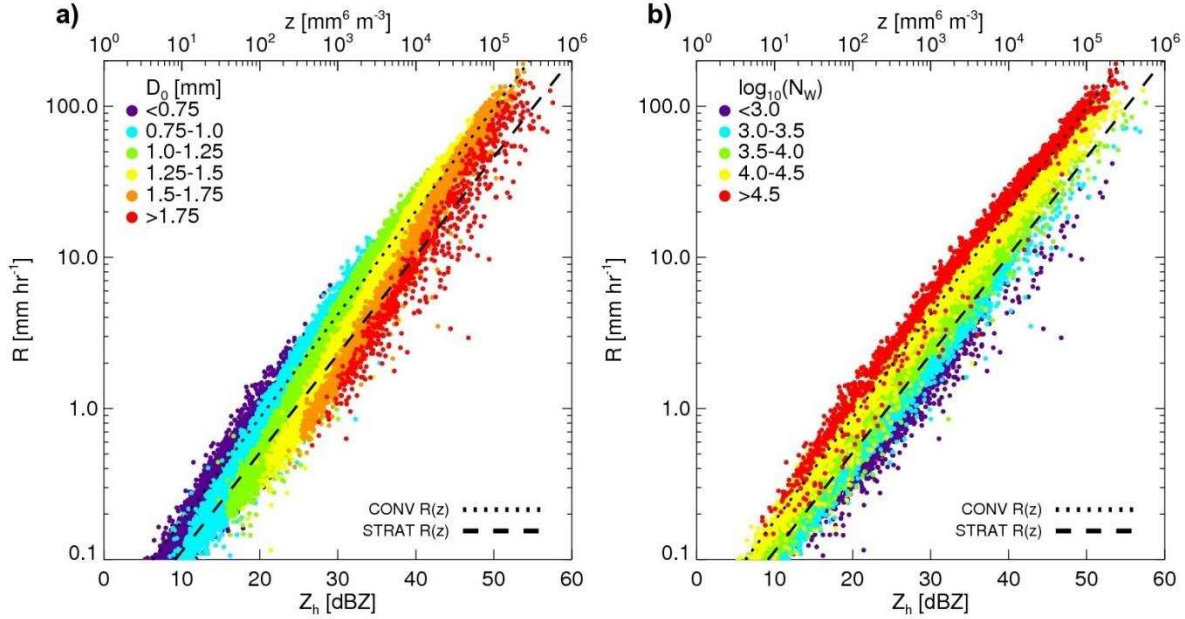
Figure 2.19: Manus Is. $R(z)$ color-coded by a) D_0 and b) $\log_{10}N_W$ plotted with C/S $R(z)$. only experienced in the upper (convective) $R(z)$ mode. Sauvageot and Lacaux (1995), Tokay

et al. (1999), Testud et al. (2001), Morrison et al. (2009), TH10, and Bringi et al. (2012) also

suggested that number concentration explained more rain variability over the tropical Warm Pool

than variations in median drop diameter. This corresponds to concentration-controlled DSD

variability as opposed to size-controlled or a combination thereof, described mathematically by

Steiner et al. (2004). For instance, the two main $R(z)$ modes of variability in this dataset (**Fig.**

2.18) share nearly the entire range of median drop diameter (D_0) but have mutually exclusive

number concentration ($\log_{10}N_W$) ranges, which is consistent with **Table 2.1**, **Table 2.5** and

Figs.2.3-2.4.

2.6.2   Radar-based C/S rainfall estimation

It is obvious from **Fig. 2.16** and **2.18** how $R(z)_C$ and even $R(z)_{ALL}$ would overestimate

stratiform rain if applied in the wrong context, and likewise how $R(z)_S$ and $R(z)_{ALL}$ would

underestimate convective rain in many cases. **Table 2.8** assesses the impacts of applying either a combination of $R(z)_c$ and $R(z)_s$ versus $R(z)_{ALL}$ to the long-term simulated 2DVD radar reflectivity dataset. A 3% overestimation of total rain, 4% overestimation of convective rain, and only -0.01% underestimation of stratiform rain is encountered when using $R(z)_c$ and $R(z)_s$ for each distribution at Manus Is. compared to 2DVD R estimates. If the $R(z)_{ALL}$ equation is used only on the shallow, weak convective population, as in the case of uncertain C/S partitioning of this population, and separate $R(z)_c$ and $R(z)_s$ equations are used appropriately in all other instances, the total, convective, and stratiform rain accumulation errors are nearly zero. However, the percentage of rainfall by weak convection <10 mm hr^{-1} is underestimated at 11% instead of 14% as indicated by the 2DVD (**Table 2.6**). If the $R(z)_s$ equation is used on weak, shallow convection, as in the case of a misclassification, the total rainfall is underestimated by 3%, convective rainfall amounts are underestimated by 4%, and stratiform rainfall is still well reproduced. The percentage of total rainfall due to weak, convection is further underestimated to 9% compared to 2DVD R or using $R(z)_c$ appropriately (**Table 2.6**). Using a simple R >10 mm hr^{-1} threshold to denote convection and applying C/S $R(z)$ from this basis results in small total and convective rainfall errors, but a 17% overestimation of stratiform rainfall, which results in ±3% errors in S/C rain fraction. Therefore, using the individual C/S $R(z)$ relationships with inaccurate C/S partitioning method will produce misleading results. If radar-based C/S partitioning confidence is low, $R(z)_{ALL}$ should be used.

While the error in total rainfall accumulation is slightly lower (and negative) when using $R(z)_{ALL}$ compared to the C/S $R(z)$ method (-2.7%), this is overshadowed by vast over- and under-estimations of stratiform (+59%) and convective (-15%) rain accumulation. Since $R(z)$ is a power

Table 2.8: Manus Is. total, convective (C), and stratiform (S) rainfall accumulation and C/S rain fraction. Estimates are from 2DVD rain rate (R) and various methods applied to 2DVD simulated z. Percent differences between 2DVD R and other R estimates are given. Rain fraction differences are just found by subtraction. C/S $R(z)$ using $R(z)_S$ for weak C

PLACE	R Method	R_{TOTAL} [mm]	R_C [mm]	R_S [mm]	% CONV	% STRAT
Manus	2DVD	2627.33	2124.98	502.34	80.88	19.12
Gan		358.89	285.55	73.34	79.57	20.43
Manus	C/S $R(z)$	2716.65	2214.38	502.27	81.51	18.49
Gan		382.41	306.71	75.70	80.20	19.80
Manus	C/S $R(z)$ using	2617.18	2114.90	502.27	80.81	19.19
Gan	$R(z)_{ALL}$ on weak C	372.45	293.09	79.37	78.69	21.31
Manus	C/S $R(z)$ using	2542.54	2040.27	502.27	80.25	19.75
Gan	$R(z)_S$ on weak C	360.73	281.37	79.37	78.00	22.00
Manus	C/S $R(z)$	2675.77	2086.47	589.30	77.98	22.02
Gan	if C=R >10mm hr^{-1}	386.88	297.68	89.19	76.95	23.05
Manus	$R(z)ALL$	2555.85	1806.24	749.61	70.67	29.33
Gan		366.43	248.19	118.24	67.73	32.27
Manus	TOGA COARE	2800.28	2227.22	573.06	79.54	20.46
Gan	C/S $R(z)$	402.98	309.95	93.03	76.91	23.09
Manus	MISMO $R(z)ALL$	2628.39	1833.00	795.39	69.74	30.26
Gan		382.25	255.33	126.93	66.79	33.21
	PERCENT DIFFERENCES: 2DVD - ….					
Manus		3.40	4.21	-0.01	0.63	-0.63
Gan	…- C/S $R(z)$	6.55	7.41	3.22	0.64	-0.64
Manus	… - C/S $R(z)$ using	-0.39	-0.47	-0.01	-0.07	0.07
Gan	$R(z)_{ALL}$ on weak C	3.78	2.64	8.22	-0.87	0.87
Manus	… - C/S $R(z)$ using	-3.23	-3.99	-0.01	-0.63	0.63
Gan	$R(z)_S$ on weak C	0.51	-1.47	8.22	-1.57	1.57
Manus	… - C/S $R(z)$	1.84	-1.81	17.31	-2.90	2.90
Gan	if C=R >10mm hr^{-1}	7.80	4.25	21.62	-2.62	2.62
Manus	… - $R(z)_{ALL}$	-2.72	-15.00	49.22	-10.21	10.21
Gan		2.10	-13.08	61.22	-11.83	11.83

69

Manus	… - TOGA COARE	6.58	4.81	14.08	-1.34	1.34
Gan	C/S $R(z)$	12.28	8.54	26.85	-2.65	2.65
Manus	… - MISMO $R(z)_{ALL}$	0.04	-13.74	58.34	-11.14	11.14
Gan		6.51	-10.59	73.08	-12.77	12.77

results by Testud et al. (2001), $R(z)_c$, $R(z)_s$, and $R(z)_{ALL}$ explain 98.5, 96.4, and 93.9% of the total

variance in each respective population. Therefore, in addition to minimizing errors in C/S rain

accumulation, using separate C/S $R(z)$ relations for each rain population can also help explain

more total variance than a single $R(z)_{ALL}$.

The errors associated with using $R(z)_{ALL}$ have been quantified. For instance, even on these

long-term Manus and Gan Is. datasets, using the $R(z)_{ALL}$ equation on the entire dataset yields a

±10% difference in stratiform and convective rainfall fraction, respectively, compared to 2DVD

R and C/S $R(z)$ estimates in **Table 2.6**. Differences in rainfall fraction estimates due to using

$R(z)_{ALL}$ are expected to be higher for individual case studies when averaging over shorter time

periods. Therefore, ±10% is considered to be the minimum error expected when estimating

rainfall fraction due to using $R(z)_{ALL}$ instead of distinguishing and treating C/S populations

separately. Using $R(z)_c$ and $R(z)_s$ only produces a ±0.6% difference from 2DVD percentages of

C/S rain fraction. When $R(z)_{ALL}$ or $R(z)_s$ are used for weak, shallow convection and C/S

$R(z)$ equations are used appropriately for the rest of the dataset, the C/S fractions of the resulting

total rainfall from these methods hardly differ from 2DVD C/S fraction estimates and are of

opposite sign than using C/S $R(z)$. However, **Table 2.6** illustrates that the fraction of shallow,

weak convective rain decreases from 14% to 11% using $R(z)_{ALL}$ and to 8% using $R(z)_s$ in this

context.

We also consider the impact of using TOGA COARE and MISMO $R(z)$ relationships

from **Table 2.4** in **Fig. 2.17** and **Table 2.8** since these equations were formed with DSD in the

equatorial West Pacific and Indian Oceans, respectively (**Fig. 2.1**). Although not plotted, the GATE and new $R(z)_{ALL}$ equations are also very similar (**Table 2.4**). The TOGA COARE C/S relationships yield slightly different rainfall statistics than the new $R(z)_c$ and $R(z)_s$ relationships. Total rainfall and convective rainfall have similar errors as using the new C/S relationships because the $R(z)_c$ equations are nearly equivalent in **Fig. 2.20** and **Table 2.4**. However, stratiform rain is strongly overestimated by the Tokay and Short (1996) $R(z)_s$ compared to 2DVD R because their $R(z)_s$ has a lower slope. This leads to a ±1.3 difference in S/C rainfall fraction compared to the 2DVD. Since Manus Is. and TOGA-COARE are both in the Western Pacific, this difference is most likely due to Tokay and Short (1996)'s use of impact JWD disdrometers with less accurate small drop detection, the non-normalized[5] gamma DSD number concentration (N_0), a probability matching method to find $R(z)$, different DSD data processing techniques, and/or resulting differences in C/S partitioning methods ($N_0^{SEP} = 4 \times 10^9 R^{-4.9}$).

The MISMO relationship from JWD data is similar to $R(z)_{ALL}$ in **Fig. 2.20**, except that it leans toward the convective DSD more than stratiform at the lower end of the $R(z)$ spectrum. This is due to this relationship's reliance on mostly convective DSD samples from only 6 weeks of data leading up to the active MJO according to Yoneyama et al. (2008) and personal communication with Masaki Katsumata (2006). Thus, using the MISMO $R(z)_{ALL}$ leads to an 11% over- (under-) estimation of stratiform (convective) rain fraction compared to 2DVD R estimates i.e. yielding a C/S rain fraction closer to 70/30). The errors on total, convective, and stratiform

---

[5] We attempted to compute N_0 using μ estimated through our Nw and D_0 calculation method. However, μ varies greatly between raining clouds (BC01) and is not as well-constrained by our data processing techniques as Nw and D_0. The resulting N_0 vs. R distribution was very scattered. However, assuming $\mu = 0$ yielded rough agreement between our separation method and that presented by Tokay and Short (1996): $N_0^{SEP} = 4 \times 10^9 R^{-4.9}$.

rainfall accumulation using the MISMO $R(z)$ compared to 2DVD estimates are relatively small for total rain accumulation, but are -13% for convective rain, and +58% for stratiform rain.
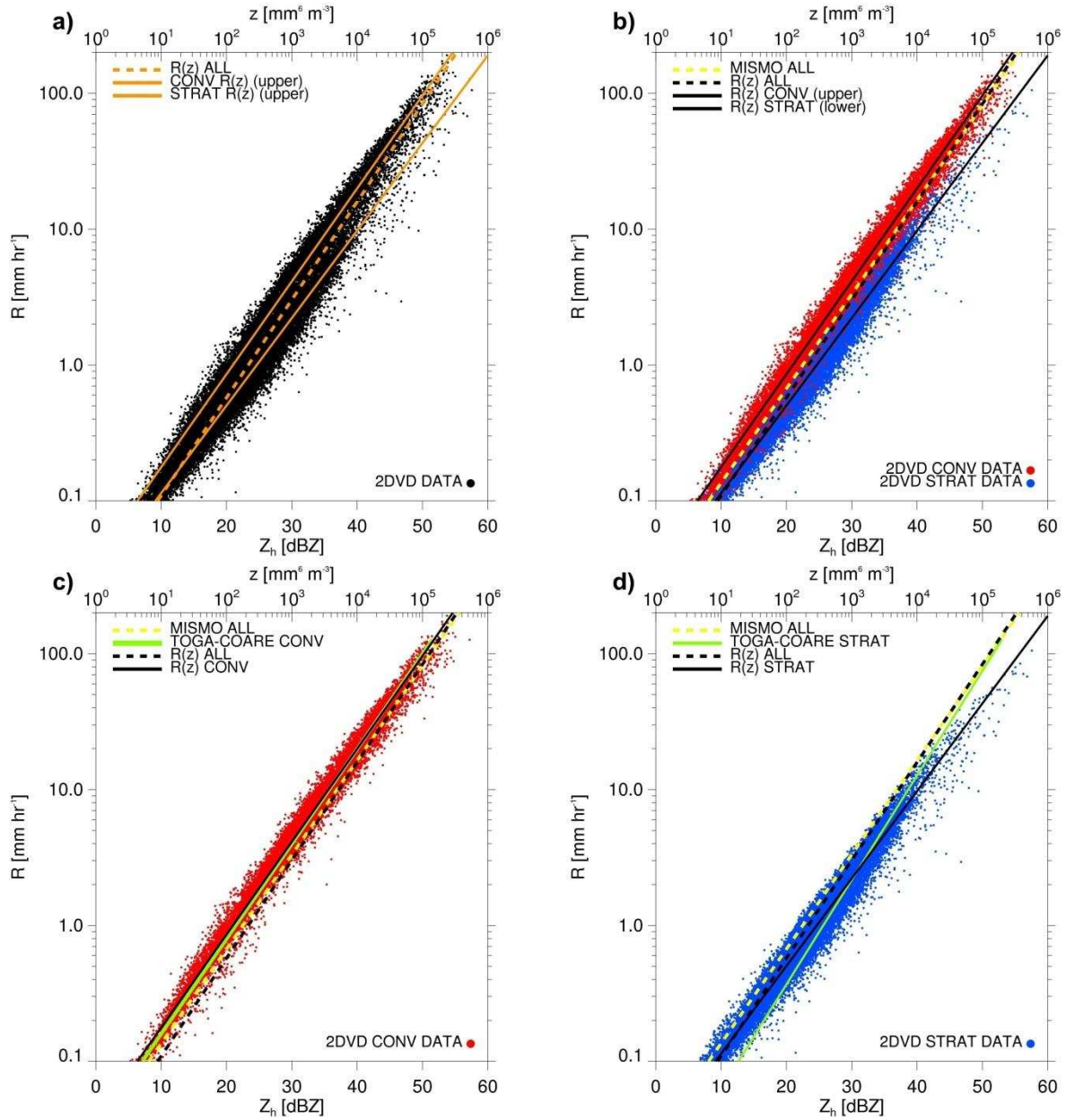
Figure 2.20: Manus Is. $R(z)$ scatter plots and regression lines for: a) the entire dataset; b) the dataset partitioned into convective and stratiform populations according to the updated $\log_{10}N_W^{SEP}$ method; c) convective points; and d) stratiform points. $R(z)$ equations in Table 2.4 from MISMO, TOGA COARE, and the current study are plotted.

Finally, we discuss the choice of $R(z)$ relationships relative to MJO evolution. DeWitt et al. (2013) described a central Indian Ocean evolution of aerosol loading as a function of MJO, which could impact the resultant DSDs. Similarly, Xu and Rutledge (2014) and Virts and Houze (2015) observed increased storm intensity and lightning activity leading up to the heaviest rain-producing phases of the MJO, which could also be related to DSD variability. However, it appears that the same $R(z)_c$, $R(z)_s$, and $R(z)_{ALL}$ relationships are applicable during all phases of the MJO because the $LWC(D_0)$ and $N_w(D_0)$ covariance as well as $\log_{10}N_W^{SEP} = 3.85$ separation between C/S rain are consistent regardless of rain *intensity* (Ulbrich and Atlas 1978). We make this distinction to emphasize that while rain intensity and accumulation vary with MJO phase, the mean DSD variability over these open ocean locations, and therefore $R(z)$, should not be directly related to MJO phase. According to the long-term DSD datasets, it appears that only one version of the $R(z)_s$, $R(z)_c$, and $R(z)_{ALL}$ equations is necessary for this tropical, oceanic rain regime. Furthermore, it would be inappropriate to partition $R(z)_{ALL}$ by MJO phase because we have shown that the spread in $R(z)$ can be succinctly explained by mutually exclusive N_w differences between C/S rain, both of which are present during all phases of the MJO according to both Manus and Gan DSD datasets and other studies in these tropical ocean basins.

2.7 Conclusions

This study documented tropical, maritime DSD variability captured by the Gan and Manus Island 2DVDs with 3.5 and 18 month records in the equatorial Indian and West Pacific Oceans, respectively. The spectra of integral rain parameters and separation between convective (C) and stratiform (S) rain were similar at each location, suggesting that cloud microphysical and dynamical properties are also similar at these locations. Both are open ocean locations with

characteristically warm sea surface temperatures and influenced by similar large scale forcing

such as the ITCZ and MJO. DSDs were characterized by high number concentrations (N_w) and

small to medium drop diameters (95% of $D_0 < 1.7$ mm; $D_{MAX} < 4$ mm) compared to continental

DSD. These DSD were consistent with maritime, warm-rain processes such as condensation and

coalescence as well as some riming growth in more intense convection. In contrast, stratiform

rain had an order of magnitude lower N_w compared to convection, consistent with aggregation

above the melting level.

The conceptual model in **Fig. 2.21** illustrates the dominant cloud microphysical processes

giving rise to Manus and Gan Island DSD in various quadrants of the $N_w(D_0)$ space. Arrows

indicate how intensifying stratiform and convective rain (i.e. higher reflectivity, higher rain rate,

greater bright band intensity, or higher echo top height) attain higher liquid water content and

median rain drop diameters but maintain over an order of magnitude different N_w between C/S

precipitation. Compared to weaker, shallower warm rain convection, stronger, deeper convection

have higher D_0, consistent with deeper cloud depths. Stronger updrafts in these convective clouds

promote higher liquid water contents, which also promote larger particle sizes.

The $\log_{10}N_W{}^{SEP} = 3.85$ line separating C/S rain was a modification of the BR09

partitioning method based on 372 paired dual-polarization radar - 2DVD case studies and a

quantitative C/S $R(z)$ self-consistency test. While a separation "line" may not appear physically-

satisfying at first, evaluation of radar echo and DSD evolution from all 372 case studies,

previous observational studies, and theoretical evidence of number-controlled DSD (Steiner
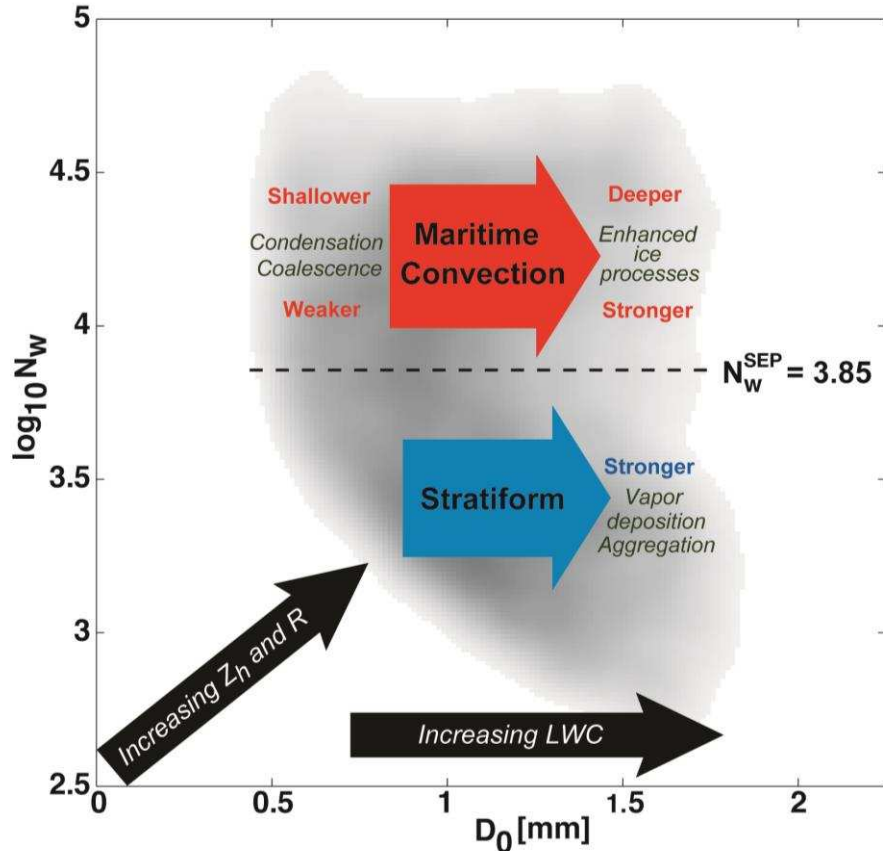
Figure 2.21: Conceptual model of dominant microphysical processes (dark green) in the $N_W(D_0)$ space. Background is gray-scale smoothed contoured frequency 2D histogram showing darker (more frequent) DSD pairs from Manus Is. 2DVD. Distinctions are made between maritime convection (red) and stratiform rain (blue) on either side of the updated $\log_{10}N_W^{SEP} = 3.85$ separator line. Thus, number concentration is the most distinguishing feature between stratiform and tropical, maritime convection. As rain intensity increases (i.e. larger rain rate (R), radar reflectivity (Z_h), bright band, or echo top height), the median drop diameter (D_0) and liquid water content (LWC) increase with much smaller variation in number concentration ($\log_{10}N_W$) for either convective or stratiform rain. Thus, the direction of red and blue arrows generally point in the direction of more intense convection and more intense stratiform precipitation by these metrics.

et al. 2004) support our conclusion that number concentration is the most discerning feature between stratiform rain DSD and convective maritime, tropical rain DSD. The new separation line is more applicable for tropical, oceanic rain regimes where weak convection ($R < 10$ mm hr^{-1} and usually $Z_h < 35$ dBZ) is ubiquitous. Weak, shallow convection by these metrics made up about 14% of rain volume and 30% of rain occurrences at the equatorial Indian and

75

West Pacific sites. We offer evidence for increased convective rain fraction and frequency estimates compared to previous tropical, oceanic studies because our high-resolution DSD dataset and corresponding C/S partitioning algorithm provide better detection and treatment of this rain type. For instance, the DSD data yielded a long-term average 41/59 C/S rainfall frequency ratio and an 81/19 C/S rain fraction.

This long-term stratiform/convective rainfall fraction was found to vary by ±10%, respectively, when a single $R(z)_{ALL}$ equation was used to calculate R compared to the directly-sensed 2DVD R. In contrast, the 2DVD rain fraction estimate was recreated within ± 0.6% when using $R(z)_c$ and $R(z)_s$ applied to the convective and stratiform rain populations, respectively. Use of separate C/S equations also minimized errors in convective and stratiform rain accumulation and statistically explained more R variance. Current radar-based C/S echo partitioning algorithms should be able to mimic the DSD-based classification technique with sufficient spatial and temporal resolution and tuning for the tropical, oceanic precipitation regime. However, current radar-based C/S partitioning has considerable uncertainty in shallow, weak convection and convective elements embedded in stratiform rain. The benefits of using C/S $R(z)$ equations will not be realized if the partitioning is incorrect. If a confident echo identification cannot be made, the best alternative is $R(z)_{ALL}$. A paired, statistical comparison between 2DVD and radar C/S classifications and rain rate would help quantify the uncertainty involved in application of different $R(z)$ relationships to real radar data, but is not possible with the given datasets (explained in Sec. 2).

This long-term, high spatiotemporal resolution dataset has provided new, comprehensive insights regarding tropical drop size distributions and rainfall variability since these types of data are not typically available in remote oceanic regions. Furthermore, characterizing and reducing

the uncertainty associated with radar-based rainfall estimates is an important step towards

confidently addressing more fundamental questions about tropical atmospheric dynamics and the

contribution of freshwater into the oceans.

CHAPTER 3: RAIN-FORMED AND DIURNAL WARMING-FORMED OCEAN MIXED LAYERS DURING TWO MJOS

3.1 Introduction and Motivation

The equatorial Indian and West Pacific Oceans exhibit intraseasonal SST, near surface current, mixed layer, and thermocline variability related to the Madden-Julian Oscillation (MJO, Madden and Julian 1994, Cronin and McPhaden 1997, Shinoda and Hendon 1998, Cronin et al. 2000, Zhang and McPhaden 2000, Han et al. 2004a,b, Lau and Waliser 2006, Duvel et al. 2004, 2007, Drushka et al. 2012, Drushka et al. 2014a, DeMott et al. 2014, McPhaden and Foltz 2013, Chi et al. 2014, DeMott et al. 2015).The MJO is a slow (5 m s^{-1}, 30-60 day time scale), eastward propagating oscillation between large areas (1000s of kilometers) / long time periods (days to weeks) of anomalously dry, calm versus rainy, windy conditions in the atmosphere (Zhang 2005). This phenomenon explains the majority of intraseasonal variability in tropical atmospheric and upper ocean fields (Hendon and Glick 1997, Woolnough et al. 2000).

While observational datasets depict MJO occurrence and eastward propagation through the IndoPacific warm pool, our physical understanding of MJO initiation, behavior, and decay is incomplete. This knowledge gap has contributed to challenges in operational prediction and climate model simulation of the MJO compared to observations (Lin et al 2006, Hung et al. 2013, Zhang et al. 2013). Improvements in air-sea coupled general circulation models have been achieved when the spatial and temporal resolution of the coupling is increased to more realistically resolve the coevolution of both fluids (DeMott et al. 2014, Wang et al. 2015, DeMott et al. 2015, and references therein). Another effort has been to improve the parameterization and

representation of clouds, entrainment, and their relationship with larger-scale atmospheric circulations (Benedict and Randall 2009, Zhu et al. 2009, Kim et al. 2009, Chikira 2014).

Current MJO theories consider the instability mechanism to be in the atmosphere and for the ocean to modify it. Several coupled feedback processes between the ocean and atmosphere appear to be important at different times during the intraseasonal cycle (de Szoeke et al. 2014, Demott et al. 2015). Much attention has been given to the net surface heat flux, which drives diurnal and intraseasonal SST variability and corresponding variability in atmospheric convection on these timescales (Duvel et al. 2004, Shinoda 2005, Duvel and Vialard 2007, Matthews et al. 2014, Seo et al. 2014, Ruppert and Johnson 2015). Mechanical mixing of the ocean by surface wind stress has also been well-studied. In contrast to the suppressed MJO and weak trade wind regime, westerly wind bursts (WWBs) in the active MJO period accelerate zonal, equatorial upper ocean jets, which generate upper ocean turbulence. This promotes deep ocean mixing and depression of the thermocline, entrainment cooling of the ocean surface from below, meridional and zonal salt and temperature advection, and barrier layer formation (Lukas and Lindstrom 1991, Smyth et al. 1996a,b, Smyth et al. 1997, Cronin and McPhaden 1997, 1998, 2002, Drushka et al. 2014, Chi et al. 2014, Moum et al. 2014).

The 1980s WEPOCS (Western Equatorial Pacific Ocean Circulation Study) and 1992-1993 TOGA-COARE (Tropical Ocean Global Atmosphere – Coupled Ocean Atmosphere Response Experiment) provided greater understanding of physical oceanography, air-sea interactions, and the MJO in the western Pacific warm pool. The 2011-2012 DYNAMO (Dynamics of the MJO) field campaign aimed to resolve these aforementioned air-sea interactions in the central Indian Ocean, the initiation region of the MJO (Yoneyama et al. 2013). The third DYNAMO hypothesis from Yoneyama et al. (2013) states that "The barrier layer,

wind- and shear driven mixing, shallow thermocline, and mixing layer entrainment all play essential roles in MJO initiation over the Indian Ocean by controlling the upper ocean heat content and sea surface temperature and thereby surface flux feedback."

The Indian Ocean mixed layer depth (MLD) and the processes that control it are of particular interest to this study. The MLD is a constantly adapting function of mechanical wind and shear driven mixing balanced by buoyancy generated from surface atmospheric freshwater and heat fluxes (Lombardo and Gregg 1989, Brainerd and Gregg 1995, 1997, Anderson et al. 1996, Yoshikawa 2015). All of these forces vary on intraseasonal, diurnal, and (atmospheric) mesoscale time scales in the west Pacific and Indian Ocean warm pool region (Lau and Waliser 2006). Lukas and Lindstrom (1991) showed that MLDs in this region can often be at the surface (~0 m) due to daytime heating or freshwater stratification in so-called diurnal warm layers (DWLs, Kawai and Wada 2007, Bellenger and Duvel 2009, Matthews et al. 2014) or rain-formed mixed layers (RFL, Miller 1976, Price 1979, Anderson et al. 1996, Soloviev and Lukas 2006, Asher et al. 2014). Diurnal warming and rain-formed shallow ocean mixed layers are important because they concentrate subsequent heat, momentum, and freshwater fluxes above the stable temperature or salinity gradients, which can promote rapid SST increases (up to 3-4°C diurnal temperature swing) or decreases. Nighttime cooling, accumulation of momentum in the diurnal warm layer, and precipitating storm gustiness can deepen the mixed layer to the barrier layer (10-40 m), the main thermocline (~60-80 m), or other relic stable layers left-over from previous mixing events. Westerly wind bursts can erode stable barrier layers and deepen the thermocline. The intraseasonal SST trend is marked by (diurnal) net ocean warming heat flux-induced warm SST during the suppressed phase and net ocean cooling and mixing-induced cool SST at the completion of the westerly wind burst period.

Despite observational and modeling evidence of diurnal and intraseasonal MLD variability in the warm pool, many state-of-the-art ocean general circulation models have insufficient resolution in the upper 10 m, i.e. first data point at 5 m or only 1-2 data points in the upper 10 m. One dimensional (1D) mixed layer parameterizations can be employed (e.g. Miller 1976, Price 1986, Fairall et al. 1996a), but do not capture advective processes that are known to be important for rain-formed mixed layers. Since fully coupled, dynamic atmosphere and ocean simulations are computationally demanding, many state-of-the-art climate models still use climatological monthly mean mixed layer depths from observational datasets and therefore do not account for diurnal or intraseasonal MLD variability (de Boyer Montegut 2004). Other models only incorporate daily mean SST data from multi-day, interpolated observational products that also do not resolve the diurnal cycle of SST governed by the MLD.

It is important to understand the physical processes that affect SST because SST variability and SST gradients are thought to affect atmospheric convection by several mechanisms. For instance, high SSTs help moisten the lower atmosphere via the latent heat flux and Clausius-Clapyeron effect of increasing sea surface saturation specific humidity. These processes can invigorate the atmospheric boundary layer kinematically by buoyancy-driven turbulent kinetic energy generation. SST also plays a role in triggering overnight atmospheric convection when radiative cooling aloft destabilizes the atmospheric column (Gray and Jacobson 1970, Randall 1991, Sui 1997). SST gradients and warm patches can also focusing mesoscale cloud circulations (O10-100 km) via thermally induced convergence (Lindzen and Nigam 1987, Raman and Riordan 1988, Sublette and Young 1996, Fu and Wang 1999, Chelton et al. 2004, Back and Bretherton 2009 a,b, Minobe et al. 2008, Bellenger et al. 2010, Hsu and Li 2012, Li and Carbone 2012, Kawai et al. 2014, Carbone and Li 2015, Ruppert and Johnson 2015).

Compared to net heat flux and wind effects on the upper ocean, much less is known about rain-formed mixed layers, their impact on SST, or the integrated effects of these high-frequency RFL events on larger or longer time scales (Clayson and Chen 2002). Rain-formed mixed layers have often been observed to form immediately after rain events cease because added kinetic energy of rain drops disturbs the upper ocean. They can deepen immediately due to elevated winds and gustiness from the same precipitating system, later that night in the normal mixing cycle, or last long enough to heat the next day or when the sun comes back out. Asher et al. (2014) found that density stratification due to rainfall is more consistent when rain rates exceed 6 mm hr^{-1} because then salinity effects outweigh mixing and rain cooling effects. Since rain is intermittent and short-lived compared to the net heat flux, daily rainfall accumulation was only weakly correlated to ocean MLD in a western Pacific Ocean study by Anderson et al. (1996). However, their coarse daily precipitation data prevented analysis of how individual or successive storms might have affected ocean MLD. It is still unknown how often freshwater events shoal the mixed layer to the surface in the IndoPacific warm pool, how often rain-formed mixed layers contribute to heating or interact with diurnal warm layers, and what types of precipitating systems are more likely to cause RFLs.

Information about storm morphology or contextual rain information beyond local rain gauges were either not available or not utilized in any aforementioned rain-ocean mixed layer interaction studies. "Strong", "impulsive", "heavy", and "convective" rain events have been implicated in mixed layer freshwater stabilization without radar data confirmation or any mention of the potential role of stratiform rain except from one modeling study (Costa et al. 2001). A comprehensive, high resolution, air-sea interaction-focused analysis is still needed to determine the effects of all tropical, oceanic precipitating system types on the tropical, equatorial

82

ocean mixed layer (Clayson and Chen 2002). Precipitating cloud variability over tropical oceans and throughout the MJO has been well-studied by Janowiak et al. 1994, Takayabu et al. 1995, Young et al. 1995, Chen and Houze 1997, Sui et al. 1997, 1998, Lemone et al. 1998, Rickenbach and Rutledge 1998, Saxen and Rutledge 1998, Yang and Slingo 2000, Houze et al. 2000, Clayson et al. 2002, Takayabu 2002, Serra and McPhaden 2005, Riley et al. 2011, Barnes and Houze 2013, Zuluaga and Houze 2013, Rowe and Houze 2014, Xu and Rutledge14, 2015a,b, Barnes et al. 2015, Thompson et al. 2015, Rowe and Houze 2015, Chen et al. 2015, and others. These studies have shown that the suppressed MJO is dominated by shallow, infrequent, weak, and small convective systems with short lifetimes and little if any stratiform rain. As wind shear and atmospheric instability increase due to higher SST as well as increasing tropospheric moisture during the disturbed MJO, precipitating systems become more frequent, deeper, and can support small stratiform rain regions. Therefore, rainfall accumulation increases during this period. The semidiurnal cycle of storms dominates during the suppressed MJO phase and most of the disturbed phase (Sui et al. 1997, Yang and Slingo 2001). During active MJO conditions, the atmosphere is conducive for all storm types throughout the diurnal cycle, including the upscale growth of individual convective elements into mesoscale convective systems (MCSs), which last 3+ hours and have large stratiform rain regions with leading or embedded convection (in linear or quasi-circular formations). When the westerly wind burst (WWB) begins during the active MJO, MCS rain events can last multiple days while wind speeds remain elevated above 6 m s^{-1}. This wind speed is thought to be the threshold for the "high-wind regime" at which the ocean tends to be well-mixed despite buoyancy forcing (Soloviev and Lukas 2006).

In addition to the mean wind, rain-cooled downdrafts called cold pools cause local cooling and gustiness, which accelerates latent and sensible cooling as well as ocean mixing.

83

Atmospheric cold pool intensity, duration, and frequency are functions of precipitating system morphology (Young et al. 1995, Saxen and Rutledge 1998), which need to be taken into account when examining how these precipitating systems affect the upper ocean.

We hypothesize that rainfall, wind, and net heat flux variability amongst various precipitating system morphologies causes different impacts on the ocean mixed layer depth. Since precipitating clouds exhibit intraseasonal variability, we hypothesize that their effect on ocean MLD is also not constant throughout the MJO. DYNAMO hypothesis 3 states that coupled air-sea interactions are important for MJO initiation in the Indian Ocean. It is important to know how precipitation-ocean mixed layer interactions physically occur and whether they play a role in intraseasonal SST and atmospheric variability, a goal motivated by the conclusions of Drushka et al. 2014a, Wang et al. 2015, and DeMott et al. 2015. The goals of this study are to:

1. Compare rain-formed and diurnal warming-formed shallow mixed layer events throughout two MJOs and identify how they interact.

2. Determine how the full spectrum of precipitating systems observed throughout the MJO contributes to either stratification (shoaling) or mixing (deepening) of the upper ocean mixed layer.

3. Describe the influence of diurnal warm layers and rain-formed mixed layers on intraseasonal SST variability throughout the MJO.

A study of this scope hinges on the availability of high spatial and temporal resolution ocean temperature and salinity microstructure measurements to diagnose ocean mixed layer evolution. These ocean data are analyzed in the context of overlying air-sea fluxes and surrounding rainfall (details in Sec. 2). Section 3 discusses the long term variability of surface and upper ocean conditions throughout two DYNAMO MJO events. Examples of individual

diurnal warming and rain formed mixed layer shoaling events are discussed in Sec. 4 and

summarized in Section 5. Section 6 discusses why certain precipitating systems are more capable

of producing salinity stratified rain formed mixed layers in the upper 5 m of the ocean compared

to others. Rain freshening and diurnal warming mixed layer stratification effects on intraseasonal

SST variability are discussed in Section 7. A summary follows in Section 8.

3.2   Data and Methods

Data were collected at the research vessel *(R/V) Roger Revelle* research throughout the

second and third of four total DYNAMO cruises (Johnson and Ciesielski 2013, Yoneyama et al.

2013, Moum et al. 2014). Cruises 1 and 4 were not utilized because coincident oceanographic

and atmospheric data were not collected in the primary equatorial MJO waveguide. Data

considered in this study are exclusively from time spent on station at 80.5° E and the Equator: 5-

27 October and 12-30 November 2011. 43 total days are investigated, punctuated by a 15 day

restaffing and refueling period between 29 October - 11 November. All precipitation radar,

surface meteorology, air-sea flux, and oceanographic data have been interpolated to a 10 minute

time series. Data are available at ftp://dynamo.dms.uconn.edu/ linked from the Earth

Observatory Laboratory (EOL) field catalog:

http://data.eol.ucar.edu/master_list/?project=DYNAMO.

MJO conditions are defined locally in this study, which was roughly in agreement with

the global wind and outgoing longwave radiation-based Wheeler and Henden Real-time

Multivariate MJO Index (WH RMM, http://monitor.cicsnc.org/mjo/curent/rmm/). The

"suppressed" phase encompasses WH phases 5, 6, and 7. All phase 8 days in November 2011

and all but two phase 8 days in October are included in suppressed conditions. The local onset of

the "disturbed" MJO is considered to be the first day when rain occurs locally during the daytime hours, as opposed to pre-dawn and late afternoon, which included all phase 1 days in October and November and the first WH phase 2 day in October and November. The first "active" MJO days are determined to be when rain and clouds persist through a majority of the daytime hours according to radar data. This includes all remaining phase 2 and 3 days in each month. "Westerly wind burst (WWB)" time periods are the active MJO days when the wind speed was sustained over 6 m s^{-1}. **Table 3.1** lists the resulting time periods of suppressed, disturbed, active, and WWB MJO phases used in this study.

Table 3.1: MJO conditions based loosely on Wheeler and Hendon RMM Index as well as local rain and cloud conditions.

Suppressed MJO	5 Oct 00 Z – 13 Oct 00 Z	12 Nov 00 Z – 17 Nov 00 Z
Disturbed MJO	13 Oct 00 Z – 20 Oct 22 Z	17 Nov 00 Z – 21 Nov 21 Z
Active MJO	20 Oct 22 Z – 27 Oct 00 Z	21 Nov 18 Z – 1 Dec 00 Z
Westerly Wind Burst (WWB)	27 Oct 00 Z – 28 Oct 00 Z	24 Nov 08 Z – 27 Nov 00 Z
		27 Nov 18 Z – 01 Dec 00 Z

Use of this bulk terminology is consistent with analysis of the larger scale atmospheric variability during DYNAMO by Gottschalck (2013). RMM index calculation can vary 1-2 days depending on temporal and spatial filtering and is not a comprehensive indicator of local MJO conditions, so strict adherence to this metric is not necessary.

3.2.1   *Surface meteorology data and cold pool identification*

Air-sea fluxes were computed using the COARE 3.5 bulk aerodynamic algorithm (Fairall et al. 1996b, Fairall et al. 2003, Edson et al. 2013, de Szoeke et al. 2014). A total of 121 atmospheric cold pool events were identified within the observation period in this study by a sudden drop in temperature and simultaneous or preceding increase in wind speed. The 1-minute flux data were first filtered using two 1-2-1 temporal averaging windows. Then -0.5°C and +1 m s^{-1} thresholds were required to be met for event classification. This ensured that gradual cooling

or gradual increases in wind were not classified as cold pools. A cold pool was considered to

have "ended" locally when the latent heat flux (LHF, also filtered with a 1-2-1 averaging

window) returned to within 5 W m^{-2} of the 5 minute average LHF prior to the event start. The

LHF often did not recover to pre-cold pool values between successive cold pools events. In these

cases, the cold pool recovery time was determined to be the final recovery time of the train of

successive cold pools.

3.2.2 *Radar data and precipitation event identification*

Since this study requires knowledge of rain morphology surrounding and at the location

of ship oceanographic measurements, NASA TOGA C-band Doppler radar data from the R/V

Revelle were re-gridded to a fine 0.5 km horizontal, 0.75 km vertical Cartesian grid within 50 km

of the ship using Radx2Grid by NCAR. This gridding process aimed to preserve the high native

resolution of the radar data close to the ship. The radar scanning strategy unfortunately placed

the ship in the cone of silence, such that the first 0-2 km AGL radar data available begin at 2 km

range (Xu and Rutledge 2014a). The standard Yuter and Houze (1997) convective and stratiform

radar echo partitioning algorithm was applied to radar reflectivity in order to identify convective

and stratiform echoes. The algorithm's tunable parameters were tested to produce the most

physically realistic partitioning between convective and stratiform portions of storms given the

knowledge and experience gained from Chapter 2. The algorithm yielded the most physically-

consistent results with a 4 km smoothed reflectivity field, a = 60, b = 100, and requiring that the

local reflectivity exceed the background reflectivity by 17 dBZ. Partitioning was performed at

0.75 km AGL using gridded radar reflectivity and then separate convective and stratiform rain

equations developed by Thompson et al. (2015, i.e. Chapter 2) for the tropical warm pool were

used to estimate rain rate throughout the radar domain.

Precipitation gauges are often unrepresentative of an area due to localized wind and

blocking effects given the high spatial variability of rainfall. For instance, there were many

occasions when rain appeared to surround the ship according to the scanning radar but no rain

was recorded by the ship gauge. Due to these point measurement limitations, the ship's 1-minute

resolution rain rate dataset (optimally interpolated from over 20 different sensors on the ship)

was combined with the maximum radar-derived rain rate between 2-3 km ranges of the ship. To

gain an idea of when rain was within close vicinity of the ship, the highest value from either

source was chosen for the combined rain rate field, which is used throughout the study. The 1

minute resolution ship gauge rain rates were used in this combination rain product because the

10 minute resolution rain rate data from the *Revelle* flux dataset is an average of 1 min

instantaneous rain rates over each 10 minute period, resulting in drastically reduced rain rate

magnitudes that do not agree with instantaneous rain rates estimated from radar.

The combined rain rate field was then used to isolate continuous time periods of rain rate

exceeding 0.5 mm hr^{-1} without non-raining interruptions lasting longer than 30 min. This method

identified 68 precipitation events crossing the ship. Using standard radar and mesoscale

meteorology definitions (Doviak and Zrnic 2006, Cotton 2011, Houze 2015) as well as the radar

convective/stratiform partitioning algorithm, radar data within 25 km of the ship were

investigated to manually classify each event as either a mesoscale convective system with

stratiform rain (max dimension > 150 km, abbreviated MCS), submesoscale linear or quasi-

circular convective systems with stratiform rain (max dimension < 150 km, abbreviated LCS or

ICS), or isolated, submesoscale linear or quasi-circular convective events without stratiform rain

(abbreviated LC or IC). *Revelle* radar data examples of each storm type are shown in **Figure 3.1**.

The resulting convective and stratiform partitioning is in **Fig. 3.2**. Stratiform areas exceed 10 km
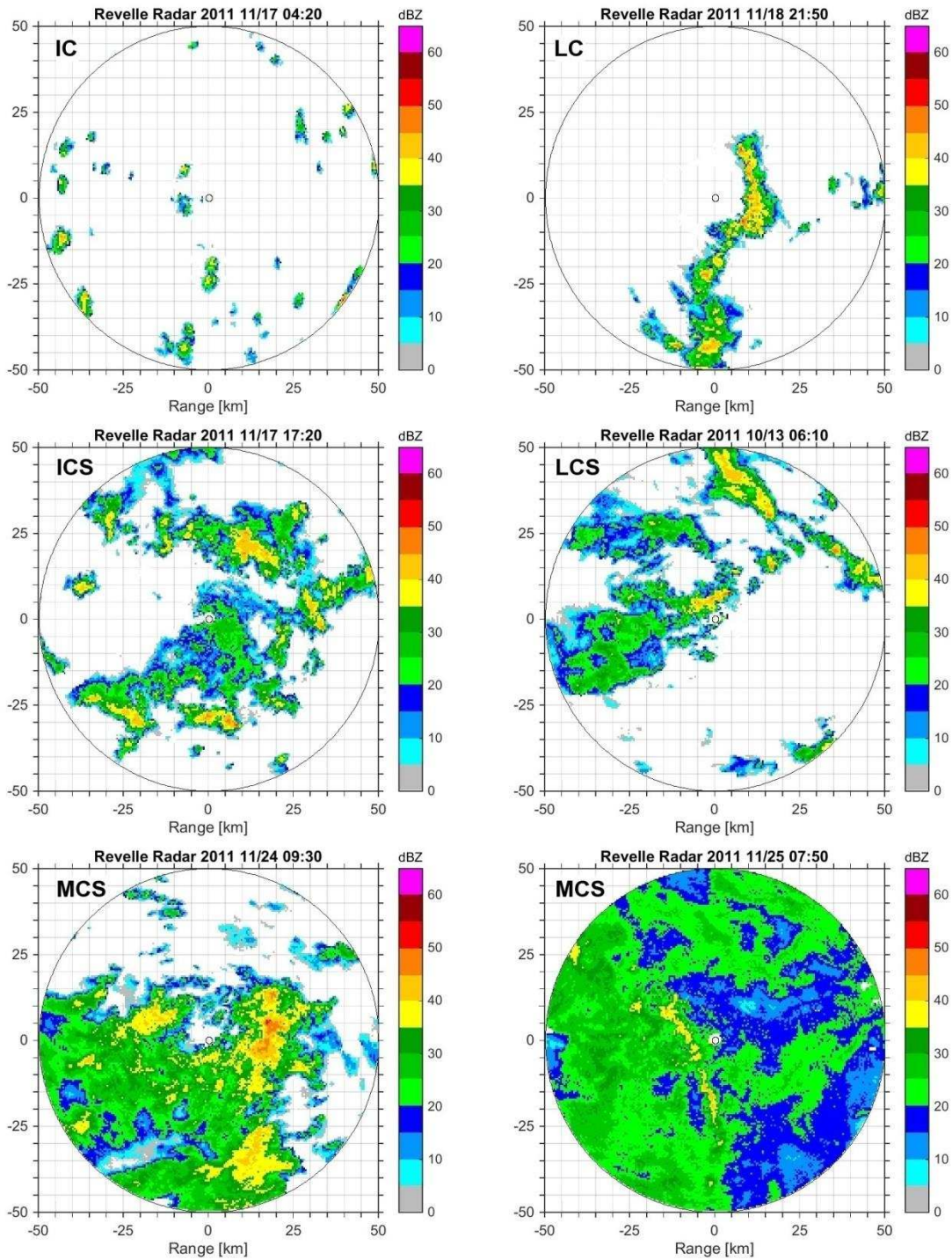
Figure 3.1: *R/V Revelle* ship-borne C-band radar representative examples of central Indian Ocean submesoscale non-linear isolated convection (IC), linear convection (LC), non-linear convective system with stratiform rain (ICS), and linear convective system with stratiform rain (LCS) as well as two examples of mesoscale convective systems (MCSs) with leading connection and embedded linear convection.
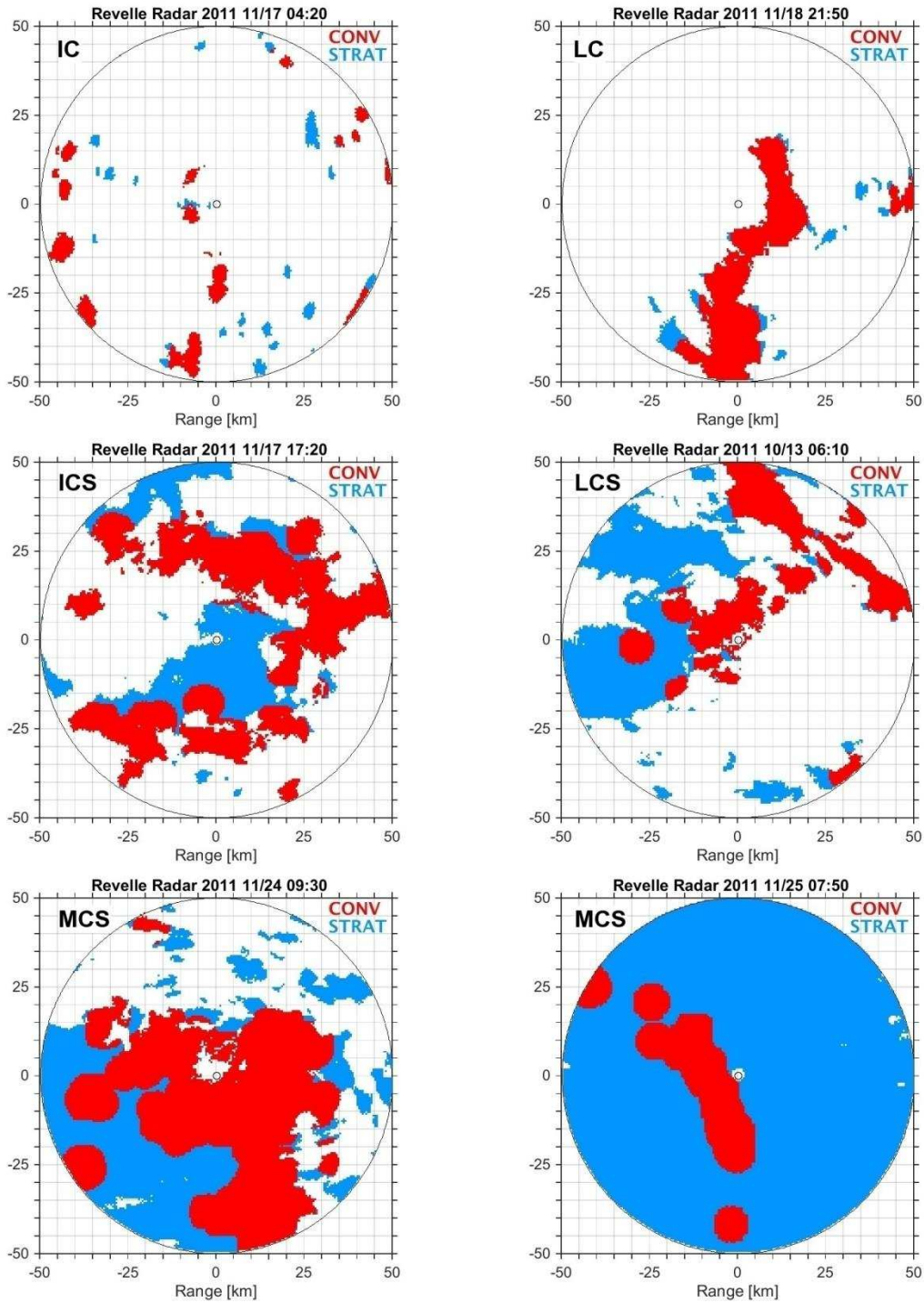
Figure 3.2: Convective and stratiform rain partitioning of radar examples in Fig. 3.1 of central Indian Ocean submesoscale non-linear isolated convection (IC), linear convection (LC), non-linear convective system with stratiform rain (ICS), and linear convective system with stratiform rain (LCS) as well as two examples of mesoscale convective systems (MCSs) with leading connection and embedded linear convection.

dimension in the ICS and LCS cases. The partitioning algorithm is known to misclassify weak, small isolated convective showers as stratiform, as in the case of IC in **Fig. 3.1** and **3.2** (Schumacher et al. 2003). Submesoscale convection with or without stratiform regions (IC vs. ICS or LC vs. LCS) are not always distinguished in previous radar studies (Rickenbach and Rutledge 1998, Saxen and Rutledge 1998, Barnes and Houze 2013, Rowe and Houze 2013, Zuluaga and Houze 2013, Xu and Rutledge 2014b, Houze 2015). However, we consider these five categories of precipitating systems because Chapter 2 revealed that stratiform rain is distinctly different from convection in terms of rain rate magnitudes, variability with time, and drop sizes. According to the literature review, all of these factors appear to be important when determining whether storms will be able to stratify the upper ocean or not. Rain puddles appear to spread out over the ocean surface (Soloviev and Lukas 2006), so both rain accumulation, the extent of the puddle, time period of puddle formation, and perhaps the manner in which it was laid down could be important for determining the structure, resilience, and frequency of rain-formed mixed layers in the ocean.

3.2.3   *Upper ocean data*

Three independent sets of ocean measurements at the *Revelle* during DYNAMO were collected, quality-controlled, and provided by the Oregon State University Ocean Mixing research group. The ship thermosalinigraph provided the closest measurement to sea surface salinity (SSS) as possible every minute, which was the salinity of water "mixed" between the surface to the 3 m intake depth, measured at 3 m and available in the flux dataset. Skin SST was calculated and provided in the flux dataset. SST and SSS hourly trends were calculated by subtracting the -30 min value from the +30 min values of these fields, then using a 1-2-1 filter.

The Chameleon profiler provided salinity and temperature microstructure measurements from the stern of the ship at 7-minute intervals and 1-m vertical resolution between 350 m and 2-4 m depth depending on waves (Moum 1990). The Chameleon temperature microstructure measurements were augmented by a 0-5 m depth, 1 m vertical interpolated resolution ocean temperature dataset from thermistors anchored off to the starboard side of the ship's bow. These data were originally collected at 0.1 m and between 1.6 – 7.5 m depth at 20 cm intervals. Both the Chameleon and thermistor chain datasets were interpolated to 10 min intervals to match overlying atmospheric datasets.

Since the bow and stern temperature data did not agree because of mixing by the ship's wake, the actual temperature records from the two ocean datasets were not combined. When assessing the stability of the ocean, the temperature gradients from the thermistor chain between 0-5 m were used. The temperature gradients from the Chameleon and thermistor chain were averaged at 5 m for consistency, and then the chameleon temperature gradients were used below 5 m. These gradients were used to produce an integrated dataset N^2, the Brunt Vaisala frequency. N is the frequency at which gravity waves, or waves whose restoring force is gravity, would propagate in a given medium. It is a measure of static stability. For seawater, this quantity is often analyzed as:

$$N^2 = \frac{g}{\sigma} \frac{d\sigma}{dz} \ [\text{s}^{-2}] \tag{2}$$

where σ is the potential sea water density, which is a function of pressure, temperature, and salinity. N^2 is positive for statically stable layers of water and negative for unstable conditions, which are prone to convective overturning. The linear approximation of the equation of state leads to an expression of N^2 that can be scaled by the individual effects of salinity and temperature on the density of sea water such that:

92

$$N^2 \sim N_T^2 + N_S^2 \tag{3}$$

$$N_T^2 = g\alpha \, \frac{dT}{dz} \tag{4}$$

$$N_S^2 = -g\beta \, \frac{dS}{dz} \tag{5}$$

where $\alpha = -\frac{1}{\sigma}\frac{\partial\sigma}{\partial T}$ [°C^{-1}] is the thermal expansion coefficient of seawater and $\qquad$ (6)

$\beta = \frac{1}{\sigma}\frac{\partial\sigma}{\partial S}$ [PSU^{-1}] is the salt contraction coefficient of seawater. $\qquad$ (7)

Signs on these equations ensure that density increases as water becomes colder and saltier. Stable layers exist where temperature decreases with depth and salinity increases with depth. The α and β coefficients were calculated using Gibb's seawater MATLAB routines for each time and depth pair of S and T measurements during DYNAMO. N_S^2 and N_T^2 were calculated at every depth and time interval using the measured vertical salinity and temperature gradients. Their sum, N_{S+T}^2, is nearly equivalent to N^2 calculated with the vertical density gradient. N_S^2 is available starting at 2-3 m, while N_T^2 is calculated from 0-350 m using the combined thermistor chain and Chameleon dT/dz field. Therefore, the total N^2 sum (N_{S+T}^2) is dominated by N_T^2 from 0-1 m.

3.2.4 Ocean mixed layer depth and stable layer depth

The mixed layer of the ocean is the portion of the water column where heat, momentum, and salt (freshwater) are evenly distributed. The maximum depth to which these tracers are evenly distributed marks the equilibrium level where the generation of turbulence from ocean waves, current shear, and wind stress balanced the buoyant suppression of turbulence from surface heating and rainfall at some point in recent history. The mixed layer depth is defined as the last depth where the ocean is apparently well mixed, i.e. where the sum of N_S^2 and N_T^2, N_{ST}^2, remains neutral, i.e. between -0.0004 and +0.0004 s^{-2} for at least 3 consecutive meters. These thresholds were manually tested until they yielded physically consistent results across all 43 days

93

of analysis. Mixed layer depth classifications such as those summarized by Anderson et al. (1996), Kara et al. (00a, 00b), and de Boyer Montegut (2004) using thresholds of density, temperature, or salinity between the surface and some depth were not used in this study since high resolution vertical gradients of both S and T can be directly analyzed. Turbulent dissipation rate data in the upper 15 m of the ocean were not available to determine where mixing was actually occurring.

Due to mixing within the mixed layer, stable gradients of temperature, salinity, or both are concentrated at the base of the mixed layer. Turbulence is suppressed within and below this stable layer (Price 1986, Lombardo and Gregg 1989, Brainerd and Gregg 1995, 1997, Smyth et al. 1996a, Cronin and McPhaden 1997, Vialard and Delecluse 1998, Wijesekera et al., 1999, Sutherland et al. 2014). The extent of the stable layer is defined to span between the mixed layer depth to the last depth over which total N^2 is elevated above $+0.0004$ s^{-2} for at least 3 consecutive meters. If the stable layer is at the surface due to either heating or freshwater, the mixed layer depth is 0 m. The top of the main thermocline was defined as the first depth over which $N^2 > +0.000175$ s^{-2} for at least 3 consecutive meters. If the automatic algorithm denoted a mixed layer below 45 m or within 10 m of the thermocline, the mixed layer depth was reassigned to the thermocline depth. After these rules were applied, the mixed layer depth, stable layer depth, and thermocline depth were temporally smoothed with a 1-2-1 filter.

3.2.5 *Identification of salinity and temperature stratification layers*

The 1-2-1 temporally filtered 0-5 m mean N_S^2 and N_T^2 traces were analyzed during time periods when the mixed layer depth (MLD) was already above or rose above 5 m. These times were classified as salinity or temperature stratification events depending on whether each mean, filtered, 0-5 m N_S^2 or N_T^2 variable exceeded $+0.000015$ s^{-2} or was associated with a MLD

94

shoaling event. Not all stratification events shoaled the mixed layer, since the mixed layer could already be stratified with respect to temperature or salinity. Both temperature and salinity stratification events were manually checked for physical consistency. Events were required to last at least 30 min and be at least 1 hour apart from each other for each type (S or T). This classification method resulted in identification of 30 temperature stratification layers and 38 salinity stratification layers.

3.3 Intraseasonal surface and upper ocean evolution

The macroscopic atmospheric and upper ocean environment throughout each of the two DYNAMO MJOs is described in this section. This overview provides context for more detailed description and tracking of salinity and temperature stratification layers in future sections. Chi et al. (2014) used mooring data to describe the surface and upper ocean states during this time, but were limited by coarser 5 m resolution upper ocean data. **Figure 3.3** shows an October – December 2011 time series of 10 m AGL zonal wind, SST, zonal 1.8 m ocean current, SSS, and areal- hourly-averaged radar derived rainfall within 50 km of the *R/V Revelle*, at 0.5 S, 80.5 E. A 15 day port call interrupts the data record between each month. **Table 3.2** summarizes mean surface and upper ocean variables during each MJO phase of each month. Suppressed MJO periods generally consisted of light winds, infrequent and weak convective rain, and an amplified SST diurnal cycle consistent with previous studies (Webster et al. 1996, Matthews et al. 2014, Ruppert and Johnson 2015, Chen et al. 2015).

Diurnal warming spikes in the ocean skin temperature record appear to get warmer each day, contributing to a positive SST trend from suppressed to disturbed MJO phases (also shown by Shinoda 2005, Mujumdar et al. 2011, and Matthews et al. 2014). Compared to the October

suppressed phase, the diurnal cycle of SST was more amplified in the November suppressed period. Near-surface zonal current and wind speed were reduced in the November suppressed phase, indicating that less wind-stress driven mixing took place. Differences between the two MJO events sampled makes generalization of results with respect to the MJO difficult. The upward SST trend halted in the active MJO phases when rainfall and therefore cloud cover, mean wind, and wind gustiness became enhanced. Storm activity also increased throughout this progression, and precipitating systems started to have larger stratiform rain regions that contributed more to areal mean rain accumulation (**Fig. 3.3c**). The October data record ends
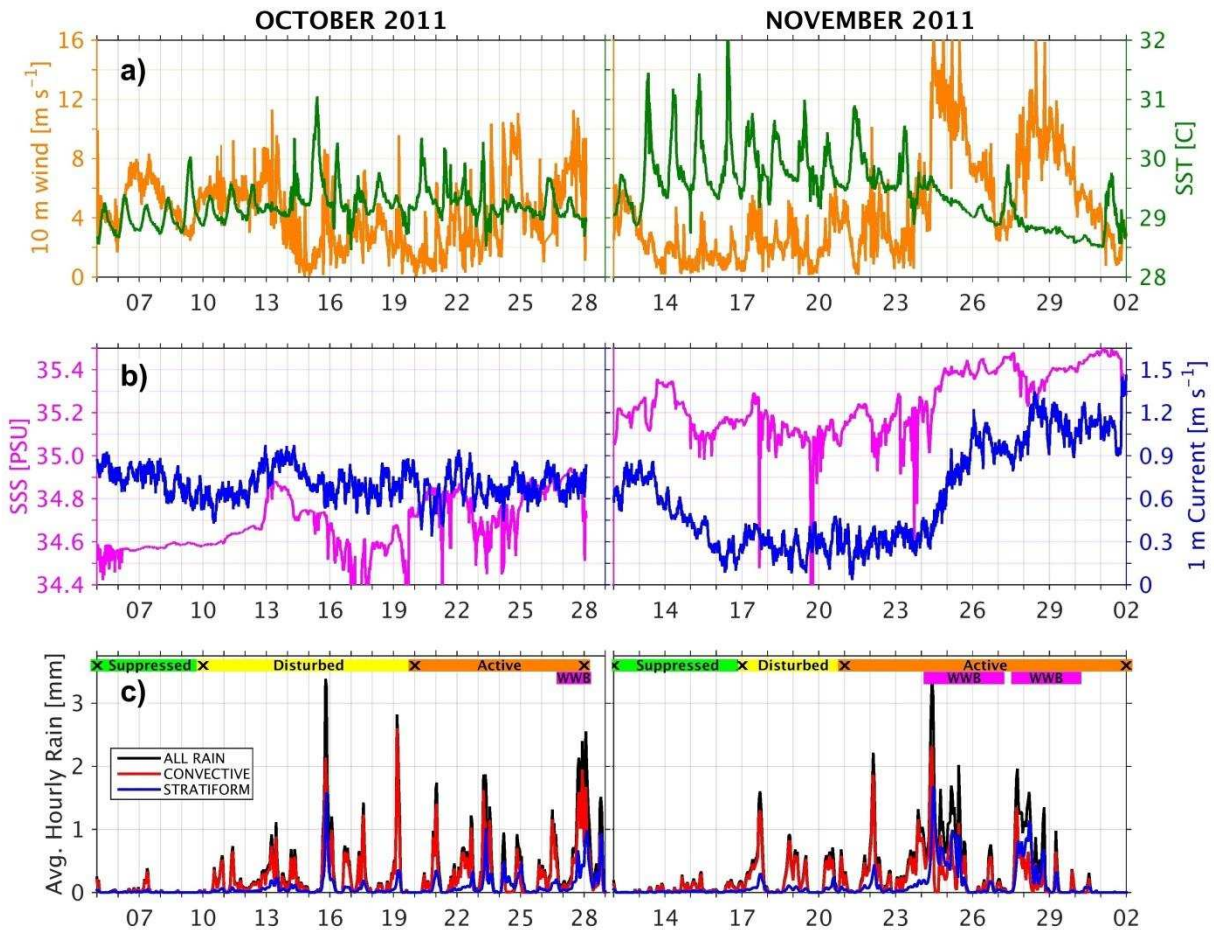
Figure 3.3: Central Indian Ocean October and November 2011 time series of (a) 10 m zonal wind and skin SST, (b) 1.8 m zonal ocean current and 0-3 m mixed thermosalinigraph SSS, and (c) radar-derived areal-averaged hourly rainfall accumulation divided into convective, stratiform, and total rainfall amounts. Suppressed, disturbed, active, and westerly wind burst (WWB) MJO conditions are marked.

Table 3.2: Central Indian Ocean mean net heat flux (negative when heating the ocean), daytime downwelling shortwave radiation, latent heat flux, sensible heat flux, 10 m zonal wind, near-surface ocean current, wind stress, as well as min, mean, and max skin SST and 0-3 m mixed SSS. Time periods are broken down to MJO phase according to Table 1 for both October and November 2011.

		OCT SUPPRESSED	NOV SUPPRESSED	OCT DISTURBED	NOV DISTURBED	OCT ACTIVE	NOV ACTIVE	OCT WWB	NOV WWB
mean net flux	[W m^{-2}]	-109.04	-126.70	-50.71	-99.15	12.04	58.28	-59.22	149.80
mean DAY SW	[W m^{-2}]	-658.62	-615.33	-452.13	-550.27	-384.93	-324.50	-634.87	-243.48
mean LHF	[W m^{-2}]	114.30	76.81	85.20	86.83	113.89	134.38	143.56	178.28
mean SHF	[W m^{-2}]	4.54	5.03	9.21	9.76	13.20	15.75	14.86	21.61
mean U10	[m s^{-1}]	5.28	2.13	2.82	2.48	4.55	6.74	7.45	9.26
mean current	[m s^{-1}]	0.70	0.50	0.72	0.28	0.69	0.79	0.69	0.95
mean stress	[N m^{-2}]	0.03	0.01	0.02	0.01	0.04	0.08	0.07	0.13
min SST	[°C]	28.55	28.74	28.46	29.15	28.52	28.50	28.68	28.57
mean SST	[°C]	29.06	29.78	29.35	29.91	29.22	29.16	29.09	29.01
max SST	[°C]	30.03	32.03	31.05	30.99	30.28	30.56	29.36	29.72
min SSS	[PSU]	34.42	34.98	33.75	33.76	34.16	34.61	34.51	35.07
mean SSS	[PSU]	34.59	35.19	34.65	35.11	34.78	35.32	34.89	35.37
max SSS	[PSU]	34.79	35.36	34.88	35.29	34.94	35.49	34.94	35.45

before the active first MJO cycle is complete, but nearby RAMA mooring data shown in Johnson and Ciesielski (2013) indicate that the SSTs remained near 29°C during the 14 day interim period. In contrast, the November active MJO phase and WWBs were associated with stronger zonal winds and greatly reduced SST. Mixed layer heat budget studies of the November MJO by Moum et al. (2014) and Chi et al. (2014) attributed the SST cooling during this time to a combination of wind-induced latent cooling and mechanical mixing that entrained cooler subsurface water upwards.

SSS was markedly higher when the *Revelle* data record began again on November 12, which is attributed to an advection event from the Arabian Sea (Moum et al. 2014). Although Lukas and Lindstrom (1991), Cronin and McPhaden (1998), Feng et al. (1998), and others have shown that SSS is highly dependent on advection in these tropical equatorial regions, many depressions in SSS in **Fig. 3.3** can be traced to precipitation events from the radar rainfall record. Despite long-lived, widespread, heavy rain accumulation in the active and WWB phases of the MJO, the sea surface became saltier during each active MJO phase due to entrainment mixing of cool, salty water upward (Moum et al. 2014).
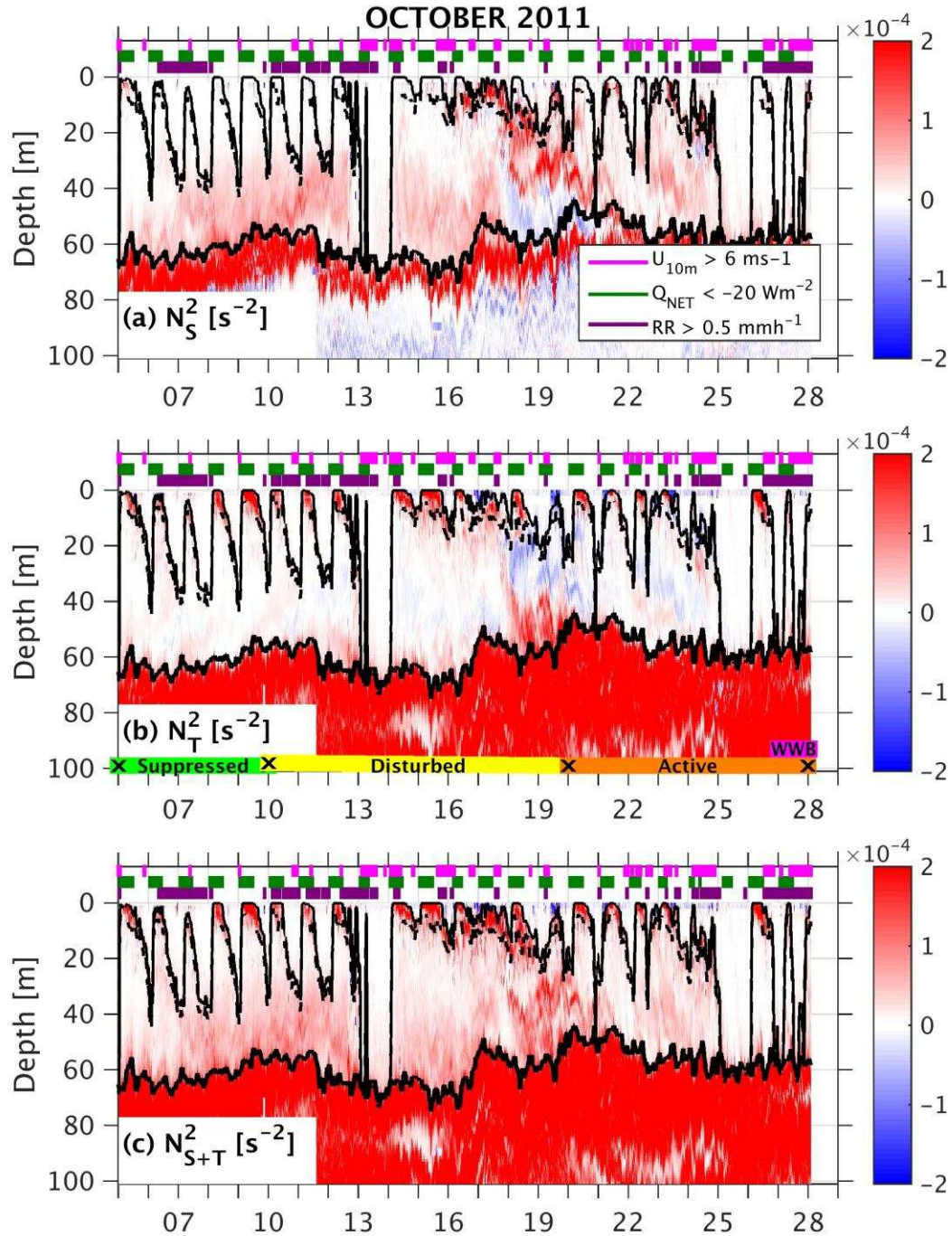
Figure 3.4.1: Central Indian Ocean October 2011 time series with depth of Brunt Vaisala frequency, N^2. Total N^2 (base) is decomposed into N_S^2 (top) and N_T^2 (middle) to demark stratification (positive N^2) due to salinity or temperature. Mixed layer, stable layer, and thermocline depth calculated in the current study based on total N^2 are denoted. Suppressed, disturbed, active, and westerly wind burst (WWB) MJO conditions are denoted. Pink, green, and purple lines atop each plot signify times when the 10 m zonal wind > 6 m s^{-1}, the net heat flux < -20 W m^{-2} was heating the ocean, and local ship rain rate > 0.5 mm hr^{-1}. Mixed, stable, and thermocline layer depths marked in solid, dashed, and thick solid lines.

Figure 3.4.2: Central Indian Ocean November 2011 time series with depth of Brunt Vaisala frequency, N^2. Total N2 (base) is decomposed into NS2 (top) and NT2 (middle) to demark stratification (positive N^2) due to salinity or temperature. Mixed layer, stable layer, and thermocline depth calculated in the current study based on total N^2 are denoted. Suppressed, disturbed, active, and westerly wind burst (WWB) MJO conditions are denoted. Pink, green, and purple lines atop each plot signify times when the 10 m zonal wind > 6 m s^{-1}, the net heat flux < -20 W m^{-2} was heating the ocean, and local ship rain rate > 0.5 mm hr^{-1}. Mixed, stable, and thermocline layer depths marked in solid, dashed, and thick solid lines.

To provide context for these surface data records, **Figure 3.4** shows the 0-100 m depth N_S^2, N_T^2, and total N^2 fields with outlines of mixed layer depth, stable layer depth, and thermocline depth. N^2 decomposition is explained in Sect. 2. Tick marks are at 00 UTC, or 6 AM local time. Sunrise and sunset were at 6:30 AM and PM each day. Pink bars above the stability-shaded plots denote time periods when zonal winds exceeded 6 m s-1, which appear to precede pronounced mixed layer deepening events, sometimes down to the thermocline. Most mornings, especially in the suppressed and disturbed MJO phases, the net heat flux warmed the upper most meters of the ocean (green bars) and usually contributed to temperature stratification of the ocean mixed layer to the surface. This was particularly common when winds were weak (< 6 m s-1), clouds were absent, and shortwave heating contributed to net ocean heating. Stable diurnal warm layers (DWLs) have been documented in each tropical ocean, considered to be default, calm, tropical ocean state reminiscent of suppressed MJO conditions (Kawai and Wada et al. 2007, Webster et al. 1996, Bellenger and Duvel 2009, Bellenger et al.2010, Matthews et al. 2014).

Each night, momentum accumulation in the diurnal warm layer and the switch to longwave radiation heat loss from the ocean surface promoted convective overturning to some depth determined by the competition between underlying stable layers and convective mixing. In October suppressed and disturbed conditions, diurnal warm layers appear to mix down to some moderate salinity stratification region between 40-60 m. During the November suppressed and disturbed days, diurnal warm layers formed on top of and mixed downward to a barrier layer. Miller (1976), Lukas and Lindstrom (1991), Gregg and Brainerd 1995, 1997, Cronin et al. (2002), Drushka et al. (2014a), and many other studies have highlighted the role of the barrier layer in contributing to shallow mixed layer depths by limiting mixing and entrainment cooling from below. Barrier layers are a common climatological feature of tropical oceans caused by

advection, subduction, and local rainfall (Sprintall and Tomczak 1992). The barrier layer in November 2011 in the central Indian Ocean was most likely affected by the advection event between cruises from the Arabian Sea (Moum et al. 2014) as well as heavy rainfall from the previous October MJO. This stable barrier layer sometimes extended between the surface and 30 m during the November time period, reinforced from above by increasing diurnal heating under light winds, rainfall events in the disturbed and active periods, and suppressed overnight mixing. Nighttime mixing hardly extended below 10 m during the November suppressed period due to the barrier layer's contribution to upper ocean stability. This led to decreased overnight cooling, increased daytime heating, and rising mean daily SST (**Fig. 3.3**). We hypothesize that the more stable upper ocean created by the barrier layer, weak winds, weak current, and therefore reduced upper ocean mixing during the November suppressed MJO contributed to the warmer and more rapidly warming SST variability observed in November compared to October suppressed MJO phases.

As each disturbed MJO phase progressed, salinity stratification near the surface started to contribute more toward total stratification. Rain events often produced fresh, stable salinity gradients in addition to slightly cool, unstable temperature gradients. One mixing event extended to the thermocline during the October disturbed phase on a particularly windy, rainy day. This occurred again during the active and WWB October and November MJO phases. Despite strong winds during these WWBs, some active MJO heavy rain events in both months shoaled the mixed layer to the surface several times. One weak diurnal warm layer also occurred in a break between the strong winds and cloud cover during this active MJO time. DWLs are rare during the active MJO because of inhibiting cloud cover and wind (Weller and Anderson 1996). The very strong WWBs in November broke through the persistent mid-level barrier layer

stratification and then mixed all water from the thermocline to the surface for several days. The mixing stretched stable gradients of temperature and salinity upwards (seen by light red shading of weak stability extending upwards from the thermocline). This eroded the thermocline and depressed it downwards from about 56 to 82 meters from suppressed to post WWB conditions meters. Restratification by temperature occurred in a break between the two WWB pulses in November, followed by brief salinity stratification layers that eventually gave way to thermocline deepening once again. In contrast, the October WWB either was not strong enough or long-lived enough to deepen the thermocline, so the mean October top of thermocline depth was 59 m.

In contrast to the progression from the weak October MJO to strong November MJO (with respect to wind mixing, SST depression, rainfall activity in the WWB phases), Johnson and Ciesielski (2013) showed that SST warming during the next December 2011 suppressed phase following the strong November MJO was muted. Gottschalck (2013) confirmed that eastward propagating rainfall signal associated with the December MJO active phase was not as robust or coherent as the previous October and November MJOs. We hypothesize that SST recovery after the November WWB was hampered by continued strong mixing and SST cooling following the strong November MJO and associated WWBs. Chi et al. (2014) and Moum et al. (2014) showed that the near surface current and upper ocean shear from the Wyrtki Jet remained elevated for several days after winds calmed down following the November WWB. In addition to lower SST in December, unfavorably strong low level westerly winds and wind shear also contributed to weaker atmospheric convection during the December MJO (Gottschalck 2013). These winds would have also contributed to great upper ocean mixing and less diurnal warming.

Table 3.3 summarizes the intraseasonal behavior of the upper ocean during the October

and November DYNAMO MJOs according to data presented in **Figures 3.3** and **3.4**. The

intraseasonal SST shift from maximum suppressed phase to minimum WWB SST was 1.35°C in

October. Since SST actually peaked in the disturbed phase of the October MJO because the

current and winds were more vigorous during the suppressed phase, the disturbed to WWB

intraseasonal SST shift was higher, 2.37°C. The extreme stratification, even lower wind speeds,

lower current, and resulting higher amplitude diurnal SST cycle in the November suppressed

phase yielded a 3.46°C intraseasonal SST shift from this MJO's suppressed to WWB conditions.

As Chapter 1 and the introduction of Chapter 3 explain, the mixed layer is well-mixed

due to turbulence. The base of the mixed layer, or mixed layer depth, is defined by the recent

maximum extent of mixing, which produces stable temperature and/or salinity gradients below.

Table 3.3, Figure 3.4, and Figure 3.5a show that the mixed layer depth was determined to be at

Table 3.3: Central Indian Ocean intraseasonal SST differences between suppressed or disturbed phases to WWB phases in October as well as disturbed to WWB phases in November. The mean thermocline depth and stable layer width for different months and time periods as well as the mean mixed layer depth for the entire data record are given. Then the percentage of the two MJO cycles of data when the mixed layer depth is between certain vertical levels and the thermocline are calculated. The mean stable layer depth and maximum stable layer extent of both diurnal warm layers and rain freshening layers is also provided.

```
        Oct Intraseasonal (supp) dSST    [°C]   1.35
        Oct Intraseasonal (dist) dSST    [°C]   2.37
              Nov Intraseasonal dSST     [°C]   3.46
                Oct thermocline depth     [m]     59
        Nov pre-WWB thermocline depth     [m]     56
       Nov post-WWB thermocline depth     [m]     82
           Oct stable layer thickness     [m]      5
   Nov pre-WWB stable layer thickness     [m]     10
                    mixed layer depth     [m]     20
                       time MLD <= 2 m    [%]     31
                       time MLD <= 4 m    [%]     39
                   time 5 < MLD < 10 m    [%]     15
          time 10 m < MLD < thermocline   [%]     24
         time MLD ~ thermocline depth     [%]     19
               mean stable layer depth    [m]     10
                max stable layer depth    [m]     24
```

or above 2 m 31% of the DYNAMO time record throughout the two MJOs. That is to say, the

stable layer was in contact with the surface or observed to begin at 2 m. The mixed layer was at

least as shallow as 4 m a total of 39% of the time, which is important to consider since ARGO

floats begin routine measurements at 5 m depth. Therefore, ARGO floats would not be able to

detect the upper ocean mixed layer or its defining stable layer during 40% of the DYNAMO

record, as Gould et al. (2004) and Anderson and Riser (2014) cautioned. ARGO floats only make

one set of near-surface measurements every 5-10 days, so are not sufficient for ML temporal

evolution studies either. The mixed layer depth was ≤ 5 meters 42% of this data record. Mixed

layer depths between 5-10 m were often just instances when the mixed layer was cycling

between a deep, well-mixed state and a near-surface stable layer, only observed 15% of the time.

Another 24% of the time, the MLD was somewhere between 10 m depth and the thermocline.

The entire upper ocean was well-mixed to the thermocline during 20% of the DYNAMO record.

Fig. 3.5c shows that the thermocline depth at this location ranged mostly between 45 – 85 m,

accounting for WWB deepening in November 2011. The top of thermocline was most commonly

at 55 m depth during suppressed, disturbed, and active MJO conditions before WWBs.
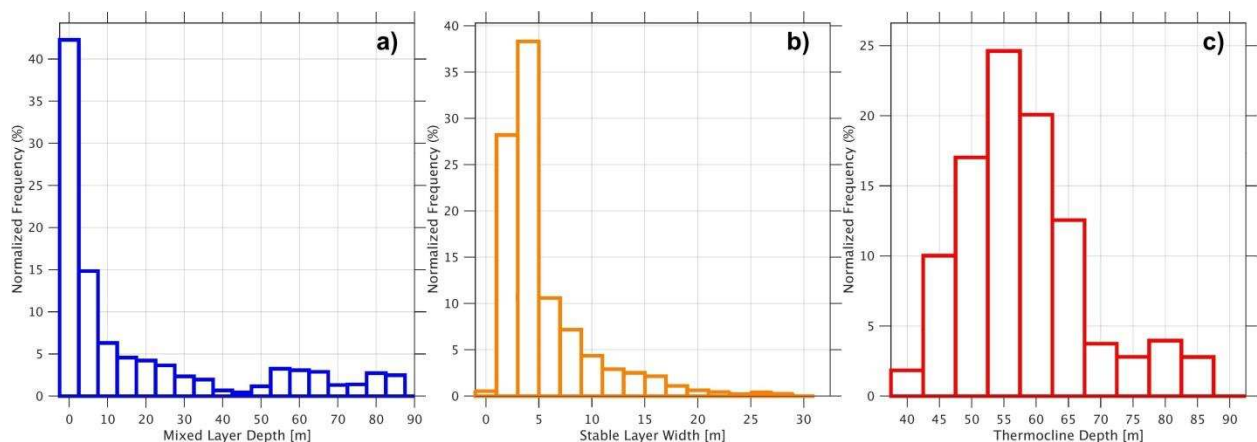
Figure 3.5: Normalized histograms of upper central Indian Ocean mixed layer depth, stable
layer thickness, and thermocline depth according to N^2 methodology in the current study. The
stable layer exists at the base of the mixed layer, marked by stable temperature and/or salinity
gradients beneath the well-mixed surface layer.

These statistics and **Figs. 3.4-3.5** reveal that a daily mean MLD or an intraseasonal mean MLD of 20 m as reported in **Table 3.3** is not representative of the actual daily or intraseasonal mixing and stabilizing cycles, which has implications for mixed layer heating and heat capacity calculations that could potentially affect the atmosphere. The climatological mixed layer depth determined by de Boyer Montegut (2004) in this central, equatorial Indian Ocean region during boreal winter is 10-30 m. However, their analysis specifically "avoided" the upper 10 meters of the ocean. Therefore, the de Boyer Montegut (2004) climatology purposefully dismissed near surface mixed layer depths above 10 m, which apparently occur 57% of the time in the tropical Indian Ocean and potentially other tropical, equatorial ocean basins. The Monthly Isopycnal and Mixed-layer Ocean Climatology (MIMOC, Schmidtko et al., 2013) database is also mainly derived from 5 m and deeper ARGO float data, so also discounts prevalent near-surface upper ocean mixed layer depths. The minimum mixed layer depth detectable from the current analysis was 0 m for temperature stratification and 2 m for salinity stratification due to data quality constraints. Shallower stable temperature and salinity gradients could and should exist, but cannot be identified with the datasets available.

Fig. 3.5b and **Table 3.3** report that the thickness of the near surface stable layer that constitutes the mixed layer region above can be as thin as 2 meters, with a mean thickness of 5 m wide during the October MJO. This is consistent with modeling estimates and observations by Miller (1979), Price et al. (1986), Lombardo and Gregg (1989), and Lukas and Lindstrom (1991). Miller (1976) suggested that the stable layer thickness was determined by sheared flow stability criterion, i.e. the Richardson number. Since this stable layer is often 2-5 m thick, models and observational systems need to have at least 1-2 m vertical resolution in the upper ocean for studies designed to resolve mixed layer depth and therefore SST variability. For instance,

105

RAMA and TOA moorings with ocean salinity and temperature data points at 1 m, 5 m, and every 5 m below would not resolve stable layers as thick as, or thinner than, 5 m. The near surface stable layer often combined with the barrier layer in November so the average combined stable layer thickness was 10 m during this MJO (pre-WWB). The mean extent of the stable layer at the base of diurnal warming- and rain-formed mixed layers was 10 meters with a maximum depth of 25 m (estimates were within 2 m for T or S stratification layers). The stable layer width and depth are important because ocean properties become well mixed throughout the mixed layer while turbulence is suppressed inside the stable layer. Turbulence is also reduced below the stable layer except for shear driven mixing at the interface. The deeper ocean is isolated or shielded from surface turbulent kinetic energy sources. The magnitude and depth of stability concentrated in the stable layer represents a potential energy barrier that must be eroded by mechanical mixing or convective destabilization in order for the mixed layer depth to deepen.

According to the N^2 decomposition during DYNAMO in **Fig. 3.4**, surface heating and therefore stable temperature gradients play a dominant role in stabilizing the upper ocean during all MJO phases. Salinity stratification becomes more prominent in the disturbed and active phases, coexisting with temperature stratification. The WWB phases of the MJO produce unfavorably high winds, cooling net heat flux, and strong ocean currents for either salinity or temperature stratification to occur, but some strong rain events and weak diurnal warming events during breaks between storms are still capable of shoaling the mixed layer. The following section investigates individual salt and temperature stratified layers in more detail.

3.4   Rain freshening and diurnal warm layers

Table 3.4 presents the number of salinity and temperature stratification events detected

across the entire DYNAMO time series seen in **Fig. 3.4** that shoal the mixed layer ≤ 5 m.

Table 3.4: Central Indian Ocean Oct-Nov 2011 salt stratification (rain freshening layer) and temperature stratification (diurnal warm layer) event occurrences and occurrences per day as a function of MJO phase.

	# of days	Salt Stratification		Temp Stratification	
	# of days	Count [#]	Count per day [#]	Count [#]	Count per day [#]
Suppressed	13	2	0.2	13	1.0
Disturbed	13	18	1.4	10	0.8
Active	10	15	1.5	6	0.6
WWB	6	3	0.5	1	0.2
TOTAL	43	38	---	30	---

Thirty DWLs were identified under sunny conditions. These events spanned a total of 308

observation hours, or 29% of the data record. Thirty-eight salinity stratification events occurred

that can be explained by local rain events at the ship or rain events within 5-10 km of the ship (6

advected events). Since the salinity stratification was always observed to originate and then

descend from the surface, and could always be linked to local or nearby rain activity, the depth

between the surface and stable salinity gradients is called a rain freshening layers or rain-formed

mixed layer (RFLs). RFL terminology implies rain freshening as the source of stratification.

Stable salinity gradients define the base of the shallow rain-formed mixed layer. The freshwater

lens is the layer of freshwater trapped near the surface, which sits atop salty water. The salinity

gradients between freshwater and ocean water constitute the stability that manifest the RFL.

RFLs shoaled the mixed layer to or above 5 m for a total of 220 hours throughout the DYNAMO

record, which accounts for 21% of the total DYNAMO observation period. The frequency and

duration of salinity stratification is comparable to that by temperature stratification. Only 8% of

the data record, or 86 hours, were stratified with respect to both salinity and temperature.

The number of RFLs and DWLS observed per day in each MJO phase in **Table 3.5** shows that DWLs occur on every suppressed day, consistent with previous studies such as Bellenger et al. (2010) and Matthews et al. (2014). **Table 3.5** can also be interpreted to mean that DWLs were present on 80% of disturbed MJO days, and on only half the active MJO days (results consistent between both MJOs). Only one WWB DWL was observed (in October). Only two RFLs were observed in suppressed MJO conditions, when rain is infrequent and weak. Both events occurred on the earliest days of each month's suppressed phase. Salinity stratification events were most common in disturbed and active MJO conditions when rainfall is more frequent, intense, and long-lived. There were often multiple RFLs per day during these time periods. RFLS were infrequent in the WWB phase when upper ocean mixing and wind were strong, as shown in **Figs. 3.3, 3.4**, and **Table 3.5**.

The intraseasonal cycle of upper ocean stratification in **Fig. 3.4** is now analyzed on the daily time scale to identify atmospheric and oceanic processes that lead to near-surface salinity and temperature stratification layers during each MJO phase. 43 total days from both DYNAMO *R/V Revelle* cruises have been examined and analyzed. Fourteen representative days are shown to summarize the analysis. These examples describe the full spectrum of diurnal warm layers, the interaction between diurnal warming and rain freshening layers as well as with the barrier layer, days dominated solely by rain freshening stratification, and finally windy, stormy days without any stable layers.

3.4.1 DWLs without rain or cold pool influence

The highest SST recorded during DYNAMO occurred in a diurnal warm layer that formed above the barrier layer and then merged with the barrier layer as it gradually rose to the surface. During this suppressed day on 16 Nov (**Fig. 3.6**), there was intense temperature and salinity stratification between 0 and 20-25 m depth. No storms or cold pools were observed and winds were between 0-2 m s^{-1} during this day at the *Revelle*. SST rapidly rose nearly 2°C beginning around 3:30 pm to reach the daytime maximum of 32°C at 4:30 pm. Six out of 30 DWLs made contact with the BL. Four other DWLs formed above a barrier layer lingering between 10-25 m but did not join it as on 16 Nov (**Fig. 3.6**).
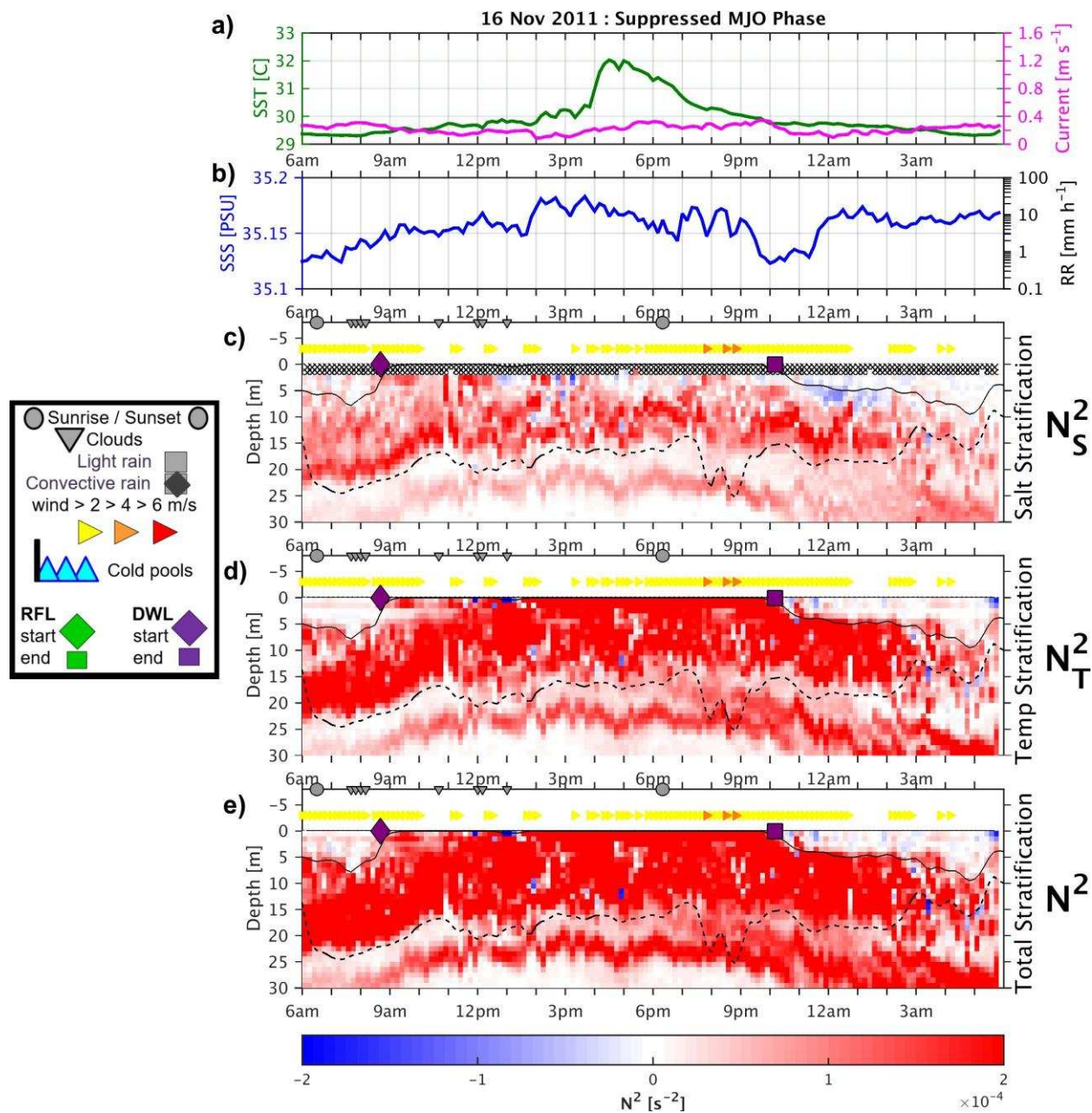
Figure 3.6: 16 Nov 2011, suppressed MJO central Indian Ocean daily time series of SST, near-surface zonal current, SSS, and rain rate at the *R/V Revelle* in the central Indian Ocean. Time vs. depth plots of N_S^2: salt stratification, N_T^2: temperature stratification, and their sum, N^2: total stratification. Color shading is depicted below markers that indicate sunrise, sunset, cloudiness compared to modeled clear-sky downwelling solar radiation, color scaled rightward pointing triangles for zonal surface wind speed, grey squares to indicate local precipitation with dark grey diamonds for convective rain, bold vertical black lines to denote atmospheric cold pool passage, and upward pointing blue triangles representing duration of enhanced latent heat flux out of the ocean due to cold pool passage, which was used to determine cold pool recovery time.

Five other diurnal warm layers occurred without any cold pool, precipitation, or barrier layer interaction. These events were all during the suppressed phases of November and October. The strongest DWL of these five occurrences is on 9 Oct (**Fig. 3.7**), which shows stronger winds between 2-4 m s^{-1} compared to the previous calm example. The surface was strongly stratified with respect to temperature between 9 AM and 7 PM. The maximum SST was 30°C, reached around 4:30 PM after SST gradually rose from 9 AM onward. Evaporation led to negative salinity stratification within the diurnal warm layer, a common occurrence of DWLs without rainfall modification (Saunders 1967, Soloviev and Lukas 1997, Asher et al. 2015, Drushka et al. 2014b). The 0-3 m SSS increases throughout the DWL event on 9 Oct (**Fig. 3.7**). The maximum SSS increase throughout a DWL without rain influence observed during DYNAMO was 0.103 PSU, at a rate of 0.0105 PSU/hr, which is similar to values found by Asher et al. 2014, Drushka et al. 2014b, and Soloviev and Vershinsky (1982). It is important to note that DWLs without interaction with freshwater stratification, storms, or cold pools, only occurred during suppressed MJO conditions. Fourteen out of 43 observation days showed DWLs without interaction with RFLs, 13 of which occurred in the suppressed phase with only one occurring during disturbed MJO phases.
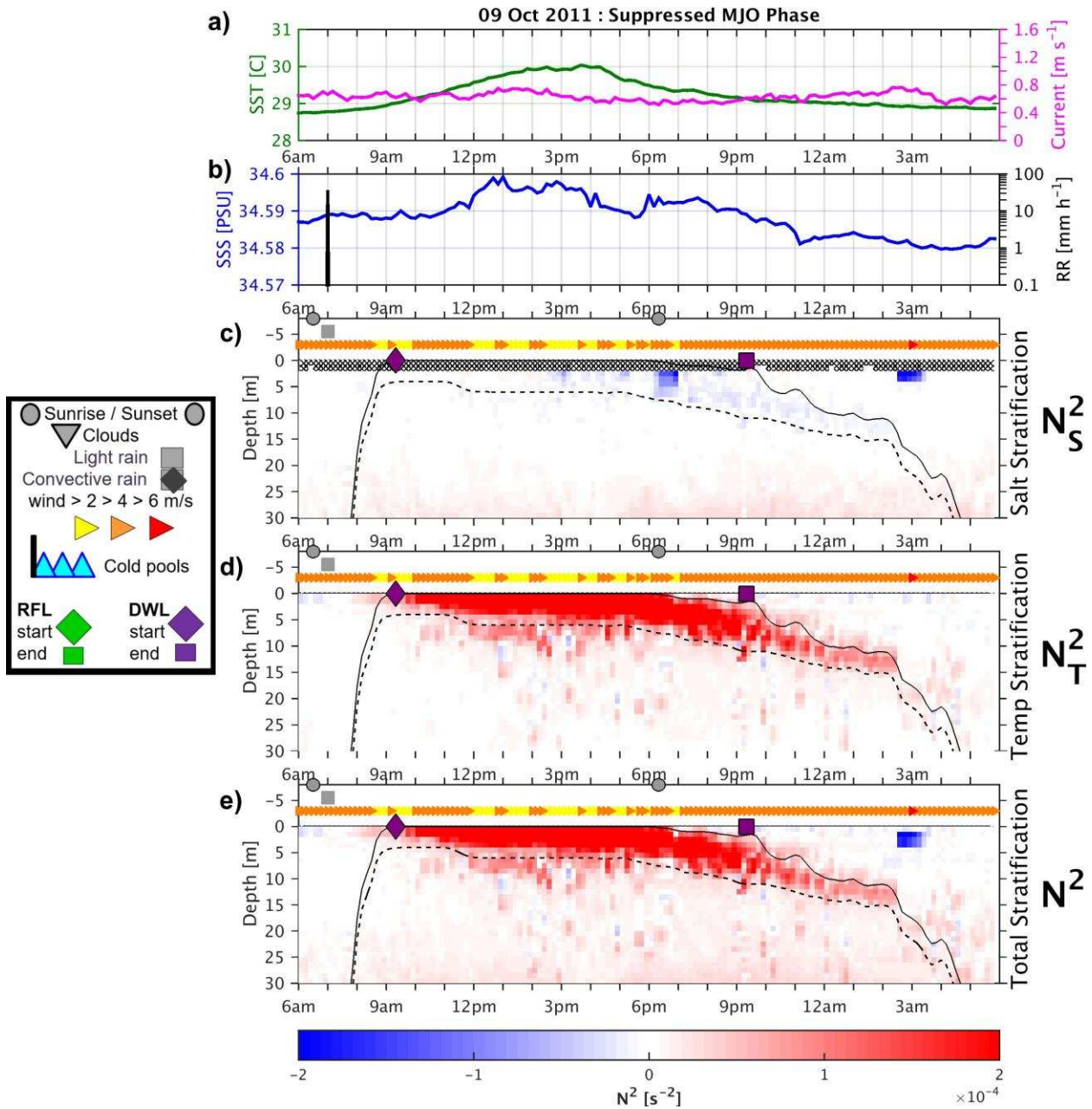
Figure 3.7: As in Fig. 5 for 09 Oct 2011, suppressed MJO central Indian Ocean daily time series.

3.4.2 DWLs ended by convection and cold pools

Three DWLs in the suppressed phases of the MJO were ended by small, isolated convective rain events with cold pools. **Fig. 3.8** (7 Oct) shows one example when winds were over 6 m s^{-1} and the mixed layer depth reached no higher than 5 m. The temperatures

stratification is notably weaker in magnitude because of the influence of upper ocean mixing, despite clear skies before the onset of convection at 3 pm. In contrast to the previous strong DWL example, **Fig. 3.8** (7 Oct) shows that DWLs can exist in winds > 6 m s^{-1} and current ~ 0.8 m s^{-1} and don't always shoal the mixed layer to the ocean surface. This struggling DWL was easily mixed downward by gustiness or cooling from weak, isolated convection at 3 pm. The evaporation signature in the DWL is present but also suppressed during the strong mixing.
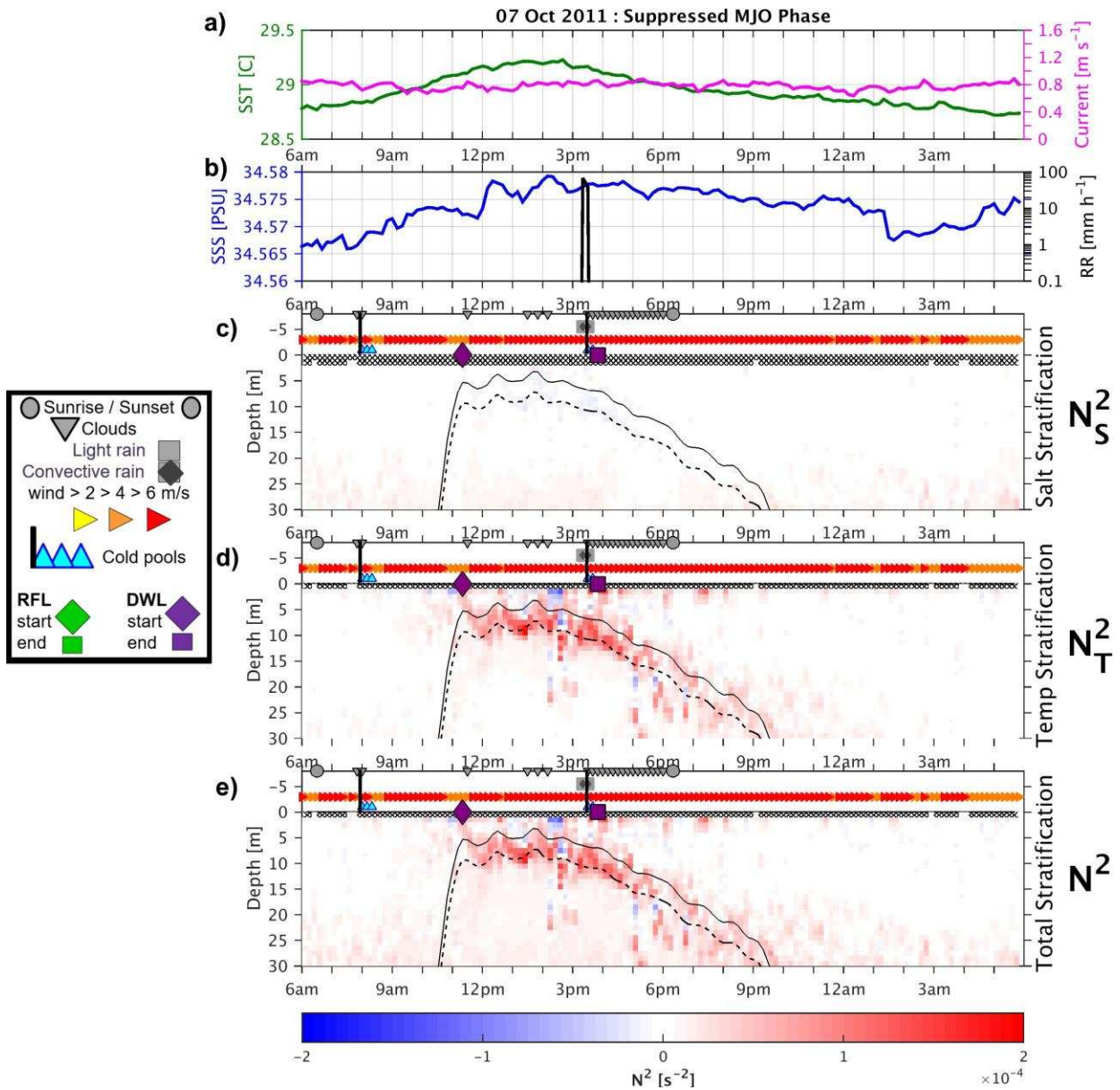
Figure 3.8: As in Fig. 5 for 07 Oct 2011, suppressed MJO central Indian Ocean daily time series.

Another DWL that was interrupted by a cold pool from isolated convection is shown in

Fig. 3.9 (15 Nov)**.** In this example, lingering upper ocean salinity and temperature stratification

from the previous day allowed the surface to restratify just after dawn (6:30 AM local time

throughout the experiment). A maximum daytime temperature of 31.5C was reached by 2 pm.
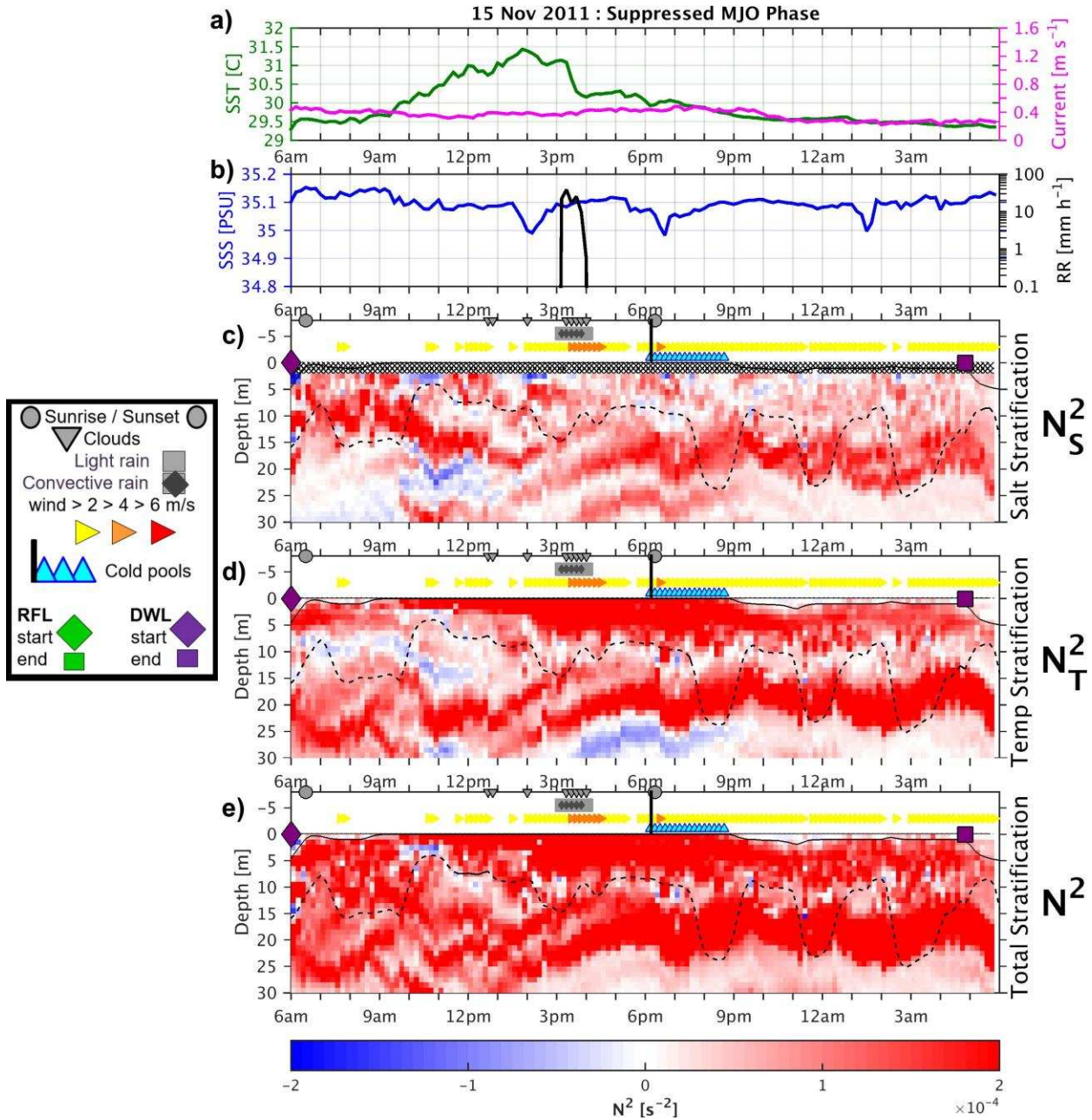
Figure 3.9: As in Fig. 5 for 15 Nov 2011, suppressed MJO central Indian Ocean daily time series.

A storm developed and went over the ship between 3-4 pm with a cold pool passage at 6 pm linked to nearby convective activity. The weak storm makes no visible impact on upper ocean salinity stratification (although the upper 2 meters of salinity data were unavailable, so we cannot rule out any interaction). However, the cold pool mixes out the temperature gradients in the top 1-2 m enough to depress the mixed layer depth to 2 m. The upper 5 meters of the ocean remains stratified until just before dawn. The following day ensues as shown in **Fig. 3.6** (16 Nov), when SSTs reached the all-time record high for this experiment. We hypothesize that the long duration DWL and subdued overnight mixing/cooling due to the barrier layer in **Fig. 3.9** (15 Nov) followed by another DWL contributed to the high SST occurrence on 16 Nov (**Fig. 3.6**).

Four DWLs in the disturbed and active MJO phases were ended by about 6 PM with the onset of isolated convective events with cold pools but without any noticeable freshwater influence. It is unknown how long these DWLs would have kept the ocean mixed layer depth at the surface if the convective activity had not occurred. Considering all examples, DWLs always mixed downward immediately, if not within a couple hours, of afternoon convection with cold pools. One westerly wind burst diurnal warm layer on 27 Oct **(Fig. 3.10)** struggled to form under winds greater than 6 m s^{-1} while skies were clear between heavy rain events. The mixed layer depth still reached the surface and fostered warming. Strong wind-induced mixing and decently strong current speed appear to have mixed the temperature gradients enough to appear very stretched and diffuse and produce only weakly stable temperature stratification. This DWL is mixed away abruptly with the onset of strong evening convection and associated cold pools.

These examples show that diurnal warm layers can occur in all phases of the MJO and can still contribute to SST warming in the most active phases of the MJO when the atmosphere is conducive for deep atmospheric convection. Precipitation is inhibited in the suppressed phases of
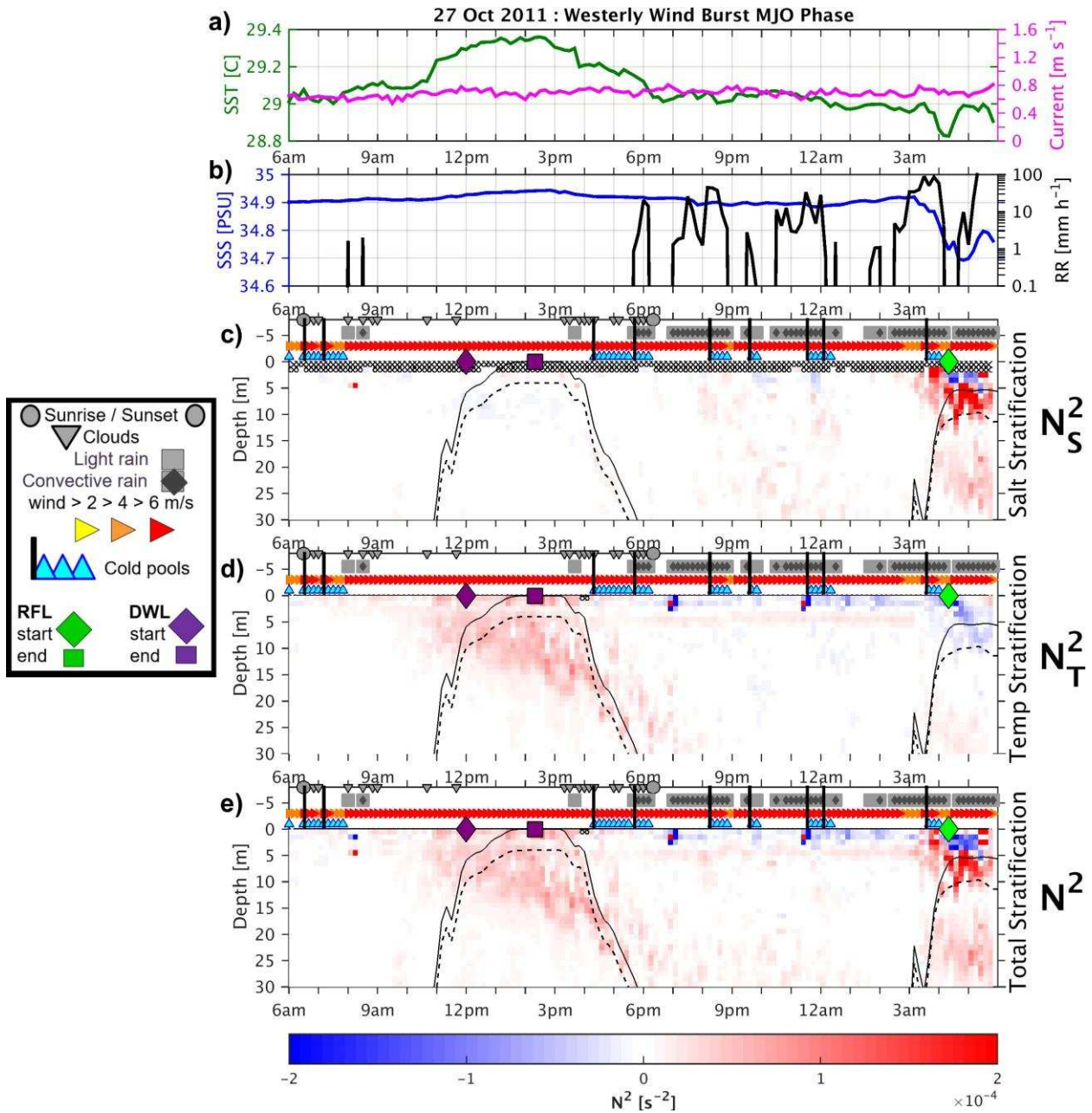
Figure 3.10: As in Fig. 5 for 27 Oct 2011, westerly wind burst MJO central Indian Ocean daily time series.

the MJO because of dry tropospheric, descending atmospheric conditions. However, we

hypothesize that the storms that do occur have more wind forcing than rain forcing and therefore

break ocean mixed layer stratification instead of adding to it by creating rain-formed mixed

layers. Precipitating clouds in the suppressed phase of the MJO tend to obey the semidiurnal

cycle, mostly occurring in the late afternoon in response to surface heating (Bellenger et al. 2010, Ruppert and Johnson 2015) and in pre-dawn, overnight hours due to radiative destabilization (Gray and Jacobson 1977, Randall 1991, Cronin and McPhaden 1999, Sui et al. 1997). Because of the late afternoon and early morning rainfall timing, DWLS are uninhibited by storms most of the daytime hours (Ruppert and Johnson 2015, Rowe and Houze 2015). Since cold pools and convection do not end DWLs until evening or late afternoon when heating has mostly ended, the mean relationship between atmospheric convection and cold pools and DWLs is one of coexistence during the suppressed phase.

3.4.3 DWLs catching RFLs

Five DWLs in the disturbed MJO and four DWLs in the active MJO periods appear to "catch" or concentrate new salinity stratification within the preexisting stable temperature gradient layer beneath the mixed layer. The salinity stratification is produced by precipitation events that occur over or nearby the *Revelle*. This was also observed by Reverdin et al. (2012) and Wijesekera et al. (1999). **Fig. 3.11** (15 Oct) shows two enhanced salinity stratification events during the disturbed MJO period that were contained within a strong, long-lived diurnal warm layer. No rainfall was observed at the ship but scattered, isolated, small convective showers were within 5 km and upstream of the ship, nearly crossing the ship. The duration of these salinity stratification periods is commensurate with the small size of the nearby rain events hypothesized to create them. Rain cells about 5 km wide observed nearby with the NASA-TOGA *Revelle* precipitation radar would have produced freshwater puddles around the same size. When advected from the west at 0.7 m s^{-1} on this particular day, they should have appeared for about 2 hours, which matches salinity stratification observations in **Fig. 3.11** (15 Oct). Diurnal warm layer forcing has been shown to be very widespread and uniform where wind speeds are low and

117

solar insolation is high. The global survey of DWLs by Bellenger and Duvel (2009) showed that

DWLs can span several thousand kilometers when ideal sunny, light wind conditions are present.

Salinity stratification appeared to be advected into the *Revelle* sensors from nearby, upstream,
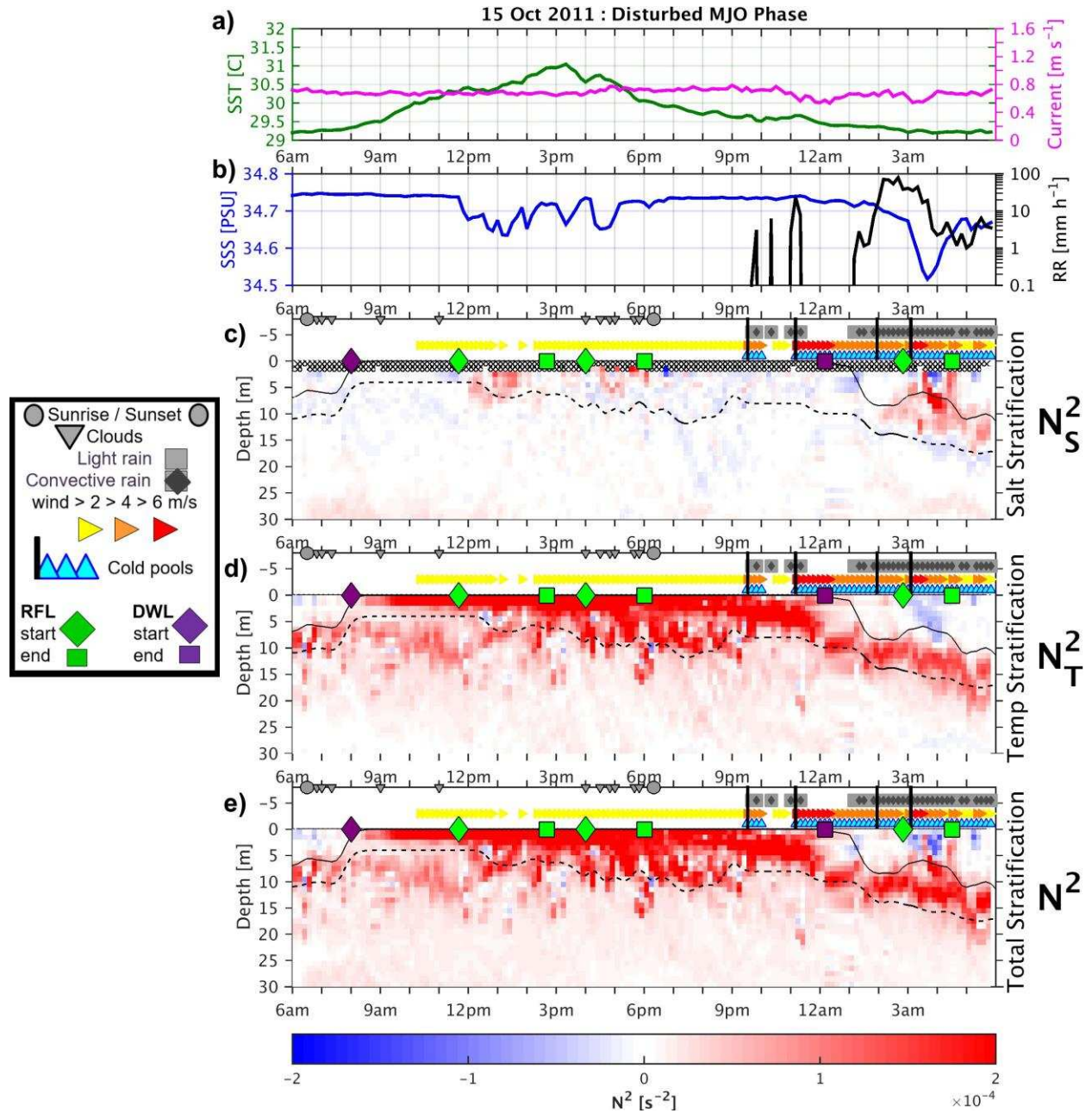
Figure 3.11: As in Fig. 5 for 15 Oct 2011, disturbed MJO central Indian Ocean daily time series.

isolated convective precipitation events on 6 total occasions (mean 0.8 m s^{-1} eastward current throughout DYNAMO), 3 of which occurred inside a DWL where turbulent mixing was already suppressed.

Another active MJO example of a DWL catching and accumulating salinity stratification is shown in **Fig. 3.12** (22 Oct).
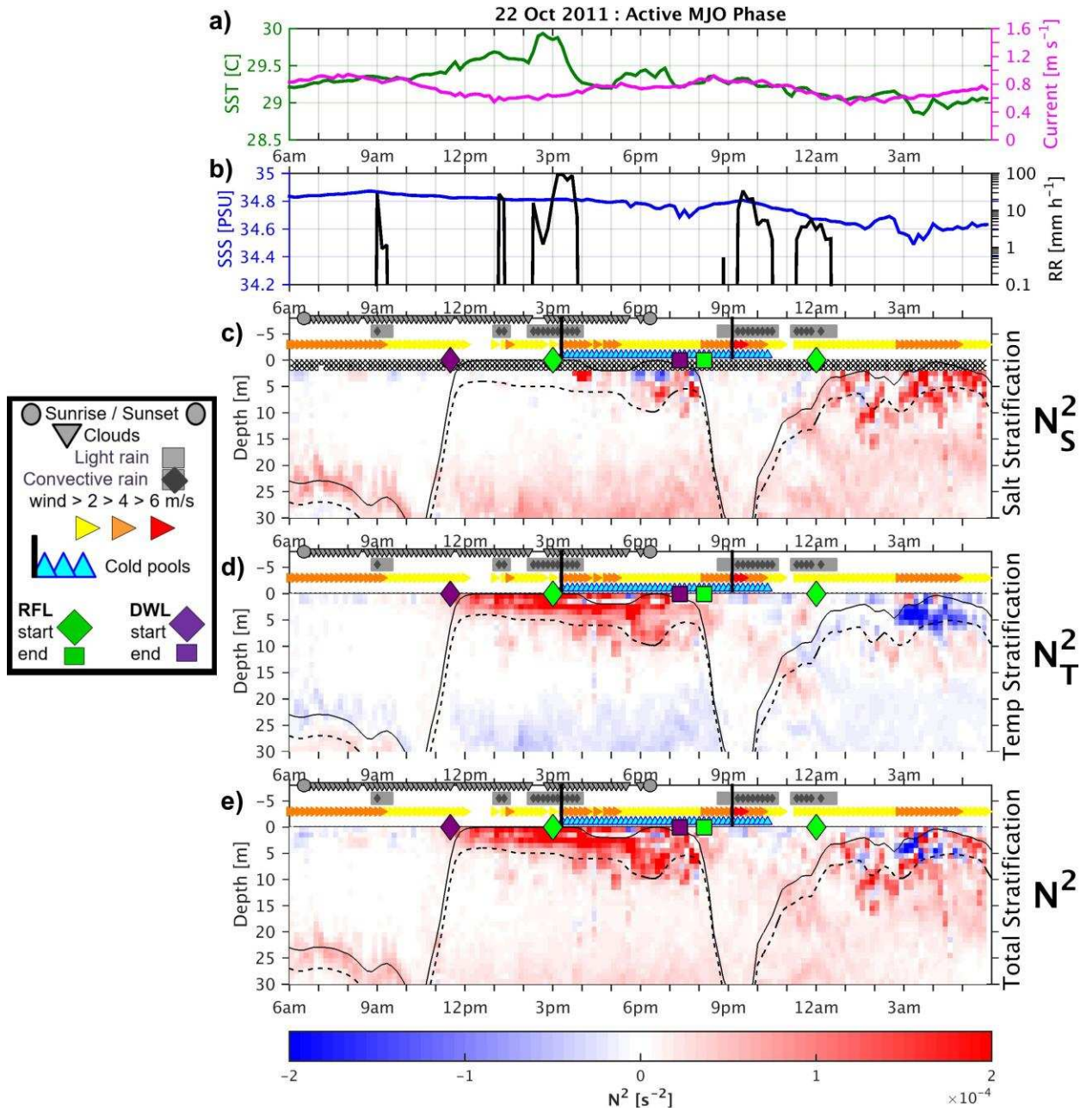
Figure 3.12: As in Fig. 5 for 22 Oct 2011, active MJO central Indian Ocean daily time series.

On this day, a morning isolated, weak, and small convective event occurred without making any impact on the upper ocean. Then a diurnal warm layer formed by 12 PM despite some cloudy conditions but weak winds. A series of isolated convective events passed over the ship at 1 pm and then from 2 pm – 4 pm. By 3:30 PM, SST dropped and positive salinity stratification filled the diurnal warm layer. The freshening and rain stratification appear time-lagged behind the passage of local storms, potentially because the top 2 meters of salinity data are not available and time passed before salinity gradients appeared below. Temperature stratification remained positive in the DWL until 8 pm, 1.5 hours after 6:30 pm sunset time. Winds increased when another storm went over the *Revelle*, which broke the surface stratification and mixed deeply.

The storms that create stable salinity gradients inside diurnal warm layers are not particularly strong, and might not have exhibited high enough rain accumulation to produce near surface salinity stratification on their own from a well-mixed ocean state. The relationship between rain freshening stratification adding to a DWL appears to be symbiotic. The rain events add salinity stratification to the temperature stratification layer without overwhelming it with wind, which would mix the stable layer way. The RFL addition strengthens the diurnal warm layer stratification in magnitude and was observed to extend the duration of total near-surface stratification on two occasions. This provides a longer time period for the atmosphere to be in contact with a very responsive surface mixed layer that is essentially 0 m deep. DWLs were not observed to catch RFLs in the suppressed or WWB periods of the MJO when wind forcing outweighs rain forcing and convective activity always ends DWLs.

3.4.4 Nighttime RFLs

Rain freshening layers shoaled the mixed layer at night 15 times, on 14 out of 43 observation days (two events occurred in one night). **Fig. 3.10** (27 Oct) shows the impacts of a

much stronger, long-lived submesoscale and then a mesoscale convective system with trailing stratiform rain event on the ocean mixed layer at night. The initial early evening convection depressed the temperature stratified mixed layer when cold pools and strong winds occurred. Rain accumulation from another strong convective precipitation event during a brief period of winds below 6 m s^{-1} shoaled the mixed layer again around 3 AM. The continued freshwater flux from this storm was concentrated in a relatively shallow layer above 10 m and produced positive salinity stratification that was higher in magnitude than the negative temperature stratification due to rain cooling and latent heat loss by the storm. Despite winds > 6 m s^{-1} during this WWB, the ocean surface remained stratified with respect to salinity until the October data record ended at 8 AM the next morning.

Fig. 3.11 (15 Oct) shows a brief nighttime RFL formed from an intermediate stable layer, which was a depressed, decayed DWL from the day before. A moderately unstable rain cooling signature is coincident and competing with the stable RFL. While this salinity stratification shoaled the mixed layer for only a short amount of time, it added stratification to the intermediate depth stable layer and suppressed overnight mixing and cooling. As dawn approached, the salinity and temperature stratification were sequestered back down into a weak, relic stable layer between 10-15 m. The mixed layer shoaled the next day from this lingering intermediate stable layer depth due to another rain event at 8 AM.

The later part of **Fig. 3.12** (22 Oct) also showed nighttime rain freshening stratification. The freshwater accumulation from this overnight storm shoaled the mixed layer to the surface at midnight when winds subsided. Advection was likely important in creating this RFL since the storm stalled upstream of the ship even after rain ended locally (evident with radar). The salinity

stratification outweighed the slightly negative rain-cooling and latent-cooling temperature signature, lasting well into the daytime hours and eventually heating the next day.

3.4.5 Heated RFLs

The final way that precipitation events were observed to modify diurnal warm layers was when storms shoaled the mixed layer due to salinity stratification for a long enough time that a diurnal warm layer formed on top (Soloviev and Lukas 2006, Reverdin et al. 2012). This occurred on both of the first suppressed days on record in October and November periods. The storms that produced these RFLs occurred at or just before dawn and were isolated convective events. In **Fig. 3.13** (5 Oct), a RFL formed just after dawn and then the surface became stratified with respect to both temperature and salinity from 11 AM – 3:30 PM. Under light to moderate winds, an evaporation signature took over inside the DWL at 3:30 PM. The stable layer subsided downwards and eroded due to nighttime mixing by 8 PM. The RFL brought the mixed layer to the surface earlier than most diurnal warm layers normally occur (usually 9 AM). While a very weakly stable layer persisted near 15 m overnight, a weak isolated convective rain event occurred without any effect on upper ocean stratification or SSS. An almost identical sequence of events to 5 Oct **(Fig. 3.13)** occurred on Nov 12 in the suppressed November MJO (not shown).
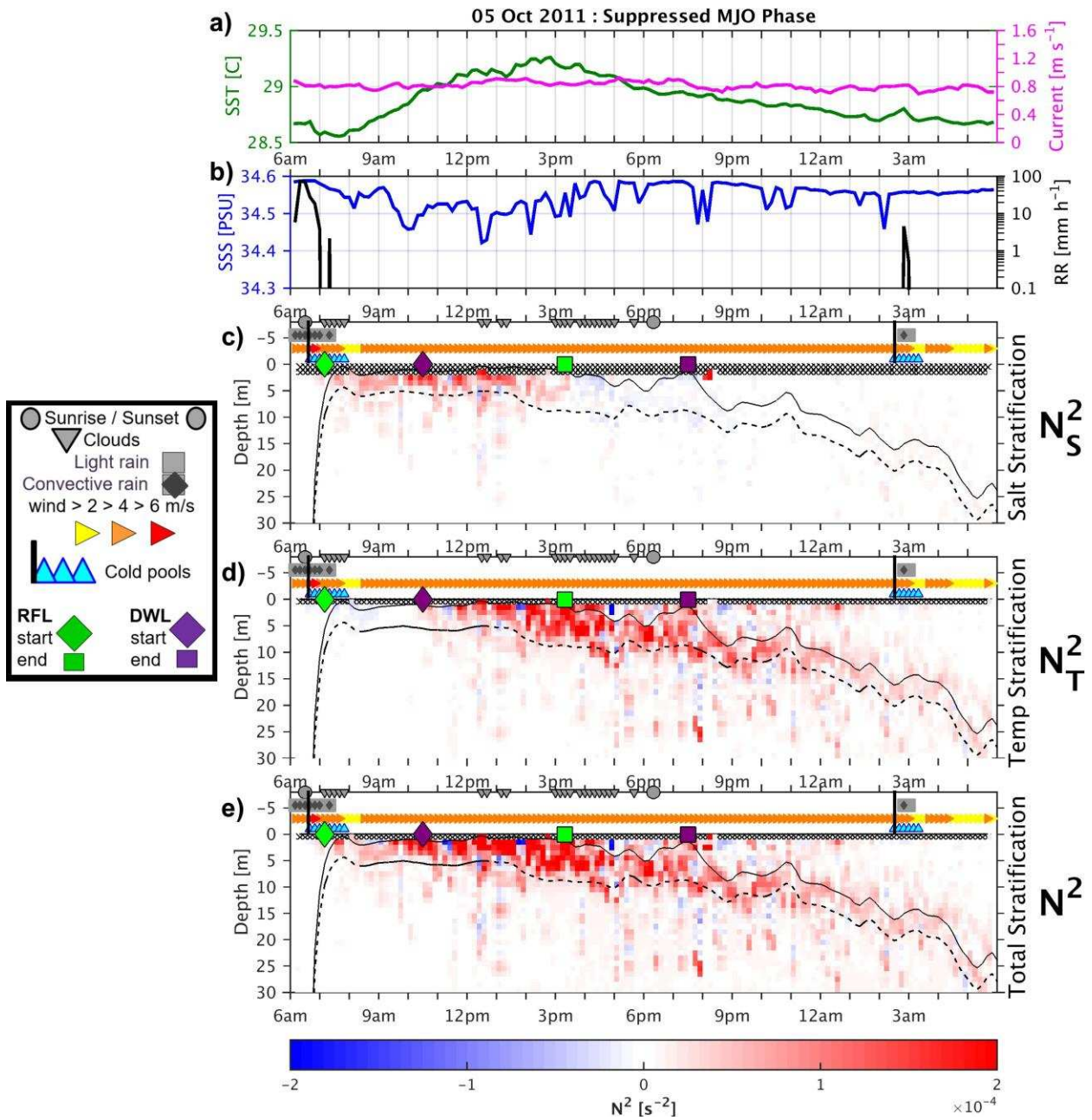
Figure 3.13: As in Fig. 5 for 05 Oct 2011, suppressed MJO central Indian Ocean daily time series.

On 16 Oct (**Fig. 3.14**), the day following 15 Oct (**Fig. 3.11**), an early morning MCS caused a brief period of winds greater than 6 m s^{-1} and heavy rain. The lingering temperature and salinity stratification from the night before was mixed upwards and/or added to, which appeared to shoal the mixed layer briefly at the start of the rain event. Then by the end of the rain event, which was upstream of the ship, salinity stratification became established between 0-15 m with a rain-cooling signature of weakly negative temperature stratification. When the skies cleared and winds slackened, the salinity stratification remained and most likely lifted above the 2 m observation level, while the upper 0-2 m of water heated rapidly. At the end of the DWL, the salinity stratification became more prominent, possibly associated with salinity stratification lowering into view of the 2 m salinity microstructure measurements. *This underscores the need for high vertical and temporal resolution near-surface ocean salinity measurements.*
The upper 5 m remains stratified with respect to salinity until oscillating up and down with the occurrence of rain events over night. The first shoaling event was from a detached stratiform event that produced hardly any rainfall accumulation. Then a linear convective storm crossed over the ship with a cold pool but only moderate wind speeds and increased salinity stratification as well as rain cooling, negative stratification above. The temperature signature of rain and cooling in this case is much clearer than the salinity signatures because the temperature observations in the upper 5 m are superior in coverage and resolution. The stable salinity stratification and unstable temperature stratification layer remained at the surface and extended to 15 m until 9 pm the next day, sustaining another heating event during the daytime hours.
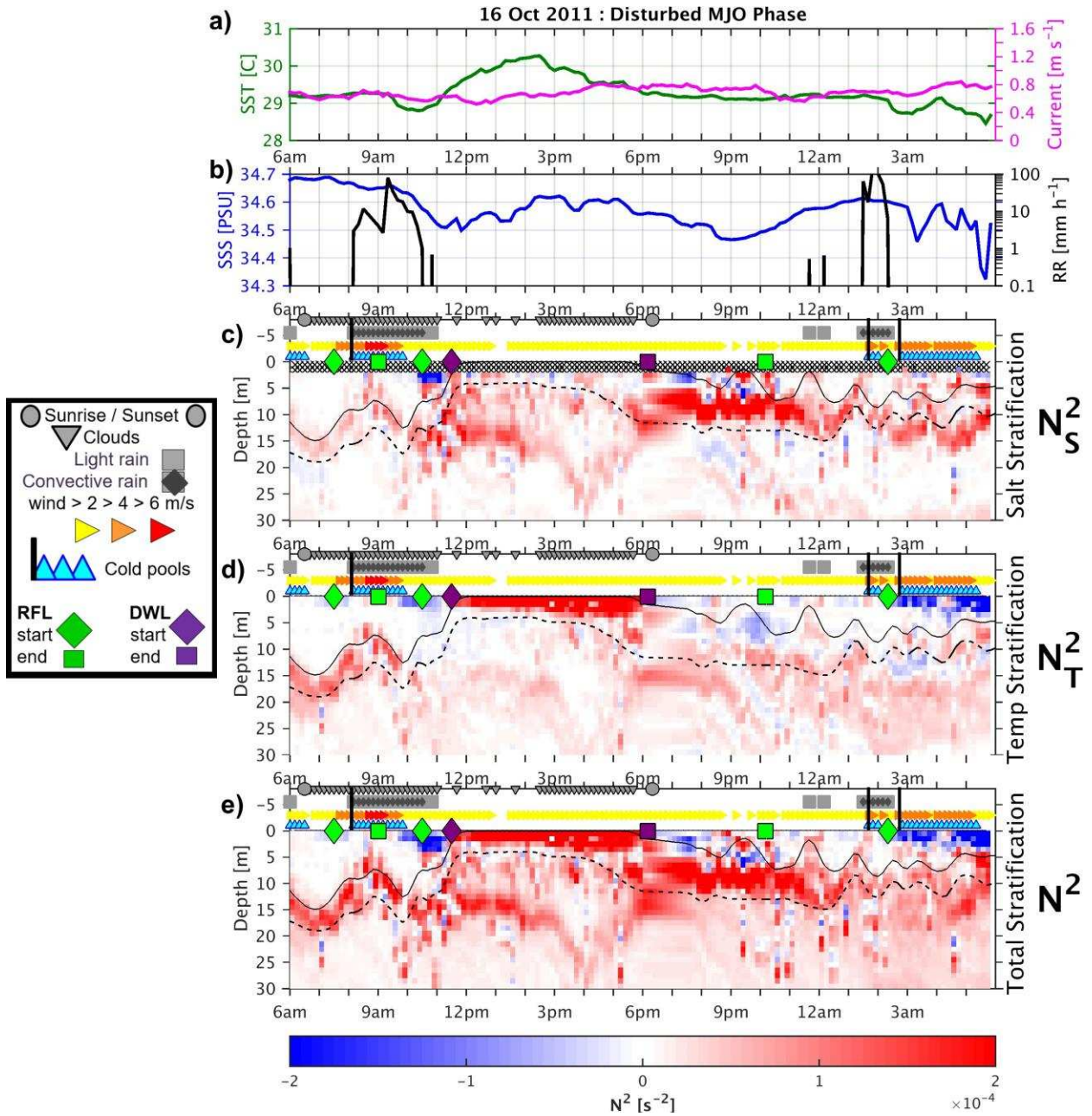
Figure 3.14: As in Fig. 5 for 16 Oct 2011, disturbed MJO central Indian Ocean daily time series.

Another morning RFL that was able to stratify the mixed layer to the surface and then heat as a diurnal warm layer is shown in **Fig. 3.15** (21 Oct). A prolonged rain event occurred at the ship from 5 AM – 7 AM but caused more extensive, long-lived rainfall upstream of the ship. Once winds subsided, stable salinity stratification concentrated the mixed layer to 4 m below rain cooled negative temperature stratification closest to the surface. Then rapid SST warming led to formation of a diurnal warm layer on top of the rain cooled, fresh stable layer at 2:30 PM. SST reached just over 30°C at 4 PM. The diurnal warm layer was in contact with the surface until 7 pm, and the stable temperature gradients lingered within the top 5 m underneath cooler surface waters until 11 PM. Nighttime mixing and potentially advection removed or eroded all local stability in the column at 11 PM. A weaker, overnight, small, isolated convective rain event occurred without any impact on ocean freshening or stratification.

Fig. 3.16 (23 Oct) shows the day following the overnight RFL from **Fig. 3.12** (22 Oct). Salinity stratification and weak rain cooling negative stratification remained near the surface and might have lifted above the 2 m salinity sensor briefly when a diurnal warm layer further stratified the first 2 m at 9 AM. SST rose 1.2°C in only 2.5 hours, reaching 30.2°C by 11:30 AM. A second strong convective storm with stratiform rain went over this layer at the time of maximum SST and produced strong surface cooling and associated negative temperature stratification in the upper 0-2 m during gusty winds and a cold pool. The rain cooling finally ended the DWL and extended the stratification to 8 m at 5 pm, but salinity stratification was still positive in this layer since this rain event added to the RFL from overnight. The surface remained stratified with respect to salinity until 9 PM, when an even gustier storm with winds greater than 6 m s^{-1} for several hours but little rain affected the area. After mixing, a salinity
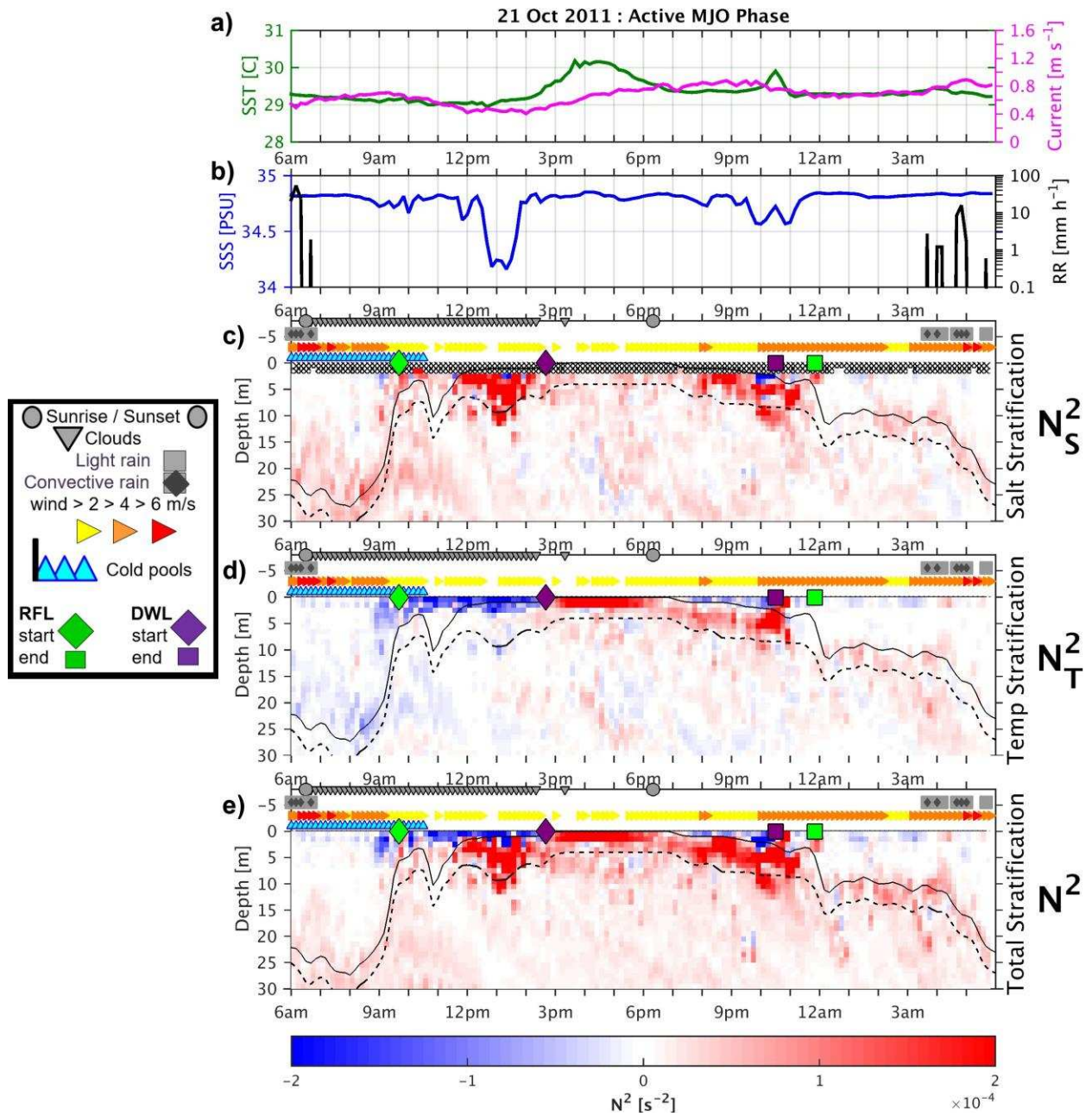
Figure 3.15: As in Fig. 5 for 21 Oct 2011, active MJO central Indian Ocean daily time series.
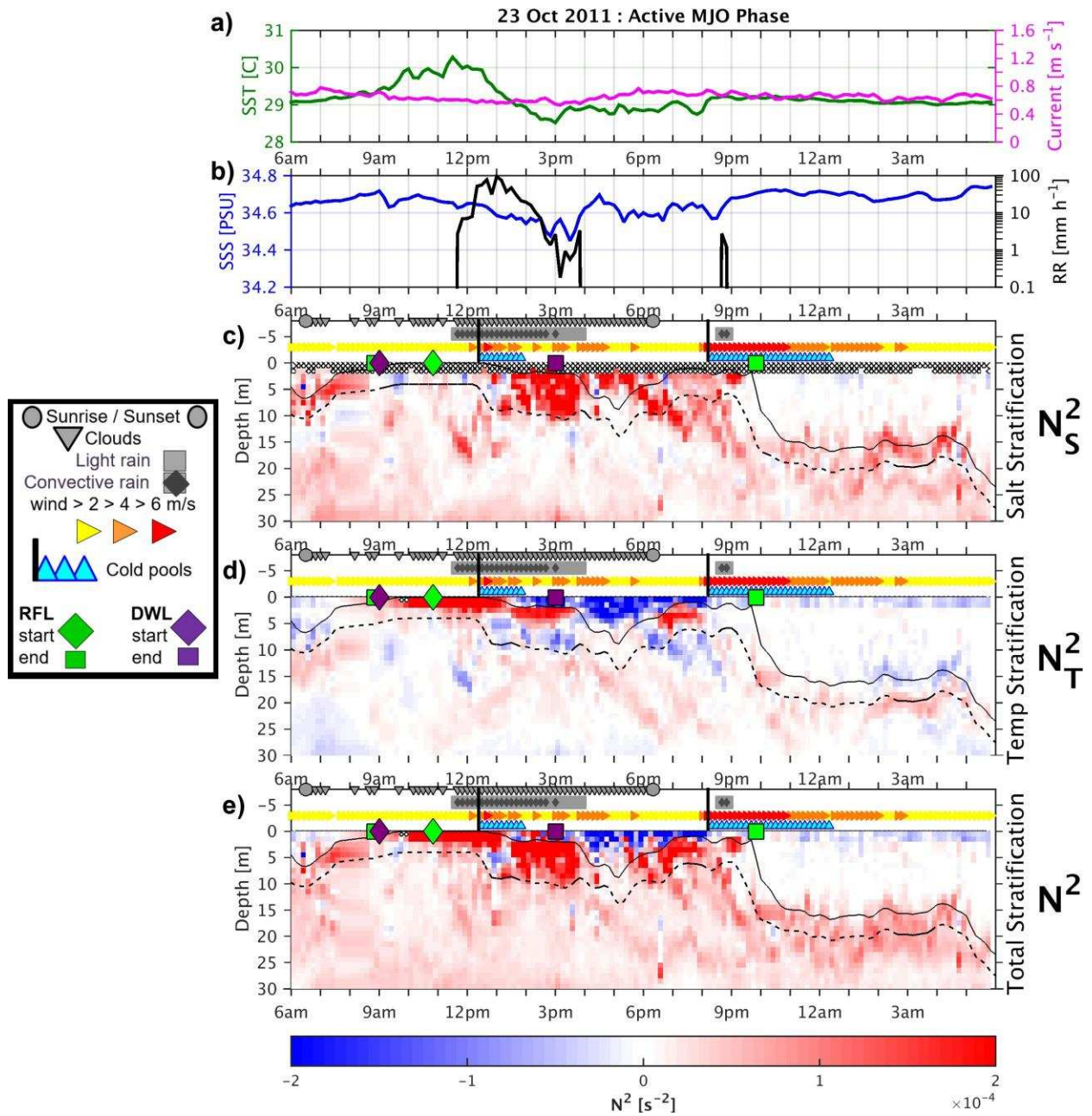
Figure 3.16: As in Fig. 5 for 23 Oct 2011, active MJO central Indian Ocean daily time series.

stratification layer with negative rain cooled temperature stratification lingered around 10-20 m between 2 – 5 AM.

In addition to the two early suppressed phase heated RFLs, four storms produced heated freshwater lenses in the disturbed MJO phases and three more events occurred in the active MJO phases of Oct-Nov 2011. This totals to nine heated rain-formed mixed layers during the entire DYNAMO period, or about 25% of all 38 RFLs observed. Six had stratiform rain components in addition to convective rain. Five of the nine heated RFL events occurred from morning freshwater stratification (suppressed and disturbed MJO) while the other four were from overnight RFLs that never mixed downward (disturbed and active MJO). There were no heated RFLs in the WWB stages of the MJO.

3.4.6 *RFLs without DWL influence*

Salinity stratification can also shoal the mixed layer to the surface during the day and prevent any diurnal warm layer stable temperature stratification from occurring. These events occurred on days dominated by widespread, long-lived rain events with associated wind and widespread cloud cover blocking solar radiation. This occurred on 13 Oct (**Fig. 3.17**) in the disturbed MJO phase when clouds were widespread enough to prevent any daytime warming and a linear convective system with stratiform rain produced copious rain that stratified the mixed layer briefly despite cold pools and strong winds. The stratification occurred during a lull in the wind, between cold pools. Several additional rain events occurred throughout the day but apparently did not leave behind enough freshwater to stratify the ocean in the presence of such strong winds and therefore strong ocean mixing.

129
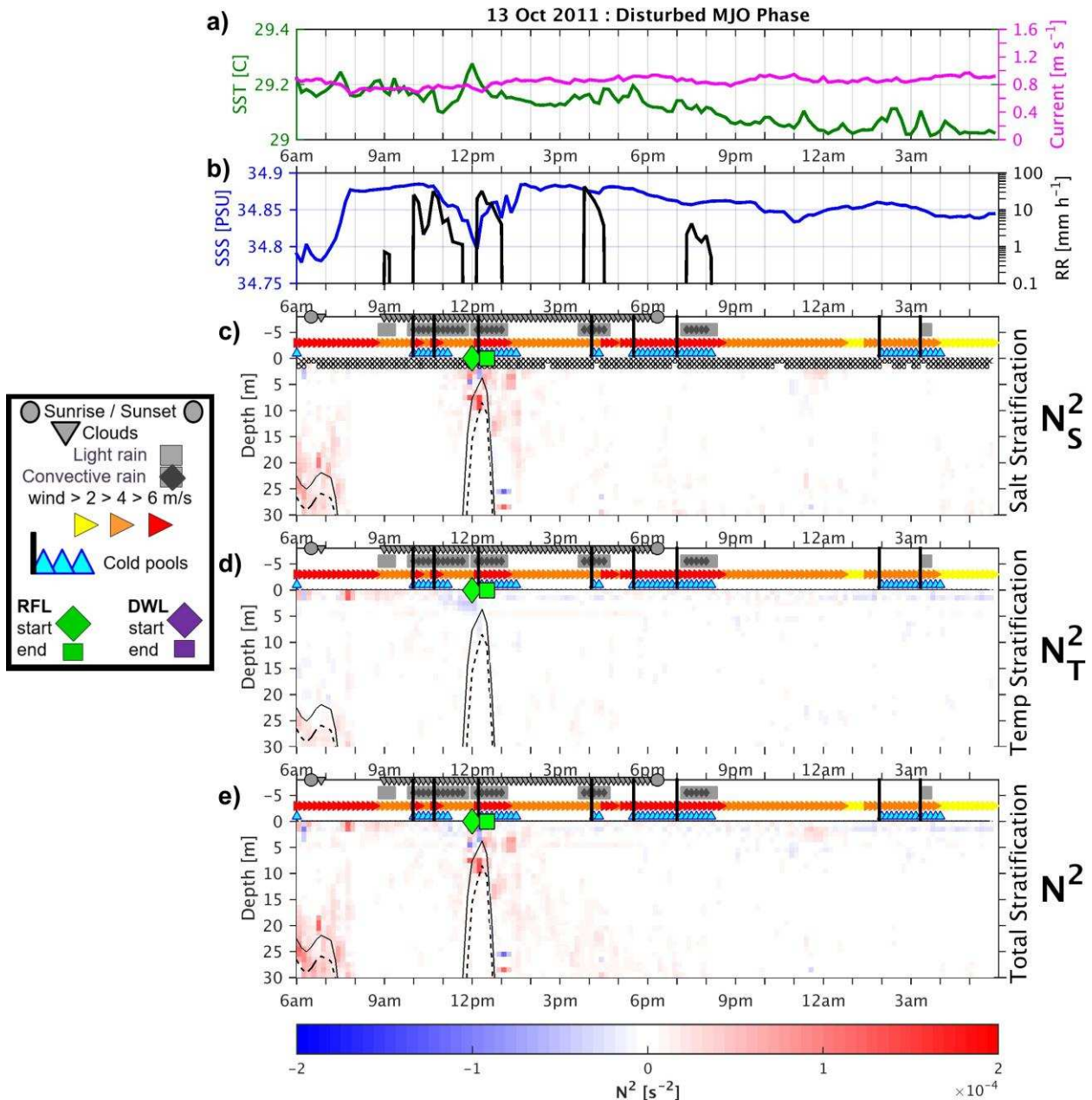
Figure 3.17: As in Fig. 5 for 13 Oct 2011, disturbed MJO central Indian Ocean daily time series.

Another disturbed phase RFL day occurred on 19 Oct (**Fig. 3.18**) from a large MCS that

stalled upstream of the ship and advected into the ships sensors hours later. This was the

strongest RFL in the DYNAMO database with a very strong corresponding rain cooling

signature. This signature dominated the total stratification signal in the upper 2 m in part because

there was no salinity data at the 0 and 1 meter levels. The abrupt changes in SSS and SST at the
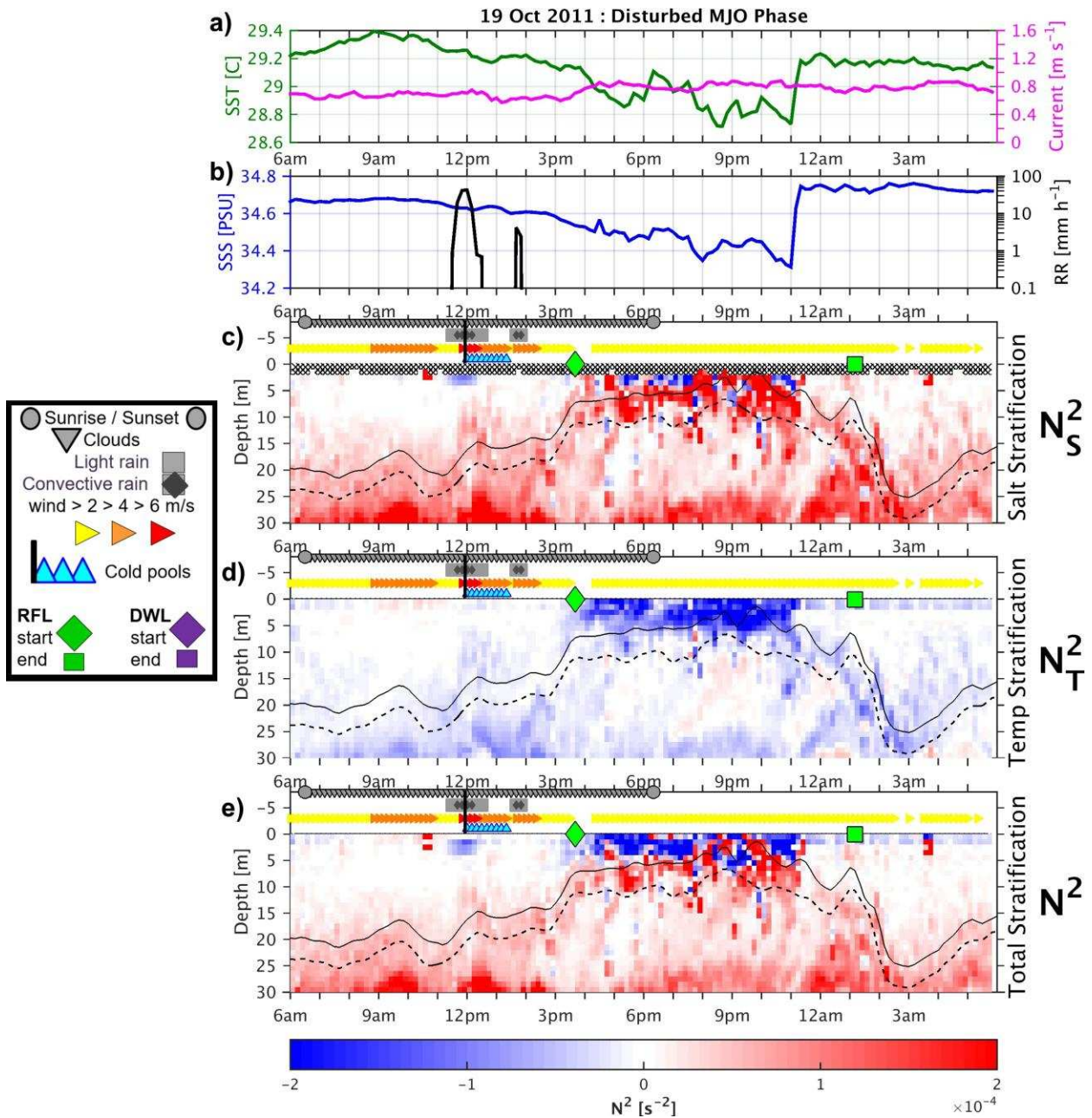
Figure 3.18: As in Fig. 5 for 19 Oct 2011, disturbed MJO central Indian Ocean daily time series.

end of the RFL event signal the role of advection or propagation in ending this event locally at the ship. These and other previous examples highlight the importance of contextual rain information, such as from radar or satellite, since local rain data are not sufficient for understanding upper ocean salinity stratification evolution.

Aside from these 2 disturbed MJO examples, 2 other daytime RFL days without DWLs or heating occurred in the active MJO phase and 3 more during WWB with widespread clouds and rain despite strong winds. For instance, the November barrier layer was finally broken on 24 Nov (**Fig. 3.19**) after several storms had mixed salinity stratification into it. Rain events had actually shoaled the mixed layer depth due to salinity stratification earlier that day and on the previous day, which mixed down to the barrier layer each time when overwhelmed by wind mixing. Intense cold pools and very strong winds overcame rain forcing at 3 pm, at which time the mixed layer deepened towards the thermocline for the next two days. Upon mixing the warm, salty barrier layer water upwards, both the SSS and SST initially increased before latent and entrainment cooling drove SSTs downwards (Moum et al. 2014). According to **Fig. 3.3** and **3.4**, this first WWB pulse lasted two days with strong rain and winds but salinity stratification events. Then low level winds reduced below 4 m s^{-1} and no rain occurred for almost one day on Nov 27. Overnight, the second WWB pulse began. **Fig. 3.20** (28 Nov) shows rain stratifying the upper ocean briefly during the second WWB despite strong winds above 6 m s^{-1}, current > 1 m s^{-1} and several long lasting cold pools. Strong salinity gradients shoaled the mixed layer briefly to just 25 m from 4-6 PM following a heavy rain period, but then quickly mixed downwards to the thermocline once again.

Salinity stratification without DWL influence occurred in the disturbed (8 events), active (5 events), and WWB (5 events) phases of the MJO. These events occurred from all types of storms. While these rain freshening layers do not typically last long, and are not coincident with warming net heat flux into the ocean, they do suppress upper ocean mixing and entrainment cooling for some amount of time and have impacts on when and where rainfall is mixed downward into the column. Therefore, these rain formed mixed layers and the stable density

132

gradients at their base are important for the momentum and freshwater budgets of the upper

ocean. They can also be responsible for rapid SST cooling.
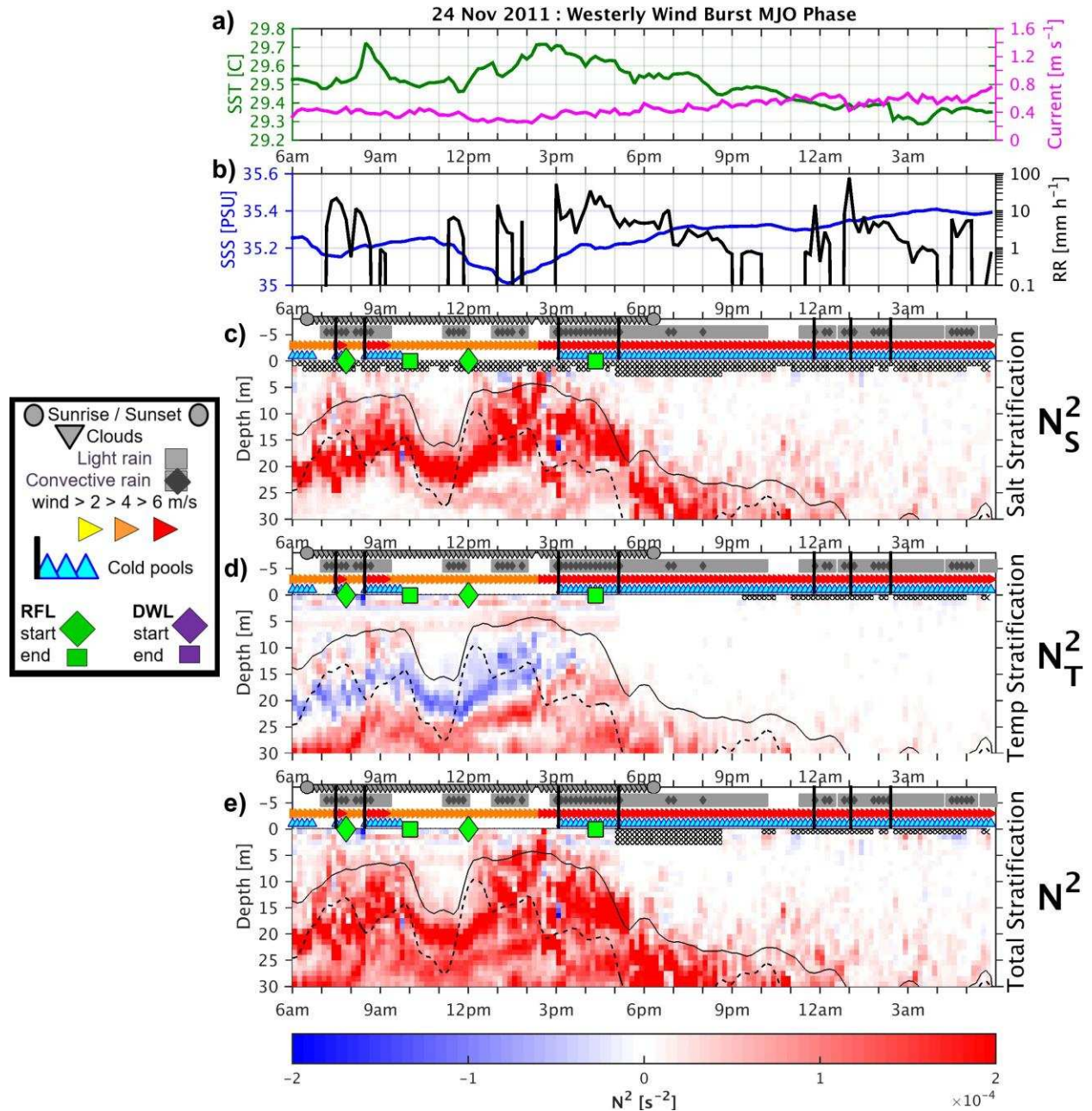
Figure 3.19: As in Fig. 5 for 24 Nov 2011, westerly wind burst MJO central Indian Ocean daily time series.
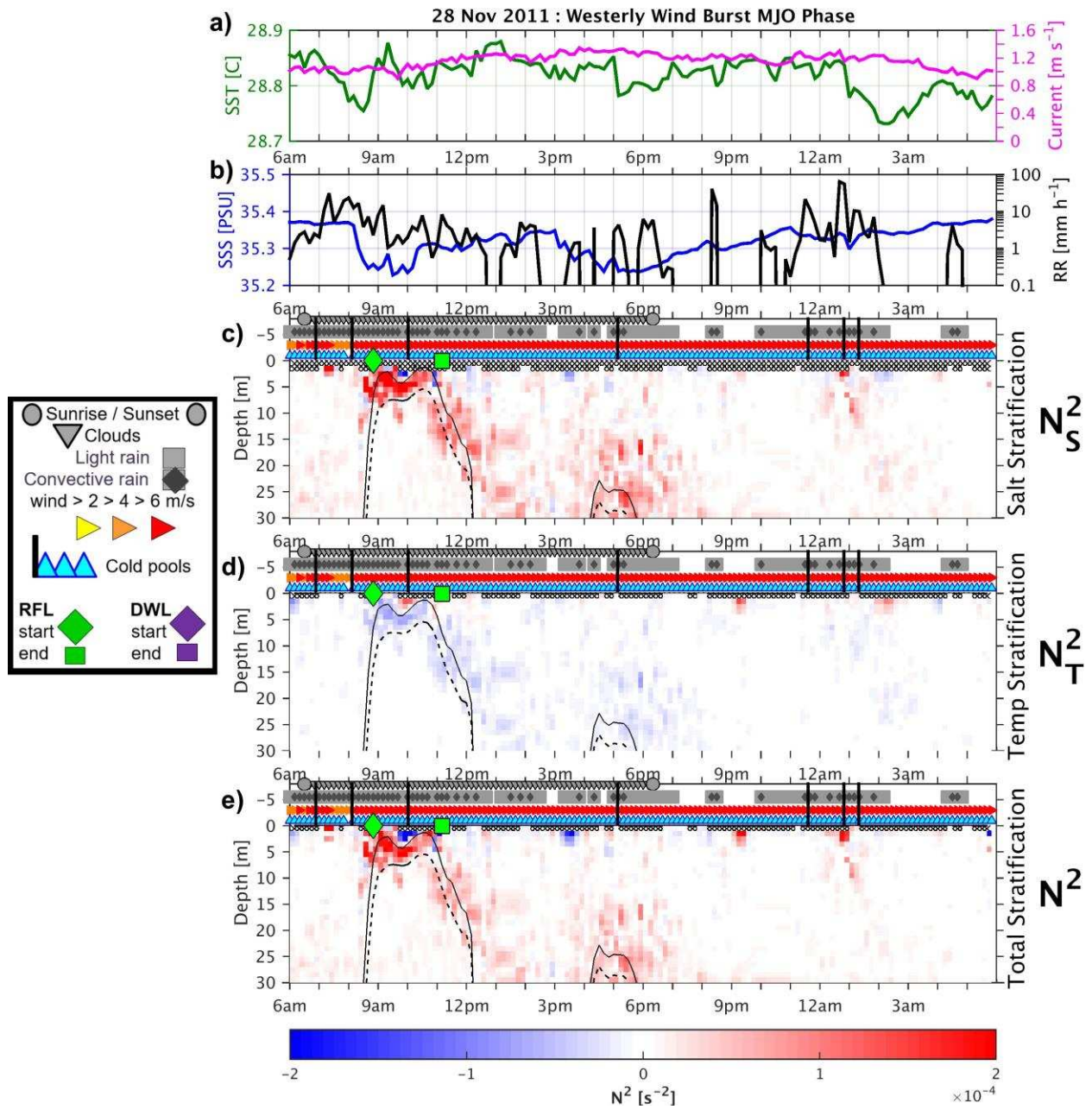
Figure 3.20: As in Fig. 5 for 28 Nov 2011, suppressed MJO central Indian Ocean daily time series.

3.4.7 No RFLs or DWLs

There were four days, 3 during the two November WWB pulses and 1 following the second pulse, when no mixed layer stratification was observed at all. The ocean was completely mixed by strong intraseasonal winds > 6 m s^{-1} and current speed greater than 1 m s^{-1} on these days. Copious amounts of rain immediately mixed downwards on 2 of the four days. The other two days were cloudy without any rain, but zonal winds and current were elevated enough that no temperature stratification or advected RFLs occurred. During these days, the mixed layer was equal to the thermocline and the thermocline stability eroded downward, entraining salty, cool water upwards. **Figures 3.3-3.4** shows how the prolonged, multi-day, deep mixing events during the stronger November WWBs depressed the thermocline depth. In contrast, short-lived deep mixing in October did not change the thermocline depth or enable as much entrainment cooling from below.

3.5 Bulk Characteristics of DWLs and RFLs

3.5.1 Stability

Table 3.5 and **Figure 3.21** summarize the bulk characteristics of all DWLs and RFLs, including the representative examples shown in Section 4. DWLs have mean N_T^2 of 1.33 x 10^{-4} s^{-2} and maximum N_T^2 of 4.86 x 10^{-4} s^{-2}. The mean N_S^2 in DWLs have an order of magnitude lower N_S^2, but since DWLs can catch weak RFLs inside the strong temperature stratification when storms are not windy enough to mix the stable layer away, DWLs can have N_S^2 as high as 3.5 x 10^{-4} s^{-2}, which is nearly as high as the maximum N_T^2 in DWLs. The mean total N^2 in DWLs is 1.6 x 10^{-4} s^{-2} and can be as high as 5.1 x 10^{-4} s^{-2}. The total stratification in RFL can exceed that of DWLs. maximum value of 8.3 x 10^{-4} s^{-2}, but the mean RFL N^2 is lower, 1.05 x 10^{-4} s^{-2}. In contrast, RFLs

can exhibit much higher N_S^2, up to 1.01×10^{-3} s^{-2}, with a mean of 9.77×10^{-5} s^{-2}. The N_T^2 in

RFLs can be strongly negative due to rain and latent cooling, as low as -2.9×10^{-4} s^{-2}, 5th

percentile values of -1.39×10^{-4} s^{-2}, and with a mean N_T^2 of 3.17×10^{-5} s^{-2}, which is slightly

stable with respect to temperature. These distributions show that RFLs can be as stable, if not

more stable, as DWLs despite the small magnitude, negative rain and latent cooling effect of

rain.

3.5.2 *Duration / Dimension*

The minimum duration of DWLs and RFLs is 30 min because of how these events were

classified. Both types of near surface stable layers can last up to about 22 hours long. This local

duration converts to a linear dimension of at least 40 km considering the local current speed at

the time of each stable layer and assuming a circular aspect ratio. However, since many RFLs are

short duration, the mean DWL duration (9.3 hr) is longer than the mean RFL duration (5.9 hr, 11

km wide). However, these are just approximate local duration and equivalent dimensions.

Bellenger and Duvel (2009) showed that DWLs can actually span areas as large as 1000s of km

due to the uniform atmospheric forcing on the ocean which produces them. RFLs are created by

precipitating systems, which have spatial and temporal scales commensurate with the inferred

RFL dimensions and local RFL durations reported in **Fig. 3.21** and **Table 3.5**. A linear system

moving through a region over a great distance could leave behind a freshwater footprint much

greater than the dimension of the system itself. However, puddles propagate laterally and

become dissipated and mixed vertically, so we do not expect precipitating systems to leave

behind mirror-image freshwater lenses below.

136
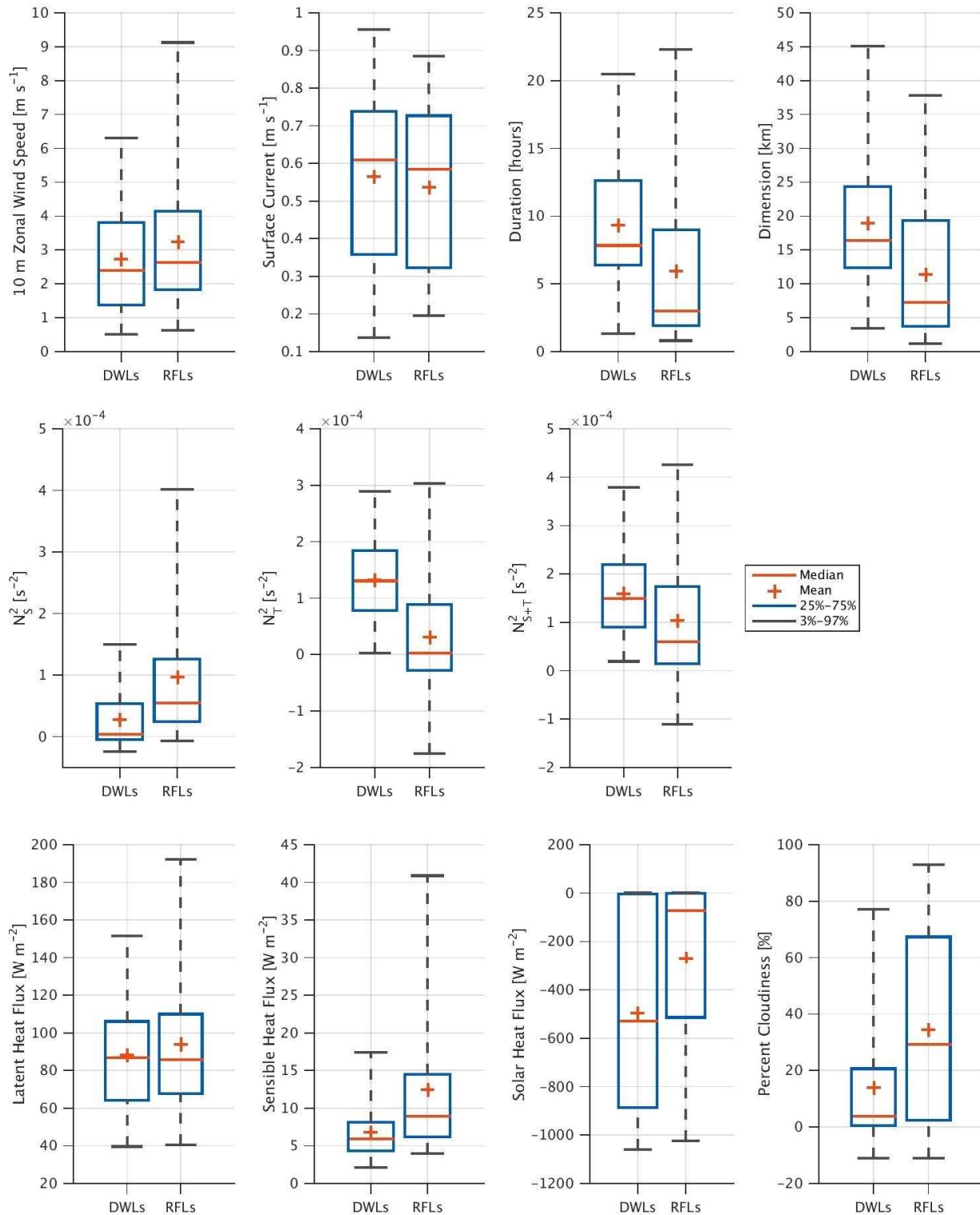
Figure 3.21: Box and whisker plots of 10 m zonal wind speed, surface zonal current, stable layer duration, inferred dimension given the local current speed, N_S^2, N_T^2, N_{S+T}^2, latent heat flux, sensible heat flux, solar heat flux, and percent cloudiness conditions experienced during 30 diurnal warming-formed mixed layers (DWL) and 38 rain-formed mixed layers (RFL).

Table 3.5: Central Indian Ocean Oct-Nov 2011 mean N_S^2, N_T^2, total N^2, duration, estimated size, current speed, zonal 10 m wind speed, latent heat flux, sensible heat flux, and downwelling short wave radiation (negative heating the ocean) during temperature stratification (diurnal warm layers) and salinity stratification (rain freshening layers).

```
---------------- TEMP STRATIFICATION ---------------
            NS²         NT²          N²    duration   size   clouds  current    U10m      LHF      SHF        SW
     [kg m⁻²s⁻¹] [kg m⁻²s⁻¹] [kg m⁻²s⁻¹]      [hr]   [km]      [%]  [m s⁻¹] [m s⁻¹]  [W m⁻²]  [W m⁻²]   [W m⁻²]
   min -1.39e-04  -1.60e-04  -1.70e-04      0.50    2.57  -114.73     0.03    0.14    27.24     0.32  -1223.25
    5% -1.63e-05   1.61e-05   2.84e-05      2.19    4.51    -7.92     0.17    0.60    43.91     2.50  -1040.55
  mean  2.81e-05   1.33e-04   1.59e-04      9.33   18.99    14.16     0.57    2.73    88.33     6.88   -495.82
median  4.22e-06   1.31e-04   1.49e-04      7.83   16.37     3.77     0.61    2.39    86.75     5.93   -528.87
   95%  1.33e-04   2.63e-04   3.27e-04     17.95   44.23    67.55     0.90    5.94   142.56    14.37      0.92
   max  3.50e-04   4.86e-04   5.10e-04     22.83   45.26    96.66     1.49    9.24   203.80    38.83      2.75


---------------- SALT STRATIFICATION ---------------
            NS²         NT²          N²    duration   size   clouds  current    U10m      LHF      SHF        SW
     [kg m⁻²s⁻¹] [kg m⁻²s⁻¹] [kg m⁻²s⁻¹]      [hr]   [km]      [%]  [m s⁻¹] [m s⁻¹]  [W m⁻²]  [W m⁻²]   [W m⁻²]
   min -1.14e-04  -2.92e-04  -2.77e-04      0.50    0.86   -37.61     0.08    0.15    31.05     2.18  -1223.25
    5% -9.79e-07  -1.39e-04  -7.67e-05      1.00    1.51    -7.41     0.21    0.82    45.80     4.22   -988.51
  mean  9.77e-05   3.17e-05   1.05e-04      5.97   11.49    34.56     0.54    3.25    94.05    12.48   -269.40
median  5.44e-05   2.34e-06   5.98e-05      3.00    7.29    29.16     0.58    2.64    85.75     8.93    -72.89
   95%  3.10e-04   2.66e-04   3.88e-04     20.71   32.08    88.19     0.85    8.09   173.32    35.23      0.40
   max  1.01e-03   4.76e-04   8.29e-04     22.50   44.40    99.14     1.17   14.16   288.80    68.61      2.75
```

3.5.3 *Wind, current, and cloudiness*

According to current, wind, and net heat flux data collected at 10 min intervals within 38 RFLs (220 hours) and 30 DWLs (308 hours), RFLs can be sustained at higher winds, higher current, cloudier conditions (~percentage of modeled clear sky solar radiation) with less solar radiation, greater latent cooling, and greater sensible cooling of the ocean. In **Table 3.5**, LHF and SHF are positive when cooling the ocean and warming the atmosphere. The downwelling solar heat flux is negative when directed downward and warming the ocean. Downwelling solar radiation during DWLs is between 0 (i.e. extending into nighttime) and -1040 W m^{-2}, with a mean of -495 W m^{-2}. In comparison, mean solar forcing is only -269 W m^{-2} in RFLs, and the median value is only -72 W m^{-2}. These weak solar forcing characteristics associated with RFLs account for the fact that 14 out of 43 observation days show RFLs occurring at night and other RFLs can form in varying combinations of cloudiness during precipitation to sunny conditions afterwards. Sensible and latent cooling are stronger during RFL than DWLs, which is understandable from wind speeds being higher in RFLs. Therefore, RFLs can provide at least as much latent and sensible heat flux moistening and warming to the atmosphere from the ocean during each type of upper ocean stable layer.

Wind speeds are mostly between 0.6 – 5.9 m s^{-1} in DWLs (5th and 95th percentile values), with minima and maxima of 0.14 m s^{-1} and 9.24 m s^{-1}. The mean and median near surface wind speeds are 2.7 and 2.4 m s^{-1} in DWLs. RFLs exist during higher wind speeds at all percentile, mean, median, minima, and maxima values. The mean wind speed in RFLs is 3.25 m s^{-1}, while the 95th and maximum values reach 8 m s^{-1} and 14 m s^{-1}. The higher N^2 values in some RFL compared to DWLs suggest that RFLs can be more stable and withstand higher wind speeds than DWLs. The near surface zonal current is mostly driven by and in the same direction as the zonal

mean wind at this equatorial, location. The percentile, mean, median, and minimum current values are within about 0.05 m s^{-1} for temperature and salt stratification layers, within one standard deviation of the current (0.6 m s^{-1}). The ideal current speeds conducive for DWL and RFL formation and maintenance appear to be within 0.2 – 0.9 m s^{-1}, with maximal values reaching 1.2 – 1.5 m s^{-1} for the few RFLs and DWLs observed during WWBs.

3.5.4 Cold pool interactions

Table 3.6 shows the fraction of each day experiencing a cold pool or rain event at the *Revelle* as well as the average number of these events per day during each MJO phase.

Table 3.6: Central Indian Ocean Oct-Nov 2011 percentage of each day, number of events per day, and days without either atmosphere cold pools or rain events as a function of MJO phase.

MJO PHASE	TOTAL DAYS	% of day with cold pool	cold pools per day	days w/o cold pools	% of day with rain	rain events per day	days w/o rain events
SUPPRESSED	13	5	1	3	3	1	4
DIST	13	25	3	0	16	2	0
ACTIVE	10	27	3	1	22	2	3
WWB	6	54	6	0	52	1	1

The percentage of each day experiencing cold pools increases dramatically from the suppressed phase (7% of the day, with many days experiencing no cold pools at all) to the disturbed phase, when cold pools can affect the local area 25% of the day, similar to results by Rowe and Houze (2015). In the active phase, this percentage increases to 31% of each day, and then to 41% of the day during the WWB phase, with some days experiencing cold pools all day. The average number of cold pools per day also increases from 2 cold pools per day in suppressed and disturbed phases, to 3 per day in active MJO conditions, and then 6 per day during WWBs. Some storms can produce multiple cold pools throughout their lifetime, so the average number of storms per day only changes from 1 in the suppressed phase, to 2 per day in the disturbed and active phase. On average, only 1 storm per day occurs in the WWB phase when raining

conditions at the ship sometimes persist for over one day. The average percentage of each day experiencing rain locally is very low in the suppressed phase when many days are entirely rain free. Then the percentage of time raining per day jumps to 17% in the disturbed phase, 20% in the active phase, and 50% in the WWB phase.

Given the statistics in **Table 3.6, Table 3.7** highlights the DWL and RFL interactions with cold pools**.** Of the 38 RFLs observed during DYNAMO, only 15 occurred without a cold pool while the other 22 stabilized the upper ocean despite the elevated winds, gustiness, and surface cooling associated with cold pools. About one third of RFLs start when cold pools are present, and therefore have enough rain freshening buoyancy forcing to withstand mechanical mixing and cooling effects. Sixteen RFLs ended with cold pool onset, 10 of which mixed away to an intermediate depth stable layer below and 6 of which mixed deeper to the thermocline. Three RFLs mixed deeper towards the thermocline and 3 to lower stable layers *without* any cold pool modification.

Table 3.7: Central Indian Ocean Oct-Nov 2011 diurnal warm layer and rain freshening layer interactions with cold pools and each other.

	Count [#]	Percentage of Category [%]
DWLs	30	---
DWLs without cold pools	13	43
DWLs with cold pools but no effect	0	0
DWLs with cold pool modification	19	63
DWLs starts with cold pool	0	3
DWLs ends with cold pool onset	12	40
DWLs eventually ends during cold pool	7	23
DWLs end without cold pool with rain effect	5	17
DWLs end without cold pool or rain effect	8	27
DWLs with BL interaction	6	20
DWLs without RFL interaction	15	50
DWLs with RFL interaction	19	63

```
--------------------------------------------------------------------------
                                      RFLs          38              ---

                  RFLs without cold pools           16              39
           RFLs with cold pools but no effect        0               0
             RFLs with cold pool modification       22              58
--------------------------------------------------------------------------
                  RFLs start with cold pool         13              34
             RFLs mixed away with cold pools         6              16
          RFLs mixed away without cold pools         3               8
    RFLs mixed to stable layer with cold pools      10              26
RFLs mixed to stable layer without cold pools        4               8
--------------------------------------------------------------------------
                   RFL no DWL interaction           13              34
          RFL at night no DWL interaction            5              13
            RFL daytime no DWL interaction           8              21
--------------------------------------------------------------------------
```

While many RFLs can form during and withstand cold pools, cold pools always end DWLs when both phenomena are present. All 19 DWLs (63% of all DWLs) that experienced a cold pool were either immediately deepened (12 DWLs) or ended within 1-2 hours (7 DWLs). No DWLs began with cold pools, but often formed once winds slackened and cold pools ended. Five diurnal warm layers ended without cold pools but with RFL modification (17% of all DWLs). Eight DWLs, or 27% of all DWLS, ended without cold pools or rain events due to natural causes such as momentum accumulation in the DWL causing shear instability or radiational cooling initiating convective mixing. Eleven out of 30 (47%) of DWLs observed during DYNAMO did not experience any cold pools. Six of these events accounted for the only 6 days of the experiment when no cold pools were observed at all at the *Revelle*.

3.5.5 *Daily mixed layer shoaling, deepening, and maximum SST*

The average shoaling time of the mixed layer is 3-4 UTC, or 9-10 AM LST. Days when DWLs formed on top of barrier layers can shoal earlier (as early as dawn ~ 6:30 AM) because the ocean is already stratified at an intermediate depth of 10-15 m or shallower. The enhanced upper ocean stability on days when diurnal warm layers formed on top of, or merged with, the barrier layer also dictated that the deepening time was later in the day, as late as 22 UTC, 4 AM,

with a mean of 16 UTC, or 10 PM. In comparison, most DWLs without barrier layer or RFL

influence deepened at 14 UTC, 8 PM, with the 75th percentile of deepening hour of 17 UTC, 11

PM. Heated RFL days tended to shoal latest (mean of 4:30 UTC, 10:30 AM) and deepen earliest

(mean of 12 UTC, 6 PM).

To summarize, DWLs interacting with the barrier layer last the longest, on average 13

hours, normal DWLs without RFL or barrier layer interaction last around 11 hours in the mean

sense, and DWLs that form on top of RFLs only last 7 hours, on average. We hypothesize that

the DWLs formed inside of RFLs are slow to form and faster to subside because of the more

active atmospheric conditions present on days where RFLs are more active and since the DWLs

have to overcome the effects of rain and wind cooling. DWLs that catch RFLs have very similar

shoaling times, deepening times, and durations as DWLs without RFL interaction. The time of

maximum SST varies between 6-8 UTC, Noon-2 PM, for all cases depending on atmospheric

conditions such as clouds and wind and also the underlying ocean stratification. SST warming

and maximum SST often occurred during a lull in the wind when clouds gave way to sunny

skies, which highlights the responsiveness of the ocean to mesoscale atmospheric activity on the

order of hours.

3.5.6   RFL decay processes

Of the 38 shallow rain-formed mixed layers, only 9 mixed, propagated, or advected away

completely, about half of these incidents coincident with cold pools. Five of these RFLs that

mixed away occurred during the day and the other four at night, meaning there was no

preference for RFL mixing extent based on the net heat flux. RFL decay seemed more dependent

on upper ocean stratification structure below the RFL and wind (i.e. ocean mixing). 6 nighttime

RFLs and 9 daytime RFLs mixed to a stable layer, meaning that some of the RFL salinity

stratification accumulated into the intermediate depth stable layer although some was likely eroded in the downward mixing process. Of the 10 RFLs that added to DWLs without breaking them, two outlasted the original DWL and mixed away to either the stable layer or deeper as previously described. 3 nighttime RFLs lasted through the night and grew DWLs on the ocean surface. 4 early morning RFLs also turned into DWLs that day.

3.6 Storms that stratify or deepen the ocean mixed layer

The examples in Section 4 showed that rain events were capable of stratifying the upper ocean depending on the preexisting stratification of the ocean as well as accompanying wind and rain amount. In general, storms were more likely to stratify when they produced more rainfall accumulation at lower wind speeds and when the ocean was calmer with respect to turbulence and current speed. **Fig. 3.22a** compares the distribution of each rain event's total rainfall accumulation sensed at the *Revelle* against the distribution of 10 m zonal wind speed values experienced during the entire storm. Note: this is a 2D histogram, not a line plot, so wind speed and rain rate are not correlated or connected. *Quartile ranges for all storms that stratify the upper ocean or not reveal that storms that stratify the upper ocean usually have local rain accumulations greater than 10 mm and wind speeds lower than 8 m s^{-1}*. However, there is no local rain rate or rain accumulation minimum threshold that determines whether a storm will shoal the mixed layer or not. Six out of 38 salinity stratification events were caused by storms 5-10 km upstream of the ship when the freshwater stable gradients advected into the domain without any local rainfall. Many other local rain events produced local rain traces but also produced upstream precipitation accumulation that appeared important for RFL formation. In general, more widespread storms, particularly upstream of the ship, tended to be more successful

144
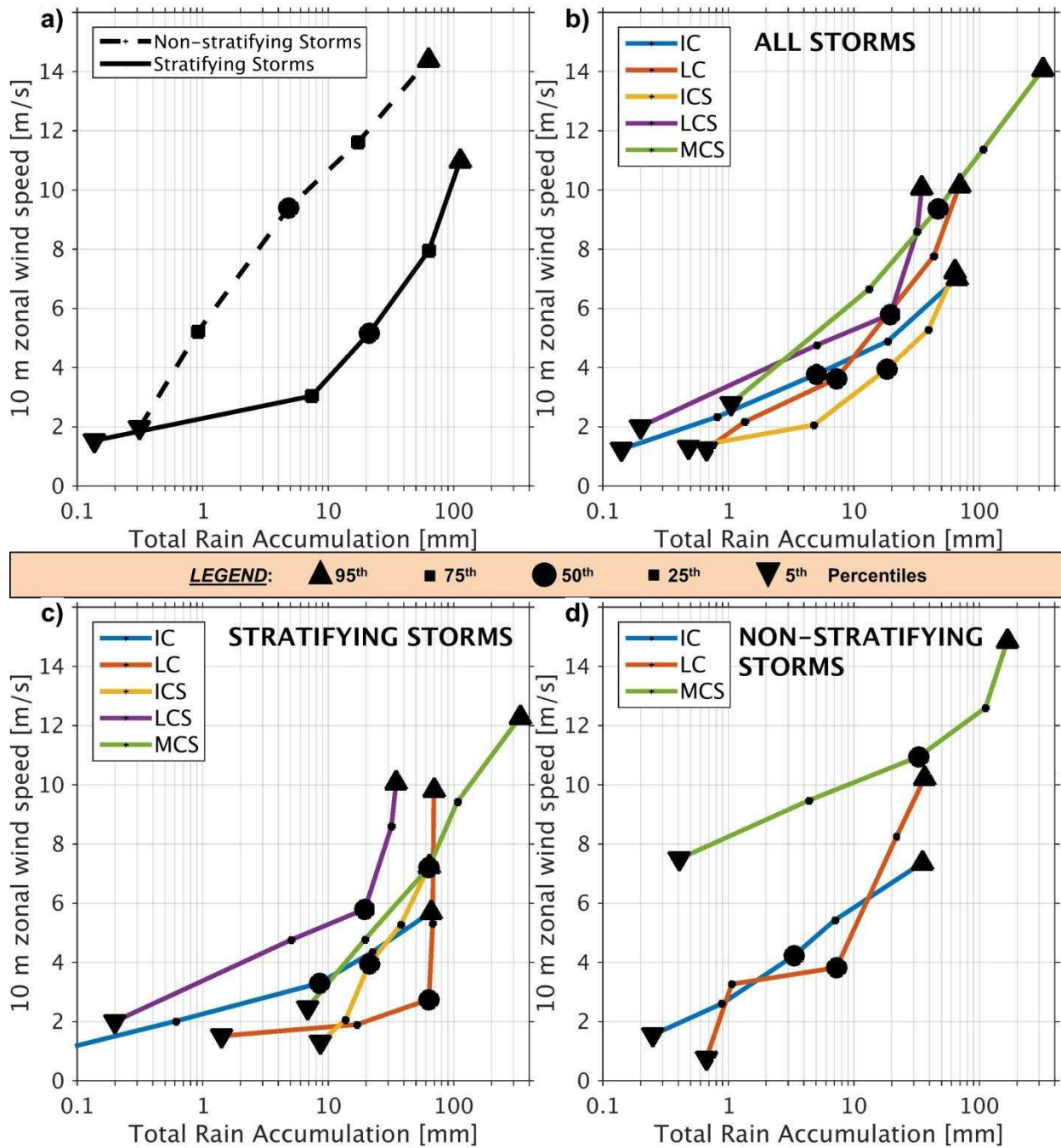
Figure 3.22: 5th, 25th, 50th (median), 75th, and 95th percentiles of central Indian Ocean precipitating system total event local rainfall accumulation and instantaneous 10 m zonal wind speeds during (a) all stratifying and non-stratifying storms; (b) all storms based on radar-indicated storm type: isolated non-linear (IC) and linear (LC) convection, sub-mesoscale non-linear (ICS) and linear (LCS) convective systems with stratiform rain, and mesoscale convective systems (MCSs); (c) stratifying storms by storm type; and (d) non-stratifying storms by storm type.

at stratifying the upper ocean. Similarly, there was no single wind speed threshold that could predict whether a storm would be too windy to shoal the mixed layer or strong enough to deepen the mixed layer. For every rain accumulation quartile range, the winds were higher for storms that did not stratify. Their kinetic energy available to mix the upper ocean exceeded the potential freshening buoyancy flux available stabilize the upper ocean. Almost 75% of storms that did not stratify had winds above 6 m s^{-1}, but some stratifying storms that produced more rainfall, i.e. greater than 10 mm locally, could withstand winds of this magnitude or higher.

Fig. 3.22b shows the distributions of wind speed and total rainfall accumulation for each type of storm morphology (Lemone et al. 1998, Xu and Rutledge 2015). Storms with rainfall accumulations over 30-40 mm appear capable of producing stable rain-formed mixed layers that can withstand wind speeds > 8 m s^{-1}. **Figs. 3.22c** and **3.22d** break up the data from **3.22b** into stratifying and nonstratifying storm types. While the bounds of rainfall accumulation and wind overlap for storms that do or do not stratify, IC, LC, and MCSs that do not stratify tend to have higher winds for a given rainfall range and lower rainfall for a given wind speed range than those that shoal the mixed layer. For instance, the median MCS rainfall and wind of stratifying storms was 50 mm and 7 m s^{-1}, while the median values for nonstratifying storms are 20 mm and 11 m s^{-1}. Similar, but also overlapping trends exist between stratifying or non-stratifying LC and IC storms. All LCS and ICS storms observed at the *Revelle* stratified the mixed layer with respect to salinity. Mean total rainfall accumulation and wind speeds during for these storms were 10 mm and 4-6 m s^{-1}.

A sea surface freshening event usually preceded salinity stratification events, ranging from 0 to -1.3 PSU freshening or -0.6 PSU hr^{-1} freshening rates similar to values reported by Boutin et al. (2013) and Reverdin et al. (2012). However, storms did not always produce a

measurable SSS change depending on wind, advection, ocean mixed layer depth, and the fact that SSS in this study is a measure of water mixed between 0-3 m. High resolution salinity observations in the upper 2 meters could reveal more conclusive trends about surface freshening rates of storms that stratify versus those that do not. Observed freshening rates were higher magnitude inside RFLs or DWLs because the incoming freshwater was concentrated inside a shallower layer. In this way, rain freshening layers can add to each other or maintain each other when several storms train over the same area and wind speeds remain sufficiently weak. This often occurred when storms were becoming more frequent and widespread, i.e. during the disturbed and active MJO phases before strong WWB winds > 6 m/s. Since some storms can stratify from a well-mixed ocean state while others simply add to preexisting stratification or shoal the mixed layer further from some intermediate depth, the freshening rates and freshening events preceding stratification events and non-stratification events are overlapping. There is no minimum freshening rate required to produce salinity stratification because not all stratifying storms produce a freshening trend.

Table 3.8 summarizes analysis of all 68 local precipitation events observed at the *Revelle* and whether they were able to stratify the upper ocean or not. Unlike **Fig. 3.22,** this table also takes the preexisting ocean stability structure into account. Fifty-four percent of all storms (37 rain events) observed at the *Revelle* during DYNAMO stratified the upper ocean mixed layer ≤ 5 m for some period of time while 46% of storms (31 storms) either had no effect (19 storms) or deepened the ocean mixed layer (12 storms). The most common way storms stratified the upper ocean was by falling into a pre-existing, active DWL, or over a 5-15 m depth barrier layer stable with respect to both salinity and temperature. The freshwater flux can then become concentrated in a thin layer and lead to salinity stratification.

Table 3.8: Central Indian Ocean Oct-Nov 2011 counts and percentages of all storm types and individual storm types to stratify or shoal the upper ocean mixed layer, cause no observable effect, or deepen the mixed layer from either a deep, well-mixed state or from a shallower stable layer between 0-20 m such as the barrier layer or active/decaying/depressed DWLs/ RFLs.

```
--------------------------------------------------------------------------------
--------------RFL FORMATION PROCESSES BY STORM TYPE ------------------------
--------------------------------------------------------------------------------
          All Storm Types
     All Events (68 Total)        Stratifies ML   No ML Effect   Deepens ML
            Total Count    [#]          37             20            11
            Total Percentage [%]        54             29            16
   rain over stable layer   [#]         25              6            11
     rain over MLD > 20 m   [#]         12             14            --
--------------------------------------------------------------------------------
        Isolated Convection
      IC Events (32 Total)        Stratifies ML   No ML Effect   Deepens ML
            Total Count    [#]          12             13             7
            Total Percentage [%]        38             41            22
   rain over stable layer   [#]         10              5             7
     rain over MLD > 20 m   [#]          2              8
--------------------------------------------------------------------------------
         Linear Convection
      LC Events (9 Total)         Stratifies ML   No ML Effect   Deepens ML
            Total Count    [#]           4              3             2
            Total Percentage [%]        44             33            22
   rain over stable layer   [#]          3              1             2
     rain over MLD > 20 m   [#]          1              2            --
--------------------------------------------------------------------------------
   Non-Linear Convection + Stratiform
     ICS Events (8 Total)         Stratifies ML   No ML Effect   Deepens ML
            Total Count    [#]           8              0             0
            Total Percentage [%]       100              0             0
   rain over stable layer   [#]          6              0             0
     rain over MLD > 20 m   [#]          2              0            --
--------------------------------------------------------------------------------
     Linear Convection + Stratiform
     LCS Events (4 Total)         Stratifies ML   No ML Effect   Deepens ML
            Total Count    [#]           4              0             0
            Total Percentage [%]       100              0             0
   rain over stable layer   [#]          2              0             0
     rain over MLD > 20 m   [#]          2              0
--------------------------------------------------------------------------------
       Mesoscale Convective Systems
     MCS Events (12 Total)        Stratifies ML   No ML Effect   Deepens ML
            Total Count    [#]           8              2             2
            Total Percentage [%]        67             17            17
   rain over stable layer   [#]          3              0             2
     rain over MLD > 20 m   [#]          5              2
--------------------------------------------------------------------------------
       Detached Stratiform
      S Events (3 Total)          Stratifies ML   No ML Effect   Deepens ML
            Total Count    [#]           1              2             0
            Total Percentage [%]        33             67             0
   rain over stable layer   [#]          1              0             0
     rain over MLD > 20 m   [#]          0              2            --
--------------------------------------------------------------------------------
```

Excessive winds for a given rain amount tend to deepen or break the diurnal warm layer stratification (7 storms), and likewise for the barrier layer (2 storms). It was rare for a storm to cause no effect at all over the barrier layer (3 storms) or a DWL (2 storms). The next most common way for storms to stratify the upper ocean or shoal the mixed layer was by starting from a well-mixed ocean without any stratification features in the upper 20-30 m (9 events). Storms that stratified the upper ocean from a well-mixed state must supply enough rain accumulation to overcome preexisting ocean turbulence and any turbulence the storm might add. Fifteen other rain events occurred over a well-mixed ocean and had no effect on the upper ocean at all. These storms had various amounts of rainfall but apparently not enough to stratify the upper ocean. Six storms simply added to preexisting RFLs consecutively, while two storms ended a previous storm's RFL. Most storms that fell over a 5-10 m depth decaying, depressed, relic RFL or DWL restratified the upper ocean and shoaled the mixed layer back towards the surface (8 events total). Few storms passed over a decaying, depressed RFL and either broke the layer completely (1 rain event) or did nothing to ocean stability (1 rain event).

Table 3.8 also summarizes the stratification likelihoods and formation processes of storms based on their mesoscale organization. Thirty-two isolated convective events were observed over 190 total hours, but only 38% (12) of them stratified the upper ocean. In fact, 10 of these weak, small, isolated storms stratified the mixed layer inside or over an intermediate depth stable layer. Only 2 other IC events were able to stratify from a well-mixed, deep ocean state. Of the 20 other IC events that did not stratify, 3 did not stratify even though they fell into or were just above a stable layer, 8 occurred over a deep, well-mixed ocean state but did nothing, and 7 ICs fell into or over a preexisting stable layer but had more wind forcing than stabilizing rain forcing and thus mixed away the stable layer. To summarize, the relatively few ICs that did

149

stratify did so mostly when oceanic conditions allow the weak storm to maintain stratification or build upon it. Only 2/32 ICs are able to stratify the mixed layer from a well-mixed state. These results are important to consider because weak, small ICs are by far the most common storm type over tropical oceans and dominate the suppressed phase of the MJO (Rickenbach and Rutledge 1997, Johnson et al. 1999, Riley et al. 2011, Barnes and Houze 2013, Xu and Rutledge 2014, 15a,b).

Linear convective storms passed over the *Revelle* 9 times, totaling only 42 observation hours, and 44% (4 events) stratified the upper ocean. Three of these stratifying LCs were over a preexisting stable layer. One other LC had no effect over a stable layer and 2 other LCs deepened the preexisting stable layer. Only 1 LC stratified from well-mixed conditions, while 2 others had no observable effect on the upper ocean when the mixed layer was already deep.

According to Thompson et al. (2015), these small, usually weaker convective IC and LC events are composed of numerous small rain drops. Since freshwater penetration depth depends on rain drop size, wind, and potentially rain rate, it is possible that these small rain drop size distributions sit closer to the surface and are hard to detect by our first salinity measurements at 2-3 m (Katsaros and Buettner 1969, Soloviev and Lukas 2006). More detailed salinity measurements in the upper 0-2 m are needed to conclusively determine the effect of weak convection on the upper ocean.

All sub-mesoscale (< 150 km) linear (4) and quasi-circular (8) storms that produced some stratiform rain area stratified the upper ocean. ICS are more common than LCS. Two of each type of sub-MCS scale storms occurred over well-mixed ocean conditions and were still able to stratify the ocean mixed layer to the surface. Six other ICS and 2 other LCS events stabilized the upper ocean from preexisting stable layers in the upper ocean. **Fig 3.22c** shows that ICS and

150

LCS tend to have wind speeds less than 8 m s^{-1} most of the time, and have higher rain accumulation at each quartile range compared to IC and LC storms, which apparently are less probable to stratify the upper ocean. We hypothesize that the relatively weak winds associated with weakly organized ICS and LCS storms, but with more ample precipitation compared to IC and LC storms, allows ICS and LCS to stratify the ocean more often. The stratiform rain components of ICS and LCS storms produce a longer-lived, uniform, low rain rate freshwater forcing over the ocean surface. The weakly organized state of an ICS or LCS also dictates that these storms tend to stall or train over a particular region, which was often observed according to manual radar data analysis. These storms typically have very slow propagation speeds or even sometimes retrograde, going through multiple cycles of invigoration and decay before clearing the area. This allowed for more rain accumulation in one area without strong wind speeds, which would otherwise have fostered stronger storm propagation as well as upper ocean mixing.

Mesoscale (> 150 km) convective systems were often composed of leading or embedded linear convective structures in addition to some isolated convective bursts amidst large, long-lived stratiform rain regions. Of the 12 MCSs observed, 8 stratified the upper ocean, 3 of which occurred over preexisting stable layers and 5 from well-mixed deep ocean mixed layer states. Two other MCSs occurred over some intermediate stable or barrier layer but had enough wind mixing power to break through that stratification. Then two MCSs occurred over the well-mixed ocean but resulted in no salinity stratification since they generally had more wind but lower rain accumulation (see summarized statistics in **Fig. 3.22c and 3.22d**). It has been shown by many authors that MCSs are relatively rare compared to other storm types but consistently produce the majority of total rainfall over tropical warm pools in a climatological sense (Short et al. 1997, Rickenbach and Rutledge 1998, Cotton et al. 2011, Xu and Rutledge 2015, Houze 2014, Houze

et al. 2015). Although these storms produce the highest accumulated rainfall of any storm type according to this analysis, they also have the most cold pools, highest wind speeds, and therefore occur over stronger ocean currents because of their timing with respect to the MJO active phases (Houze 2000, Moum et al. 2014, **Fig 3.3**). The statistics in **Table 3.8** and **Figure 3.22** provide another example of the fact that a single rain accumulation or wind speed threshold does not determine whether a storm will mix the upper ocean due to wind or shoal the mixed layer to the surface by freshwater. The wind and rain accumulation bounds overlap for each storm type between stratifying and non-stratifying events, including MCSs that usually produce the most rain overall.

Three episodes of detached stratiform rain without any convection within 50 km occurred at the *Revelle*. These storms produced little to no rainfall, but one occurred over a shallow, depressed, decayed RFL and managed to shoal the mixed layer for about an hour. The other two events had no effect on the upper ocean, both taking place over a well-mixed deep mixed layer. These examples are a proof-of-concept that while the existence of stratiform rain components in ICS, LCS, and MCS storms appear to drastically enhance their ability to stratify the upper ocean over IC and LC events, the presence of stratiform rain alone is insufficient to shoal the ocean mixed layer. The rain accumulations in these very weak detached stratiform rain events are apparently not great enough to stabilize the upper ocean.

Why are ICS, LCS, and MCS storms more likely to stratify than IC or LC storms? The two IC events that stratified from a well-mixed state indeed produced more rain accumulation, lasted longer, and had weak winds compared to other nonstratifying ICs. The rest of the IC and LC events that stratified or shoaled the mixed layer appeared to depend on favorable preexisting ocean stability structure. In contrast, the existence of stratiform rain in a precipitation system

152

increased its likelihood to stratify, no matter the upper ocean stratification structure, current, or wind speed. For instance, 54% of all storms shoaled the ocean mixed layer or added stratification to it, while 22/24 (92%) of all ICS, LCS, and MCS type storms stratified the upper ocean.

Three hypotheses arise to explain why precipitating systems with stratiform rain are more likely to shoal the mixed layer: (1) Stratiform rain drop size distributions have lower number concentrations but larger mean drop sizes for a given rain rate than maritime convection according to analysis by Thompson et al. (2015, i.e. Chapter 2) and their review of related literature. These larger stratiform rain drops should be more capable of breaking the surface tension of the ocean and being incorporated deeper into the ocean column with which to affect salinity gradients and constitute stability (Katsaros and Buettner 1969, Soloviev and Lukas 2006).On the other hand, small, convective drops could aid in forming shallower, more concentrated fresh water lens near the surface because the small drops would not penetrate as deep or aid in mixing. However, these puddles would be short-lived with small dimensions according to the duration and size of IC or LC events. These convective puddles might be more susceptible to fresh water lens dissipation because they would be small. As previously discussed, small convective storms appear to provide more wind mixing than freshwater stabilization to the upper ocean, which often deepens the mixed layer. High resolution upper ocean salinity and temperature microstructure measurements extending to the surface with rain drop size distribution observations above are needed to test these hypotheses further. (2) Stratiform rain rates are lower, but cover a larger area and last much longer than convective cores. Stratiform rain's uniform, widespread forcing might produce larger, more uniform, more protected freshwater lenses that would be less susceptible to freshwater lens vertical and lateral dissipation, diffusion, propagation, and mixing effects (Soloviev and Lukas 2006). (3) Stratiform rain regions

of storms can have less gusty winds compared to convective regions except for short lived, embedded convective features and WWB time periods when the mean wind is very elevated even during stratiform rain (Houze 2000). In reality, all three hypotheses might be acting in concert to allow precipitating systems with stratiform rain regions to be more likely to shoal the mixed layer.

How can stratiform rain be so important if it is usually limited to, or below, 10 mm hr^{-1}? "Strong, convective, and heavy" rain events have been implicated in created fresh water lenses and salinity stratification in the oceanography literature (Wijesekera and Gregg 1996, Wijesekera et al. 2003, Soloviev and Lukas 2006, Boutin et al. 2013, Soloviev et al. 2015, Walesby et al. 2015). This makes sense because convective rain rates can range from 0.5 to 100+ mm hr^{-1}, potentially creating large local rain accumulations despite the fact that convective rain area and local rain duration are very small. In comparison, many studies have shown that stratiform rain is naturally limited to at or below 10 mm hr^{-1} (Tokay et al. 1999, Thompson et al. 2015, and references therein). **Fig. 3.23** show the equivalent surface buoyancy mass flux into the ocean by various rain rates accounting for evaporation, solar heating, and rain cooling, calculated according to Dorrestein (1979) in units of mass per unit area per unit time:

$$\text{Mb} = \text{SSS}\beta(P - E) - (\alpha/c_p)(\text{LHF} + \text{SHF} + \text{SWNET} + \text{LWNET}) + \alpha P\delta T \ [\text{kg m}^{-2}\text{ s}^{-1}]. \tag{8}$$

The first term can be thought of as the net effects of rain freshening and evaporation salinification. This is followed by the net heat flux term and the rain cooling term, which is the same as the sensible heat flux due to rain (Fairall et al. 1996), so is not included in the net heat flux term. SSS and SST are sea surface salinity and temperature (~35.06 PSU and 29.34°C means value for DYNAMO). Coefficients α and β are the thermal contraction and salt expansion coefficients (~ 3.3 x 10^{-4} °C^{-1} and 7.34 x 10^{-4} PSU^{-1}, respectively for these SSS and SST). The

154

specific heat of seawater (c_p) is about 4000 J kg^{-1} °C^{-1} for these mean SSS and SST. P and E are

precipitation and evaporation mass fluxes [kg m^{-2} s^{-1}], which are found by multiplying rates in

[mm hr^{-1}] by the density of pure water (1000 kg m^{-3}) and then dividing by 3600 [seconds per

min] x 1000 [mm per m]. Equation (8) proves that precipitation almost always increases

buoyancy since it dilutes seawater and rain cooling effects are usually of smaller magnitude than

freshening. Asher et al. (2014) reported that freshening-induced stable density gradients are more

likely when R > 6 mm hr^{-1} because the freshening effect is more likely to outweigh both storm-

aided mixing and rain cooling effects, which is consistent with **Fig. 3.23.** Evaporation makes the

surface denser because it leaves behind salt, but this is usually a small term. Heating creates a

positive net buoyancy flux, making the upper most ocean less dense than below, whereas surface

cooling can destabilize the column.
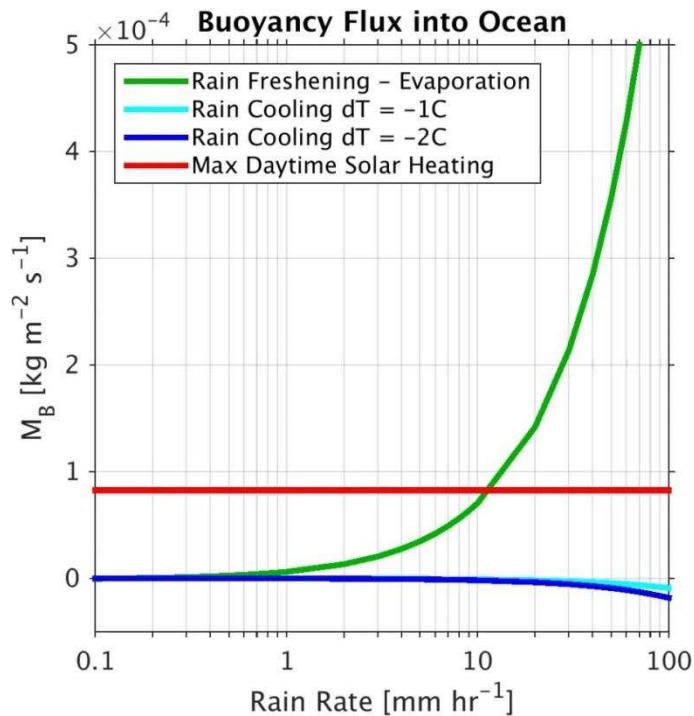
Figure 3.23: Surface buoyancy mass flux into the ocean from rain freshening – evaporation and rain cooling for either dSST = 1°C or dSST = 2°C as a function of rain rate as well as maximum daytime solar heating as a reference (1000 W m^{-2}).

Table 3.9 relates that maximum, daytime solar heat fluxes on the order of 1000 W m^{-2} can produce buoyancy fluxes on the order of 8.3E-5 kg m^{-2} s^{-1}, which are applied for a large part of the daytime hours in sunny conditions. This forcing is responsible for DWLs. In contrast, evaporation rates are on the order of 0.05 – 0.6 mm hr^{-1} and only produce weakly unstable buoyancy fluxes. Convective precipitation rates range from 0.1 mm hr^{-1} to over 100 mm hr^{-1} while stratiform rain rates are limited to or below 10 mm hr^{-1} (Thompson et al. 2015, Chapter 2). A precipitation rate of only 10 mm hr^{-1} is actually equivalent to that of maximum solar heating. When applied over a large area or over a long time period, as in an ICS, LCS, or MCS storm, the buoyancy forcing of stratiform rain can be comparable to daytime solar heating. This calculation explains why stratiform rain in convective systems is capable of stratifying the upper ocean so efficiently.

Table 3.9: Surface buoyancy mass flux into the ocean for typical values of maximum daytime downwelling short wave radiation, evaporation rates of salt gain, rain rates of salt loss, and rain cooling (i.e. sensible heat flux due to rain).

ATMOSPHERIC FORCING		Surface Buoyancy Mass Flux [kg m^{-2} s^{-1}]
Max Daytime Solar Heating:	1000 W m^{-2}	8.25x10^{-5}
Weak Evaporation:	0.05 mm hr^{-1}	3.57x10^{-7}
Moderate Evaporation:	0.15 mm hr^{-1}	1.07x10^{-6}
Strong Evaporation:	0.6 mm hr^{-1}	4.29x10^{-6}
Very light rain rate:	0.1 mm hr^{-1}	7.15x10^{-7}
Light rain rate:	2 mm hr^{-1}	1.43x10^{-5}
Max stratiform rain rate:	10 mm hr^{-1}	7.15x10^{-5}
Strong convective rain rate:	50 mm hr^{-1}	3.57x10^{-4}
Very Strong convective rain rate:	100 mm hr^{-1}	7.15x10^{-4}
Weak Rain Cooling at 10 mm hr^{-1}:	-0.05 °C	-1.18x10^{-9}
Strong Rain Cooling at 10 mm hr^{-1}:	-2 °C	-4.72x10^{-8}

These results explain why the observed increase in stratiform rain fraction and rain accumulation as a function of the MJO is accompanied by more frequent rain freshening layer stratification events. As stratiform rain contributions increase in the disturbed and active phases

of the MJO **(see Fig. 3.3)**, rain freshening layers also become more common **(Fig. 3.4** and **Table 3.4)**. Convective rain rates produce an order of magnitude more buoyancy flux, but do not last nearly as long – less than an hour usually – and cover small areas. A small, localized, but high accumulation rain puddle from a convective event without stratiform rain might be more susceptible to diffusion, propagation, mixing, and dissipative effects (Soloveiv and Lukas 2006). For instance, ubiquitous, weak, isolated connective rain events < 10 mm hr^{-1} appear to not usually have enough rain freshening buoyancy to overcome rain cooling and mixing effects.

3.7   Influence of DWLs and RFLs on the Intraseasonal SST Cycle

DWLs are obviously associated with heating and have been proven to contribute to the intraseasonal SST cycle as well as MJO storm activity (Duvel et al. 2004, Duvel and Vialard 2007, Shinoda 2005, Bellenger et al. 2010, Ruppert and Johnson 2015, and reviewed by Demott et al. 2014 and 2015). RFLs can only be important to the MJO if they last long enough to affect heating and turbulence suppression or can interact constructively with DWLs to amplify heating prior to the heavy rain period of the MJO. This section determines whether these requirements were met during the DYNAMO period.

3.7.1   Duration of stratification

However frequent RFLs are, as discussed in previous sections, the ability of a RFL to affect SST, SST cooling or warming rates, or turbulence suppression depends on its duration. Some salinity stratification events can last for several hours depending on wind conditions and rain accumulation (Miller 1976, Wijesekera et al. 1999, Boutin and Martin 2006, Honecq et al. 2010). Only 9 out of 37 RFLs heat to create new DWLs. These heated RFLs were linked to isolated convective events in the suppressed phase, LC, ICS, and MCSs in the disturbed phase,

as well as ICS and MCS storms in the active phase. These heated RFLs lasted the longest of any RFLs observed, between 2 – 23 hours, with the longest durations happening in the disturbed and active phases. Longer RFL durations during this time are due to the moderately sized footprints of ICS and MCS storms compared to less organized storms in the suppressed phases, as well as the added stability from diurnal warming happening inside the RFL. The DWLs associated with heated RFLs lasted between 6-9 hrs. Ten other RFLS got caught in DWLs. These were from IC storms in both the disturbed and active phase, while ICS and MCS storms also produced this interaction in the active phase. RFLs caught inside DWLs lasted between 2 – 13 hours and their DWLs lasted 6 – 18 hours, the longest of any disturbed phase DWLs observed. Together, these 19 combination DWL-RFL events had the potential to affect heating rates and foster high SSTs by concentrating incoming solar radiation into a thin layer. The other 18 RFLs during DYNAMO that did not endure heating due to cloud cover or nighttime occurrence still suppressed turbulent mixing inside and below the stable layer, which also affected cooling rates and freshwater storage. These RFLs were only between 1-3 hours long though, with one exception due to an advected RFL lasting over 6 hours (**Fig. 3.18: 19 Oct**). These RFL-only events occurred in disturbed, active, and WWB MJO conditions. The main conclusion of this subsection is that RFLs last much longer when they interact with DWLs. RFLs often last long enough to affect SST when they interact with DWLs. RFLs can strengthen DWLs instead of ending them, which promotes some long-lived DWLS although other DWLs without RFLs also last as long or longer.

3.7.2   SST warming rates

Simple physics guarantees that a thin mixed layer will heat up and cool down faster than a deeper mixed layer. In fact, **Fig. 3.24a** shows that hourly SST heating rates from the 10 minute

flux dataset from both DYNAMO months are highest when the mixed layer is above 4 m, particularly when both salinity and temperature stratification exist. When both kinds of stable layers exist at the same time, as in a heated rain freshening layer or when diurnal warm layers catch and concentrate salinity stratification from weak storms, heating rates can regularly be between 0.075 and $0.3°$ C hr^{-1}, sometimes exceeding $0.5°$ C hr^{-1}. In comparison, the intraseasonal mean daily SST anomaly between suppressed and westerly wind burst time periods is only about ±0.5 °C. Diurnal warm layers without RFL influence can also produce high magnitude dSST/dt heating trends (maximum of $0.68°$ C hr^{-1}, but only in the suppressed period). Rain freshening layers must combat rain cooling effects and mixing so have lower heating rates when not associated with DWLs in any way (97th percentile at $0.4°$ C hr^{-1}).

Warming rates are much lower (usually below $0.1°$ C hr^{-1}) for mixed layer depths between 5-10 m depth, and even lower for deeper mixed layers (less than $0.05°$ C hr^{-1} for times when the ocean mixes down to the thermocline). These deeper ocean mixed layer heating trends are commensurate with those from times when the upper 5 meters has no salinity or temperature stratification layer present, mostly below $0.07°$ C hr^{-1}. This result indicates that if a coupled numerical model or mixed layer parameterization cannot account for advected stable layers, DWL-RFL interactions, and DWL/RFL interactions with the barrier layer, the model will struggle to reproduce the proper mixed layer depth. Then the model would not be able to reproduce accurate SST heating rates since heating is controlled by mixed layer depth. SST cooling rates in **Fig. 3.24b** can be nearly the same magnitude as heating rates, but of opposite sign, and also exhibit higher magnitudes when mixed layer depth is shallower and stratified with respect to both salinity and temperature.
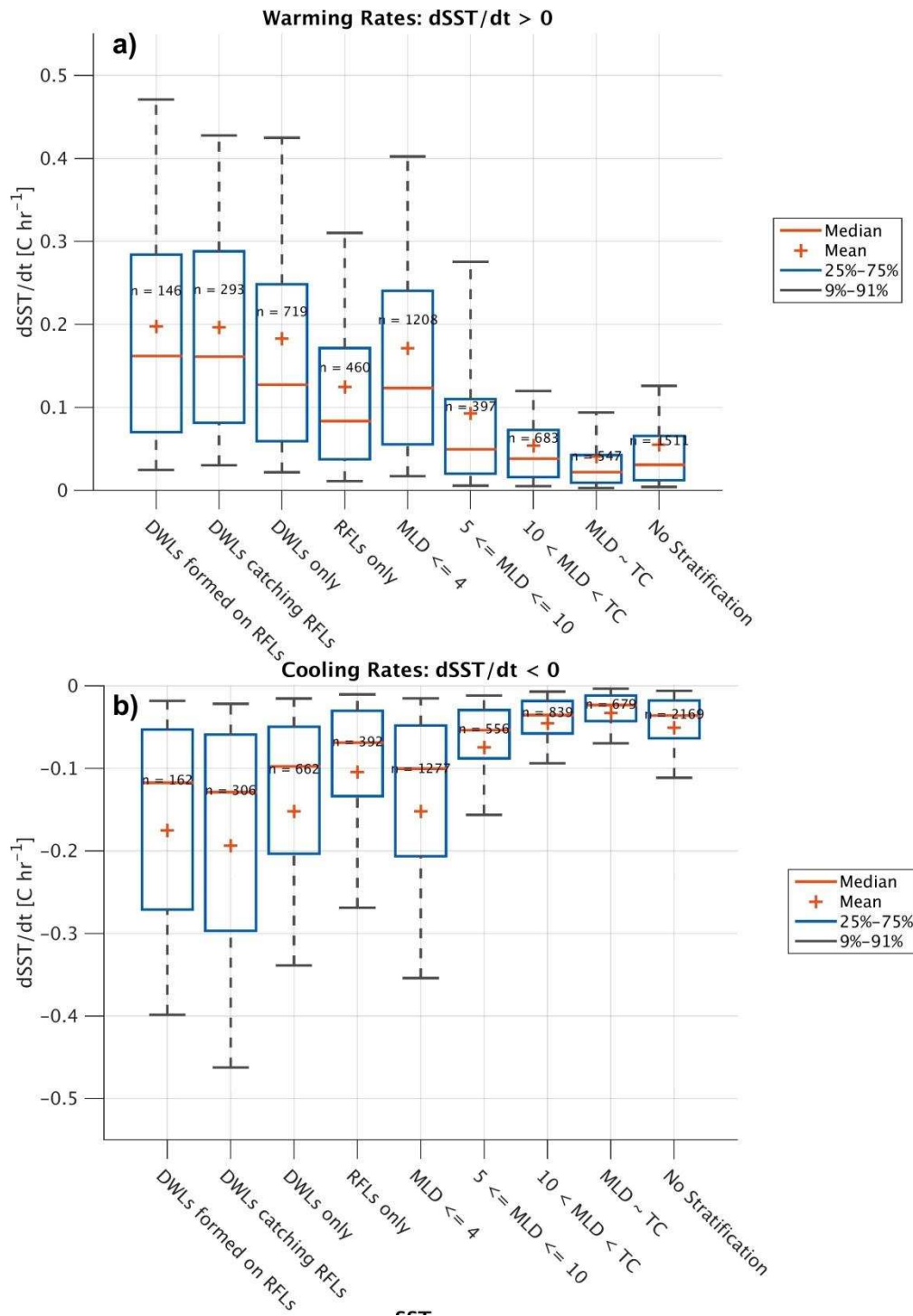
Figure 3.24: Box and whisker plots of (a) warming rates $> 0°$ C hr^{-1} and (b) cooling rates $< 0°$ C hr^{-1} during central Indian Ocean time periods when DWLs formed on top of heated RFLs, when DWLs caught RFLs, when only a DWL or RFL occurred without interaction, when the mixed layer depth was between certain vertical levels or merged with the thermocline (TC), and times without diurnal warm layer or rain freshening layer regardless of ocean mixed layer depth. Sample size of distributions shown on each box (n= …).

160

Fig. 3.25 shows the intraseasonal variability of heating rates during RFLs, DWLs, and their interactions. DWLs without RFL interaction foster the highest SST warming rates during the suppressed period (maximum rate of $0.68°$ C hr^{-1}), due in part to lower storm frequency and lower rain accumulation from storms that do occur during this MJO phase. Disturbed MJO conditions allow for many more DWLs catching RFLs and RFLs heating into DWLs, which have similar 25-75th percentile ranges of heating rates between $0.08 – 0.3°$ C hr^{-1}. Mean and median disturbed period warming rates are slightly higher for times when DWLs form inside RFLs, up to $0.225°$ C hr^{-1}. The maximum disturbed phase heating rates for DWLs when they catch RFLs are $0.6°$ C hr^{-1} due to IC and LC storms. The rates also reach $0.6°$ C hr^{-1} in heated RFLs from MCSs that create new DWLs. Rates were as high as $0.5°$ C hr^{-1} for heated RFLs due to ICS storms and only up to $0.4°$ C hr^{-1} due to LC events. Diurnal warm layers without RFL interaction can also produce high heating rates in the disturbed MJO period, with maximum values barely higher than in DWL-RFL combination layers.

Active MJO phase conditions prior to the westerly wind burst were also conducive to high SST warming rates in heated RFLs, which reached $0.6°$ C hr^{-1} due to MCSs and up to $0.5°$ C hr^{-1} due to ICSs. DWLs that catch RFLs and DWLs alone had lower quartile ranges of SST heating rates during this cloudier, active precipitation time period compared to heated RFLs and compared to the disturbed phase. The maximum SST heating rates in a DWL that caught an MCS still reached a maximum value of $0.52°$ C hr^{-1} in the active phase while ICs that got caught in a DWL only reached $0.5°$ C hr^{-1} during this time. WWB conditions did not support DWLs that caught RFLs or DWLs that formed on top of RFLs. The RFLs and single DWL that occurred during this time did not last long and exhibited very weak warming rates. However, the heating rates were largest in the mean and upper percentile ranges for RFLs than for no stratification at
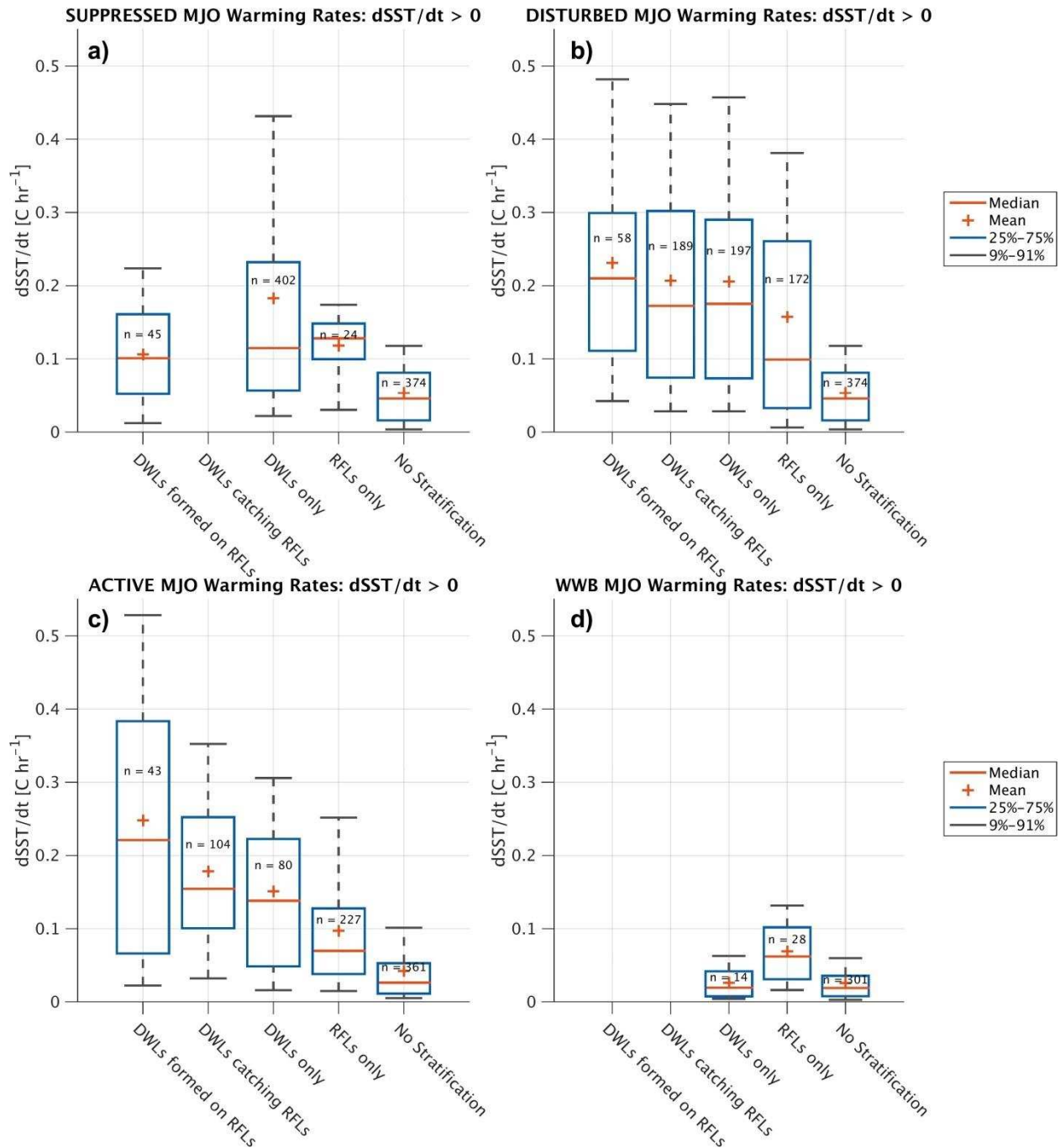
Figure 3.25: Box and whisker plots of warming rates > 0° C hr^{-1} during central Indian Ocean MJO (a) suppressed, (b) disturbed, (c) active, and (d) westerly wind burst time periods when DWLs formed on top of heated RFLs, when DWLs caught RFLs, when only a DWL or RFL occurred without interaction, and times without diurnal warm layer or rain freshening layer regardless of ocean mixed layer depth. Sample size of distributions shown on each box (n= …).

all. This is consistent with reduced turbulent mixing and cooling from below during the WWB in times of salinity stratification. Heating rates during times of no upper ocean stratification whatsoever consistently remain below $0.15 - 0.1°$ C hr^{-1} for all MJO phases since the mixed layer depth is deeper during these times.

3.7.3 SST

The importance of rain freshening and diurnal warming stratification to SST and therefore tropical air sea interactions is summarized by **Fig. 3.26**. SSTs were binned as a function of the mixed layer stratification type and depth. SSTs in heated freshwater layers and RFLs caught inside DWLs were, on average, as high as SSTs accomplished in temperature stratification layers alone. High SSTs in all three forms of upper ocean stratification were determined in part by the high magnitude heating rates accomplished in these shallow mixed layers (**Fig. 3.25**). DWLs, RFLs, or some combination of the two when the resulting mixed layer is in the topmost 4 meters of the ocean. The maximum SST recorded during DYNAMO as well as the 97th percentile values are higher during times when only diurnal warming was occurring without RFL influence. The 75% values of SST are higher in RFLs that heat or get caught in DWLs. RFLs without DWL influence have lower SST, most likely due to cloudy conditions, overnight RFL occurrences, as well as coincident latent and sensible cooling effects. Including all DWL, RFL, and DWL-RFL interactions, these times when the MLD is at or above 4 m are still higher than **Fig. 3.26** shows that the entirety of time when SSTs are above 30°C were accomplished in either any time when the MLD is deeper, on average. This corresponds to the lower heating rates achieved throughout deeper mixed layer depths. SSTs do not usually exceed 29.5°C when there is no stratification layer present. Times when the MLD is between 5-10 m can

foster SST as high as 29.75°C, but mixed layer depths lower than that have higher heat capacities

and do not warm to temperatures much higher than 29.3°C.
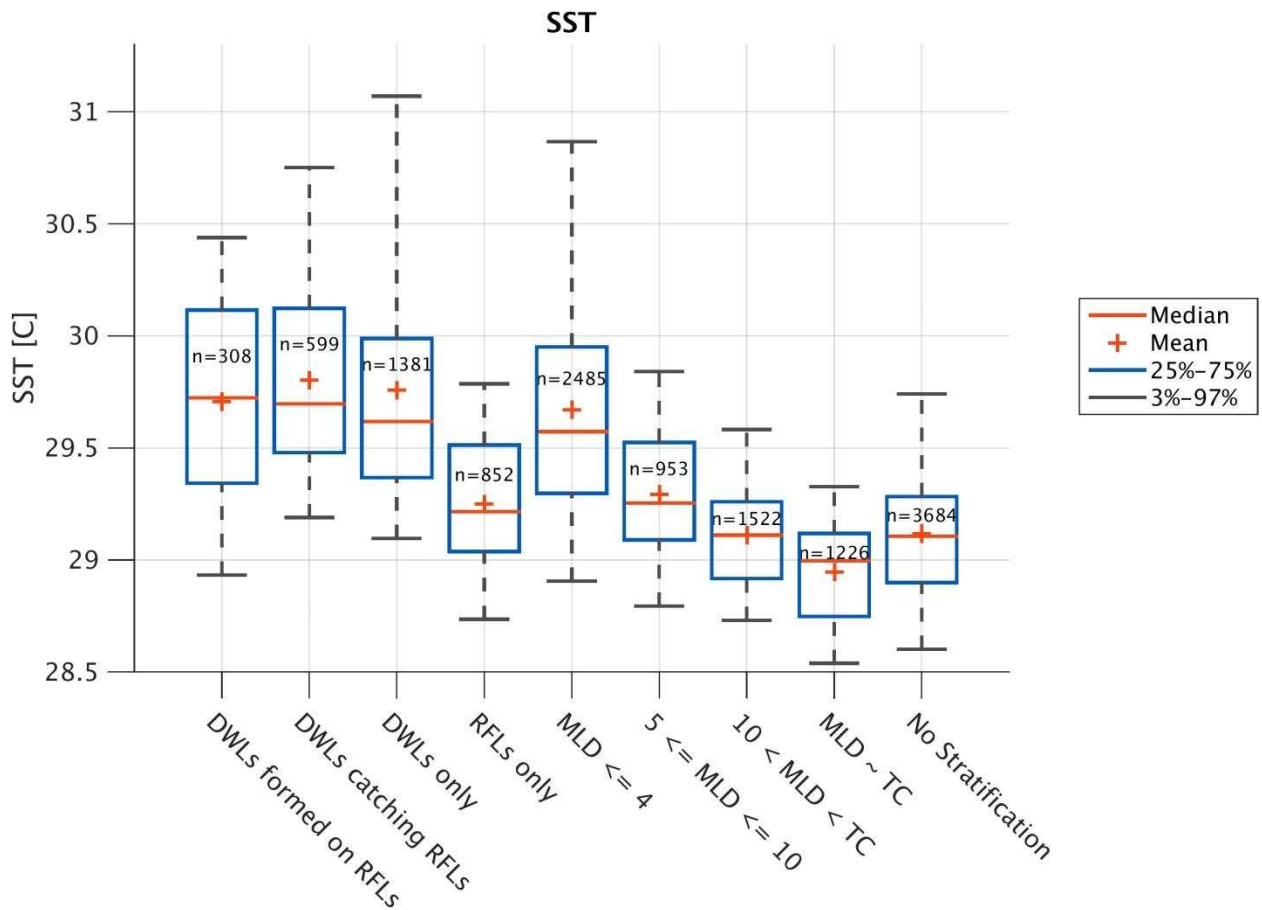
Figure 3.26: Box and whisker plots of SST during central Indian Ocean time periods when DWLs formed on top of heated RFLs, when DWLs caught RFLs, when only a DWL or RFL occurred without interaction, when the mixed layer depth was between certain vertical levels or merged with the thermocline (TC), and times without diurnal warm layer or rain freshening layer regardless of ocean mixed layer depth. Sample size of distributions shown on each box (n= …).

Fig. 3.27 decomposes **Fig. 3.25** into MJO phase for each type of near-surface ocean stratification

(see **Fig. 3.3** and **3.4** for corresponding surface and ocean conditions during these time periods).

As shown previously, the highest DYNAMO SST of about 32°C occurred in a DWL without

RFL influence but in contact with the barrier layer during the suppressed MJO. The two RFLs

that heated during suppressed conditions did not reach very high SSTs but also occurred in the

first days of each time record, prior to the mean daily SST warming trend experienced

throughout the suppressed and disturbed phases (**Fig. 3.3, 3.4**). Disturbed phase SST reached

maximum values of 30.6°C in heated RFLs due to LC and ICS storms, 31°C when DWLs caught

several IC and LC storms, and 31°C when DWLs had no interaction with RFLs. The disturbed

phase 25-75th percentile ranges of SST are highest for heated RFLs, then comparable for DWLs

that catch RFLs and DWLs only in this disturbed MJO phase. Disturbed phase RFLs without

DWL influence and times without any surface stratification were much lower, 90% of the time

below 29.75°C. Active MJO SST 75th and 97th percentile SST ranges are highest for RFLs

caught in DWLs and DWLs formed in RFLs. The maximum SST values for a DWL that caught

ICs reached 30.25°C while DWLs that caught ICs and MCS storms reached 30.5°C. Mean SSTs

in RFL-DWL combinations and DWLs are nearly the same in the active period, between 29 –

29.2°C. WWB SST are generally lower, due in part to less opportunity for near-surface mixed

layer stratification because of strong winds and wind-driven mixing. However, WWB SSTs were

highest during times of RFLs (maximum of 29.7°C) than when no stratification was present at all

(maximum of 29.6°C and much lower quartile ranges) or during a weak DWL (29.4°C max).

      Figs. 3.24-3.27 illustrate that times when the ocean mixed layer depth is between 0-5 m

are important for producing high SST heating rates and high SSTs prior to the heaviest rain and

most active westerly wind burst periods of the MJO. Since these near surface stable layers and

their interactions are important for SST variability, slab ocean mixed layer models with fixed

ocean mixed layers (especially if set $\geq$ 10 m) as well as models and observational datasets with

insufficient vertical resolution to resolve the upper 10 meters of both ocean temperature and

salinity are incapable of fully capturing the dynamics of SST variability observed in the tropical

Indian Ocean. The highest SSTs in all phases of the MJO are byproducts of concentrated
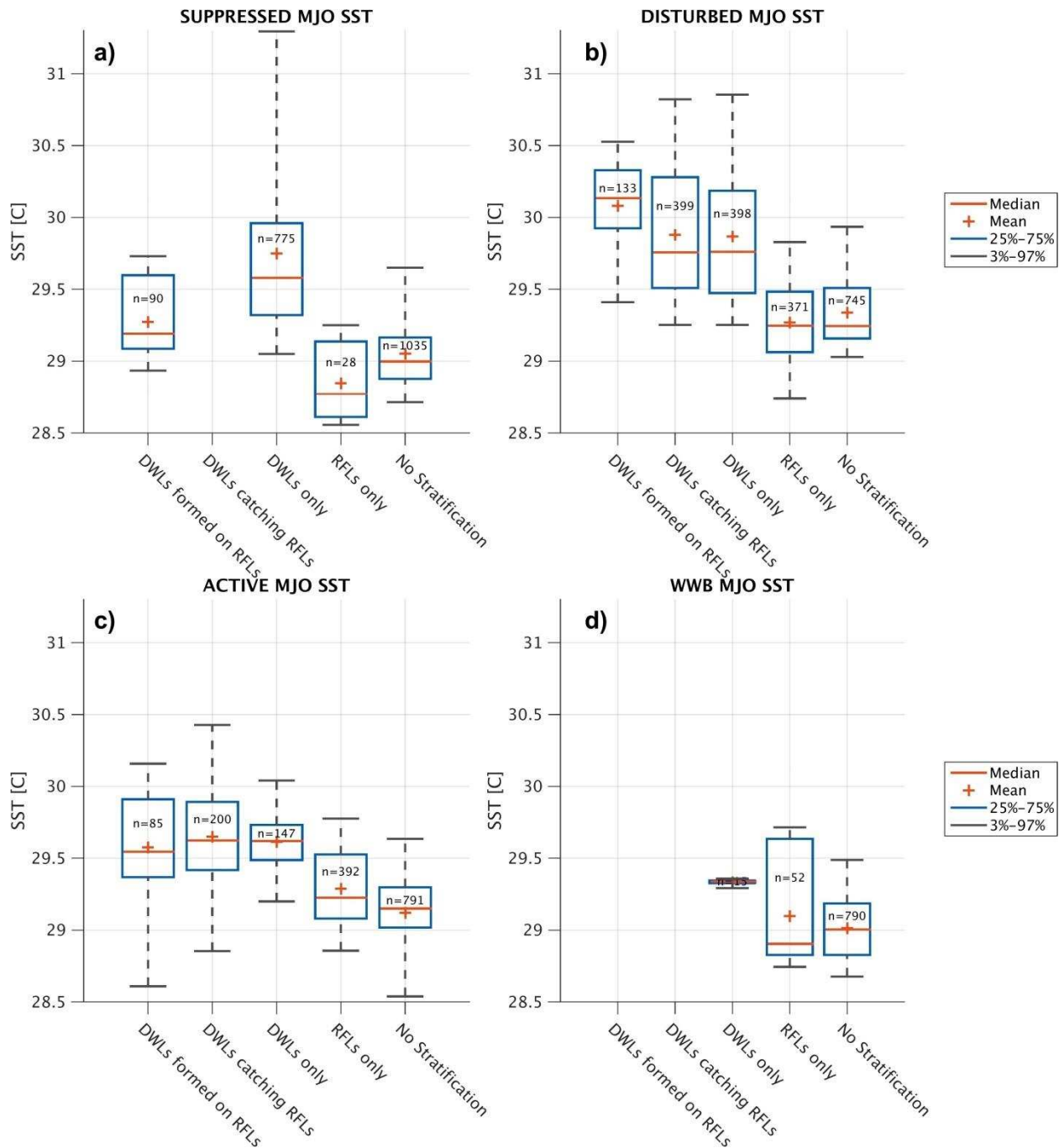
Figure 3.27: Box and whisker plots of SST °C during central Indian Ocean MJO (a) suppressed, (b) disturbed, (c) active, and (d) westerly wind burst time periods when DWLs formed on top of heated RFLs, when DWLs caught RFLs, when only a DWL or RFL occurred without interaction, and times without diurnal warm layer or rain freshening layer regardless of ocean mixed layer depth. Sample size of distributions shown on each box (n= …).

warming rates inside thin mixed layers (0-5 m depth), which are themselves byproducts of initial

warming and/or freshening. Diurnal warm layer parameterization and other 1D ocean model

parameterizations have been implemented successfully for several decades (e.g. Price et al. 1986,

Fairall et al. 1996, Clayson et al. 1996, Lloyd and Vecchi 2010). However, parameterizations of

shallow rain-formed mixed layers and their interactions with DWLs have not been explored.

3.7.4   *Storm morphology*

Figure 3.28 shows the intraseasonal variability of storms observed at *Revelle* according

to storm morphology as well as how many were able to stratify/shoal the ocean mixed layer.

Favorable atmospheric and oceanic conditions to support RFL stratification, as well as more

active precipitating cloud fields, in the disturbed and active MJOs provides a chance for all storm
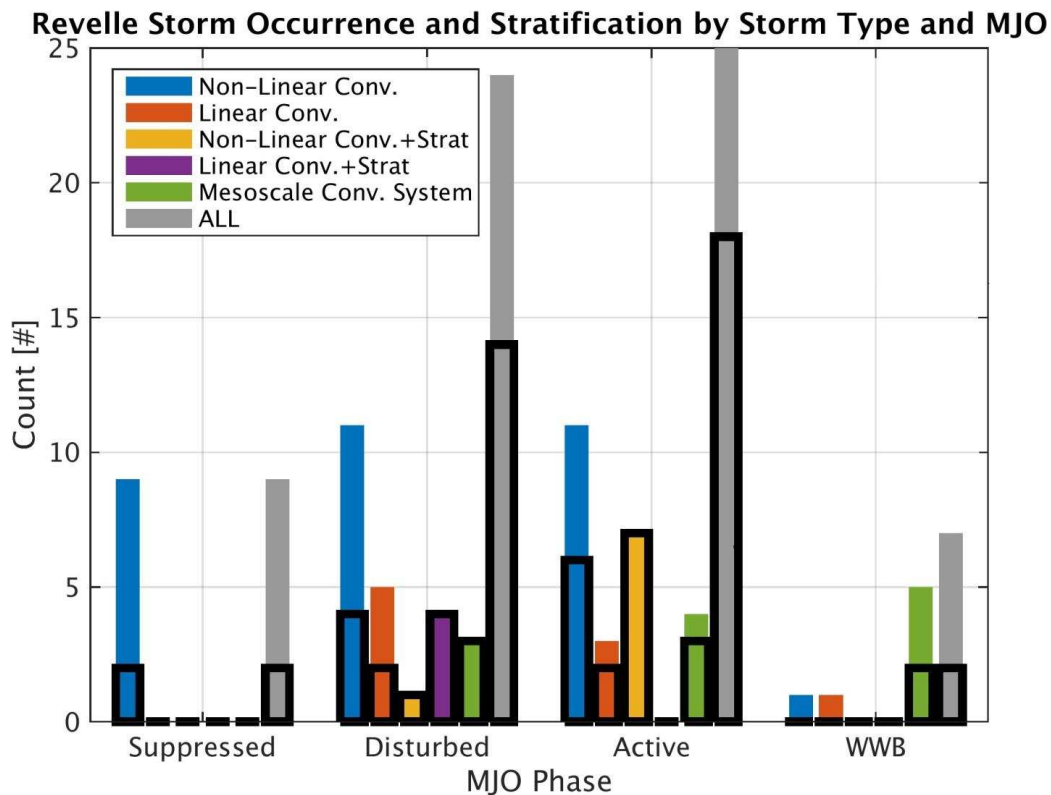
Figure 3.28: Central Indian Ocean histograms of storm occurrence and rain freshening layer occurrence by type of storm and MJO phase observed at the *Revelle* during DYNAMO. Some MCSs can produce more than one RFL per precipitating system lifetime, only one RFL per storm is tracked here.

types (IC, LC, ICS, LCS, and MCS) to stratify the upper ocean at some point. However, ICS, LCS, and MCS events are much more frequent in the disturbed and active MJO periods and have much higher probabilities of stratifying the upper ocean compared to IC and LC, which dominate in suppressed and disturbed time periods. For instance, 2/8 (25% of) storms observed at the *Revelle* during suppressed MJO conditions created salinity stratification, all of the IC morphology. Then sixteen (70%) of the 23 storms observed during the disturbed MJO stratified the mixed layer above 5 m, ranging across all five storm types. Note that one disturbed phase MCS produced multiple RFLs, so the number of MCS RFLs exceeds MCS occurrences in this period. All but 1 of the 8 ICS, LCS, and MCS storms during this disturbed period (88%) led to salinity stratification, whereas only about 50% of LC and IC storms were able to shoal the mixed layer during this time, most often from preexisting intermediate depth stable layers.

Twelve (70%) of the seventeen ICS, LCS, and MCS storms that occurred during active MJO conditions stratified the mixed layer while only about 40% of IC and LC storms were able to shoal the mixed layer during this time. This led to only 54% of all storms stratifying the upper ocean above 5 m in the active MJO phase prior to the WWB and heaviest rainfall. Then in WWB conditions only 3 MCS salinity stratification events were observed due to 2 individual MCSs out of the 5 MCS, 1 IC, and 1 LC storms observed at the *Revelle* throughout this period (an overall 30% stratification rate). During this time, large accumulated rainfall amounts from strong MCSs could not always compete with upper ocean mixing due to high intraseasonal mean winds in addition to storm gustiness, which resulted in deeper mixed layer depths often extending to the thermocline (see **Figs. 3.3-3.4**).

Therefore, the observed tendency for more RFLs to occur and constructively complement the diurnal warming cycle during disturbed and early active MJO periods leading up the most

active MJO conditions can also be explained by conducive atmospheric and oceanic conditions to create and maintain RFLs during this time, the prevalence of ICS, LCS, and MCS storms during disturbed and active phases, as well as their overall high likelihood of stratifying the upper ocean. The likelihood for all storms to stratify the upper ocean and shoal the mixed layer to the surface peaks in disturbed MJO and secondarily in active MJO periods prior to the WWBf, accomplished mainly by the high likelihood of ICS, LCS, and MCSs to shoal the mixed layer and their high occurrence rate during this time. IC and LC storms typically always exhibit less than a 50% chance to stratify the upper ocean, but are the most frequent storm type in suppressed, disturbed, and active MJO phases, increasing in frequency during disturbed and active periods compared to suppressed conditions. Increased IC and LC frequency, considering their low stratification efficiency, still contributes to the number of RFLs observed during disturbed and active MJO phases.

3.7.5 Summary

The suppressed phase DWLs without rain modification accomplish diurnal warming with accompanying day-to-day SST increases. The disturbed phase of the MJO experiences more rainfall and particularly more ICS, LCS, and MCS storms. Many of these storms occur during late afternoon and early morning (Janowiak et al. 1994, Cronin and McPhaden 1999, Yang and Slingo 2001) so as not to disrupt or inhibit the DWL cycle greatly. On the contrary, DWLs and RFLs appear to act constructively during the disturbed phase, which helped produce some of the highest SSTs and SST warming rates observed in this period. Then the active phase of the MJO experiences more daytime precipitation with continued ICS, LCS, and MCS occurrences and less preference toward the semidiurnal cycle of storms, i.e. storms occur at all hours of the day in this period. Daytime RFLs sometimes take the place of DWLs during these active MJO conditions

(**Table 3.4**). On other active MJO days, RFLs can heat between breaks in the clouds, especially when barrier layer stratification shields the upper ocean from mixing and cooling. In this way, RFLs and DWLs participate in stratifying the upper ocean together during the active phase, and their combinations lead to the highest SST warming rates and SSTs in this period. The westerly wind burst phases struggle to support any upper ocean stratification due to high winds, turbulence, and cooling net heat flux, but at times can experience weak, short-lived DWLs and RFLs during some short-lived sunny conditions and high rain accumulation storms. WWB RFLs shield the surface from turbulent mixing and cooling for several hours, supporting the highest SSTs and SST warming rates in this time period when SST is otherwise dropping rapidly (**Fig. 3.3**).

According to the two MJO events observed during DYNAMO, there appears to be a "sweet-spot" or "sweet-time" in the intraseasonal cycle between suppressed and most active, WWB phases when storms are capable of raining a decent amount, i.e. greater than 10 mm, but winds are still calm enough ($< 6\text{-}8 \text{ m s}^{-1}$) to not always mix away DWL or RFL stratification. These trends between the suppressed and most active MJO phases occur because the lower troposphere is becoming moister, wind shear increases moderately, and storms become more organized to support stratiform rain areas. All ICS and LCS, as well as most MCS storms can meet the ample rain without too much wind salinity stratification criteria. About half of the IC and LC storms during disturbed and active MJO conditions can also create salinity stratification, and occur quite frequently.

Storms stratify the upper ocean during disturbed and early active MJO time periods for long enough to affect the diurnal warming cycle such that accelerated warming rates can occur for a large part of the day and foster high SSTs leading up to the windiest, heaviest raining MJO

period. The synergy between RFLs and DWLs in the disturbed and active MJO periods prior to the WWB and heaviest rain accumulation time period is hypothesized to be due in part to the symbiotic semidiurnal predawn and later afternoon timing of storms and their RFLs compared to daytime DWLs, the prevalence of storms that are most likely to stratify the upper ocean, and favorably low wind and current values during this time.

While not all RFLs heat or participate symbiotically with DWL stratification, the prevalence of RFLs in the disturbed and active MJO certainly still plays a role in suppressing SST cooling by keeping the mixed layer near the surface due to fresh water stratification. RFLs that last overnight isolate the near surface water from deeper, cooler water, thereby shielding the surface from the normal nighttime mixing and entrainment cycle due to heat flux and mechanical mixing forces. SSTs rise mostly due to DWLs alone in the suppressed phase of the MJO when storms are infrequent and weak. We hypothesize that RFLs help keep SSTs high in the disturbed and early active MJO periods leading up to the heavy rain periods by keeping the mixed layer shallow enough to sustain strong heating when wind conditions are variable and stronger. RFLs can withstand higher winds, higher currents, less solar heating, as well as more latent and sensible cooling than DWLs. During the heaviest rain and wind periods of the WWB, some rain and temperature stratification does occur, which delays vertical mixing and entrainment cooling briefly for 1-3 hours. The lack of surface stratification during most of the WWB time period exposes the surface to the well-mixed waters below and erodes the thermocline such that even colder water is mixed upwards.

3.8 Summary

Temperature (T) and salinity (S) microstructure measurements were analyzed in the central Indian Ocean throughout two Madden-Julian Oscillation (MJO) events with and without a barrier layer during DYNAMO. Vertical gradients of T and S were scaled by their respective contributions to the density of seawater so that stable layers with respect to salinity, temperature, or both could be identified and tracked. Under light-wind, mostly clear conditions, stable temperature gradients due to daytime surface heating shoaled the mixed layer to the surface, which have been called diurnal warm layers (DWLs). Stable salinity gradients due to rain freshening and only minor rain cooling can also shoal mixed layers, which are referred to as rain freshening or rain-formed layers (RFLs).

All 38 rain freshening stratification events were linked to specific rain events, 31 of which crossed the ship and 6 of which occurred within 5-10 km upstream of the ship and advected into the domain of ship sensors. Non-linear isolated convective (IC) events occurred most often at the ship, but only about 1/3 of this rain type shoaled the mixed layer. These RFLs often formed in or shoaled from a preexisting stratification layer either with respect to temperature or salinity or both. It was very rare for an IC storm to stratify the ocean from a well-mixed state because usually these storms have some gustiness but little rain with which to stratify the mixed layer. For instance, weak convective storms accompanied by cold pools often ended DWL stratification events rather than starting RFLs. It was also shown that weak convective rain rates below 10 mm hr^{-1} might not be enough to stratify the upper ocean. When these weak to moderate buoyancy fluxes are applied over the ocean in small, short-lived patches such as from IC storms, they might often be overcome by dissipation, and diffusional effects. Linear convective (LC) storms (absent a stratiform component) also only showed about a 40%

chance of stratifying or shoaling the mixed layer, most often occurring when a preexisting stratification layer existed prior to the rain event. In contrast, all sub-mesoscale (<150 km) quasi-circular (ICS) and linear (LCS) convective systems with stratiform rain components were able to shoal the mixed layer and stratify the upper ocean, many from well-mixed ocean states and others over preexisting stable layers. Only 2/3 of MCSs stratified the upper ocean because some had particularly strong winds, which accelerated the surface current and upper ocean turbulence enough to overcome the buoyancy flux by rain freshening. Therefore, storm morphology, stratiform rain occurrence within the convective system, the preexisting stability and turbulence structure of the ocean, and mechanical mixing by wind, cold pools, and current shear need to be taken into account when considering whether a storm might shoal the mixed layer, do nothing, or deepen the upper ocean mixed layer.

Surface stratification event tracking showed that DWLs and RFLs can occur during all phases of the MJO, but have preferential intraseasonal behavior according to the co-evolution of the atmosphere and ocean over the course of the MJO cycle. For instance, ICS, LCS, and MCS storms with stratiform rain shields shoal the mixed layer 92% of time when present and are most common during the disturbed and active phases of the MJO prior to the WWB. During this time, RFLs and DWLs can both exist because maximum cloud shading and mean wind speeds greater than 6 m s^{-1} in the most active periods of the MJO and westerly wind bursts have not yet begun. There appears to be a sweet-spot or sweet-time in the disturbed and early active MJO periods when instability is enhanced and wind shear is increasing so that storm organization increases and therefore the storms can sustain larger stratiform rain regions, last longer, and cause more rain accumulation. However, wind shear is still not great enough to assist in fast storm propagation or strong surface winds with which to mix the upper ocean. Therefore, RFLs occur

most often, and are most likely to occur given storm activity, during the disturbed and active

MJO periods. The impact of rainfall on the upper ocean is not constant throughout the MJO.

Even for a given storm type, the ability of certain storm types to produce RFLs changes

throughout the MJO since the mean atmospheric and oceanic states are more turbulent in the

WWB and suppressed MJO conditions prevent much rainfall from happening at all, or provides

storms with more gustiness and not enough rainfall to shoal the mixed layer.

Diurnal warm layers occurred in all phases of the MJO, but preferentially during

suppressed phases, trailing off in frequency towards more active phases as cloud shading

increased. Diurnal warm layers mostly occurred without interaction from rain-formed mixed

layers in the suppressed MJO, but were often ended by afternoon atmospheric convective activity

(weak rain with cold pools) that exhibited very little rain but enough wind to mix away the stable

temperature gradient at the base of the DWL. The barrier layer intensified DWL daytime SST

warming and reduced nighttime cooling and mixing during the November MJO. For instance, the

highest SSTs during the entire experiment were due to a suppressed phase DWL merging with

the barrier layer, which created intense stability in the entire upper 25 m of the ocean with which

to concentrate atmospheric heat fluxes.

During the disturbed phase, diurnal warm layers frequently caught RFLs within the layer

of stable temperature gradients. These DWLs that catch RFLs foster some of the highest SST

warming rates observed during DYANAMO. One such event resulted in the highest surface

temperature observed during the October DYNAMO MJO. RFLs can also occur in the morning

or at night and last long enough for a DWL to grow inside the RFL, thus creating a heated

freshwater lens of intense stability. This process was observed nine times during DYNAMO

during the disturbed and active MJO periods prior to the heaviest rain accumulation and westerly

wind burst conditions. These interactions yielded surface stratification and shoaling of the mixed layer to near 0 m for time periods as long as 23 hours. These layers produced the highest SST warming rates of the active period, as high as the disturbed period, and some of the highest SSTs in both disturbed and active time periods. Accounting for all MJO phases, DWLs that catch RFLs and RFLs that form DWLs can warm as rapidly and be as warm as DWLs alone, on average and within 25th – 75th percentile ranges.

Compared to DWL, RFL, and DWL-RFL interaction events, the surface heating rates were lower by a factor of 2 during times when the mixed layer was between 5-10 m, when no stratification events were detected, and especially when the mixed layer was below 10 m. SST rarely exceeded 29.5°C when the mixed layer was below 5 m, but could reach maximum values of 32°C during DWLs and 31°C when RFLs were caught in RFLs or DWL began in RFLs. Thus, strong diurnal and intraseasonal ocean heating anomalies are accomplished in near-surface stratification layers such as DWLs, DWLs that catch RFLs, and heated RFLs that turn into new DWLs. Models and observational datasets need to account for these stability features in the upper 5 meters of the ocean (i.e. mixed layer depths between 0-5 m) to accurate diagnose mixed layer heat budgets, SST variability, upper ocean mixing, as well as potential feedbacks of SST onto surface heat fluxes and ultimately atmospheric convection. For instance, the high resolution microstructure measurements used in this study reveal that the ocean mixed layer depth is at or above 2 m 31% of the data record spanning two MJO events, 39% of the time above 5 m - the minimum ARGO float data point and second data point of most moorings, and above 10 m 54% of the record, which is where the de Boyer Montegut (2004) climatology began considering mixed layer depth.

RFLs can stratify the ocean at any time of the day, occur more often than DWLs, exhibit stronger combined N^2 stability than DWLs, and can last as long as DWLs. Eighteen out of 38 RFLs did not foster heating or interact with DWLs, but still reduced turbulent mixing inside and below this layer for some period of time (at night for 14 out of 43 days), which still affected freshwater advection, freshwater storage, and the vertical profile of mixing. For instance, strong wind conditions during the WWB without any form of ocean stratification yielded deep vertical mixing and erosion of the thermocline, deepening it and cooling SST. Because of their higher maximum magnitude total stratification, RFLs can actually withstand greater wind speeds, sometimes during WWBs, last through cold pools, and don't require sunlight to survive. For instance, RFLs during DYNAMO WWBs were associated with the highest SSTs during this high wind period, consistent with the idea of reduced turbulent mixing and entrainment cooling from below due to shallow mixed layer stratification, even though this only lasted for 3-6 hours.

DWLs have become recognized as an integral part of the air-sea coupled system for their role in concentrating heat fluxes within a shallow layer and fostering high daytime SSTs that can amplify the intraseasonal SST and mean SST warming cycles. We show evidence that RFLs can assist DWLs in this process, and preferentially do so in the disturbed and early active phases leading up to the heaviest rain, strongest wind period of the MJO when atmospheric convection is still building and can respond to these surface processes. Therefore, we hypothesize that the interactions between DWLS and RFLs in shoaling the mixed layer and controlling SST variability are important for MJO initiation in the central Indian Ocean.

This work also highlighted the role of mesoscale rain morphology (i.e. the presence of stratiform rain components) and the vertical structure of stability in determining whether a rain event could shoal the mixed layer. Therefore, we also suggest that two-way, high spatio-temporal

resolution coupled models (i.e. resolving or representing atmospheric mesoscale storm morphology and with at least 1 m vertical resolution in the upper 10 m of the ocean) are necessary to reproduce the observed mixed layer depth and SST variability throughout the MJO. We hypothesize that storms are more likely to stratify/shoal the mixed layer when stratiform rain occurs within the precipitating system. The characteristics of stratiform rain, i.e. large area, long duration, steady, protected freshwater flux of rain rates up to 10 mm hr^{-1} (equivalent buoyancy flux to maximum daytime solar heating), led to upper ocean stabilization in 20/24 precipitating systems. Stratiform rain also occurs more frequently within precipitating systems during disturbed, active, and WWB phases of the MJO, which contributes greatly to maximum overall RFL occurrences in the disturbed and active phases. Convective rain events can produce more rain but also gustiness and do not cover as large of an area or last as long without stratiform rain, so might be more prone to diffusion and dissipative effects. Chapter 2 also suggests that the larger rain drop sizes in stratiform rain could be more capable of breaking the surface tension of the water, extending deeper into the column, and contributing to stable salinity gradients in the upper 5 m of the ocean compared to weak convective rain, which is typically composed of more numerous small rain drops. However, more comprehensive salinity measurements in the upper 2 meters of the ocean are required to test this hypothesis.

Because previous studies have shown that the variability of rainfall, acceleration of ocean turbulence and zonal jets during WWBs, diurnal warm layer occurrences, and wind speed variability in the central Indian Ocean and west Pacific Ocean associated with the MJO are very similar, we hypothesize that the diurnal warm layer and rain freshening layer variability documented during DYNAMO is applicable to the entire equatorial IndoPacific warm pool. Advection of accumulated rainfall from storms upstream of the ship appeared to be important in

stratifying the mixed layer locally, so the surface current at other locations needs to be taken into account. Research on air-sea interactions and the MJO off of the equator, even as close as 8 S, have found that Rossby wave activity modulates SST (Webber et al. 2010, Webber et al. 2011, Seiki et al. 2013) and different storm activity occurs (Xu and Rutledge 2015b), so RFL and DWL variability are expected to be different in non-equatorial regions away from the main MJO equatorial wave guide.

CHAPTER 4: SUMMARY AND CONCLUSIONS

Leading up to this dissertation, the variability of convective and stratiform rain drop size distributions and rainfall accumulations over the tropical warm pool and the impact of the full spectrum of precipitating events on the upper ocean mixed layer depth throughout the MJO cycle were unknown. Chapter 2 used a longer and higher resolution drop size distribution (DSD) dataset than ever available before to distinguish convective and stratiform rain by rain drop number concentration alone because drop size was not a very distinguishing factor in the tropical, oceanic precipitation regime. This classification scheme also led to improved tropical, oceanic radar rainfall estimation equations for use in Chapter 3. Convective rain drop size distributions were dominated by numerous, small drops while stratiform rain samples exhibited up to an order of magnitude lower number concentration but larger drop size. We hypothesized that this was because iced-based convective microphysical processes such as riming and hail growth are limited and muted in these regions of relatively low surface atmospheric buoyancy fluxes compared to land regions. Almost all convective and stratiform rain drop distribution sizes were above the critical radius thought to determine whether raindrops will sit atop the ocean or coalesce and penetrate deeper into the water, even at very low rain rates between 0.5-1 mm hr^{-1}. However, stratiform rain might penetrate deeper because they have larger median drop sizes for a given rain rate. While total rainfall accumulation was mostly due to convective rain rates because of their higher magnitude, weak, convective rain (< 10 mm hr^{-1}) was found to contribute more total rainfall occurrence and accumulation over the tropical warm pool than originally thought.

However, Chapter 3 still found that precipitating systems with stratiform rain components were much more likely to contribute to preexisting upper ocean stratification and mixed layer shoaling than convective rain events alone. Only 37% of all storms shoaled the mixed layer while 40% of convective rain events without stratiform rain were able to stratify the upper ocean. In contrast, 92% of submesoscale and mesoscale storms with stratiform rain were able to shoal the mixed layer to within 0-5 m of the surface due to stable salinity gradients. We hypothesize that stratiform rain helps contribute to upper ocean stratification because, as evidenced from statistics from Chapter 2, stratiform rain rates are usually between 1-10 mm hr^{-1} and cover a much larger area / percentage of time than convective rain cores. Although weaker than strong convection, stratiform rain rates are still on the order of the stabilizing buoyancy flux of maximum solar daytime heating, known to often produce diurnal warm layer stratification of the mixed layer. Stratiform rain could not shoal the mixed layer without some convective rain within the precipitation episode. We hypothesize that the uniform, protected, steady, long-lived stratiform rain forcing amidst convection allows rain to accumulate in a more protected, larger area than short duration, small, strong convective rain events. Larger, more uniform freshwater lenses might be less susceptible to dissipative, dispersive, or diffusional effects compared to smaller surface freshwater pools.

Despite the predominance of long-lived stratiform rain within some mesoscale convective systems, some of these highly-organized phenomena have too strong of mean winds or wind gustiness to support surface mixed layer stratification by freshwater, sometimes succumbing to deep ocean mixing. Submesoscale convective events without stratiform rain that were able to shoal the mixed layer or add to its stratification often relied on preexisting surface or intermediate depth stratification features from which to stabilize the upper ocean. In contrast,

many convective systems with stratiform rain were able to shoal the mixed layer from a well-mixed, deep ocean mixed layer state. We hypothesize that smaller convective systems without stratiform rain tend to promote more upper ocean wind mixing than freshwater stabilization compared to the larger, more organized precipitation systems with stratiform rain. This mixing / rain imbalance led many weak, small convective events to deepen the ocean mixed layer or impart no noticeable effect on the upper ocean at all, despite some locally high rain rates. This was an interesting finding since weak convective events are the most frequent rain event over tropical oceans climatologically.

Some RFLs were contained or caught inside diurnal warm layers. Other RFLs formed new diurnal warm layers when exposed to daytime heating after the storm ended. These DWL-RFL combination stratification events were responsible for the highest SSTs and SST warming rates leading up to the most enhanced wind and rain MJO phases observed during DYNAMO. Temperature stratification layers alone were mostly responsible for diurnal heating and mean SST warming trends in the suppressed phase of the MJO when rain was infrequent and weak. The synergy between DWLs and RFLs in the disturbed and early active MJO periods contributed to continued heating and may be an important physical process to the intraseasonal SST cycle. During the most active MJO periods, some RFLs were still able to form despite strong wind mixing, which helped shield SST from entrainment cooling, albeit only for 1-4 hours.

Thus, RFLs have a non-negligible effect on upper ocean heating as well as turbulent mixing and need to be represented in numerical models of air-sea interactions in the tropical warm pool. The third DYNAMO hypothesis originally stated that "the barrier layer, wind- and shear-driven mixing, shallow thermocline, and mixing layer entrainment all play essential roles in MJO initiation over the Indian Ocean by controlling the upper ocean heat content and sea

surface temperature and thereby surface flux feedback" (Yoneyama et al. 2013). Results from this dissertation suggest that the hypothesis should also state that shallow diurnal warm layers and rain-formed mixed layers, and their interactions, are also important for MJO initiation over the Indian Ocean because they are the physical mechanisms that support and sustain strong SST heating prior to the heaviest raining, strongest wind period of the oscillation.

Together, the two main chapters of this dissertation have closed a very large, long-standing observational knowledge gap concerning tropical rainfall variability and its impact on the upper ocean. These observations will be able to help numerical models initialize and simulate rain and rain-formed mixed layers over the tropical warm pool. For instance, high resolution coupled modeling studies and parameterization scheme tests could be motivated from the observational analysis herein to further investigate ocean mixed layer evolution due to rain, resulting SST variability, and the potential feedbacks of these processes to atmospheric convection. For instance, warm and rapidly warming SSTs in the disturbed and active phases of the MJO prior to the WWB due to interactions between shallow diurnal warming and rain-formed mixed layers could have affected the buildup of MJO convection during these time periods. Since rain effects on the mixed layer depend strongly on the presence of stratiform rain within the precipitating system, atmospheric simulations of this scope should attempt to parameterize or resolve precipitation morphology before attempting to couple with ocean simulations below.

One-dimensional simulations of rain-formed mixed layers and their interactions with diurnal warm layers seem inadequate based on many observations of rain accumulation upstream of the ship advecting into the microstructure profiler in the current study. Therefore, 2D or 3D ocean simulations are needed to capture advective and lateral processes associated with

freshwater lenses and their stratification of the ocean mixed layer. Contextual rain information and precipitating system morphology surrounding oceanographic measurements appeared necessary to make sense of the salinity stratification and freshening observed in the ocean during DYNAMO. Therefore, we recommend use of high resolution satellite or scanning radar data in addition to ship rain gauges when attempting to study rain effects on the ocean in the future. Future field campaigns should ideally deploy multiple ocean microstructure stations with both temperature and salinity observations in the upper most meters of the ocean throughout a well-resolved domain of radar- or satellite-sensed precipitation to move beyond the 1D analysis completed in this study.

REFERENCES

Adamec, D. and R. W. Garwood, Jr., 1985: The simulated response of an upper-ocean density front to local atmospheric forcing. *J. Geophys. Res.*, **20**, 917–928.

Anderson, J. E. and S. C. Riser, 2014: Near-surface variability of temperature and salinity in the near-tropical ocean: Observations from profiling floats. *J. Geophys. Res.*, **119**, 7433–7448.

Anderson, S. P., R. A. Weller, and R. B. Lukas, 1996: Surface buoyancy forcing and the mixed layer of the Western Pacific Warm Pool: Observations and 1D model results. *J. Climate*, **9**, 3056–3085.

Asher, W. E., A. T. Jessup, R. Branch, and D. Clark, 2014: Observations of rain-induced near-surface salinity anomalies. *J. Geophys. Res.*, **119**, 5483–5500.

Asher, W. E., A. T. Jessup, and D. Clark, 2015: Stable near-surface ocean salinity stratifications due to evaporation observed during STRASSE. *J. Geophys. Res.*, **119**, 3219–3233.

Atlas, D., R. C. Srivastava, and R. S. Sekhon, 1973: Doppler radar characteristics of precipitation at vertical incidence. *Reviews of Geophysics*, **11**, 1–35.

Atlas, D. and C. W. Ulbrich, 2000: An observationally based conceptual model of warm oceanic convective rain in the tropics. *J. Appl. Meteorol.*, **39**, 2165–2181.

Atlas, D., C. W. Ulbrich, F. D. Marks, R. A. Black, E. Amitai, P. T. Willis, and C. E. Samsur, 2000: Partitioning tropical oceanic convective and stratiform rains by draft strength. *J. Geophys. Res.*, **105**, 2259–2267.

Atlas, D., C. W. Ulbrich, F. D. Marks, Jr., E. Amitai, and C. R. Williams, 1999: Systematic variation of drop size and radar-rainfall relations. *J. Geophys. Res.*, **104**, 6155–6169.

Atlas, D., C. W. Ulbrich, and R. Meneghini, 1984: The multiparameter remote measurement of rainfall. *J. Hydrometorol.*, **19**, 3–22.

Austin, P. M. and S. G. Geotis, 1979: Raindrop sizes and related parameters for GATE. *J. Appl. Meteorol.*, **18**, 569–575.

Back, L. E. and C. S. Bretherton, 2009a: On the relationship between SST gradients, boundary layer winds, and convergence over the tropical oceans. *J. Climate*, **22**, 4182–4196.

Back, L. E. and C. S. Bretherton, 2009b: A simple model of climatological rainfall and vertical motion patterns over the tropical oceans. *J. Climate*, **22**, 6477–6497.

Barnes, H. C. and R. A. Houze, Jr., 2013: The precipitating cloud population of the Madden-Julian Oscillation over the Indian and west Pacific Oceans. *J. Geophys. Res.*, **118**, 6996–7023.

Barnes, H. C. and R. A. Houze, Jr., 2014: Precipitation hydrometeor type relative to the mesoscale airflow in mature oceanic deep convection of the Madden-Julian Oscillation. *J. Geophys. Res.*, **119**, 13 990–14 014.

Barnes, H. C., M. D. Zuluaga, and R. A. Houze, Jr., 2015: Latent heating characteristics of the MJO computed from TRMM observations. *J. Geophys. Res.*, **0**, DOI: 10.1002/2014JD022 530.

Battan, L. J., 1973: Radar observation of the atmosphere. pp. 324.

Bell, T. L. and R. Suhasini, 1994: Principal modes of variation of rain-rate probability distributions. *J. Appl. Meteorol.*, **33**, 1067–1078.

Bellenger, H. and J.-P. Duvel, 1993: An analysis of tropical ocean diurnal warm layers. *J. Climate*, **22**, 3629–3646.

Bellenger, H., Y. N. Takayabu, T. Ushiyama, and K. Yoneyama, 2010: Role of diurnal warm layers in the diurnal cycle of convection over the tropical Indian Ocean during MISMO. *Mon. Weather Rev.*, **138**, 2426–2433.

Benedict, J. J. and D. A. Randall, 2007: Observed characteristics of the mjo relative to maximum rainfall. *J. Atmos. Sci.*, **64**, 2332–2354.

Benedict, J. J. and D. A. Randall, 2009: Structure of the Madden-Julian Oscillation in the superparameterized CAM. *J. Atmos. Sci.*, **66**, 3277–3296.

Biggerstaff, M. I. and R. A. Houze, Jr., 1993: Kinematics and microphysics of the transition zone of the 10-11 june 1985 squall line. *J. Atmos. Sci.*, **50**, 3091–3110.

Boutin, J. and N. Martin, 2006: ARGO upper salinity measurements: Perspectives for L-Band radiometers calibration and retrieved sea surface salinity validation. *IEEE Geosci. Remote Sens. Lett.*, **3**, 202–206.

Boutin, J., N. Martin, G. Reverdin, S. Morisset, X. Yin, L. Centurioni, and N. Reul, 2014: Sea surface salinity under rain cells: SMOS satellite and in situ drifters observations. *J. Geophys. Res.*, **119**, 5533–5545.

Boutin, J., N. Martin, G. Reverdin, X. Yin, and F. Gaillard, 2013: Sea surface freshening inferred from SMOS and ARGO salinity: impact of rain. *Ocean Sci.*, **9**, 183–192.

Brandes, E. A. and K. Ikeda, 2004: Freezing-level estimation with polarimetric radar. *J. Appl. Meteorol.*, **43**, 1541–1553.

Brandes, E. A., G. Zhang, and J. Vivekanandan, 2004: Drop size distribution retrieval with polarimetric radar: Model and application. *J. Appl. Meteor.*, **43**, 461–475.

Brainerd, K. E. and M. C. Gregg, 1995: Surface mixed and mixing layer depths. *Deep-Sea Res. Pt. I*, **42**, 1521–1543.

Braun, S. A. and R. A. Houze, Jr., 1994: The transition zone and secondary maximum of radar reflectivity behind a midlatitude squall line: Results retrieved from Doppler radar data. *J. Atmos. Sci.*, **51**, 2733–2755.

Brainerd, K. and M. Gregg, 1997: Turbulence and stratification on the tropical ocean-global atmosphere-coupled ocean-atmosphere response experiment microstructure pilot cruise. *J. Geophys. Res.*, **102**, 10 437–10 455.

Bringi, V. N. and V. Chandrasekar, 2001: *Polarimetric Doppler Weather Radar: Principles and Applications*. Cambridge University Press, Cambridge, United Kingdom, pp. 636 pp.

Bringi, V. N., V. Chandrasekhar, J. Hubbert, E. Gorgucci, W. L. Randeu, and M. Schönhuber, 2003: Raindrop size distribution in different climatic regimes from disdrometer and dual-polarized radar analysis. *J. Atmos. Sci.*, **60**, 354–365.

Bringi, V. N., G.-J. Huang, S. J. Munchak, C. D. Kummerow, D. A. Marks, and D. B. Wolff, 2012: Comparison of drop size distribution parameter (D_0) and rain rate from S-band dual-polarized ground radar, TRMM Precipitation Radar (PR), and combined PR-TMI: Two events from Kwajalein Atoll. *J. Atmos. Oceanic Technol.*, **29**, 1603–1616.

Bringi, V. N., M. A. Rico-Ramirez, and M. Thurai, 2011: Rainfall estimation with an operational polarimetric C-band radar in the United Kingdom: Comparison with a gauge network and error analysis. *J. Hydrometeor.*, **12**, 935–954.

Bringi, V. N., C. R. Williams, M. Thurai, and P. T. May, 2009: Using dual-polarized radar and dual-frequency profiler for DSD characterization: A case study from Darwin, Australia. *J. Atmos. Oceanic Technol.*, **26**, 2107–2122.

Carbone, R. E. and Y. Li, 2015: Tropical oceanic rainfall and sea surface temperature structure: Parsing causation from correlation in the MJO. *J. Atmos. Sci.*, **72**, 2703–2718.

Chelton, D. B., M. G. Schlax, M. H. Freilich, and R. F. Milliff, 2004: Satellite measurements reveal persistent small-scale features in ocean winds. *Science*, **303**, 978–983.

Chen, S., et al., 2015: A study of CINDY/DYNAMO MJO suppressed phase. *J. Atmos. Sci.*, **72**, 3755–3779.

Chen, S. S. and R. A. Houze, Jr., 1997: Diurnal variation and life-cycle of deep convective systems over the tropical Pacific Warm Pool. *Q. J. R. Meteorol. Soc.*, **123**, 357–388.

Cheng, C. P. and R. A. Houze, Jr., 1979: The distribution of convective and mesoscale precipitation in GATE radar echo patterns. *Mon. Wea. Rev.*, **107**, 1370–1381.

Chi, N.-H., R.-C. Lien, E. A. D'Asaro, and B. B. Ma, 2014: The surface mixed layer heat budget from mooring observations in the central Indian Ocean during Madden-Julian Oscillation events. *J. Geophys. Res.*, **119**, 4638–4652.

Chikira, M., 2014: Eastward-propagating intraseasonal oscillation represented by Chikira-Sugiyama Cumulus Parameterization. Part II: Understanding moisture variation under weak temperature gradient balance. *J. Atmos. Sci.*, **71**, 615–639.

Clayson, C. A. and A. S. Bogdanoff, 2013: The effect of diurnal sea surface temperature warming on climatological airsea fluxes. *J. Climate*, **26**, 2546–2556.

Clayson, C. A. and A. Chen, 2002: Sensitivity of a coupled single-column model in the tropics to treatment of the interfacial parameterizations. *J. Climate*, **15**, 1805–1831.

Clement, A. C., R. Seager, and R. Murtugudde, 2008: Why are there tropical warm pools? *J. Climate*, **18**, 5294–5311.

Costa, A. A., W. R. Cotton, R. L. Walko, and R. A. Pielke, 2001: Coupled ocean-cloud-resolving simulations of the air-sea interaction over the Equatorial Western Pacific. *J. Atmos. Sci.*, **58**, 3357–3375.

Cotton, W. R., G. H. Bryan, and S. C. van den Heever, 2011: *Storm and Cloud Dynamics*. 2d ed., Elsevier Academic Press, Oxford, pp. 809 pp.

Cronin, M. F. and M. J. McPhaden, 1997: The upper ocean heat balance in the western equatorial Pacific warm pool during September-December 1992. *J. Geophys. Res*, **102**, 8533–8553.

Cronin, M. F. and M. J. McPhaden, 1998: Upper ocean salinity balance in the Western Equatorial Pacific. *J. Geophys. Res*, **103**, 27 567–27 587.

Cronin, M. F. and M. J. McPhaden, 1999: Diurnal cycle of rainfall and surface salinity in the western Pacific warm pool. *Geophys. Res. Lett.*, **26**, 3465–3468.

Cronin, M. F., M. J. McPhaden, and R. H. Weisberg, 2000: Wind-forced reversing jets in the Western Equatorial Pacific. *J. Phys. Oceanogr.*, **30**, 657–676.

Cunning, J. B. and R. I. Sax, 1977: A Z-R relationship for the GATE B-scale array. *Mon. Weather Rev.*, **105**, 1330–1336.

de Boyer Montégut, C., G. Madec, A. S. Fischer, A. Lazar, and D. Iudicone, 2004: Mixed layer depth over the global ocean: An examination of profile data and a profile-based climatology. *J. Geophys. Res.*, **109**, C12.

de Szoeke, S. P., J. B. Edson, J. R. Marion, C. W. Fairall, and L. Bariteau, 2014: The MJO and air-sea interaction in TOGA COARE and DYNAMO. *J. Climate*, **28**, 597–622.

DeMott, C. A., N. P. Klingaman, and S. J. Woolnough, 2015: Atmosphere-ocean coupled processes in the Madden-Julian oscillation. *Rev. Geophys.*, **0**, (accepted).

DeMott, C. A., C. Stan, D. A. Randall, and M. D. Branson, 2014: Intraseasonal variability in coupled GCMs: The roles of ocean feedbacks and model physics. *J. Climate*, **27**, 4970–4995.

DeWitt, H. L., D. J. Coffman, K. J. Schulz, W. A. Brewer, T. S. Bates, and P. K. Quinn, 2013: Atmospheric aerosol properties over the equatorial Indian Ocean and the impact of the Madden-Julian Oscillation. *Bull. Am. Meteorol. Soc.*, **94**, 1871–1891.

Dorrestein, R., 1979: On the vertical buoyancy flux below the sea surface as induced by atmospheric factors. *J. Phys. Oceanogr.*, **9**, 229–231.

Doviak, J. and D. S. Zrnic, 2006: *Doppler Radar and Weather Observations*. 2d ed., Dover Publications, pp. 592 pp.

Drushka, K., S. T. Gille, and J. Sprintall, 2014b: The diurnal salinity cycle in the tropics. *J. Geophys. Res.*, **119**, 5874–5890.

Drushka, K., J. Sprintall, and S. T. Gille, 2014a: Subseasonal variations in salinity and barrier-layer thickness in the eastern equatorial Indian Ocean. *J. Geophys. Res.*, **119**, 805–823.

Drushka, K., J. Sprintall, S. T. Gille, and S. Wijffels, 2012: In situ observations of Madden-Julian Oscillation mixed layer dynamics in the Indian and Western Pacific Oceans. *J. Climate*, **25**, 2306–2328.

Duvel, J. P., R. Roca, and J. Vialard, 2004: Ocean mixed layer temperature variations induced by intraseasonal convective perturbations over the Indian Ocean. *J. Atmos. Sci.*, **61**, 1004–1023.

Duvel, J. P. and J. Vialard, 2007: Indo-Pacific sea surface temperature perturbations associated with intraseasonal oscillations of tropical convection. *J. Climate*, **20**, 3056–3082.

Edson, J. B., et al., 2013: On the exchange of momentum over the open ocean. *J. Phys. Oceanogr.*, **43**, 1589–1610.

Fairall, C. W., E. F. Bradley, J. S. Godfrey, G. A. Wick, J. B. Edson, and G. S. Young, 1996a: Cool-skin and warm-layer effects on sea surface temperature. *J. Geophys. Res.*, **101**, 1295–1308.

Fairall, C. W., E. F. Bradley, J. E. Hare, A. A. Grachev, , and J. B. Edson, 2003: Bulk parameterization of air-sea fluxes: Updates and verification for the COARE algorithm. *J. Climate*, **16**, 571–591.

Fairall, C. W., E. F. Bradley, D. . P. Rogers, J. B. Edson, and G. S. Young, 1996b: Bulk parameterization of air-sea fluxes for Tropical Ocean- Global Atmosphere Coupled-Ocean Atmosphere Response Experiment. *J. Geophys. Res.*, **101**, 3747–3764.

Feng, M., P. Hacker, and R. ukas, 1998: Upper ocean heat and salt balances in response to a westerly wind burst in the western equatorial Pacific during TOGA COARE. *J. Geophys. Res.*, **103**, 10 289–10 311.

Funk, A. and C. Schumacher, 2013: Analysis of rain classifications over the tropics by version 7 of the TRMM PR 2A23 algorithm. *J. Meteor. Soc. Japan*, **91**, 257–272.

Godfrey, J. S. and E. J. Lindstrom, 1989: The heat budget of the equatorial western Pacific surface mixed layer. *J. Geophys. Res.*, **94**, 8007–8017.

Gottschalck, J., P. E. Roundy, C. J. S. III, A. Vintzileos, and C. Zhang, 2013: Large-scale atmospheric and oceanic conditions during the 2011-2012 DYNAMO field campaign. *Mon. Weather Rev.*, **141**, 4173–4196.

Green, T. and D. F. Houk, 1979: The removal of organic surface films by rain. *Limnol. Oceanogr.*, **24**, 966–970.

Gunn, K. L. S. and J. S. Marshall, 1955: The effect of wind shear on falling precipitation. *J. Meteor.*, **12**, 339–349. Gunn, R. and G. D. Kinzer, 1949: The terminal velocity of fall for water droplets in stagnant air. *J. Meteor.*, **6**, 243–248.

Guy, N. and D. P. Jorgensen, 2014: Kinematic and precipitation characteristics of convective systems observed by airborne Doppler radar during the life cycle of a Madden-Julian Oscillation in the Indian Ocean. *Monthly Weather Review*, **142**, 1385–1402.

Han, W., 2005: Origins and dynamics of the 90-day and 30-60-day variations in the equatorial Indian Ocean. *J. Phys. Oceanogr.*, **35**, 708–728.

Han, W., P. Webster, R. Lukas, P. Hacker, and A. Hu, 2004: Impact of atmospheric intraseasonal variability in the Indian Ocean: Low-frequency rectification in equatorial surface current and transport. *J. Phys. Oceanogr.*, **34**, 1350–1372.

Hendon, H. H. and J. Glick, 1997: Intraseasonal air-sea interaction in the tropical Indian and Pacific Oceans. *J. Climate*, **10**, 647–661.

Henocq, C., J. Boutin, G. Reverdin, F. Petitcolin, S. Arnault, and P. Lattes, 2010: Vertical variability of near-surface salinity in the tropics: Consequences for l-band radiometer calibration and validation. *J. Atmos. Oceanic Technol.*, **27**, 192–209.

Houze, R. A., Jr., 1997: Stratiform precipitation in regions of convection: A meteorological paradox? *Bull. Am. Meteorol. Soc.*, **78**, 2179–2196. Houze, R. A., Jr., 2004: Mesoscale convective systems. *Rev. Geophys.*, **42**, RG4003.

Houze, R. A., Jr., 2014: *Cloud Dynamics*. 2d ed., Academic Press, International Geophysics (Book 104), pp. 496 pp.

Houze, R. A., Jr., S. S. Chen, D. E. Kingsmill, Y. Serra, and S. E. Yuter, 2000: Convection over the Pacific Warm Pool in relation to the atmospheric Kelvin-Rossby wave. *J. Atmos. Sci.*, **57**, 3058–3089.

Houze, R. A., Jr., K. L. Rasmussen, M. D. Zuluaga, and S. R. Brodzik, 2015: The variable nature of convection in the tropics and subtropics: A legacy of 16 years of the Tropical Rainfall Measuring Mission satellite. *Rev. Geophys.*, **53**, 994–1021.

Hsiao, M., S. Lichter, and L. G. Quintero, 1988: The critical Weber number for vortex and jet formation for drops impinging on a liquid pool. *Phys. Fluids*, **31**, 3560–3562.

Hsu, P.-C. and T. Li, 2012: Role of the boundary layer moisture asymmetry in causing the eastward propagation of the Madden-Julian Oscillation. *J. Climate*, **25**, 4914–4931.

Huang, G.-J., V. N. Bringi, and M. Thurai, 2008: Orientation angle distributions of drops after an 80-m fall using a 2D video disdrometer. *J. Atmos. Oceanic Technol.*, **25**, 1717–1723.

Hudlow, M. D., 1979: Mean rainfall patterns for the three phases of GATE. *J. Appl. Meteorol.*, **18**, 1656–1669. Illingworth, A. J. and T. M. Blackman, 2002: The need to represent raindrop size spectra as normalized gamma distributions for the interpretation of polarization radar observations. *J. Appl. Meteorol.*, **41**, 286–297.

Hung, M.-P., J.-L. Lin, W. Wang, D. Kim, T. Shinoda, and S. J. Weaver, 2013: MJO and convectively coupled equatorial waves simulated by CMIP5 climate models. *J. Climate*, **26**, 6185–6214.

Islam, T., M. A. Rico-Ramirez, M. Thurai, and D. Han, 2012: Characteristics of raindrop spectra as normalized gamma distribution from a Joss-Waldvogel disdrometer. *Atmos. Res.*, **108**, 57–73.

Jakob, C. and C. Schumacher, 2008: Precipitation and latent heating characteristics of the major tropical western pacific cloud regimes. *J. Climate*, **21**, 4348–4364.

Janowiak, J. E., P. A. Arkin, and M. Morrissey, 1994: An examination of the diurnal cycle in oceanic tropical rainfall using satellite and in situ data. *Mon. Weather Rev.*, **122**, 2296–2311.

Johnson, R. H. and X. Lin, 1997: Episodic trade-wind regimes over the Western Pacific Warm Pool. *J. Atmos. Sci.*, **54**, 2020–2034. Johnson, R. H., T. M.

Johnson, R. H., T. M. Rickenbach, S. A. Rutledge, P. E. Ciesielski, and W. H. Schubert, 1999: Trimodal characteristics of tropical convection. *J. Climate*, **12**, 2397–2418.

Johnson, R. and P. Ciesielski, 2013: Structure and properties of Madden-Julian Oscillations deduced from DYNAMO sounding arrays. *J. Atmos. Sci.*, **70**, 3157–3179.

Kara, A. B., P. A. Rochford, and H. E. Hurlburt, 2000a: Mixed layer depth variability over the global ocean. *J. Geophys. Res.*, **108**, 0.

Kara, A. B., P. A. Rochford, and H. E. Hurlburt, 2000b: An optimal definition for ocean mixed layer depth. *J. Geophys. Res.*, **105**, 16 803–16 821.

Kara, A. B., P. A. Rochford, and H. E. Hurlburt, 2003: Mixed layer depth variability and barrier layer formation over the North Pacific Ocean. *J. Geophys. Res.*, **105**, 16 783–16 801.

Katsaros, K. and K. J. Buettner, 1969: Influence of rainfall on temperature and salinity of the ocean surface. *J. Appl. Meteorol.*, **8**, 15–18.

Kawai, Y. and A. Wada, 2007: Diurnal sea surface temperature variation and its impact on the atmosphere and ocean: A review. *Oceanography*, **63**, 721–744.

Keenan, T. D., L. D. Carey, D. S. Zrnić, and P. T. May, 2001: Sensitivity of 5-cm wavelength polarimetric radar variables to raindrop axial ratio and drop size distribution. *J. Appl. Meteorol.*, **40**, 526–545.

Kemball-Cook, S. R. and B. C. Weare, 2001: The onset of convection in the Madden-Julian Oscillation. *J. Climate*, **14**, 780–793.

Kennedy, P. C. and S. A. Rutledge, 2011: S-band dual-polarization radar observations of winter storms. *J. Appl. Meteor. Climatol.*, **50**, 844–858.

Kiladis, G. N., K. H. Straub, and P. T. Haertel, 2005: Zonal and vertical structure of the Madden-Julian Oscillation. *J. Atmos. Sci.*, **62**, 2790–2809.

Kim, D., et al., 2009: Application of MJO simulation diagnostics to climate models. *J. Climate*, **22**, 6413–6436.

Kliche, D. V., P. L. Smith, and R. W. Johnson, 2008: L-moment estimators as applied to gamma drop size distributions. *J. Appl. Meteor. Climatol.*, **47**, 3117–3130.

Kumjian, M. R., 2013: Principles and applications of dual-polarization weather radar. part I: Description of the polarimetric radar variables. *J. Operational Meteor.*, **1**, 226–242.

Kumjian, M. R. and O. P. Prat, 2014: The impact of raindrop collisional processes on the polarimetric radar variables. *J. Atmos. Sci.*, **71**, 3052–3067.

Lau, W. K. M. and D. E. Waliser, 2005: *Intraseasonal Variability of the Atmosphere-Ocean Climate System*. Springer, Heidelberg, Germany, pp. 474 pp.

Lee, G. W., I. Zawadzki, W. Szyrmer, D. Sempere-Torres, and R. Uijlenhoet, 2004: A general approach to double-moment normalization of drop size distributions. *J. Appl. Meteorol.*, **43**, 264–281.

LeMone, M. A., E. J. Zipser, and S. B. Trier, 1998: The role of environmental shear and thermodynamic conditions in determining the structure and evolution of mesoscale convective systems during TOGA COARE. *J. Atmos. Sci.*, **55**, 3493–3518.

Levitus, S., 1982: Climatological atlas of the world ocean, NOAA professional paper. *U.S. Gov. Printing Office*, **13**, 190 pp.

Lewis, M., M. Carr, G. Feldmann, W. Essaias, and C. McClain, 1990: Influence of penetrating solar radiation on the heat budget of the equatorial Pacific Ocean. *Nature*, **347**, 543–545.

Li, Y. and R. E. Carbone, 2012: Excitation of rainfall over the tropical Western Pacific. *J. Atmos. Sci.*, **69**, 2983–2994.

Lilly, D. K., 1960: On the theory of disturbances in a conditionally unstable atmosphere. *Mon. Weather Rev.*, **88**, 1–17.

Lin, X. and R. H. Johnson, 1996: Heating, moistening, and rainfall over the Western Pacific Warm Pool during TOGA COARE. *J. Atmos. Sci.*, **53**, 3367–3383. Lo, K. K. and R. E. Passarelli, 1982: The growth of snow in winter storms: An airborne observational study. *J. Atmos. Sci.*, **39**, 697–706.

Lin, J.-L., et al., 2006: Tropical intraseasonal variability in 14 IPCC AR4 climate models. Part i: Convective signals. *J. Climate*, **19**, 2665–2690.

Lindzen, R. and S. Nigam, 1987: On the role of sea surface temperature gradients in forcing low level winds and convergence in the tropics. *J. Atmos. Sci.*, **44**, 2418–2436.

Lloyd, I. D. and G. A. Vecchi, 2010: Submonthly Indian Ocean cooling events and their interaction with large-scale conditions. *J. Climate*, **23**, 700–716.

Lombardo, C. P. and M. C. Gregg, 1999: Similarity scaling of viscous and thermal dissipation in a convecting surface boundary layer. *J. Geophys. Res.*, **94**, 6273–6284.

Lukas, R. and E. Lindstrom, 1991: The mixed layer of the Western Equatorial Pacific Ocean. *J. Geophys. Res.*, **96**, 3343–335.

Madden, R. A. and P. R. Julian, 1994: Observations of the 40-50-day tropical oscillation-a review. *Mon. Weather Rev.*, **122**, 814–837.

Maloney, E. D. and A. H. Sobel, 2004: Surface fluxes and ocean coupling in the tropical Intraseasonal Oscillation. *J. Climate*, **17**, 4368–4386.

Mapes, B., S. Tulich, J. Lin, and P. Zuidema, 2006: The mesoscale convection life cycle: Building block or prototype for large-scale tropical waves? *Dyn. Atmos. Oceans*, **42**, 3–29.

Matthews, A. J., D. B. Baranowski, K. J. Heywood, P. J. Flatau, and S. Schmidtko, 2014: The surface diurnal warm layer in the Indian Ocean during CINDY/DYNAMO. *J. Climate*, **27**, 1658–1672.

Marshall, J. S. and W. M. K. Palmer, 1948: The distribution of raindrops with size. *J. Meteor.*, **5**, 165–166.

Matsuno, T., 1966: Quasi-geostrophic motions in the equatorial area. *J. Meteor. Soc. Japan*, **44**, 25–53.

McCulloch, M., P. Spurgeon, and A. Chuprin, 2012: Have mid-latitude ocean rain-lenses been seen by the SMOS satellite? *Ocean Modell.*, **43**, 108–111.

McPhaden, M. J. and G. R. Foltz, 2013: Intraseasonal variations in the surface layer heat balance of the central equatorial Indian Ocean: The importance of zonal advection and vertical mixing. *J. Geophys. Res.*, **40**, 2737–2741.

Miller, J., 1976: The Salinity Effect in a Mixed Layer Ocean Model. *J. Phys. Oceanogr.*, **6**, 29–35.

Minobe, S. and S. Takebayashi, 2008: Influence of the Gulf Stream on the troposphere. *Climate Dyn.*, **44**, 2079–2095.

Minor, H. A., R. M. Rauber, S. Göke, and L. D. Girolamo, 2011: Trade wind cloud evolution observed by polarization radar: Relationship to giant condensation nuclei concentrations and cloud organization. *J. Atmos. Sci.*, **68**, 1075–1096.

Mishchenko, M. I., L. D. Travis, and D. W. Mackowski, 1996: T-matrix computations of light scattering by nonspherical particles: A review. *J. Quant. Spectrosc. Radiat. Transfer*, **55**, 535–575.

Morrison, H., G. Thompson, and V. Tatarskii, 2009: Impact of cloud microphysics on the development of trailing stratiform precipitation in a simulated squall line: Comparison of one- and two-moment schemes. *Mon. Weather Rev.*, **137**, 991–1007.

Moum, J. N., 1990: Profiler measurements of vertical velocity fluctuations in the ocean. *J. Atmos. Oceanic Technol.*, **7**, 323–333.

Moum, J. N., et al., 2014: Air-sea interactions from MJO westerly wind bursts. *Bull. Am. Meteorol. Soc.*, **95**, 1185–1199.

Mujumdar, M., K. Salunke, S. A. Rao, M. Ravichandran, and B. N. Goswami, 2011: Diurnal cycle induced amplification of sea surface temperature intraseasonal oscillations over the Bay of Bengal in summer monsoon season. *IEEE Geosci. Remote Sens. Lett.*, **8**, 206–210.

Munchak, S. J., C. D. Kummerow, and G. Elsaesser, 2012: Relationships between the raindrop size distribution and properties of the environment and clouds inferred from trmm. *J. Climate*, **25**, 2963–2978.

Niller, P. P. and E. B. Kraus, 1977: *One-dimensional models. Modeling and Prediction of the upper layers of the ocean*. Pergamon Press, pp. 285 pp.

Nitta, T. and S. Esbensen, 1974: Heat and moisture budget analyses using BOMEX data. *Mon. Wea. Rev.*, **102**, 17–28.

Ostapoff, F., Y. Tarbeyev, and S. Worthem, 1973: Heat fluxes and precipitation estimates from oceanographic observations. *Science*, **180**, 960–962.

Penide, G., V. V. Kumar, A. Protat, and P. T. May, 2013: Statistics of drop size distribution parameters and rain rates for stratiform and convective precipitation during the north Australian wet season. *Mon. Weather Rev.*, **141**, 3222–3237.

Plueddemann, A. and J. Farrar, 2006: Observations and models of the energy flux from the wind to mixed-layer inertial currents. *Deep-Sea Res. Pt. II*, **53**, 5–30.

Powell, S. W. and R. A. Houze, Jr., 2013: The cloud population and onset of the Madden-Julian Oscillation over the Indian Ocean during DYNAMO-AMIE. *J. Geophys. Res.*, **118**, 11 979–11 995.

Price, J. F., 1979: Observations of a rain-formed mixed layer. *J. Phys. Oceanogr.*, **9**, 643–649.

Price, J. F., R. A. Weller, and R. Pinkel, 1986: Diurnal cycling: Observations and models of the upper ocean response to diurnal heating, cooling, and wind mixing. *J. Geophys. Res.*, **91**, 8411–8427.

Prosperetti, A. and H. N. Oguz, 1993: The impact of drops on liquid surfaces and the underwater noise of rain. *Ann. Rev. Fluid Mech.*, **25**, 577–602.

Pruppacher, H. R. and J. D. Klett, 1997: *Microphysics of Clouds and Precipitation*. 2d ed., Kluwer Academic Publishers, Dordereht, The Netherlands, pp. 954 pp.

Prytherch, J., J. T. Farrar, and R. A. Weller, 2013: Moored surface buoy observations of the diurnal warm layer. *J. Geophys. Res.*, **118**, 4553–4569.

Raman, S. and A. J. Riordan, 1988: The genesis of Atlantic lows experiment: The planetary-boundary-layer subprogram of gale. *Bull. Amer. Meteor. Soc.*, **69**, 161–172.

Rauber, R. M., et al., 2007: Rain in shallow cumulus over the ocean: The RICO campaign. *Bulletin of the American Meteorological Society*, **88**, 1912–1928.

Reverdin, G., S. Morisset, J. Boutin, and N. Martin, 2012: Rain-induced variability of near sea-surface T and S from drifter data. *J. Geophys. Res.*, **117**, C02 032.

Rickenbach, T. M. and S. A. Rutledge, 1988: Convection in TOGA COARE: Horizontal scale, morphology, and rainfall production. *J. Atmos. Sci.*, **55**, 2715–2729.

Riley, E. M., B. E. Mapes, and S. N. Tulich, 2011: Clouds associated with the Madden-Julian Oscillation: A new perspective from CloudSat. *J. Atmos. Sci.*, **68**, 3032–3051.

Rodriguez, F. and R. J. Mesler, 1988: The penetration of drop-formed vortex rings into pools of liquid. *J. Colloid. Interface Sci.*, **121**, 121–129.

Rowe, A. K. and R. A. Houze, Jr., 2014: Microphysical characteristics of MJO convection over the Indian Ocean during DYNAMO. *J. Geophys. Res.*, **119**, 2543–2554.

Rowe, A. K. and R. A. Houze, Jr., 2015: Cloud organization and growth during the transition from suppressed to active MJO conditions. *J. Geophys. Res.*, **120**, 10 324–10 350.

Ruppert, J. H. and R. H. Johnson, 2015: Diurnally modulated cumulus moistening in the pre-onset stage of the Madden-Julian Oscillation during DYNAMO. *J. Atmos. Sci..*, **72**, 1622–1647.

Ryzhkov, A. V., S. E. Giangrande, V. M. Melnikov, and T. J. Schuur, 2005: Calibration issues of dual-polarization radar measurements. *J. Atmos. Oceanic Technol.*, **22**, 1138–1155.

Salles, C. and J.-D. Creutin, 2003: Instrumental uncertainties in Z-R relationships and raindrop fall velocities. *J. Appl. Meteorol.*, **42**, 279–290.

Sauvageot, H. and J.-P. Lacaux, 1995: The shape of averaged drop size distributions. *J. Atmos. Sci.*, **52**, 1070–1083.

S. Schmidtko, S., G. C. Johnson, and J. M. Lyman, 2013a: A global monthly isopycnal upper-ocean climatology with mixed layers. *J. Geophys. Res.*, **118**, 1658–1672.

Schönhuber, M., G. Lammer, and W. L. Randeu, 2008: *The 2D-Video-Disdrometer*. S. Michaelides, Springer, 3-31 pp.

Saxen, T. R. and S. A. Rutledge, 1998: Surface fluxes and boundary layer recovery in TOGA COARE: Sensitivity to convective organization. *J. Atmos. Sci.*, **55**, 2763–2781.

Schneider, N. and B. Qiu, 2015: The atmospheric response to weak sea surface temperature fronts. *J. Atmos. Sci.*, **72**, 3356–3377.

Schumacher, C. and R. A. Houze, Jr., 2003: The TRMM Precipitation Radar's view of shallow, isolated rain. *J. Appl. Meteorol.*, **42**, 1519–1524.

Schumacher, C., R. A. Houze, Jr., and I. Kraucunas, 2004: The tropical dynamical response to latent heating estimates derived from the TRMM precipitation radar. *J. Atmos. Sci.*, **61**, 1341–1358.

Schumacher, C., S. N. Stevenson, and C. R. Williams, 2015: Vertical motions of the tropical convective cloud spectrum over Darwin, Australia. *Quarterly Journal of the Royal Meteorological Society*, **0**, 0.

Seiki, A., M. Katsumata, T. Horii, T. Hasegawa, K. J. Richards, K. Yoneyama, and R. Shirooka, 2013: Abrupt cooling associated with the oceanic Rossby wave and lateral advection during CINDY2011. *J. Geophys. Res.*, **118**, 5523–5535.

Seo, H., A. C. Subramanian, A. J. Miller, and N. R. Cavanaugh, 2014: Coupled impacts of the diurnal cycle of sea surface temperature on the Madden-Julian Oscillation. *J. Climate*, **27**, 8422–8443.

Serra, Y. L. and M. J. McPhaden, 2004: In situ observations of diurnal variability in rainfall over the tropical Pacific and Atlantic Oceans. *J. Climate*, **17**, 3496–3509.

Sharma, S., M. Konwar, D. K. Sarma, M. C. R. Kalapureddy, and A. R. Jain, 2009: Characteristics of rain integral parameters during tropical convective, transition, and stratiform rain at Gadanki and its application in rain retrieval. *J. Appl. Meteor. Climatol.*, **48**, 1245–1266.

Shinoda, T., 2005: Impact of the diurnal cycle of solar radiation on intraseasonal SST variability in the western equatorial Pacific. *J. Climate*, **18**, 2628–2636.

Shinoda, T. and H. H. Hendon, 1998: Mixed layer modeling of intraseasonal variability in the tropical Western Pacific and Indian Oceans. *J. Climate*, **11**, 2668–2685.

Shinoda, T. and H. H. Hendon, 2001: Upper-ocean heat budget in response to the Madden-Julian Oscillation in the Western Equatorial Pacific. *J. Climate*, **14**, 4147–4165.

Short, D. A., P. A. Kucera, B. S. Ferrier, J. C. Gerlach, S. A. Rutledge, and O. W. Thiele, 1997: Shipboard radar rainfall patterns within the TOGA COARE IFA. *Bull. Am. Meteorol. Soc.*, **12**, 2817–2836.

Siegel, D. A., J. Ohlmann, L. Washburn, R. Bidigare, E. F. C. Nosse, and Y. Zhou, 1995: Solar radiation, phytoplankton pigments and radiant heating of the equatorial Pacific. *J. Geophys. Res.*, **100**, 4885–4891.

Smith, P. L. and D. V. Kliche, 2005: The bias in moment estimators for parameters of drop size distribution functions: Sampling from exponential distributions. *J. Appl. Meteorol.*, **44**, 1195–1205.

Smyth, W. D., D. Hebert, and J. N. Moum, 1996a: Local ocean response to a multiphase westerly wind burst: 1. dynamic response. *J. Geophys. Res.*, **101**, 22 495–22 512.

Smyth, W. D., D. Hebert, and J. N. Moum, 1996b: Local ocean response to a multiphase westerly wind burst: 2. thermal and freshwater responses. *J. Geophys. Res.*, **101**, 22 513–22 533.

Soloviev, A. and R. Lukas, 2006: *The Near-Surface Layer of the Ocean: Structure, Dynamics and Applications*. Springer, Netherlands, pp. 574 pp.

Soloviev, A. and N. Vershinsky, 1982: The vertical structure of the thin surface layer of the ocean under conditions of low wind speed. *Deep Sea Res.*, **29**, 1437–1449.

Sprintall, J. and M. Tomczak, 1992: Evidence of the barrier layer in the surface layer of the tropics. *J. Geophys. Res.*, **97**, 7305–7316.

Steiner, M., R. A. Houze, Jr., and S. E. Yuter, 1995: Climatological characterization of three-dimensional storm structure from operational radar and rain gauge data. *J. Appl. Meteorol.*, **34**, 1978–2007.

Steiner, M., J. A. Smith, and R. Uijlenhoet, 2004: A microphysical interpretation of radar reflectivity-rain rate relationships. *J. Atmos. Sci.*, **61**, 1114–1131.

Straka, J. M., D. S. Zrnić, and A. V. Ryzhkov, 2000: Bulk hydrometeor classification and quantification using polarimetric radar data: Synthesis of relations. *J. Appl. Meteorol.*, **39**, 1341–1372.

Stull, R. B., 1988: *An Introduction to Boundary Layer Meteorology*, Kluwer Academic.

Sublette, M. S. and G. S. Young, 1996: Warm-season effects of the Gulf Stream on mesoscale characteristics of the atmospheric boundary layer. *Mon. Wea. Rev.*, **124**, 653–667.

Sui, C.-H., X. Li, and K.-M. Lau, 1988: Radiative-convective processes in simulated diurnal variations of tropical oceanic convection. *J. Atmos. Sci.*, **55**, 2345–2357.

Sui, C.-H., X. Li, K.-M. Lau, and D. Adamec, 1997: Diurnal variations in tropical oceanic cumulus convection during TOGA COARE. *Mon. Weather Rev.*, **125**, 448–462.

Sui, C.-H., X. Li, M. M. Rienecker, K.-M. Lau, I. Laszlo, and R. T. Pinker, 2003: The role of daily surface forcing in the upper ocean over the tropical Pacific: A numerical study. *J. Climate*, **16**, 756–766.

Sutherland, G., G. Reverdin, L. Mari, and B. Ward, 2014: Mixed and mixing layer depths in the ocean surface boundary layer under conditions of diurnal stratification. *Geophys. Res. Lett.*, **41**, 8469–8476.

Takayabu, Y. N., 2002: Spectral representation of rain profiles and diurnal variations observed with TRMM PR over the equatorial area. *Geophys. Res. Lett.*, **29**, 25–1 – 25–4.

Takayabu, Y. N., K.-M. Lau, and C.-H. Sui, 1995: Observation of a quasi-2-day wave during TOGA COARE. *Mon. Wea. Rev.*, **124**, 1892–1913.

Testud, J., S. Oury, R. A. Black, P. Amayenc, and X. Dou, 2001: The concept of "normalized" distribution to describe raindrop spectra: A tool for cloud physics and cloud remote sensing. *J. Appl. Meteorol.*, **40**, 1118–1140.

Thompson, E. J., S. A. Rutledge, B. Dolan, V. Chandrasekar, and B.-L. Cheong, 2014: A dual-polarization radar hydrometeor classification algorithm for winter precipitation. *J. Atmos. Oceanic Technol.*, **31**, 1457–1481.

Thompson, E. J., S. A. Rutledge, B. Dolan, and M. Thurai, 2015: Drop size distributions and radar observations of convective and stratiform rain over the equatorial Indian and west Pacific Oceans. *J. Atmos. Sci.*, **72**, 4091–4125.

Thurai, M., G. J. Huang, V. N. Bringi, W. L. Randeu, and M. Schönhuber, 2007: Drop shapes, model comparisons, and calculatinos of polarimetric radar parameters in rain. *J. Atmos. Oceanic Technol.*, **24**, 1019–1032.

Thurai, M., V. N. Bringi, and P. T. May, 2010: Cpol radar-derived drop size distribution statistics of stratiform and convective rain for two regimes in Darwin, Australia. *J. Atmos. Oceanic Technol.*, **27**, 932–942.

Thurai, M., C. R. Williams, and V. N. Bringi, 2014: Examining the correlations between drop size distribution parameters using data from two side-by-side 2D-video disdrometers'. *Atmos. Res.*, **144**, 95–110.

Tokay, A., P. G. Bashor, and K. R. Wolff, 2005: Error characteristics of rainfall measurements by collocated Joss-Waldvogel disdrometers. *J. Atmos. Oceanic Technol.*, **22**, 513–527.

Tokay, A., A. Kruger, and W. F. Krajewski, 2001: Comparison of drop size distribution measurements by impact and optical disdrometers. *J. Appl. Meteorol.*, **40**, 2083–2097.

Tokay, A., W. A. Petersen, P. Gatlin, and M. Wingo, 2013: Comparison of raindrop size distribution measurements by collocated disdrometers. *J. Atmos. Oceanic Technol.*, **30**, 1672–1690.

Tokay, A. and D. A. Short, 1996: Evidence from tropical raindrop spectra of the origin of rain from stratiform versus convective clouds. *J. Appl. Meteorol.*, **35**, 355–371.

Tokay, A., D. A. Short, C. R. Williams, W. L. Ecklund, and K. S. Gage, 1999: Tropical rainfall associated with convective and stratiform clouds: Intercomparison of disdrometer and profiler measurements. *J. Appl. Meteorol.*, **99**, 302–320.

Turner, J. S., 1973: *Buoyancy Effects in Fluids*. 1st ed., Cambridge University Press, pp. 367 pp.

Twomey, S., 1977: The influence of pollution on the shortwave albedo of clouds. *J. Atmos. Sci.*, **34**, 1149–1152.

Uijlenhoet, R., M. Steiner, and J. A. Smith, 2003: Variability of raindrop size distributions in a squall line and implications for radar rainfall estimation. *J. Hydrometeor.*, **4**, 43–61.

Ulbrich, C. W., 1983: Natural variations in the analytical form of the raindrop size distribution. *J. Climate Appl. Meteor.*, **22**, 1764–1775.

Ulbrich, C. W. and D. Atlas, 1978: The rain parameter diagram: Methods and applications. *J. Geophys. Res.*, **83**, 1319–1325.

Ulbrich, C. W. and D. Atlas, 1998: Rainfall microphysics and radar properties: Analysis methods for drop size spectra. *J. Appl. Meteorol.*, **37**, 912–923.

Ulbrich, C. W. and D. Atlas, 2002: On the separation of tropical convective and stratiform rains. *J. Appl. Meteorol.*, **41**, 188–195.

Ulbrich, C. W. and D. Atlas, 2007: Microphysics of raindrop size spectra: Tropical continental and maritime storms. *J. Appl. Meteor. Climatol.*, **46**, 1777–1791.

Vialard, J. and P. Delecluse, 1998a: An OGCM study for the TOGA Decade. Part I: Role of salinity in the physics of the Western Pacific Fresh Pool. *J. Phys. Oceanogr.*, **28**, 1071–1088.

Vialard, J. and P. Delecluse, 1998b: An OGCM study for the TOGA Decade. Part II: Barrier-layer formation and variability. *J. Phys. Oceanogr.*, **28**, 1089–1106.

Virts, K. S. and R. A. Houze, Jr., 2015: Variation of lightning and convective rain fraction in mesoscale convective systems of the MJO. *Journal of the Atmospheric Sciences*, **72**, 1932–1944.

Waldvogel, A., 1974: The N0 jump of raindrop spectra. *J. Atmos. Sci.*, **31**, 1067–1078.

Walesby, K., J. Vialard, P. J. Minnett, A. H. Callaghan, and B. Ward, 2015: Observations indicative of rain-induced double diffusion in the ocean surface boundary layer. *Geophys. Res. Lett.*, **42**, 3963–3972.

Wang, W., A. Kumar, J. X. Fu, and M.-P. Hung, 2015: What is the role of the sea surface temperature uncertainty in the prediction of tropical convection associated with the MJO? *Mon. Wea. Rev.*, **143**, 3156–3175.

Ward, B., 2006: Near-surface ocean temperature. *J. Geophys. Res.*, **111**, C02 004.

Waterman, P. C., 1971: Symmetry, unitarity, and geometry in electromagnetic scattering. *Phys. Rev.*, **3**, 805–812.

Webber, B. G. M., A. J. Matthews, and K. J. Heywood, 2010: A dynamical ocean feedback mechanism for the Madden-Julian Oscillation. *Q. J. R. Meteorol. Soc.*, **136**, 740–754.

Webber, B. G. M., A. J. Matthews, K. J. Heywood, and D. P. Stevens, 2011: Ocean Rossby waves as a triggering mechanism for primary Madden-Julian events. *Q. J. R. Meteorol. Soc.*, **138**, 514–527.

Webster, P. J., C. A. Clayson, and J. A. Curry, 1996: Clouds, radiation, and the diurnal cycle of sea surface temperature in the tropical Western Pacific. *J. Climate*, **9**, 1712–1730.

Webster, P. J. and R. Lukas, 1992: TOGA COARE: The coupled ocean-atmosphere response experiment. *Bull. Am. Meteorol. Soc.*, **73**, 1377–1416.

Weller, R. A. and S. P. Anderson, 1996: Surface meteorology and air-sea fluxes in the Western Equatorial Pacific Warm Pool during the TOGA Coupled Ocean-Atmosphere Response Experiment. *J. Climate*, **9**, 1–30.

Wheeler, M. C. and H. H. Hendon, 2004: An all-season real-time multivariate MJO index: Development of an index for monitoring and prediction. *Mon. Weather Rev.*, **132**, 1917–1932.

Williams, C. R., W. L. Ecklund, and K. S. Gage, 1995: Classification of precipitating clouds in the tropics using 915-mhz wind profilers. *J. Atmos. Oceanic Technol.*, **12**, 996–1012.

Wijesekera, H. W. and M. C. Gregg, 1996: Surface layer response to weak winds, westerly bursts, and rain squalls in the western Pacific warm pool. *J. Geophys. Res.*, **101**, 977–997.

Wijesekera, H. W., C. A. Paulson, and A. Huyer, 1999: The effect of rainfall on the surface layer during a westerly wind burst in the western equatorial Pacific. *J. Geophys. Res.*, **29**, 612–632.

Wijesekera, H. W., D. L. Rudnick, C. A. Paulson, S. D. Pierce, W. S. Pegau, J. Mickett, and M. C. Gregg, 2005: Upper ocean heat and freshwater budgets in the eastern Pacific warm pool. *J. Geophys. Res.*, **110**, 2156–2202.

Willis, P. T., 1984: Functional fits to some observed drop size distributions and parameterization of rain. *J. Atmos. Sci.*, **41**, 1648–1661.

Wilson, E. A., A. L. Gordon, and D. Kim, 2013: Observations of the madden julian oscillation during indian ocean dipole events. *J. Geophys. Res.*, **118**, 2588–2599.

Woolnough, S. J., J. M. Slingo, and B. J. Hoskins, 2000: The relationship between convection and sea surface temperature on intraseasonal timescales. *J. Climate*, **13**, 2086–2104.

Woolnough, S. J., J. M. Slingo, and B. J. Hoskins, 2001: The organization of tropical convection by intraseasonal sea surface temperature anomalies. *Q. J. R. Meteorol. Soc.*, **127**, 887–907.

Woolnough, S. J., F. Vitart, and M. A. Balmaseda, 2007: The role of the ocean in the Madden-Julian Oscillation: Implications for MJO prediction. *Q. J. Roy. Meteorol. Soc.*, **133**, 117–119.

Xu, W. and S. A. Rutledge, 2014: Convective characteristics of the Madden-Julian Oscillation over the Central Indian Ocean Observed by Shipborne Radar during DYNAMO. *J. Atmos. Sci.*, **71**, 2859–2877.

Xu, W. and S. A. Rutledge, 2015: Morphology, intensity, and rainfall production of MJO convection: Observations from DYNAMO and TRMM. *J. Atmos. Sci.*, **72**, 623–640.

Xu, W., S. A. Rutledge, C. Schumacher, and M. Katsumata, 2015: Evolution, properties, and spatial variability of MJO convection near and off the equator during DYNAMO. *J. Atmos. Sci.*, **72**, 4126–4147.

Yang, G.-Y. and J. Slingo, 2001: The diurnal cycle in the tropic. *Mon. Weather Rev.*, **129**, 784–801.

Yanai, M., S. Esbensen, and J.-H. Chu, 1973: Determination of bulk properties of tropical cloud clusters from large-scale heat and moisture budgets. *Journal of the Atmospheric Sciences*, **30**, 611–627.

Yoneyama, K., C. Zhang, and C. N. Long, 2013: Tracking pulses of the Madden-Julian oscillation. *Bull. Am. Meteorol. Soc.*, **94**, 1871–1891.

Yoneyama, K., et al., 2008: MISMO field experiment in the equatorial Indian Ocean. *Bull. Am. Meteorol. Soc.*, **89**, 1889–1903.

Yoshikawa, Y., 2015: Scaling surface mixing/mixed layer depth under stabilizing buoyancy flux. *J. Phys. Oceanogr.*, **45**, 247–258.

You, Y., 1995: Salinity Variability and Its Role in the Barrier-Layer Formation during TOGA-COARE. J. Phys. Oceanogr., 25, 2778–2807.

Young, G. S., S. M. Perugini, and C. W. Fairall, 1995: Convective wakes in the equatorial Western Pacific during TOGA. *Mon. Weather Rev.*, **125**, 110–123.

Yuter, S. E. and R. A. Houze, Jr., 1997: Measurements of raindrop size distributions over the pacific warm pool and implications for z-r relations. *J. Appl. Meteorol.*, **36**, 847–867.

Yuter, S. and R. A. Houze, Jr., 1998: The natural variability of precipitating clouds over the Western Pacific Warm Pool. *Q. J. Roy. Met. Soc.*, **124**, 53–99.

Yuter, S. E. and R. A. Houze, Jr., 2002: Comment on "partitioning tropical oceanic convective and stratiform rains by draft strength" by David Atlas et al. *J. Geophys. Res.*, **107**, ACL 4–1.

Zhang, C., 2005: Madden-Julian Oscillation. *Rev. Geophys.*, **43**, RG2003.

Zhang, C. and S. M. Hagos, 2009: Bi-modal structure and variability of large-scale diabatic heating in the tropics. *J. Atmos. Sci.*, **66**, 3621–3640.

Zhang, C., J. Gottschalck, E. D. Maloney, M. W. Moncrieff, F. Vitart, D. E. Waliser, B. Wang, and M. C. Wheeler, 2013: Cracking the MJO nut. *Geophys. Res. Lett.*, **40**, 1223–1230.

Zhang, C. and M. J. McPhaden, 2000: Intraseasonal surface cooling in the Equatorial Western Pacific. *J. Climate*, **13**, 2261–2276.

Zhu, S., X. Guo, G. Lu, and L. Guo, 2015: Ice crystal habits and growth processes in stratiform clouds with embedded convection examined through aircraft observation in northern China. *Journal of the Atmospheric Sciences*, **72**, 2011–2032.

Zhu, H., H. H. Hendon, and C. Jakob, 2009: Convection in a parameterized and superparameterized model and its role in the representation of the MJO. *J. Atmos. Sci.*, **66**, 2796–2811.

Zipser, E. J., 2003: Some views on "hot towers" after 50 years of tropical field programs and two years of TRMM data. *Meteorological Monographs*, **29**, 49–49.

Zipser, E. J. and M. A. LeMone, 1980: Cumulonimbus vertical velocity events in gate. Part II: Synthesis and model core structure. *J. Atmos. Sci.*, **37**, 2458–2469.

Zuidema, P., et al., 2012: On trade wind cumulus cold pools. *J. Atmos. Sci.*, **69**, 258–280.

Zuluaga, M. D. and R. A. Houze, Jr., 2013: Evolution of the population of precipitating convective systems over the equatorial Indian Ocean in active phases of the Madden-Julian Oscillation. *J. Atmos. Sci.*, **70**, 2713–2725.